UNIVERSITY OF BIRMINGHAM

Synthesis and Characterisation of New Phosphate and Fluorophosphate Materials

by

Julie Marie Rutter

A thesis submitted to
the University of Birmingham
for the degree of
Doctor of Philosophy

The School of Chemistry
College of Engineering and Physical Sciences
The University of Birmingham
November 2013

Abstract

This thesis focuses on the use of the monofluorophosphate anion to synthesise a range of materials as potential biomaterials. Here we report the novel synthesis of a monazite structured $SrPO_3F$, formed from a readily available PO_3F^{2-} precursor via a precipitation reaction. Subsequently, through modifications to the reaction temperature a novel hydrated phase has also been synthesised. Both structures consist of distorted PO_3F^{2-} tetrahedron with an apparent ordering of the P-F bond.

$SrPO_3F$ is the first example of a monazite system containing divalent cations. To investigate the compositional tolerance of this system, a range of mixed metal systems were explored using Ca^{2+}, Ba^{2+}, Eu^{2+}. The incorporation of trivalent ions (La^{3+} and PO_4^{3-}) into the $SrPO_3F$ phase was pursued as it has been reported previously that low levels of Sr^{2+} incorporation into $LaPO_4$ produced a proton conducting material.

In addition, a successful synthesis of a modified gypsum system, involving inclusion of fluorophosphate ($Ca(SO_4)_x(PO_3F)_{1-x}\cdot 2H_2O$, where x = 0-1), has been achieved via a precipitation reaction. Initial solubility results suggest that cements formed with calcium fluorophosphates offer greater water stability, a current limiting factor in the wider use of gypsum.

This thesis also describes a study into the stabilisation of synthetic amorphous calcium carbonate (ACC) using the orthophosphate, fluorophosphate and pyrophosphate species. Results suggest that crystallisation of ACC is inhibited through exposure to appropriate levels of these simple inorganic species orthophosphate, fluorophosphate and pyrophosphate.

Acknowledgements

Firstly, I would like to thank my supervisor Dr. Adrian Wright for all his support and guidance throughout the PhD. Although the work has been challenging at times, I have thoroughly enjoyed my time over the past four years. I would also like to thank past and present members of the Wright group for all of their help, support and advice during the PhD and for making it such an enjoyable group to work with. In particular, my thanks go to Tom and Yasmin for our many conversations over a hot chocolate in starbucks.

I would like to thank members of fifth floor for all of their help and for making my time here one to remember. In particular I would like to express my gratitude to Victoria, Colin, Annabelle and Jackie for the many hours spent with the XRF. I would also like to thank Dr. Jackie Deans for all her help with the other equipment and for all of the daily chats over a cup of tea.

I would like to thank the EPSRC and the University of Birmingham for funding to do this PhD and to Dr. Kevin Knight and Dr. Ron Smith (ISIS) for their help with the data collection at ISIS, particularly Dr Knight who helped with some tricky matrix transformations. Also, thanks to Dr. John Hanna and Scott King (University of Warwick) for the collection of the ^{31}P and ^{19}F NMR data and for allowing me to assist with some of the measurements.

Finally, a special thanks to Mariana, Annabelle and Michaela for making the past four years very memorable both inside and outside of uni and for always being there. Last but by no means least, I would like to thank two more people, first of all my mom, for all of her constant love, support and encouragement that she has given me over the years

and lastly Geoff, who has been so supportive and helpful throughout this whole process, for which I am very grateful.

Abbreviations

α-TCP	Alpha tri-calcium phosphate
μ-$CaCO_3$	Mu-calcium carbonate
ABCC	Amorphous basic calcium carbonate
ACC	Amorphous calcium carbonate
ALP	Alkaline phosphatase
BP's	Bisphosphonates
BVS	Bond Valence Sum
$CaCO_3$	Calcium Carbonate
CHA	Carbonated hydroxyapatite
CSA	Chemical shift anisotropy
DCPD	Di-calcium phosphate dihydrate/Brushite
DTA	Differential thermal analysis
EDAX	Energy dispersive x-ray analysis
EDXRF	Energy dispersive x-ray fluorescence spectroscopy
EXAFS	Extended x-ray absorption fine structure
FHA	Fluorapatite
FID	Free induction decay
FWHM	Full width half maximum
GSAS	General structure analysis system
HA	Hydroxyapatite

HRPD	High resolution powder diffraction
ICDD ®	International center for diffraction database
MAS	Magic angle spinning
MCA	Multichannel analyser
MCPM	Mono-calcium phosphate monohydrate
MOF's	Metal organic frameworks
NMR	Nuclear magnetic resonance
NPD	Neutron powder diffraction
PAA	Poly(acrylic acid)
PDF	Pair distribution function
PDf	Powder diffraction file
poly-HEMA	Poly(2-hydroxyethylmethacrylate)
Ppi's	Pyrophosphates
PMMA	Polymethylmethacrylate
PSD	Position sensitive detector
PSS	Poly(sodium 4-styrene sulfonate)
PXRD	Powder x-ray diffraction
rf	Radio frequency
SEM	Scanning electron microscopy
TCP	Tri-calcium phosphate
TGA-MS	Thermogravimetric analysis mass spectrometry

TTCP	Tetra-calcium phosphate
Uiso	Isotropic temperature factor
WDXRF	Wavelength dispersive x-ray fluorescence spectroscopy
Wt %	Weight percent
XRF	X-ray fluorescence spectroscopy

Table of Contents

Chapter 1

Chapter 2

Chapter 3

Chapter 4

CHAPTER 1

Introduction

The focus of this thesis is on the study of a number of inorganic materials based on phosphates as potential biomaterials. Therefore this introduction provides a general background to biomaterials and examples of their use, along with relevant inorganic systems.

1.1 What is a biomaterial?

A biomaterial is defined as a non-viable (non-living) material used in a device intended to interact with biological systems.[1-3] In order for this to be possible, the material must be biocompatible; biocompatibility being defined as the ability of a material to perform with an appropriate host response in a specific application, and not having toxic or injurious effects on biological function.[4] As a result of higher levels of natural and unnatural deterioration of the body, due mainly to the increasing life time expectancy of the population, the demand for biomaterials for the regeneration, re-growth and repair of bone is ever increasing.

1.2 Applications of biomaterials

The application of a biomaterial dictates the desired properties required from the material to perform in an appropriate manner. Examples of some common biomaterials and their associated applications are outlined in table 1.1.

Table 1.1: A table showing the most common applications of biomaterials and the materials used

Applications of Biomaterials	Types of Materials Used
Hip Replacement	Metals (Titanium) Polymers (PMMA) Ceramics (Alumina)
Bone Replacement	Metals (titanium, stainless steel) Ceramics (calcium phosphates)
Dental Implants	Metals (Titanium) Porcelain (Quartz, Felspar, Kaolin Clay) Cerium Oxide
Heart Valves	Metals (Stainless steel) Carbon Natural valves from pigs
Intraocular Lenses	Hydrogels (poly-HEMA) Silicone elastomers

1.3 Bioceramics as bone replacement materials

In the field of biomaterials, the term bioceramic is used to describe any inorganic solid state material used as a biomaterial and this term will be used exclusively in this manner in this work. Research into ceramics has increased over the past two decades, in particular the development of various calcium phosphates as bone replacement materials.[1-2, 5-15] The use of inorganic materials in biomedical applications has been found to be beneficial as these materials can exhibit a range of properties which include being virtually inert (showing no biological response), bioactive (showing a positive biological response from tissue and are secured by chemical bonds formed between the tissue and the implant), porous (implant secured through growth into the pores) and/or are resorbable (the implant material is resorbed by the body over an appropriate timescale). A comparison of common bone replacement materials can be found in table 1.2.

Table 1.2: A table showing the most common bone replacement materials and their associated advantages and disadvantages[3, 16-17]

Common Bone Replacement Materials	Advantages	Disadvantages
Apatite - Hydroxyapatite (HA) $Ca_{10}(PO_4)_6(OH)_2$ Fluorapatite (FAp) $Ca_{10}(PO_4)_6F_2$ Carbonated Apatite (CHA) $Ca_5(PO_4, CO_3)_3(OH/F)$	Similar composition to mineral phase in bone and teeth[18] Excellent biocompatibility High mechanical strength Sets at physiological pH[19] Stimulates osteoconduction Osteoconductive	Poor resorption *in vivo* Not osteoinductive
Di-calcium Phosphate Dihydrate (DCPD or Brushite) $CaHPO_4 \cdot 2H_2O$	Structure similar to HA Soluble under physiological conditions *In vivo* studies have shown it to almost fully resorb [20] Resorbed to 16-18 weeks, similar to resorption time of natural bone Osteoconductive	Fast setting times High porosity Setting retardants required Transformation into HA *via* hydrolysis [21-22] causing a decrease in the resorption rate
Calcium Phosphates - Tri-calcium Phosphate (TCP) $Ca_3(PO_4)$ Tetracalcium Phosphate (TTCP) $Ca_4(PO_4)_2O$	Similar composition to mineral in bone Dissolution better than HA	Can only be used in non-load bearing applications However dissolution rate can be an issue
Calcium Sulphates - Calcium Sulphate Dihydrate (gypsum) $CaSO_4 \cdot 2H_2O$ Calcium Sulphate Hemi-hydrate $CaSO_4 \cdot ½H_2O$	Biocompatible Used as drug delivery systems Great compressive strength No inflammatory response from body	Highly soluble Used in non load-bearing applications Becomes brittle when damp
Bio-glass© Composed of varying amounts of Na_2O, SiO_2, CaO and P_2O_5	Rapid rate of surface reaction fast tissue bonding Vary composition to alter properties for a specific applications	Mechanically weak, low fracture toughness (amorphous 2D network) 65 mol % of SiO_2 not practical for implant material Limited resorption Unsuitable for load bearing applications
Bioactive Glass-Ceramics BIOVERT I, II and III Dicor®	Ability to modify during surgical procedures Translucency and colour altered for applications (important in dentistry)	High temperatures required to form these materials
Alumina (Al_2O_3)	Inert in a physiological environment Stable compound Biocompatible Durable	Brittle

When developing new bioceramic materials many factors need to be considered to optimise their properties in order to be used as an artificial equivalent to bone in living organisms. The most important of which is that the material must have a similar behaviour to that of natural bone.[23] The candidate material must be well suited to the surrounding environment in which it will be placed and ideally encourage a similar response to that of natural bone. In some applications it is advantageous that, over a period of time, the candidate material should be fully resorbed. The rate at which this occurs will ideally be complimentary to the rate of growth of the surrounding natural bone.

1.4 Composition of natural bone

Natural bone consists of water (~25 wt %), organic materials (~15 wt %) and a predominant mineral/inorganic phase (~60 wt %) although composition can vary with location and function. The mineral phase of natural bone is carbonated calcium deficient hydroxyapatite (CHA).[3] There are other minor but significant components to the tissue of natural bone, which include osteoclast and osteoblast cells which are responsible for controlling the resorption and re-growth of new bone.

Healthy natural bone is maintained through a balance in the activity between these two types of cells, osteoblasts and osteoclasts. Osteoblasts are mononucleate cells responsible for bone formation. The number of osteoblasts are found to decrease with age.[24] Osteoclasts are cells that remove bone tissue, removing its mineralised matrix and breaking up the organic bone in a process known as bone resorption. If there is an imbalance between the activity of these cells, then significant problems can arise. When the imbalance is towards increased resorption, then diseases like osteoporosis can occur (see section 1.4.2).

1.4.1 Bone Grafts

When natural bone is subject to trauma or localised disease, the bone can become damaged. There are two types of procedure which can be employed to repair natural bone, these are the use of bone regeneration grafts or synthetic bone replacement materials. A bone graft is a surgical procedure that is used to replace missing bone (often in order to repair bone fractures that are complex), but it can provide a significant risk to the patient's health, particularly if there is a failure to heal and availability is often limited. A bone graft material must exhibit certain properties in order for it to function properly. Sufficient strength is needed for high stress areas and good cohesion, particularly in high blood perfused regions.[25]

There are three different types of bone regeneration grafts that currently exist; autograft, allograft and xenograft. The most important, and seen as the 'gold standard', is the autograft, where the graft is of tissue derived from another site in or on the body of the patient that is receiving the graft. Although rejection is not an issue with this grafting procedure, there are several disadvantages, including the limited availability and quantity of tissue, along with the associated donor site morbidity.[26-27] An alternative procedure is where a section of bone tissue is transplanted from another member of the same species and this is known as an allograft. As with autografts there are issues associated with this process including a limited supply of the tissue, however the major is the potential transfer of disease and possible rejection. Finally, a graft of tissue can also be taken from an organism of another species and is known as a xenograft. This type of bone regeneration graft also proves problematic as, once again, there are concerns regarding the transmission of disease, along with other ethical and legal issues. Concerns have also been raised associated with the longevity of these grafts, as some animals have shorter life spans than humans and so their tissues may age at a faster

rate, resulting in the patient requiring additional treatment in the future to replace the aged tissue. In general, there are three biological mechanisms that all contribute to the success of bone graft substitutes these are osteoconduction (the bone graft material acts as a scaffold for new bone that is perpetuated by native bone), osteoinduction (encourages undifferentiated cells to become osteoblasts) and osteogenesis (osteoblasts that originate from the bone graft material contribute to the re-growth of new bone.

Although autografts are the preferred method of bone replacement, their limited supply and requirement for extra surgery at the donor site, has motivated research as early as the late 1970s to develop synthetic biomaterials as bone replacement materials, offering the potential to replace the use of bone regeneration grafts for bone repair, substitution and augmentation.[28]

Many of the bioceramic materials considered for such applications are used in cement form, as this is a non-invasive process which does not require a second implantation procedure. There is no risk of rejection from the body, and the procedure is quick and relatively straightforward. The quantity of reagents, amount of water and particle size of reagents all play vital roles in the setting of the cements, as can the ease of use for the surgeon. The setting time of the cements can be influenced by either changing the amount of water added to the initial mixture or by changing the composition of the cement.[29] Often, additives such as pyrophosphate and magnesium, are added into the cement mixture in order to increase the setting time.[30-33] It was also found that the strength of various cements were affected by using a combination of additives.[31-32]

1.4.2 Osteoporosis

One of the most common diseases of the bone is osteoporosis. Osteoporosis is a progressive disease of the bone which is characterised by a decrease in both the mass and density of bone, which ultimately leads to the increase risk of fractures. There are no symptoms for osteoporosis, so early stages of osteoporosis are usually undetected, the only prognosis for this disease is the occurrence of fragility fractures with a healthy patient, a person who without this condition would not normally break a bone. Fractures are the most dangerous aspect of osteoporosis and depending on the severity of the fracture can cause chronic pain and often lead to further disability and possibly early mortality.[34] Vertebral compression fractures are more common in elderly people. Depending on the severity of the fracture can cause chronic pain and often lead to further disability and possibly early mortality.[35]

1.4.2.1 Current Treatments for Osteoporosis

Bisphosphonates (BP's) are the most common class of drugs used to treat osteoporosis.[36] This class of phosphate materials are analogous to pyrophosphates (PPi's), with the key difference being that they possess a P-C-P backbone as oppose to the P-O-P linkage for PPi's. Pyrophosphates are of interest as previous reports have suggested that pyrophosphates inhibit the formation of bone mineral and are vital in controlling the process of biomineralisation,[37-39] a process by which living organisms generate hard tissue. The release of enzyme alkaline phosphatase (ALP) by the osteoblasts has been found to hydrolyse the pyrophosphate, to form orthophosphate groups during bone formation, no longer inhibiting the formation of bone mineral.[37] This led to the other phosphonate analogues, in particular, bisphosphonates to be investigated. Unlike pyrophosphates, bisphosphonates P-C-P backbone, resist hydrolysis by the ALP enzyme which is secreted by the osteblastic cells. Over a long period of time,

bisphosphonate accumulates in the bone and retards its resorption and reaches a new steady-state level. [36]

Another recently developed treatment for osteoporosis is strontium renalate. This is the strontium (II) salt of ranelic acid and is a prescription drug for the treatment of osteoporosis in men and in post-menopausal women. It is marketed by Servier as Protelos or Protos. It is considered as a dual action bone agent as it acts to reduce the resorption of bone (osteoclastic activity) and increase the deposition of new bone (osteoblastic activity) to improve the imbalance between the activity of osteoclasts and osteoblasts in patients with osteoporosis. In 2013, randomised trials on strontium renalate showed an increase risk of myocardical infarction (heart attack) on patients taking strontium renalate. As a result of this it is now only prescribed for severe cases of osteoporosis.[40]

1.5 Bioceramic Materials

This section discusses a range of important bioceramics relevant to this current study.

1.5.1 Calcium Phosphates

Phosphates are probably the most important class of inorganic biomaterials, certainly in manallian systems, where they form hard tissues. Calcium phosphates can be used in a preformed state as either dense or porous in form. In addition, calcium phosphates via cement formation[2, 41-42] are now providing a viable alternative to both autografts and allografts to fill voids and defects in bone. One advantage here is the chemical similarity to the mineral naturally found in teeth and bone[16] and this has led to their significant use as artificial bone replacement materials and in applications in dentistry.[21, 33]

Calcium phosphate cements have been the subject of significant research since first being reported by Brown *et al.* in 1983.[43] These bioceramic materials are formed from the reaction of different calcium phosphates, and can contain a variety of phases, most commonly including brushite ($CaHPO_4 \cdot 2H_2O$) or hydroxyapatite (HA-$Ca_{10}(PO_4)_6(OH)_2$). Calcium phosphates have found to be suitable for the use in biomedical applications due to their excellent biocompatibility, osteoconductivity and ease of use in surgery.[32, 44]

Due to their inferior mechanical properties, calcium phosphates are only used for non-load bearing applications.[3, 45] However, calcium phosphates have been reported for their use as coatings for metal implants[17, 46-54] in order to promote bone healing as metal implants have no significant osteogenic properties. The anchoring of the implant to the skeleton can be improved through the use of surface treatments such as calcium phosphate coatings.[55-56] Calcium phosphate coatings on metallic substrates are also beneficial as corrosion of the metal implant can negatively affect the biocompatibility and mechanical integrity of the implant, leading to potential failure of the implant. [49] It has been suggested that compounds with a calcium to phosphorus ratio (Ca:P) less than 1 are not suitable for biological implantation as they tend to display an increase in dissolution rate.[3]

1.5.2 Hydroxyapatite (HA) and Brushite

As previously mentioned, a range of calcium phosphate bioceramics have been widely investigated as potential bone replacement materials.[6, 57] Hydroxyapatite and brushite are the most common classes of calcium phosphate cements used in biomaterials applications as they are the thermodynamically most stable forms.

1.5.2.1 Hydroxyapatite (HA)

Apatites are a family of minerals with the general formula $A_{10}(BO_4)_6X_2$. Hydroxyapatite or hydroxylapatite (HA) is a naturally occurring mineral where A = Ca, B = P and X = OH (figure 1.1). Pure HA has a Ca:P ratio of 1.67 however, various substitutions can be made within the apatite structure. Common substitutions within this system include substituting OH^- for F^- and in the case of CO_3^{2-}, substitutions can occur on both the B and X sites giving rise to B and A type carbonation respectively. These substitutions can alter the properties of apatite. Unlike pure HA, biological apatites contain minor substituents such as CO_3^{2-}, Na^+ and Mg^+, these are often referred to as carbonated HA.[28] Hydroxyapatite closely resembles the principle constituent of calciferous tissue such as dental enamel and bone.[58] As hydroxyapatite possess high mechanical strength and sets at a physiological pH,[59-60] these cements have been heavily studied and as a result there are a several commercially available products.[28] Levitt *et al.* reported one of the first examples of HA being used in biomedical applications.[50, 61]

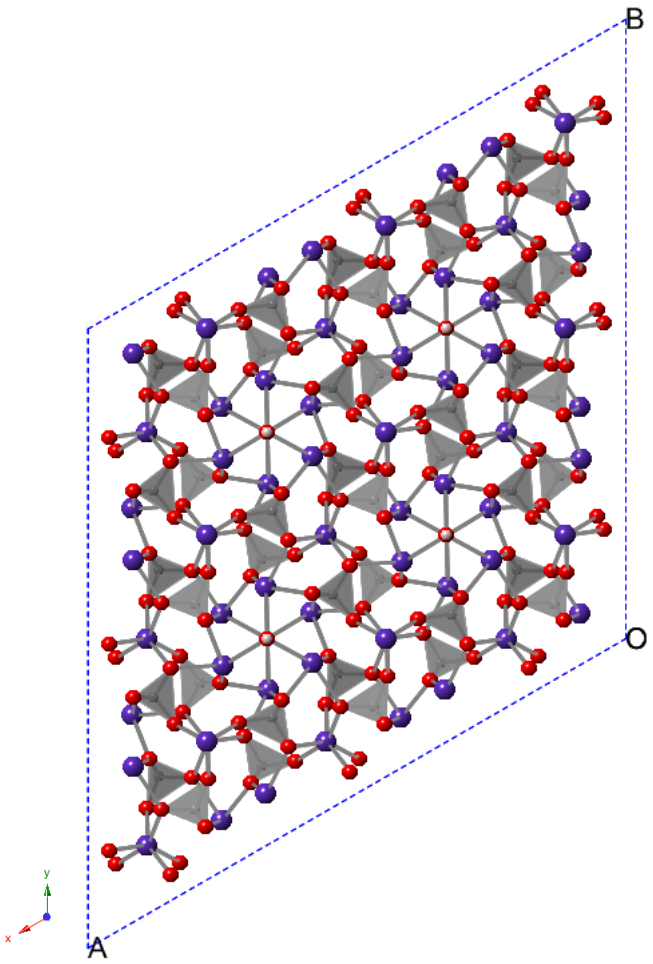

Figure 1.1: The crystal structure of hydroxyapatite (HA)
calcium (purple), PO_4 tetrahdra (grey), oxygens (red) and hydrogens (pale pink)

There are two main formulations to produce apatite cements. The first based on the original composition reported by Brown and Chow,[21] which uses a tetra-calcium phosphate and an anhydrous calcium phosphate to form hydroxyapatite as shown in equation 1.1. This cement was found to set at physiological temperature (human body temperature, 37 °C) within a period of 30-60 minutes.[62-63] Secondly, a commercially used route involving the dissolution precipitation of α-TCP into an apatite cement (see equation 1.2).[64]

$$2Ca_4(PO_4)_2O + 2CaHPO_4 \rightarrow Ca_{10}(PO_4)_6(OH)_2$$

Equation 1.1: An equation to show the formation of hydroxyapatite from tetra-calcium phosphate and anhydrous calcium phosphate

$$3\alpha\text{-}Ca_3(PO_4)_2 + H_2O \rightarrow Ca_9(HPO_4)(PO_4)_5OH$$

Equation 1.2: An equation to show the formation of an apatite cement from the dissolution of α-tri-calcium phosphate in water

Preformed monoliths of HA can also be used in bone replacement applications and these can exist to two forms: dense and porous.[65-68] The porous forms are designed to mimic the interconnecting macroporosity observed in bone which promotes vascularisation and tissue ingrowth[69] Synthetic HA and other calcium phosphate bone graft materials are engineered with a macroporous structure with pore sizes mimicking those of natural bone. The difference in the pore sizes have been reported to influence the tissues response to the bioceramic implanted.[70-76] However, increasing the microporosity of a bioceramic has been found to affect the mechanical properties (compressive strength) of the material and if this is key then dense forms must be used.[67]

HA has been synthesised by various methods including; solid-state reactions, hydrothermal reactions, compacting and sintering HA powder prepared by precipitation or hydrolysis reactions and by sol–gel methods.[28] The route in which HA is formed greatly influences its physical and chemical characteristics. Like tri-calcium phosphate, pure and stoichiometric HA (with a Ca:P ratio of 1.67) can only be obtained from solid state reactions, not under aqueous conditions. Properties of HA depends on a number of factors, the Ca:P ratio, the structure and the processing method. Despite its excellent biocompatibility, bioactivity and osteoconductivity, HA is resorbed very slowly in vivo and therefore if resorption is required there is a need to investigate new compositions with improved resorption characteristics.

1.5.2.2 Brushite

Brushite is naturally occurring in the body and can be most commonly found in callus, bone and kidney stones.[30] Subsequent to the discovery of apatite cements, brushite cements were first reported by Lemaitre *et al.*[64] from a reaction with beta tri-calcium phosphate, mono-calcium phosphate monohydrate (MCPM) and water (see equation 1.3 and figure 1.2).

$$\beta\text{-}Ca_3(PO_4)_2 + Ca(H_2PO_4)_2{\cdot}H_2O + 7H_2O \rightarrow 4\ CaHPO_4{\cdot}2H_2O$$

Equation 1.3: An equation to show the formation of brushite from β-tri calcium phosphate and monocalcium phosphate monohydrate

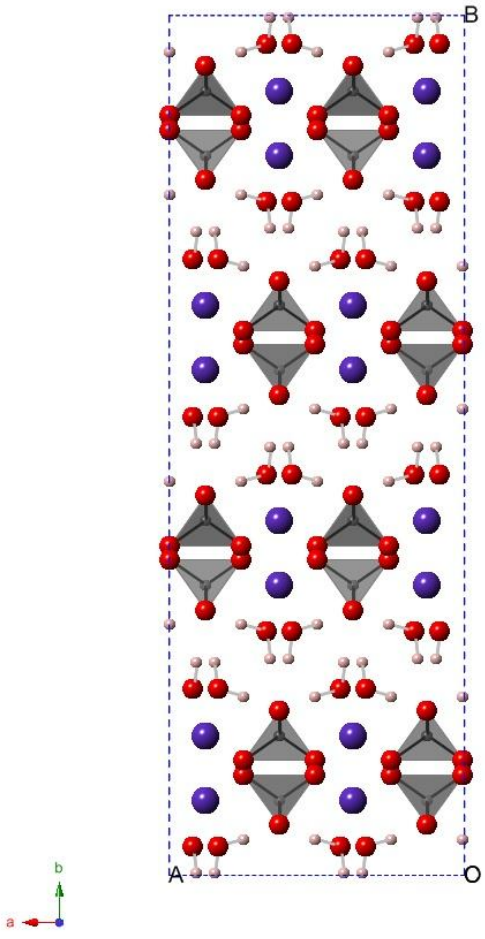

Figure 1.2: The crystal structure of brushite
calcium (purple), PO_4 tetrahedra (grey), oxygens (red) and hydrogens (pale pink)

Due to their higher solubility, they offer potential for increased resorption over HA cements. However, one of the main drawbacks with brushite cements is that they can

transform into HA (under physiological conditions) *via* hydrolysis which can impede its resorption.

In order to prevent hydrolysis of brushite into HA an inhibitor is often included. Species such as Mg^{2+}[30] and pyrophosphate ions ($P_2O_7^{4-}$)[77] have been investigated for this purpose. In vivo results from the incorporation of pyrophosphate into a brushite cement have showed that the modified cement still operates within a workable time frame and exhibits higher compressive strength (~ 25 MPa).[78] More recently, the use of an amorphous form of calcium pyrophosphate to modify a brushite cement has been found to encourage enzyme-assisted resorption and has demonstrated that the rate of bone formation *in vivo* can be enhanced.[79]

1.5.2.3 Strontium in Calcium Phosphate Systems

Whilst bioceramic systems are generally based on calcium, given the composition of bone mineral, the incorporation of strontium into calcium phosphates has recently been shown to have some potential benefit in helping to reduce the rate of bone loss for patients with osteoporosis by decreasing the differentiation and resorbing activity of osteoclasts *in vitro*. Whilst suppressing the activity of osteoclasts, the presence of Sr^{2+} also has the effect of enhancing osteoblast proliferation and the synthesis of collagen.[80] These cumulative effects result in the overall depression of bone resorption whilst maintaining bone formation. In a further *in vivo* study, the incorporation of Sr^{2+} into HA showed an increased thickness of the bone layer at the bone-cement interface[81] and thus suggesting an increase in the osteoblastic activity. These investigations justify further study into the incorporation of strontium into other calcium phosphate derivatives for potential applications in the treatment of osteoporosis and as bioactive bone cements.

1.5.3 Fluorophosphates

Fluorophosphate anions, PO_3F^{2-} often referred to as monofluorophosphates are a class of materials which are relatively unstudied, as there are fewer than 60 structurally characterised fluorophosphate materials reported. A literature search conducted for fluorophosphates materials often generates phosphate fluoride phases, materials which contain phosphate and fluorine whereby the fluorine is not bonded directly to the tetrahedral phosphate unit (PO_4F). However, in this project, fluorophosphates materials are defined as those which possess a covalent bond between the phosphorus and fluorine atoms (P-F bond).

Fluorophosphate materials have been reported to be of use in a range of applications, with over 200 patents from a search of fluorophosphate or monofluorophosphate materials.[82] These patents include the use of fluorophosphate as corrosion inhibitors,[83-87] solubility inhibitors for lead in potable water sources,[88] wood preservatives [89] and as active agents against osteoporosis or caries during biomineralisation of fluoroapatite.[90-95] However, the majority of the patents relate to fluorophosphate products for use in both oral and dental.[96] However, when fluorophosphates were first synthesised, their primary use as an additive in toothpastes was not the intended as shown from the brief history of monofluorophosphates (table 1.4).

To date, fluorophosphate materials do not appear to have been considered as biomaterials. This is surprising given that the sodium salt (Na_2PO_3F) is currently used as an additive in toothpastes to deliver fluoride to reduce the susceptibility of enamel to damage in the oral environment.[82] This occurs by the formation of fluorinated HA (FHA), which possesses lower solubility than HA. The use of monofluorophosphate materials was pioneered in the 1950s by Colgate-Palmolive's development of Colgate toothpaste,

providing competition for Crest (placed on the market by Procter and Gamble 1955, containing stannous fluoride).

Table 1.3: A table to show the a brief history of monofluorophosphates[96]

Year	Background
1927	Stumbled upon fluorophosphate formation as a hydrolysis product of phosphorus oxytrifluoride (POF_3)[97]
1929	A reaction between difluorophosphate and dilute NaOH formed monofluorophosphate (PO_3F^{2-}) A series of monofluorophosphate were formed: Na_2PO_3F, Ag_2PO_3F, $(NH_4)_2PO_3F$ and K_2PO_3F
1947	A new method for forming $(NH_4)_2PO_3F$ and Na_2PO_3F was discovered by Carl O Anderson using the corresponding metal fluoride
1950	Lange discovered that Na_2PO_3F had relatively low toxicity and as a result considered its use in dental applications but further investigations were needed[98]
1954	Research conducted by the stannous fluoride group at the university of Indiana reported the use of Na_2PO_3F for inhibition of dental caries was ineffective[99-101] Former colleague of the university of Indiana Arthur W. Radike, head of drug development at Proctor and Gamble sponsored the research the stannous fluoride group into using tin fluoride (stannous fluoride) in toothpaste which ultimately led to Crest[102]
1955	The potential inclusion of sodium or potassium fluorophosphate by Colgate-Palmolive. However, patents only referred to the use of NaF or SnF_2[103-105]
1957	Reports of Na_2PO_3F reducing periodontal disease in hamster
1959	Both Colgate-Palmolive and Proctor and Gamble reluctant to use Na_2PO_3F as an additive in toothpastes However, a patent (regarding the use monofluorophosphate in toothpastes) was filed by the Swedish representatative of dentistry in the World Health Organisation Sten Yngve Ericsson.[106-107]
1962	Investigations into the effect of Na_2PO_3F on the rate of dental caries in children[108]
1963	A series of patent were filed in the EU for the use of Na_2PO_3F in toothpaste.[109-113]
1966	The synthesis method and apparatus for the formation of Na_2PO_3F patented
1969	British patent filed by Sten Yngve Ericsson for the use of monofluorophosphate to strengthen/harden teeth and bones.[114]
1985	Monofluorophosphate patented for use as corrosion inhibitor.[115]
1991	Monofluorophosphate patented for use as solubility inhibitor.[88]

There are a variety of different methods reported for the synthesis of fluorophosphate materials which include; metal fluoride/metal phosphate fluxes, solid

state reactions between metal fluorides and phosphates, neutralisation reactions of metal salts with free monofluorophosphoric acid or reactions in aqueous solutions using the soluble diammonium fluorophosphate salt $(NH_4)_2PO_3F$ with the appropriate metal salt to form the appropriate metal fluorophosphate.[116-117] The latter method known is as a metathesis reaction and appears to be the preferred choice of synthesis, as it is considered to be the simplest method for fluorophosphate formation. Many of the reported fluorophosphates materials have been synthesised via this method an example of which is shown in equation 1.4. [85, 116-120]

$$(NH_4)_2PO_3F + Hg_2(NO_3)_2 \rightarrow Hg_2PO_3F + 2(NH_4)(NO_3)$$

Equation 1.4: The formation of mercury monofluorophosphate from a metathesis reaction with diammonium fluorophosphate and mercury (II) nitrate

A variety of metal salts (M^I or M^{II}) can be used to form the corresponding M^I or M^{II} fluorophosphates. The M^I is either an NH_4^+ or an alkali metal whilst M^{II} is an alkaline earth or a first row transition element. Many of the reported fluorophosphate materials use the diammonium fluorophosphate phase $(NH_4)_2PO_3F$ as their source of fluorophosphate, this phase must initially be synthesised before proceeding to form the desired fluorophosphate. In order to synthesise this, the method described by Schulke et al has been followed.[121]

There are many disadvantages associated with the other methods as many produce products with multiple phases and the hydrolysis of the fluorophosphate anion can readily occur when employing thermal methods.

In recent years, there has been renewed interest in fluorophosphate materials not for use as biomaterials. Weller *et al*. report the formation of a series of first row transition metal 'fluorophosphates' *via* the hydrothermal synthesis route which is

considered to be a more versatile route to obtain fluoride-containing framework materials.[122-126] Many of the structures reported do not possess the P-F bond and therefore fall outside the definition of a fluorophosphate unit used in this work. Nevertheless, the work from the Weller group has promoted renewed interest in fluorophosphates materials for a variety of applications not previously considered.[122]

1.5.4 Calcium Sulphate Hydrates (gypsum)

Whilst phosphates are more commonly used as bone cements, sulphates are a family of compounds also widely used in general cement and building materials applications. A few examples currently exist of their use as biomaterials in bone replacement/regeneration applications.[127] Gypsum is a naturally occurring mineral often precipitated from saline water.[127-129] There are three types of calcium sulphate phases that exist; gypsum ($CaSO_4 \cdot 2H_2O$), calcium sulphate hemi-hydrate ($CaSO_4 \cdot ½H_2O$) and the anhydrite ($CaSO_4$). Calcium sulphate hemi-hydrate has been extensively used for many years as a building material and is commonly known as 'Plaster of Paris'. When mixed with water and allowed to set, gypsum is formed. The decomposition of synthetic gypsum proceeds *via* two dehydration reactions; dehydration of gypsum to form the hemi-hydrate and dehydration of the hemi-hydrate to form the anhydrite (see equation 1.5 and 1.6).[130-134] These reactions occur at 95-170 °C and ~ 250 °C respectively and are fully reversible to regenerate the gypsum phase.[133]

$$CaSO_4 \cdot 2H_2O + \text{Heat} \rightarrow CaSO_4 \cdot ½H_2O + 1½H_2O$$

Equation 1.5: The first dehydration reaction of gypsum to form calcium sulphate hemi-hydrate (Plaster of Paris)

$$CaSO_4 \cdot ½H_2O \rightarrow CaSO_4 + ½\ H_2O$$

Equation 1.6: The second dehydration reaction of gypsum to form the anhydrite

However, the limiting factor for the use of gypsum is its high solubility.[135] Given the structural similarity of fluorophosphate (PO_3F^{2-}) to both phosphate (PO_4^{3-}) and sulphate (SO_4^{2-}), and the fact that fluorophosphate and sulphate are isoelectronic, there may be potential to modify current materials or form new materials through replacement of the analogous tetrahedral unit by the fluorophosphate anion.

1.6 Calcium carbonate and its polymorphs

As well as its presence in nature, calcium carbonate naturally occurs as limestone and has widespread uses in industry, not only as an ingredient in cement but in various other applications which extend beyond its uses as a construction material.[18, 136-137] However, the major disadvantage with calcium carbonate arises from its unwanted precipitation and deposition on the walls of water pipes and washing machines (limescale).[138]

There are six known polymorphs of calcium carbonate, all of which differ in stability, solubility and morphology. The three most common polymorphs are the anhydrous crystalline forms, vaterite (μ-$CaCO_3$), aragonite and calcite in order of their increasing thermodynamic stability.[139-140] Calcite and aragonite are both common in biological and geological samples. However, the occurrence of vaterite is very rare.[141] Calcium carbonate has two hydrated polymorphs monohydrocalcite ($CaCO_3 \cdot H_2O$) and calcium carbonate hexahydrate ($CaCO_3 \cdot 6H_2O$). Monohydrocalcite was first discovered in the 1930s through the dehydration of the mineral ikaite $CaCO_3 \cdot 6H_2O$.[142] Both phases are metastable and two of the least common calcium carbonate polymorphs.[143-144] The sixth polymorph in the series is amorphous calcium carbonate (ACC) and differs from the crystalline polymorphs by being softer, more soluble and highly unstable.

The key presence of ACC in a number of organisms has recently been the subject of much research, particularly its link to biomineralisation, but attempts to synthesise ACC *in vitro* yields a highly unstable materials (see section 6.1).

1.6.1 Amorphous Calcium Carbonate (ACC)

Despite being highly soluble and the least stable of the calcium carbonate polymorphs, amorphous calcium carbonate (ACC) also appears to play an important role in nature. The potential use of ACC was significantly over looked as research continued to focus on the use of the more stable crystalline calcium carbonate polymorphs (calcite and aragonite). However, research identified that amorphous calcium carbonate was more common in biology than first realised, as this phase was found to precipitate in marine invertebrates in which ACC was found to be used for structural purposes in organisms such as crustaceans, where it stiffens the exoskeletal cuticle.[139] As a result of these findings, research into amorphous calcium carbonate precipitation in biological species has significantly increased.

Amorphous calcium carbonate is believed to have three main roles in the biomineralisation process; to act as a transient precursor to more stable crystalline phases, act as a storage phase for Ca^{2+} and CO_3^{2-} ion and for structural purposes within organisms.[140-141, 144-145] An amorphous material can be described as a material which exhibits no long range structural order. In some applications, amorphous materials are the preferred choice as they are more reactive compared to their crystalline analogues. A summary of the advantages and disadvantages of using amorphous calcium carbonate can be found in table 1.5.

Table 1.4: A table to show the advantages and disadvantages of using amorphous calcium carbonate (ACC)

ADVANTAGES	DISADVANTAGES
Being a metastable phase, can tailored specifically for its intended function.[139]	Unstable, so transformation into a more crystalline polymorph (usually calcite) is favourable.[19, 146]
Their isotropic nature allows them to be easily shaped and have the ability to sustain mechanical stress from the direction to which it is being applied.	Difficult to establish whether ACC transforms immediately into calcite or proceeds via other metastable phase.[147-148]
Less brittle	There are two apparent types of amorphous calcium carbonate that exist, these are biogenic and synthetic ACC

1.6.2 Stabilisation of ACC using Organic and Inorganic Components

Since many invertebrates have utilised ACC as a precursor phase, many investigations have been carried out to discover how ACC is being stabilised *in vivo*. It has been reported that some biogenic amorphous calcium carbonate phases are known to contain traces of both magnesium and phosphate.[139, 145] It is believed that the presence of these species within the mineral phase play a significant role in stabilising amorphous calcium carbonate. Certain macromolecules (e.g. organic matrix proteins)[149-150] are intimately involved in controlling nucleation, growth, shaping and adapting.[151] From studies performed *in vitro*, where small amounts of the macromolecules were placed in saturated $CaCO_3$ solutions, it is the proteins (within these macromolecules) with differing amino acid compositions which are found to stable or ACC or induce the formation of calcite.[152] Specialised macromolecules are also found to be present in calcite crystals of organisms, [153-154] which has been found to affect the mechanical properties of calcite. In some biological organisms they are involved in shaping their morphology during growth.[155-156] These macromolecules can be used to stabilise ACC in the presence of inorganic ions such as Mg^{2+} and other additives.[140, 147, 152] Thermal behaviour studies on ACC and poly(sodium 4-styrene sulfonate) (PSS) or ACC and

poly(acrylic acid) (PAA) systems with varying Ca/PSS or Ca/PAA ratios have provided further evidence that the use of additives act as a method of stabilising ACC.[148] Results from these experiments show an increase in the crystallisation temperature of synthetic ACC compared to pure ACC previously reported by Raz *et al.*[157]

1.7 Aims

This thesis seeks to develop new inorganic materials with a view to potential use as biomaterials. A particularly understudied area is fluorophosphates, this work will therefore investigate the isolation of novel biocompatible fluorophosphates. In this work we aim to identify new synthetic routes to producing fluorophosphates and to fully characterise the products. This work also seeks to investigate gypsum cement systems, principally incorporating fluorophosphates into the formulation, given the isoeletronic nature of both sulphate and fluorophosphate. Finally, this work will explore the stability of ACC phases in the presence of various phosphate species, with their presence having previously been reported to provide stability. This study seeks to investigate the nature of this stabilising effect.

1.8 References

1. M. Vallet-Regí, *Comptes Rendus Chimie*, 2010, **13**, 174-185.
2. S. V. Dorozhkin, *Biomaterials*, 2010, **31**, 1465-1485.
3. B. D. Ratner, A. S. Hoffman, F. J. Schoen and J. E. Lemons, *Biomaterials Science: An Introduction to Materials in Medicine*, Second Edition, Elsvier Academic Press, 2004.
4. Dorland, *Illustrated Medical Dictionary*, 31st Saunders Elsevier, 2007.
5. M. Bohner, U. Gbureck and J. E. Barralet, *Biomaterials*, 2005, **26**, 6423-6429.
6. E. Charrière, S. Terrazzoni, C. Pittet, P. Mordasini, M. Dutoit, J. Lemaître and P. Zysset, *Biomaterials*, 2001, **22**, 2937-2945.
7. A. A. Mirtchi, J. Lemaitre and N. Terao, *Biomaterials*, 1989, **10**, 475-480.
8. C. Nicolazo, H. Gautier, M. J. Brandao, G. Daculsi and C. Merle, *Biomaterials*, 2003, **24**, 255-262.
9. S. Laasri, M. Taha, E. K. Hlil, A. Laghzizil and A. Hajjaji, *Comptes Rendus Mécanique*, 2012, **340**, 715-720.
10. S. M. Best, A. E. Porter, E. S. Thian and J. Huang, *Journal of the European Ceramic Society*, 2008, **28**, 1319-1327.
11. J. Chevalier and L. Gremillard, *Journal of the European Ceramic Society*, 2009, **29**, 1245-1255.
12. H. Yuan, K. Kurashina, J. D. de Bruijn, Y. Li, K. de Groot and X. Zhang, *Biomaterials*, 1999, **20**, 1799-1806.
13. M. Kohri, K. Miki, D. E. Waite, H. Nakajima and T. Okabe, *Biomaterials*, 1993, **14**, 299-304.
14. E. Champion, *Acta Biomaterialia*, 2013, **9**, 5855-5875.
15. J.-S. Sun, Y.-H. Tsuang, C.-H. Yao, H.-C. Liu, F.-H. Lin and Y.-S. Hang, *Journal of Biomedical Materials Research*, 1997, **34**, 227-233.
16. D. Predoi, R. A. Vatasescu-Balcan, I. Pasuk, R. Trusca and M. Costache, *Journal of Optoelectronics and Advanced Materials*, 2008, **10**, 2151-2155.
17. K. de Groot, *Ceramics International*, 1993, **19**, 363-366.
18. J. Chen and L. Xiang, *Powder Technology*, 2009, **189**, 64-69.
19. H. S. Lee, T. H. Ha and K. Kim, *Materials Chemistry and Physics*, 2005, **93**, 376-382.
20. K. Ohura, M. Bohner, P. Hardouin, J. Lemaitre, G. Pasquier and B. Flautre, *Journal of Biomedical Materials Research*, 1996, **30**, 193-200.
21. M. Bohner, *Journal of Materials Chemistry*, 2007, **17**, 3980-3986.
22. M. H. Alkhraisat, F. T. Marino, J. R. Retama, L. B. Jerez and E. Lopez-Cabarcos, *Journal of Biomedical Materials Research Part A*, 2008, **84A**, 710-717.
23. H. H. Beherei, G. T. El-Bassyouni and K. R. Mohamed, *Ceramics International*, 2008, **34**, 2091-2097.
24. G. D'ippolito, P. C. Schiller, C. Ricordi, B. A. Roos and G. A. Howard, *Journal of Bone and Mineral Research*, 1999, **14**, 1115-1122.
25. E. Rokita, C. Hermes, H. F. Nolting and J. Ryczek, *Journal of Crystal Growth*, 1993, **130**, 543-552.
26. M. A. A. J.C.Banwart, R.S.Hassanein, *Spine*, 1995, **20**, 1055-1060.
27. S. M. E. B.N.Summers, *Bone Joint Surg Br*, 1989, **71**, 677-680.
28. R. Z. Legeros and L. P. Legeros, *Bioceramics and their clinical applications: Chapter 16 Hydroxyapatite*, Woodhead Publishing Ltd, Japan, 2008.
29. M. P. Hofmann, A. M. Young, U. Gbureck, S. N. Nazhat and J. E. Barralet, *Journal of Materials Chemistry*, 2006, **16**, 3199-3206.
30. D. Lee and P. N. Kumta, *Materials Science and Engineering: C*, 2010, **30**, 934-943.

31. A. A. Mirtchi, J. Lemaître and E. Hunting, *Biomaterials*, 1989, **10**, 634-638.
32. M. H. Alkhraisat, F. T. Mariño, C. R. Rodríguez, L. B. Jerez and E. L. Cabarcos, *Acta Biomaterialia*, 2008, **4**, 664-670.
33. S. Panzavolta, P. Torricelli, L. Sturba, B. Bracci, R. Giardino and A. Bigi, *Journal of Biomedical Materials Research Part A*, 2008, **84A**, 965-972.
34. M. C. J.L.Old, *American Family Physician*, 2004, **69**, 111-116.
35. S. J. L. Billinge, *Zeitschrift Fur Kristallographie*, 2004, **219**, 117-121.
36. R. Graham and G. Russell, *Bone*, 2011, 2-19.
37. L. Hessle, K. A. Johnson, H.C.Anderson, S. Narisawa, A. Sali and J. W. Goding, *National Academy Sciences USA*, 2002, **99**, 9445-9449.
38. L. M. Grover, U. Gbureck, A. M. Young, A. J. Wright and J. E. Barralet, *Journal of Materials Chemistry*, 2005, **15**, 4955-4962.
39. H. Fleisch and S.Bisaz, *Nature*, 1962, **195**, 911.
40. Servier, *Important new restrictions for the use of Protelos (strontium ranelate) following new data showing an increased risk of myocardial infarction*, Ireland, 2013.
41. M. Bohner, L. Galea and N. Doebelin, *Journal of the European Ceramic Society*, 2012, **32**, 2663-2671.
42. K. A. Hing, L. F. Wilson and T. Buckland, *The Spine Journal*, 2007, **7**, 475-490.
43. W. E. Brown and L. C. Chow, *Journal of Dental Research*, 1983, **62**, 672.
44. S. Panzavolta, P. Torricelli, L. Sturba, B. Bracci, R. Giardino and A. Bigi, *Journal of Biomedical Materials Research Part A*, 2008, **84A**, 965-972.
45. M. Julien, I. Khairoun, R. Z. LeGeros, S. Delplace, P. Pilet, P. Weiss, G. Daculsi, J. M. Bouler and J. Guicheux, *Biomaterials*, 2007, **28**, 956-965.
46. S. C. G. Leeuwenburgh, J. G. C. Wolke, M. C. Siebers, J. Schoonman and J. A. Jansen, *Biomaterials*, 2006, **27**, 3368-3378.
47. M. Inagaki, Y. Yokogawa and T. Kameyama, *Thin Solid Films*, 2001, **386**, 222-226.
48. Y. C. Yang and E. Chang, *Surface and Coatings Technology*, 2005, **190**, 122-131.
49. C. Garcı´a, S. Cere´ and A. Dura´n, *Journal of Non -Crystalline Solids*, 2006, **352**, 3488-3495.
50. S. R. Levitt, P. H. Crayon, E. A. Monroe and R. A. Condrate, *Journal of Biomedical Research*, 1969, **3**, 683-684.
51. S. D. Cook, K. A. Thomas, J. F. Kay and M. Jarcho, *Clinical Orthopaedics and Related Research*, 1998, **232**, 225-243.
52. W. Bonfield, M. D. Grynpas, A. E. Tully, J. Bowman and J. Abram, *Biomaterials*, 1981, **2**, 186.
53. R. G. T. Geesink and M. T. Manley, *Hydroxlapatte Coatings in Orthopaedic Surgery*, Raven Press, New York, 1993.
54. T. S. Golec and J. T. Krauser, *Dental Clinics of North America*, 1992, **36**, 39-65.
55. J. A. J. B.León, *Thin Calcium Phosphate Coatings for Biomedical Implants*, Springer, 2009.
56. K. H. P.Ducheyne, D.E.Hutmacher, D.W.Grainger, C.J.Kirkpatrick, *Comprehensive Materials, metallic ceramic and polymeric biomaterials*, Elsvier Science Ltd, 2011.
57. G. Hannink, J. G. C. Wolke, B. W. Schreurs and P. Buma, *Journal of Biomedical Materials Research Part B: Applied Biomaterials*, 2008, **85B**, 478-488.
58. C. Slater, 2008.
59. M. P. H. L.M.Grover, U. Gbureck, B. Kumarasami and J.E. Barralet, *Acta Biomaterialia*, 2008, **4**, 1916-1923.
60. L. M. Grover, M. P. Hofmann, U. Gbureck, B. Kumarasami and J. E. Barralet, *Acta Biomaterialia*, Article in Press.

61. Z. A. Monroe, W. Votawa, D. B. Bass and J. McMullen, *Journal of Dental Research*, 1971, **50**, 860-862.
62. W. E. Brown and L. C. Chow, *Cements research progress. Westerville, OH: American Ceramic Society*, 1986, 352-379.
63. W. E. Brown and L. C. Chow, Combination of sparingly soluble calcium phopshate cements in slurries and pastes as mineralizers and cements, *United States of America Pat.*, 1986.
64. A. M. J. Lemaitre, A. Mortier, *Silicates Industriels*, 1987, **10**, 141-146.
65. A. Deptula, W. Lada, T. Olczak, A. Borillo, C. Alvani and A. DiBartolomeo, *Journal of Non Crystalline Solids*, 1992, **147-148**, 537-541.
66. H. Denisson and K. deGroot, *J Prost Dent*, 1979, **42**.
67. H. Denisson, C. Mangano and G. Venini, *Piccin Nuova Libraria, SPA:Padua*, 1985.
68. S. H. Li, J. R. de Wijn and K. DeGroot, *Journal of Biomedical Materials Research*, 2002, **61**, 109-120.
69. M. Mastrogiacomo, S. Scaglione, R. Martinetti, L. Dolcini, F. Beltrame, R. Cancedda and R. Quarto, *Biomaterials*, 2006, **27**, 3230-3237.
70. B. S. Chang, C. K. Lee, K. S. Hong, H. J. Youn, H. S. Ryu, S. S. Chung and K. W. Park, *Biomaterials*, 2000, **21**, 1291-1298.
71. O. Gauthier, J.-M. Bouler, E. Aguado, P. Pilet and G. Daculsi, *Biomaterials*, 2006, **19**, 133-139.
72. K. A. Hing, S. M. Best, K. E. Tanner, W. Bonfield and P. A. Revell, *Journal of Biomedical Materials Research*, 2004, **68A**, 187-200.
73. J. X. Liu, B. Flautre and K. Anselme, *J Mater Sci Mater Med*, 1999, **10**, 111-120.
74. W. W. Lu, F. Zhao, K. D. Luk, Y. J. Yin, K. M. Cheung, G. X. Cheng, K. D. Yao and J. C. Leong, *J Mater Sci Mater Med*, 2003, **114**, 1039-1046.
75. M. Mastrogiacomo, S. Scaglione, R. Martinette, L. Dolcini, F. Beltrame, R. Cancedda and R. Quarto, *Biomaterials*, 2006, **27**, 3230-3237.
76. N. Tamai, A. Myoui, T. Tomita, T. Nakase, J. Tanaka, T. Ochi and H. Yoshikawa, *J Biomed Mater Res*, 2002, **59**, 110-117.
77. A. Bolarinwa, U. Gbureck, P. Purnell, M. Bold and L. M. Grover, *Advances in Applied Ceramics*, 2010, **109**, 291-295.
78. L. M. Grover, U. Gbureck, A. J. Wright, M. Tremayne and J. E. Barralet, *Biomaterials*, 2006, **27**, 2178-2185.
79. L. M. Grover, A. J. Wright, U. Gbureck, A.Bolarinwa, J. Song, Y. Liu, D. F. Farrar, G. Howling, J. Rose and J. E. Barralet, *Biomaterials*, 2013, **34**, 6631-6637.
80. N. Takahashi, T. Sasaki, Y. Tsouderos and T. Suda, *Journal of Bone and Mineral Research*, 2003, **18**, 1082-1087.
81. X. P. Wang and J. D. Ye, *Journal of Materials Science-Materials in Medicine*, 2008, **19**, 1183-1186.
82. W. Lange, Dentifrice Preparation containing sodium monofluorophosphate, *Great Britain Pat.*, 1965.
83. M. Duprat, M. C. Lafont, F. Moran and S. Rocher, *Rev. Fr. Sci. Eau*, 1985, **4**, 1-15.
84. J. Durand, A. Larbot, L. Cot, M. Duprat and F. Dabosi, *Zeitschrift fur Anorganische und Allegemeine Chemie*, 1983, **504**, 163-172.
85. M. R. Laamari, A. Derja, J. Benzakour and M. Berracho, *Annales de Chimie des Science des Materiaux*, 2001, **26**, 117-130.
86. M. R. Laamari, A. Derja, J. Benzakour and M. Berracho, *Journal of Electroanalytical Chemistry and Interfacial Electrochemistry*, 2004, **569**, 1-6.
87. T. Chaussadent, V. Nobel-Pujol, F. Farcas, I. Mabille and C. Fiaud, *Cement and Concrete Research*, 2006, **36**, 556-561.

88. B.P.Boffardi and A.M.Sherbondy, Monofluorophosphate solubility inhibitor for lead in potable water sources, *United States Pat.*, 1991.
89. F. Mo¨wius, M. Meisel, H. Grunze, L. Kolditz, M. Zeibig, W. Ose, D. Standfuss, H. Kirk, R. Hesse, H. Go¨tze and W. Unger, *United States of America Pat.*, 1998.
90. F. Liote, C. Bardin, A. Liou, A. Brouard, J. L. Terrier and D. Kuntz, *Calcified Tissue International*, 1992, **50**, 209-213.
91. J. D. Ringe, C. Kipshoven, A. Coster and R. Unmbach, *Osteoporosis International*, 1999, **9**, 171-178.
92. E. J. Duff, *Caries Research*, 1983, **17 (Suppl 1)**, 77-87.
93. M. J. Root and R. S. Schreiber, *Caries Research*, 1990, **24**, 30-32.
94. C. Bruun and H. Givskov, *Caries Research*, 1993, **27**, 96-99.
95. R. W. Billington, J. A. Williams, A. Dorban and G. J. Pearson, *Biomaterials*, 2004, **25**, 3399-3402.
96. P. Meiers, http://www.fluoride-history.de/p-mfp.htm
97. *Ber. dt. chem. Ges*, 1927, **60**, 962.
98. J. H. Simons, *Fluorine Chemistry*, Academic Press, New York, 1950.
99. J. C. Muhler and H. G. Day, *Journal of Dental Research*, 1954.
100. L. C. Mosier and W. E. White, *Ind. Eng. Chem*, 1951, **43**.
101. Hein., *Journal of Dental Research*, 1951, **30**, 467.
102. J. C. Muhler,http://www.chem.indiana.edu/Alumni/pubs/w97/necrology.html.
103. R. D. Manahan and V. J. Ritcher, Fluoride Dentifrice Composition, *Austrailia Pat.*, 1957.
104. R. D. Manahan and V. J. Ritcher, Fluoride Dentifrice Composition, *United States of America Pat.*, 1957.
105. C.-P. Company, "Préparation dentifrice", *France Pat.*, 1955.
106. S. Y. Ericsson, The Association of Swedish Manufacturers of Fluoride Toothpaste, Stockholm, *Sweden Pat.*, 1959.
107. S. Y. Ericsson, Alkali Metal Monofluorophosphate and Calcium Carbonate Dentifrice, *United States of America Pat.*, 1960.
108. P. W. Goaz, L. P. McElwaine, H. A. Biswell and W. E. White, *J Dent Res*, 1963, **42**.
109. R. D. Manahan and V. J. Ritcher, Zahnpflegemittel, *Switzerland Pat.*, 1963.
110. R. D. Manahan and V. J. Ritcher, Zahnpflegemittel, *Switzerland Pat.*, 1964.
111. R. D. Manahan and V. J. Ritcher, Dentifrice Composition containing sodium monofluorophosphate, *United States of America Pat.*, 1964.
112. R. D. Manahan and V. J. Ritcher, Dentifrice Preparation, *United Kingdom Pat.*, 1963.
113. R. D. Manahan and V. J. Ritcher, Dentifrice preparation, *United States of America Pat.*, 1964.
114. S. Y. Ericsson, Compositions for hardening teeth and bones, *United Kingdom Pat.*, 1969.
115. F. Moran, S. Rocher, L. Cot, F. Dabosi, M. Duprat and J. Daurand, Anticorrosion means and compositions containing same, *France Pat.*, 1985.
116. M. Weil, M. Puchberger, E. Fuglein, E. J. Baran, J. Vannahme, H. J. Jakobsen and J. Skibsted, *Inorganic Chemistry*, 2007, **46**, 801-808.
117. M. Weil, M. Puchberger and E. J. Baran, *Inorganic Chemistry*, 2004, **43**, 8330-8335.
118. E. J. Baran and M. Weil, *Journal of Raman Spectroscopy*, 2009, **40**, 1698-1700.
119. Y. Tanizawa, H. Tsuchikane, K. Sawamura and T. Suzuki, *Journal of the Chemical Society-Faraday Transactions*, 1991, **87**, 2235-2240.
120. M. Zeibig, B. Wallis, F. Mowius and M. Meisel, *Zeitschrift Fur Anorganische Und Allgemeine Chemie*, 1991, **600**, 231-238.

121. U. Schu¨lke and R. Kayser, Zeitschrift fur *Anorganische und Allegemeine Chemie.*, 1991, **600**, 221-226.
122. J. A. Armstrong, E. R. Williams and M. T. Weller, *Journal of the American Chemical Society*, 2011, **133**, 8252-8263.
123. J. A. Armstrong, E. R. Williams and M. T. Weller, *Dalton Transactions*, 2012, **41**, 14180-14187.
124. J. A. Armstrong, E. R. Williams and M. T. Weller, *Dalton Transactions*, 2013, **42**, 2302-2308.
125. A. C. Keates, J. A. Armstrong and M. T. Weller, *Dalton Transactions*, 2013.
126. E. R. Williams, S. A. Morris and M. T. Weller, *Dalton Transactions*, 2012, **41**, 10845-10853.
127. J. L. Ricci, M. J. Weiner, S. Mamidwar and H. Alexander, *Bioceramics and their clinical applications: Chapter 14 Calcium Sulfate*, Woohead Publishing Ltd, Japan, 2008.
128. A. B. B. Merdhah and A. A. M. Yassin, *The Open Petroleum Engineering Journal*, 2008, **1**, 62-73.
129. P. G. Klepetsanis and P. G. Koutsoukos, *Journal of Crystal Growth*, 1989, **98**, 480-486.
130. B. Molony and M. J. Ridge, *Journal ofMaterials Chemistry*, 1986, **21**, 1063.
131. B. S. Bobrov, A. V. Romanshkov and A. L. Tubolev, International Journal of *Inorganic Materials*, 1988, **24**, 1006.
132. G. A. Lager, T. Armbruster, F. J. Rotella, J. D. Jorgensen and D. G. Hinks, *American Mineralogist*, 1984, **69**, 910.
133. C. A. Strydom, D. L. Hudson-Lamb, J. H. Potgieter and E. Dagg, *Thermochimica Acta*, 1995, **269–270**, 631-638.
134. M. C. Ball and L. S. Norwood, *Journal of the Chemical Society*, 1969, **4**.
135. E. P. Partridge and A. H. White, *Journal of American Chemical Society*, 1929, **51**, 360-370.
136. H. S. Lee, T. H. Ha and K. Kim, *Materials Chemistry and Physics*, 2005, **93**, 376-382.
137. H. Nebel and M. Epple, *Zeitschrift Fur Anorganische Und Allgemeine Chemie*, 2008, **634**, 1439-1443.
138. M. Faatz, F. Grohn and G. Wegner, *Advanced Materials*, 2004, **16**, 996-+.
139. L. Addadi, S. Raz and S. Weiner, *Advanced Materials*, 2003, **15**, 959-970.
140. C. Gunther, A. Becker, G. Wolf and M. Epple, *Zeitschrift Fur Anorganische Und Allgemeine Chemie*, 2005, **631**, 2830-2835.
141. R. S. K. Lam, J. M. Charnock, A. Lennie and F. C. Meldrum, *Crystengcomm*, 2007, **9**, 1226-1236.
142. M. Neumann and M. Epple, *European Journal of Inorganic Chemistry*, 2007, 1953-1957.
143. H. Tang, J. G. Yu and X. F. Zhao, *Materials Research Bulletin*, 2009, **44**, 831-835.
144. H. Nebel, M. Neumann, C. Mayer and M. Epple, *Inorganic Chemistry*, 2008, **47**, 7874-7879.
145. Y. Levi-Kalisman, S. Raz, S. Weiner, L. Addadi and I. Sagi, *Advanced Functional Materials*, 2002, **12**, 43-48.
146. E. Loste and F. C. Meldrum, *Chemical Communications*, 2001, 901-902.
147. K. Sawada, *Pure and Applied Chemistry*, 1997, **69**, 921-928.
148. X. R. Xu, A. H. Cai, R. Liu, H. H. Pan, R. K. Tang and K. W. Cho, *Journal of Crystal Growth*, 2008, **310**, 3779-3787.

149. J. Debreuil, É. Tambutté, D. Zoccola, E. Deleury, J.-M. Guigonis, M. Samson, D. Allemand and S. Tambutté, *Journal of Biological Chemistry*, 2012, **287**, 19367-19376.
150. S. J. Weiner, *Journal of Experimental Zoology*, 1985, **234**, 7-15.
151. S. Weiner and L. Addadi, *Journal of Materials Chemistry*, 1997, **7**, 689-702.
152. J. Aizenberg, G. Lambert, L. Addadi and S. Weiner, *Advanced Materials*, 1996, **8**, 222-&.
153. A. Berman, J. Hanson, L. Leiserowitz, T. F. Koetzle, S. Weiner and L. Addadi, *Science*, 1993, **259**, 5096.
154. S. Albeck, J. Aizenberg, L. Addadi and M. J. Weiner, *Journal American Chemical Society*, 1993, **115**, 11691-11697.
155. J. Aizenberg, S. Albeck, S. Weiner and L. Addadi, *Journal of Crystal Growth*, 1994, **142**, 156-164.
156. J. Aizenberg, J. Hanson, M. Ilan, L. Leiserowitz, T. F. Koetzle, L. Addadi and S. Weiner, *The FASEB Journal*, 1995, **9**, 262-268.
157. S. Raz, P. C. Hamilton, F. H. Wilt, S. Weiner and L. Addadi, *Advanced Functional Materials*, 2003, **13**, 480-486.

CHAPTER 2

Experimental and Analytical Techniques

2.1 Experimental

2.1.1 Precipitation Reaction – Fluorophosphates

The desired fluorophosphate materials were synthesised *via* a precipitation reaction using an appropriate anion containing solution (1M, 20 cm^3) and the appropriate soluble metal salt (2M, 20 cm^3). To form the target materials, the stirred anion containing solution was heated to the desired temperature before the drop-wise addition of the metal cation solution. The temperature was maintained for the duration of the reaction. Once all of the metal cation solution had been added to the fluorophosphate solution a white precipitate was obtained, which was collected by vacuum filtration, washed thoroughly with de-ionised water and left to dry in air overnight.

2.1.2 Precipitation Reaction – Fluorophosphate doped Gypsum Systems

Calcium sulphate dihydrate, calcium fluorophosphate and a series of fluorophosphate doped gypsum systems were synthesised *via* precipitation reactions carried out at both 40 and 60 °C. A solution of anhydrous calcium chloride (1M, 20 cm^3) was added to an appropriate anion containing solution (1M, 20 cm^3) in a drop-wise manner. The synthesis of these materials, particularly the synthesis of gypsum and the modified gypsum systems were based on a method reported by Liu and Nancollas.[1]

2.1.2.1 Deuteration Procedure

For neutron experiments, the synthesis of the strontium fluorophosphate hydrate, gypsum, calcium fluorophosphate dihydrate and a range of the gypsum doped fluorophosphate samples were performed using deuterium (D_2O). A two handed, non-sterile glove bag of diameter 39 x 48 inches (280 L volume) was used to store the equipment and the reagents required for the experiments. Samples were also stored in glass vials inside the glove bag once synthesised. The glove bag was not purged with nitrogen (N_2), instead a bowl of silicon desiccate was placed inside to absorb any moisture present within the bag. The silicon desiccate was replaced once the blue granules turned pink. Dissolution of the reagents was carried out inside the glove bag before transferring the sealed vessels into the fume cupboard to set up the apparatus to begin the deuteration reaction.

An appropriate mass of the anion salt was dissolved in 50 cm^3 of D_2O in a three neck round bottom flask to produce the anion containing solution. An appropriate mass of $CaCl_2$ salt(or $SrCl_2 \cdot 6H_2O$ salt for the synthesis of $SrPO_3F \cdot H_2O$) was dissolved in a beaker with 50 cm^3 of D_2O and the resulting solution was transferred into a sealed pressure equalising funnel. This was then removed from the glove bag and heated under reflux. Once at the desired temperature, the $CaCl_2$ ($SrCl_2 \cdot 6H_2O$) solution was added in a drop-wise manner over a period of one hour. However, the drop rate was adjusted for the synthesis of $SrPO_3F \cdot H_2O$, and the $SrCl_2 \cdot 6H_2O$ solution was added drop-wise (one drop per second) until all of the solution had been added. The sealed three-neck round bottom flask was transferred into the glove bag and the contents were filtered using gravity filtration. The white precipitate was washed with 20 cm^3 of D_2O and the excess D_2O was allowed to filter through before scraping the wet precipitate onto a clean watch glass and placed in a desiccator to dry for several days (typically 2-4 days).

2.1.3 Precipitation Reaction – Amorphous Calcium Carbonate (ACC)

Amorphous calcium carbonate was synthesised based on the method by Koga *et al*.[2] Equal volume solutions of Na_2CO_3 (50cm^3, 0.1 mol dm^{-3}), NaOH (50 cm^3, 0.05 mol dm^{-3}) and $CaCl_2$ (50cm^3, 0.1 mol dm^{-3}) were separately cooled to 4°C for 1 hour. Once cooled, the Na_2CO_3 and NaOH solutions were added together and stirred, before the rapid addition of the $CaCl_2$ solution. Upon addition of the calcium chloride solution, no stirring was required. The pH was monitored before and after the addition of the calcium chloride solution. The resulting white precipitate was collected by vacuum filtration and washed with 150-200 cm^3 of acetone before placing in a desiccator to dry overnight.

2.2 Analytical Techniques

2.2.1 Characterisation Techniques

A combination of analytical techniques were used to characterise the materials synthesised in this work.

2.2.2 Powder X-ray Diffraction (PXRD)[3-5]

2.2.2.1 Crystal Structures

A crystal structure is a unique, regular arrangement of atoms in a 3D crystalline lattice and the arrangement of these atoms can be represented by a repeating unit or motif known as the unit cell which is the smallest repeating unit which shows the full symmetry of the crystal structure. A lattice describes the arrangement of atoms within crystal structure but gives no information about the position of the atoms. One point within the lattice has identical surroundings to all other points. As the distribution of atoms in the unit cell are known, the entire structure of the crystal can be generated by a

translation of this unit cell. The dimensions of a unit cell can be described by a set of lattice parameters, of which there are six. Three are the axes (a,b and c) and three are the angles (α, β, γ) which represent the angles between them. Typically, the unit cell (lattice) parameters are quoted in Å (where 1 Å = 10^{-10} m or 10^{-8} cm). For three-dimensional crystal structures, there are four different lattice types: primitive (P), body-centred (I), face-centred (F) and base-centred (C). There are 7 possible lattice systems for crystalline materials.

Coupling one of the seven lattice systems with a lattice centring (P, I, F or C) produces 14 different lattice types, known as Bravais lattices. Each system is governed by the presence or absence of symmetry. All of the possible symmetries in three-dimensions can be determined from combinations of all of the different symmetry operations with the fourteen Bravais lattices in three-dimensions to generate 230 space groups.[3] These space groups describe the symmetry of the crystal structure of a material.

2.2.2.2 Lattice Planes and Miller Indices

Crystallographic planes are sets of planes which connect a repeatable array of lattice points. Within a set of lattice planes, all planes are parallel, equally spaced and pass through the origin. These crystallographic planes extend throughout the structure. The lattice planes can be described using three integer indices labelled h, k and l. These are known as Miller indices. Each plane intersects the three axis of the unit cell, with one passing through the origin. The intersections are described as fractions of the cell edge. It is the reciprocal of these intercepts which are used to assign the lattice planes as (hkl), in the form where h, k and l are integer values. The notation {hkl denotes a set of equivalent planes to (hkl) by the symmetry of the lattice. A lattice consists of an infinite number of parallel planes that are separated by a perpendicular distance, known as the inter-planar d-spacing, denoted (d_{hkl}). The d-spacings are associated with different

Miller planes which means it is possible to assign the measured peaks with a hkl value. This process is known as indexing. In the context of this work, indexing will be dicussed in more detail in section 3.3.2. Depending on the unit cell centring (whether it is P, F, I or C centred), the positions of the atoms can lead to systematic absences, whereby peaks are absent in the diffraction patterns. The conditions for systematic absences are outlined in table 2.1. Systematic absences can also be identified by using the structure factor (see section 2.2.2.8.4). Some of the lattice planes within a unit cell may be equivalent, for example the (200), (020), and (002) in a cubic system but this is dependent upon the symmetry of the system. A number of equivalent planes are known as the multiplicity (figure 2.1).

Table 2.1: hkl value determination based on the centring of the unit cell

Unit Cell Centring	hkl value determination
P	h,k,l all values observed
F	h,k,l **either** all odd or all even
I	h + k + l odd numbers are absent
C	h + k odd numbers are absent

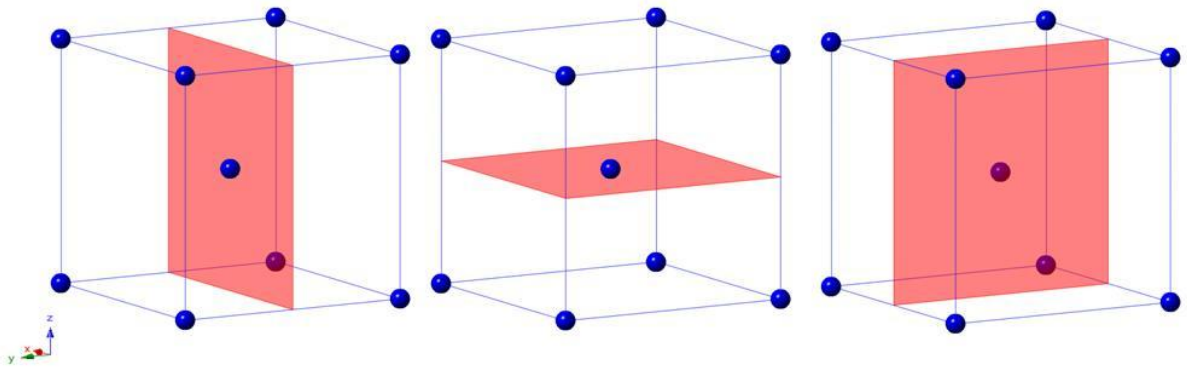

Figure 2.1: Miller planes in a body-centred cubic system (020) (002) (200)

2.2.2.3 Generation and Diffraction of X-rays

X-ray diffraction is a technique which is used to characterise crystalline materials. It provides information about the average structure of a material. Each crystalline material produces a distinctive diffraction pattern which may be used as a fingerprint for its identification. It is often possible to assess the purity of a sample and establish its identity by comparing the diffraction pattern to those on the database such as the International Center for Diffraction Data (ICDD), which contains powder diffraction files (PDf) of all of the known crystal structures.

X-rays are electromagnetic radiation with wavelengths of ~ 1 Å, which is similar to the interatomic separations (d-spacing) between atoms within a solid and therefore allows for diffraction to occur from the crystalline structure. Wavelengths of this order of magnitude can easily be produced in research laboratories where an x-ray tube is typically used as the source of x-rays/incident radiation. The x-ray tube is an evacuated enclosure where electrons are produced by passing an electric current through a tungsten filament. The electrons accelerated by a potential difference of ~ 40 kV bombard the metal target, in this case copper (Cu). Other metals such as molybdenum (Mo) and cobalt (Co) are also commonly used. The resulting x-ray spectrum from a copper target consists of two components; white radiation (Bremsstrahlung) and radiation characteristic of the metal target. White radiation is another name for the continuous background of the spectrum. It is produced due to the electrons from the electron beam losing momentum through deceleration or by stopping prior to striking the metal target. As a result some of the energy is lost and converted into electromagnetic radiation. In order to produce the x-rays used in all diffraction experiments, the energy of the accelerated electrons must be greater than a certain threshold value which is dependent on the metal anode being used. This produces a

second type of spectrum known as the characteristic radiation, which is superimposed on to the background (white radiation). As before, the electrons produced are accelerated and strike a metal target. The electrons from the incident beam have sufficient energy to ionise the core electrons of the 1s (K shell) of the atom resulting in a vacant site (hole). This hole is immediately filled by an electron from a higher energy orbital, either the 2p (L shell) or 3p (M shell), emitting x-rays of characteristic wavelength which relates to the energy of the transition (figure 2.2).

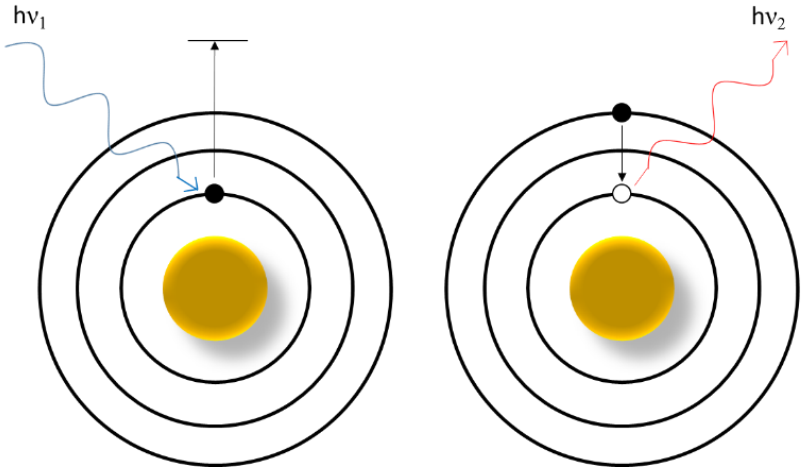

Figure 2.2: Generation of X-rays

For copper, filling of the 1s orbital can be achieved through the occurrence of two transitions; 2p (L)→1s (K) or 3p (M)→1s (K) which are known as the Kα and Kβ transitions with wavelengths of 1.54187 and 1.39223 Å respectively.[3] The Kα transition consists of two characteristic wavelengths 1.54056 and 1.54439 Å [4] which are labelled as $K\alpha_1$ and $K\alpha_2$. The similarity between the wavelengths of both $K\alpha_1$ and $K\alpha_2$ is a result of the splitting of the 2p orbitals being very small. The occurrence of this doublet arises due to the two possible spin states of the 2p electrons relative to the spin state of the 1s electron. $K\alpha_1$ and $K\alpha_2$ correspond to the $2p_{1/2} \rightarrow 1s_{1/2}$ and the $2p_{3/2} \rightarrow 1s_{1/2}$ transitions respectively. The Kα transition occurs more frequently than Kβ and is more intense,

therefore Kα radiation is used in diffraction experiments. Once the x-rays are generated, they emerge from the x-ray tube usually *via* a beryllium (Be) window.

2.2.2.4 Braggs Law

The diffraction of x-rays by the lattice planes within crystalline solids can be understood using Braggs Law, which describes the reflection of x-rays by sets of equally spaced lattice planes. This is illustrated in figure 2.3, where two parallel lattice planes, (hkl) and (hkl)', have the same Miller indices and are equally spaced, separated by a distance of d_{hkl}.

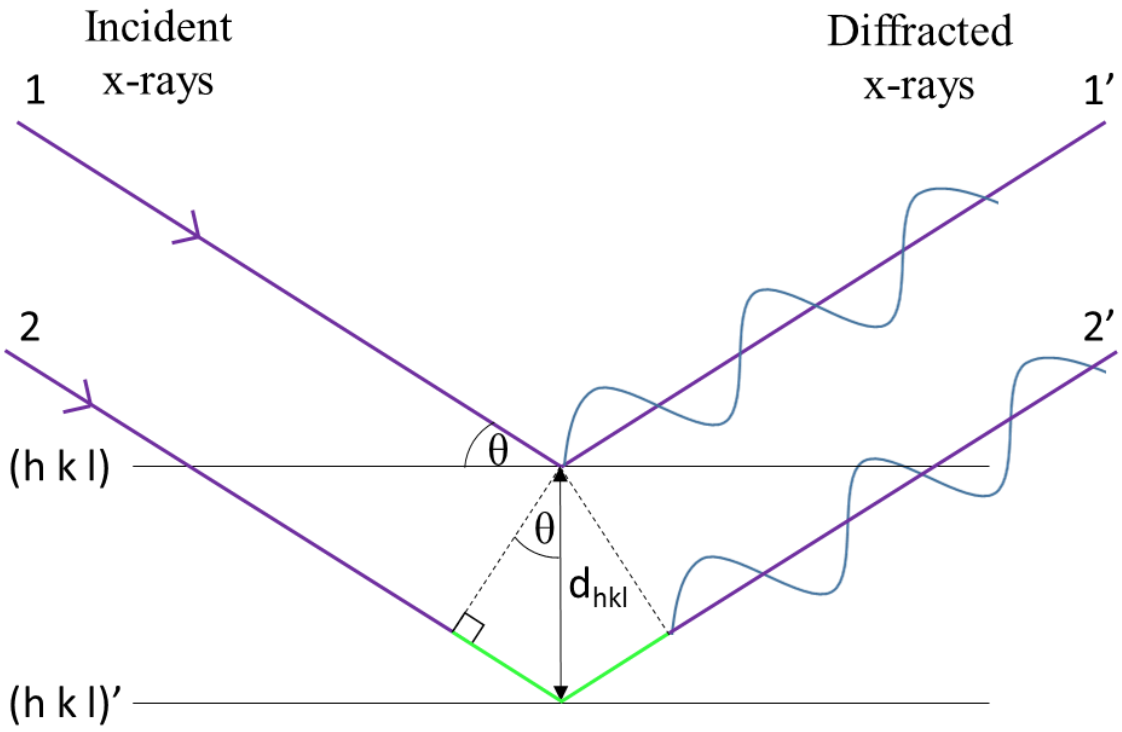

Figure 2.3: Diffraction of X-rays

Incident beams of x-rays (1 and 2) are reflected from adjacent planes. Beam 2 travels further then beam 1 by a distance of 2d sinϑ. In order for the reflected beams 1' and 2' to be in phase, the extra distance travelled by beam 2 must equal an integer number of wavelengths for constructive interference to occur and satisfy Braggs Law

(equation 2.1). Non-integer values of wavelengths would give rise to deconstructive interference.

$$n\lambda = 2d \sin\theta$$

Equation 2.1: Bragg's Law
(where n is an integer value, λ is the wavelength of the incident radiation, d is the spacing between the lattice planes and θ is the angle between the incident wave and the scattered planes)

2.2.2.5 Monochromators

For diffraction experiments, monochromatic x-rays are ideally required and all unwanted radiation must be filtered out. This can be readily achieved by using either a Nickel (Ni) filter or a crystal monochromator. Placing a uniform, thin sheet of nickel in the beam path can be used to attenuate the Kβ radiation, leaving only the Kα component. Crystal monochromators are single crystals which are set to a particular orientation so that the desired wavelength of radiation satisfies Braggs Law.

2.2.2.6 Detectors

The most common type of detectors used in laboratory diffractometers are scintillation counters. These are known as point detectors as they only register the intensity of the diffracted beam at single 2ϑ at any time. The intensity is directly proportional to the number of x-rays hitting the detector. Scintillation counters are highly effective, especially at high photon fluxes where the loss of linearity is low and the dead time is short.

Position sensitive detectors (PSD) are commonly used in modern powder diffractometry and are classed as line detectors. These detectors measure the diffracted intensity at multiple points simultaneously so collect data over a wide range of 2ϑ. As a result of this, the collection time becomes a lot faster and the duration of the diffraction experiment decreases.

2.2.2.7 Powder Diffraction

Unlike single crystals, powdered samples contain crystallites which are randomly orientated in every possible direction. The beam of monochromatic x-rays strikes the powdered sample, multiple crystallites are irradiated simultaneously with some orientated at the Bragg angle (ϑ) resulting in diffraction of these crystals. As a result, x-rays are diffracted at all possible angles, giving rise to diffraction cones, and by taking a 1D cut through the cone a powder diffraction pattern are produced.

2.2.2.8 Diffraction Patterns

A large amount of important data is contained within a powder diffraction pattern and can be summarised by considering four components; background, peak shape, peak position and peak intensity.

2.2.2.8.1 Background

Instrumental and experimental factors as well as sample effects contribute towards the continuous background of a diffraction pattern. Sample effects include x-ray absorbance and fluorescence, local effects, amorphous materials and incoherent scattering. Whilst the background component of a diffraction pattern is disregarded in x-ray diffraction, other techniques such as Pair Distribution Function (PDF) utilises the diffuse scattering component as it contains information regarding the local atomic arrangements and short range order within a material.

2.2.2.8.2 Peak Shape

The nature of the incident beam and the instrument characteristics contribute towards the shape of the peak in the diffraction pattern. The physical properties of the specimen such as the crystallinity and the grain size also contribute. The size of a crystallite can be determined using the Scherrer equation 2.2.

$$\tau = \frac{K\lambda}{B_\tau \cos\vartheta}$$

Equation 2.2: Scherrer Equation
(where τ is the average size of the crystallite region, K is the shape factor usually between 0.9 and 1, λ is the wavelength of the x-rays, B_τ is the broadening at FWHM and $\vartheta$is the Bragg angle

If crystallites are very small (typically less than 1 μm) then there will not be enough planes to give constructive interference and some intensity will be apparent at the side of the peak at the Bragg angle 2ϑ causing broadening of the observed peak.

2.2.2.8.3 Peak Position

The position of the Bragg peaks in a powder diffraction pattern corresponds to the separation between the lattice planes and is determined by the size and symmetry of the unit cell. The height of the sample can also alter the positions of the peaks. Instrumental parameters such as the zero point error and the wavelength of radiation also effect the position of a Bragg peak.

2.2.2.8.4 Peak Intensity

In a diffraction pattern, the intensity measured at different points is known as the profile intensity. The measured intensity can be described by equation 2.3, where j is the total number of data points measured, i is the sequential point number, Y_i is the profile intensity and Y_{bi} is the background intensity.

$$I_{hkl} = \sum_{i=1}^{j} \left(Y_i^{obs} - Y_{bi}\right)$$

Equation 2.3 Intensity of peaks

This measures the intensity of all points within a given range once the background has been subtracted. The integrated intensity depends on various factors relating to both

instrumental parameters and the sample. It can be calculated from the following equation 2.4 of which the terms in this equation are described in table 2.2.

$$I_{hkl} = K\ x\ \rho_{hkl}\ x\ L_\theta\ x\ P_\theta\ x\ A_\theta\ x\ T_{hkl}\ x\ E_{hkl}\ x\ |F_{hkl}|^2$$

Equation 2.4 Integrated intensity

Table 2.2: Terms from the integrated intensity equation

Symbol	Term	Definition
K	Scale Factor	Used to normalise the observed intensities with calculated intensities
$\boldsymbol{\rho_{hkl}}$	Multiplicity Factor	Accounts for the number of symmetrically equivalent reflections
$\boldsymbol{L_\theta}$	Lorentz Multiplier	Corrects for the geometry of the diffractometer
$\boldsymbol{P_\theta}$	Polarisation Factor	Accounts for polarisation of the x-ray beam
$\boldsymbol{A_\theta}$	Absorption Multiplier	Accounts for the absorption of both the incident and diffracted beams absorbed by the sample
$\boldsymbol{T_{hkl}}$	Preferred Orientation	Accounts for the deviations of complete random orientation of crystallites of a certain shape or size
$\boldsymbol{E_{hkl}}$	Extinction Multiplier	Accounts for deviations from the diffraction model. Usually ignored as these are normally very small
$\boldsymbol{F_{hkl}}$	Structure Factor	Defined by the crystal structure, atomic co-ordinates, types of atoms and thermal motions

The intensity of the diffracted Bragg peaks is largely influenced by the structure factor term, $\mathbf{F_{hkl}}$. This describes the interaction of the diffracted waves with all of the atoms within the unit cell which can be calculated for particular hkl reflections using the following equation 2.5. From this equation it is possible to determine there are systematic absences in a particular structure type. Systematic absences are special cases whereby the intensity of the scattered x-rays summed over all of the atoms in the unit cell for a given lattice plane gives a structure factor of 0 and therefore no peak is observed in the diffraction pattern.

$$F_{hkl} = \sum_{j}^{m} f_j \exp\left[2\pi_i\left(hx_j + ky_j + lz_j\right)\right]$$

Equation 2.5 Structure factor

f_j = the atomic scattering factor for the j^{th} atom in the unit cell x_j,y_j,z_j = atomic co-ordinates of the j^{th} atoms

The atomic scattering factor or form factor is a measure of how effectively atoms scatter the x-rays and is a function of the element as f is proportional to the atomic number Z. As x-rays interact with the electrons this means that it is notoriously difficult to detect light elements and differentiate between elements with similar atomic numbers. Heavier elements can easily be detected as they scatter more strongly compared to light atoms. The form factor decreases with increasing 2ϑ. This results in the overall intensity of Bragg peaks at high 2ϑ being less intense. The intensity of a Bragg peak I_{hkl} is proportional to the square of the structure factor (see equation 2.6).

$$I_{hkl} \propto [F_{hkl}]^2$$

Equation 2.6

Factors such as microabsorption effects and the thermal motion of atoms can also diminish the intensity of Bragg peaks.

2.2.2.9 Laboratory Diffractometers

In this work powder x-ray diffraction has been used to determine the structure of novel fluorophosphate materials and to assess the nature of phosphate containing amorphous calcium carbonate phases. The PXRD data were collected on a Bruker D8 diffractometer in transmission geometry. A curved Germanium monochromator was used to provide monochromatic radiation from a copper x-ray source to give Cu $K\alpha_1$ radiation with λ = 1.5406 Å. The diffracted waves were detected using a movable position sensitive detector (PSD) which has a 3° 2ϑ window. Measurements were performed in the range of $5 < 2\vartheta < 90°$, with a step size of ~ 0.02°. Samples were prepared by placing a small amount of sample between two layers of Scotch® Magic™ Tape and were rotated in the plane perpendicular to the beam of incident radiation.

2.2.3 Neutron Diffraction

In situations where x-ray diffraction may be inadequate, neutrons can be used to investigate the structures of crystalline materials. Unlike x-rays, neutrons predominantly interact with the nuclei of an atom and as it is the atomic nuclei which are responsible for the scattering. There is no dependence on the scattering power of neutrons with the atomic number and as a result neutron diffraction experiments may be utilised for the detection of light atoms, atoms with the similar atomic numbers and isotopes of an element. As neutrons scatter from the nuclei of atoms which are small, it is considered as a point scatterer, as the scattering power does not fall off with scattering angle so the atomic form factor is neglected.

Neutrons are generated in two ways; in a reactor or by spallation. In a nuclear reactor, a beam of high velocity neutrons are produced from the fission of uranium (^{235}U). However, a neutron moderator such as D_2O is required in order to slow down the neutrons, reducing the kinetic energy of the neutrons to produce thermal neutrons of use for diffraction. ^{235}U is more likely to undergo fission when colliding with thermal neutrons with suitable wavelengths which can be used for diffraction experiments. In order to select specific wavelengths, a monochromator is used, producing neutrons with a constant wavelength.

In this project, neutron powder diffraction (NPD) experiments were carried out on the HRPD and POLARIS instruments (figure 2.4) at ISIS on the Rutherford Appleton Laboratory site near Oxford. At ISIS, neutrons are produced *via* spallation. This process involves accelerating protons in a synchrotron. These protons then collide with a heavy metal target generating a pulsed neutron beam which is used in time of flight (TOF) experiments. The Bragg reflections are measured at fixed scattering angles (2ϑ) with the time of detection of the neutron taken after the neutrons are produced in the target. Neutrons used in diffraction experiments are of the order of 0.5-3 Å. From the continuous spectrum of radiation that is produced, the majority of the radiation is wasted and therefore the beam that is used is weaker in intensity. As neutrons can penetrate further into a material, neutron diffraction studies require larger sample sizes compared to those needed for x-ray diffraction. Vanadium cans are used to contain the sample of interest to be measured as it displays limited neutron scattering.

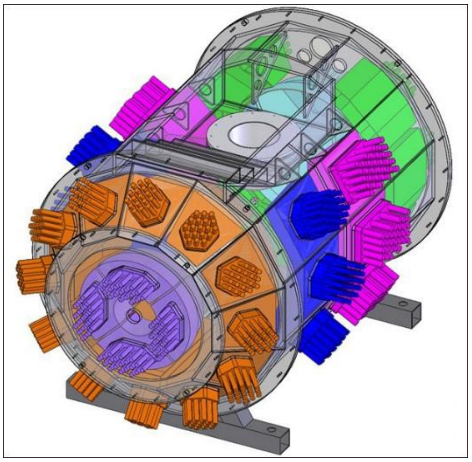

Figure 2.4 Polaris instrument at ISIS.[6] The colours represent the 5 detector banks (bank 1, 2, 3, 4 (90 ° bank) and 5 (back-scattering bank))

2.2.4 Rietveld Refinement

The Rietveld method,[7] also known as the full profile refinement, is a computer based analytical procedure designed by Hugo Rietveld[8-9] in the mid 1960s. This method was employed to extract detailed structural information about the crystal structure of a material from powder diffraction data. It was first utilised with neutron powder diffraction (NPD) data but was subsequently adapted for use with x-ray powder diffraction (PXRD) data.

In order to perform a Rietveld refinement, a reasonable starting model/models for the phase or phases present are required. This describes the shape and size of the unit cell along with the atomic co-ordinates, occupancies and thermal motions of the atoms present. These are combined with a range of experimental parameters that are used to describe the background and the peak shape to calculate a diffraction pattern, which is the calculated pattern in the refinement profile. As this is a structure refinement method, the adequacy of the model can affect the fit.

The Rietveld method uses a non-linear least squares refinement method in order to obtain the best fit between the entire patterns of both the observed and the calculated data. During the refinement, the residual S_y is being minimised over all data points (see

equation 2.7). The residual S_y represents the difference in intensities between the observed (y_i) and the calculated (y_{ci}) patterns and w_i is the weighting factor $1/y_i$.

$$S_y = \sum_i w_i (y_i - y_{ci})^2$$

Equation 2.7: The residual S_y

It is important to continuously monitor the progress of a Rietveld refinement in order to decide how to proceed; whether to continue with the refinement or decide that the refinement has reached or is near completion. There are three ways in which the quality of a Rietveld refinement can be monitored, visually, via the statistical numerical values and by the chemical sense of the resulting model.

From a Rietveld refinement a Rietveld plot is generated. This is a visual display used to assess the fit between the observed and calculated data. An example of a Rietveld plot is shown in figure 2.5.

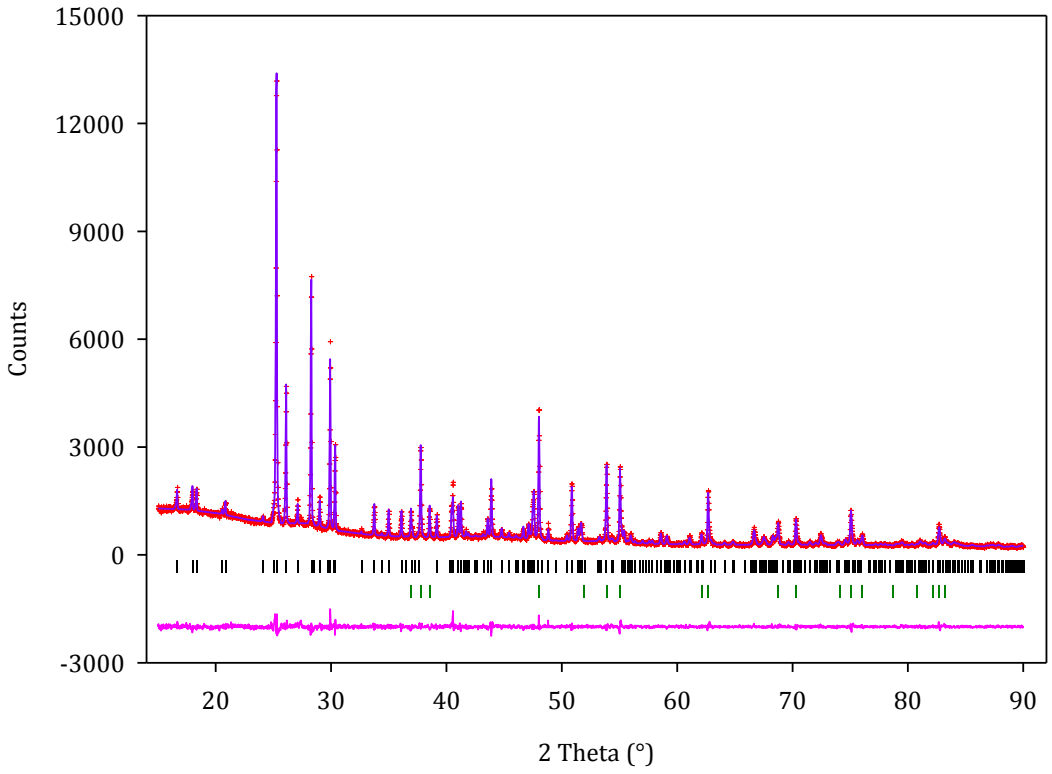

Figure 2.5: Example Rietveld Plot . Final observed (red), calculated (purple), difference profile (pink) and the tick marks represent the phases present (black – phase 1 and green phase 2)

The quality of the fit can be assessed visually by monitoring the changes in the difference line (the pink line) which can be seen below the patterns of the observed and calculated data. Ideally, for a perfect fit, this line should be flat, since there will be no discrepancies between the observed and calculated patterns.

In addition to visually monitoring the progress of the Rietveld refinement, there are several statistical values which are used to evaluate the quality of the fit. These are known as the R-Factors; R_F^2 (structure factor), R_B (Bragg factor), R_{exp} (expected), R_p (pattern) and R_{wp} (weighted pattern). As both the structure factor (R_F^2) and Bragg (R_B) factors (equations 2.8 and 2.9 respectively) are based on the Bragg intensities deduced by the model, as oppose to the observed Bragg intensities, these numerical parameters are biased towards the model being used. However, the numerical values generated from both of these terms give a good indication of the accuracy of starting model.

$$R_{F^2} = \frac{\sum \left| \left(I_{hkl}(obs)\right)^{\frac{1}{2}} - \left(I_{hkl}(calc)\right)^{\frac{1}{2}} \right|}{\sum \left(I_{hkl}(obs)\right)^{\frac{1}{2}}}$$

Equation 2.8: Structure factor

$$R_B = \frac{\sum |I_{hkl}(obs) - I_{hkl}(calc)|}{\sum I_{hkl}(obs)}$$

Equation 2.9: Bragg factor

There are several R-Factors which focus on the fitting of the observed and calculated intensities of the entire pattern. These include; R_p, R_{wp} and $R_{exp.}$ (see equations 2.10-2.12).

$$R_p = \frac{\sum |y_i - y_{ci}|}{\sum y_i}$$

Equation 2.10: R-profile

$$R_{wp} = \left\{ \frac{\sum w_i (y_i - y_{ci})^2}{\sum w_i (y_i)^2} \right\}^{\frac{1}{2}}$$

Equation 2.11: R-weighted pattern

$$R_{exp} = \left\{ \frac{n - p - c}{\sum w_i (y_i)^2} \right\}^{\frac{1}{2}}$$

Equation 2.12: R-expected

The weighted pattern (R_{wp}) is the most meaningful of the statistical values from a mathematical point of view as the numerator of this expression is the residual (S_y) being minimised in the refinements. This parameter also best reflects the progress of the refinement. The quality of the refinement should improve upon increasing the number of parameters that are being refined, meaning the fit between the observed and the calculated patterns should reach a point that is near completion. As a result of this, the final R_{wp} value should come close to the R_{exp} value, which is the best possible R-value

which can be achieved for that particular dataset. Combining the R_{wp} and R_{exp} terms gives a ratio of these two values. This produces another numerical indicator known as χ^2 (equation 2.13) which measures how well the refined model accounts for the data. Ideally, this value should tend towards 1, but this value is rarely attainable.

$$\chi^2 = \left[\frac{R_{wp}}{R_{exp}}\right]^2$$

Equation 2.13: The goodness of fit indicator

When performing refinements, it is vital to constantly monitor the refinements progression using both visual and numerical indicators in order to determine whether the refinement has been successful.

Finally, the chemical sense of the resulting model is the most important criteria of a Rietveld refinement, as both the visual fit and statistical values of the refinement could suggest a good fit between the calculated and experimental data however, when analysing the resulting bond lengths and angles this may not be the case.

Rietveld refinements of the both powder X-ray diffraction (PXRD) and neutron diffraction (NPD) data collected for this thesis were performed using the General Structural Analysis System[10] and EXPGUI[11] suite of programs.

2.2.5 Raman Spectroscopy

This is a technique which is used to investigate the vibrational and rotational modes of a molecule, both of which are determined by the symmetry of the molecule. In order for a molecule to be Raman active, a change in the polarisability of the molecule must be observed. Group theory can be used to determine whether a mode is either Raman or Infrared active.

Monochromatic light is used to irradiate the sample, interacts with the electron cloud and induces polarisation within the molecule causing it to vibrate. The photons which are absorbed cause an excitation of the molecule from the ground state to an excited virtual state. In order for this process to occur, the wavelength of the incident radiation must be sufficient in order to cause excitation of the molecule. Upon relaxation from the short lived virtual state, a photon is released. The photons which are emitted can scatter elastically (Rayleigh Scattering) or inelastically (Raman Scattering, Stokes and anti-Stokes shift) which is shown in figure 2.6.

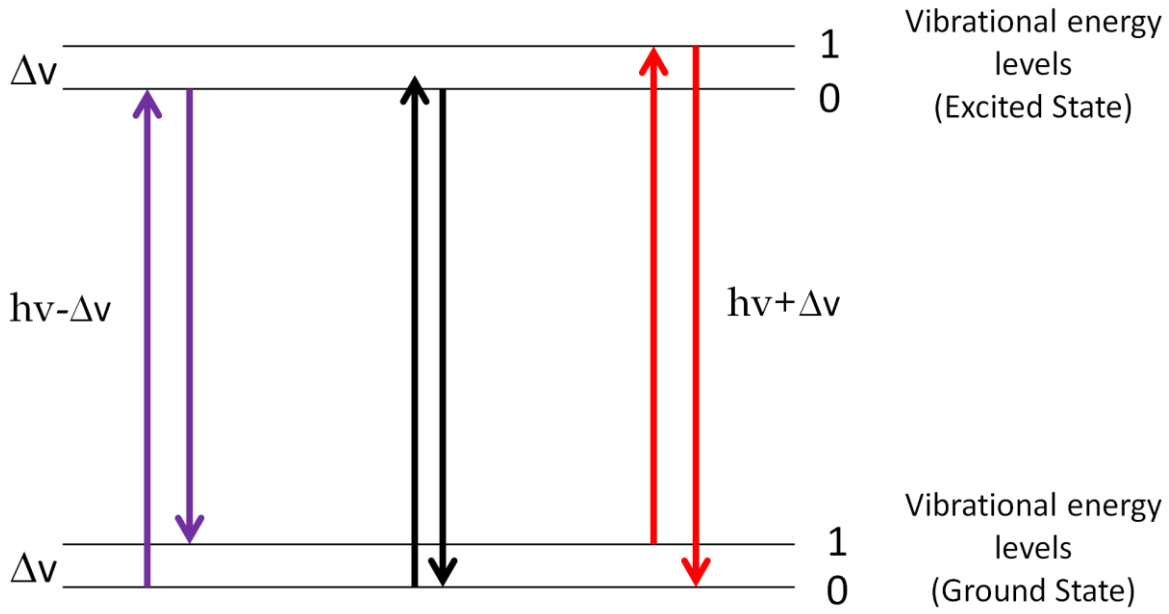

Figure 2.6: Stokes scatter (left), Rayleigh scatter (centre) and anti- Stokes scatter (right)

The majority of photons scatter elastically. This is where the molecule absorbs and emits a photon of the same energy, resulting in the molecule having no Raman active modes.

Raman scattering is less intense than Rayleigh scattering and is caused by a small minority of photons which undergo weak inelastic scattering. It is the difference in energy between the initial and final state of a molecule which causes the emitted photon to shift to either higher (Anti-Stokes shift) or lower frequency (Stokes shift). When Raman scattering occurs from the lowest energy ground state, the energy from the

incoming photon is absorbed by the molecule, which emits a photon of lower energy upon relaxation. This is known as the Stokes shift. A molecule which is already in an excited vibrational state loses energy as it is transferred to the scattered photon. As a result the emitted photon has greater energy than that of the incident photon and is known as an Anti-Stokes shift. Typically, Stokes scattering is the most dominant type of Raman scattering as most molecules are in their lowest vibrational ground state at room temperature.

For this work, Raman spectra were collected on the Renishaw InVia Raman Microscope using a green, 532 nm laser. A small amount of the desired sample was placed on to a glass slide and focussed under the microscope using x 50 magnification before the spectra was collected in the spectral region of 100-1500 cm^{-1} and over 3-6 accumulations.

2.3 Nuclear Magnetic Resonance (NMR)

In order for a nucleus to be NMR active, it must possess nuclear spin. This arises when the nuclei has unpaired protons and neutrons. For nuclei to possess nuclear angular momentum/spin it must have a non-zero quantum number ($I \neq 0$). Each nucleus has 2I+1 possible orientations, where I is the spin quantum number. The nuclei which are of particular interest in this work are ^{31}P and ^{19}F, both of which have a spin quantum number of $\frac{1}{2}$, resulting in there being 2 possible states + $\frac{1}{2}$ and - $\frac{1}{2}$.

The spin quantum number, P is a vector quantity which has both magnitude and direction. It is related to the magnetic moment (μ) and the gyromagnetic ratio (γ) as defined in equation 2.14.

$$\mu = \gamma P$$

Equation 2.14

The gyromagnetic ratio is a measure of how strongly magnetic the nucleus is. For ^{31}P, the gyromagnetic ratio is 10.84 / 10^7 T^{-1} s^{-1}.[12] In the absence of a magnetic field, the magnetic moment has no preferred direction and all of the spin states are degenerate. Once the nucleus is placed in a static magnetic field, the nucleus aligns itself relative to the field, B_0. In NMR, transitions are only allowed between adjacent energy levels as a result of the $\Delta m = \pm 1$ selection rule. A transition can only be induced if the energy is equal to the energy difference between the two states. Applying a magnetic field causes the nucleus to precess as shown in figure 2.7.

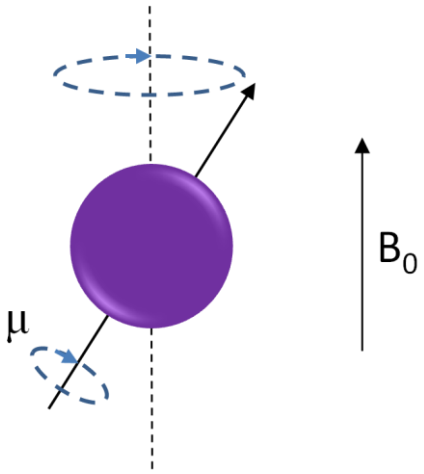

Figure 2.7: A precessing nucleus when a magnetic field has been applied

The frequency at which the nucleus precesses is called the Larmor frequency, which is dependent on the gyromagnetic ratio and the strength of the magnetic field as shown in equation 2.15.

$$v = \frac{\gamma B_0}{2\pi}$$

Equation 2.15
(where v is the Larmor frequency, $\gamma$is the gyromagnetic ratio, B_0 is the external magnetic field and π is a constant 3.14)

The nuclei distribute themselves amongst the available energy levels according to the Boltzmann distribution. The signal intensity is determined by the difference in population between the energy levels. Transitions between the energy levels can be induced by applying radiofrequency (rf) radiation that matches the Larmor frequency, which causes spin up nuclei to flip and become spin down nuclei and vice versa. The population of spins are summed, to give the magnetisation vector M_0. Maximum signal is produced when M_0 is in the transverse xy plane.

This is achieved by applying a 90° rf pulse resulting in equal population of the spin up and spin down nuclei. The magnetisation vector will oscillate as a result of the precessing nuclei. This induces a weak oscillating voltage in the rf coil, known as the free induction decay (FID). There is an exponential decrease in the intensity of the NMR signal with time due to the relaxation process. A fourier transformation of the FID generates the NMR spectrum.

2.3.1 Magic Angle Spinning (MAS)

In order to analyse samples in the solid state, the powered samples must be spun at the magic angle 54.7°[12]. Spinning at the magic angle mimics the constant tumbling motion of a liquid and is employed to eliminate the effects of dipolar coupling and chemical shift anisotropy (CSA), both of which are factors that will affect the appearance of the NMR spectrum.

2.4 Thermogravimetric Analysis-Mass Spectrometry (TGA-MS)

Thermogravimetric analysis monitors the change in mass of a sample as a function of temperature/time. The sample is heated at a constant rate and the mass remains constant until the sample begins to decompose. As thermogravimetry can only detect changes in mass, it is usually advantageous to use thermogravimetry in conjunction with differential thermal analysis (DTA), in order to monitor the thermal events which occur within a sample that do not involve a mass change, such as a polymorphic transition, melting or crystallisation. Differential thermal analysis measures the difference in temperature (ΔT) between the sample of interest and an inert reference material (Al_2O_3), where the change in temperature is detected by the net voltage of the thermocouples. Until the occurrence of a thermal event, there should be no discernible difference in temperature of both the sample and the reference material. If a thermal event occurs, it causes the temperature of the sample to differ from that of the reference material and is dependent on whether the event occurring is either exothermic or endothermic. For an exothermic event, the temperature of the sample temperature exceeds that of the reference material and for an endothermic event, the sample temperature will lag behind that of the reference material. TGA/DTA measurements can be carried out in a number of different environments including air, oxygen, nitrogen and hydrogen.

The quadrupole mass spectrometer uses an ion source to convert the gases evolved into positively charged ions, which are then accelerated by an electric field. The quadrupole selectively filters out the ions based on their m/z ratio before they are detected.

Measurements were carried out using between 30-100 mg of sample. Samples were heated up to 1000°C at a rate of 10°C/min in either an oxygen (amorphous calcium

carbonates and its phosphate derivatives) or nitrogen (fluorophosphate containing materials) atmosphere with nitrogen as the protecting gas. The mass spectrometer was set up to detect species with a maximum m/z ratio of 110, or to detect ions with specific mass to charge ratios. The products obtained were characterised by XRD. All measurements were performed on the Netzsch STA 449 F1 Jupiter Thermogravimetric analyser coupled with a Netzsch 403 C mass spectrometer.

2.5 Scanning Electron Microscopy (SEM)

A beam of high energy electrons is used to scan across the surface of a sample. These electrons lose a large proportion of their kinetic energy once they interact with the atoms on the surface of the sample. Inelastic scattering ejects the secondary electrons from the sample. It is the secondary electrons that are detected and used to produce the image. In order for a sample to be analysed by SEM, the sample must be conducting otherwise there will be an accumulation of electrons on the surface causing the sample to charge up. This will affect the quality of the image produced.

Most SEMs have a built in energy dispersive x-ray analysis (EDAX) system which is used to determine the elemental composition of the sample by discriminating against the detected photons the difference in their energies

2.6 X-Ray Fluorescence Spectroscopy

X-ray fluorescence spectroscopy is an emission technique that is utilised for the chemical and elemental analysis of a wide range of materials including glasses, metals and ceramics. This method is a non-destructive technique that provides both quantitative and qualitative analysis of the material of interest in a short time period (2-20 minutes).

Fluorescence relates to the emission of radiation (secondary radiation) from a material whose energy is lower than that of the incident beam (primary radiation). This process involves an electron from an atom absorbing radiation (photon) from the incident beam, causing it to be excited from the ground state (lowest energy state) to an excited virtual state which is higher in energy. Upon emitting a photon, the electron relaxes back down to the ground state. The emitted photon has a longer wavelength and is lower in energy compared to the primary radiation (shorter wavelength, higher in energy).

In this process, the sample is bombarded with high energy x-rays which causes the excitation of the electrons which occupy the inner atomic orbitals, usually from shells K and L. As a result of this, a core electron is ejected leaving a vacancy (hole) which is then filled by an electron from a higher energy orbital. As it does so, a fluorescent photon (x-ray fluorescence) is emitted (figure 2.8).

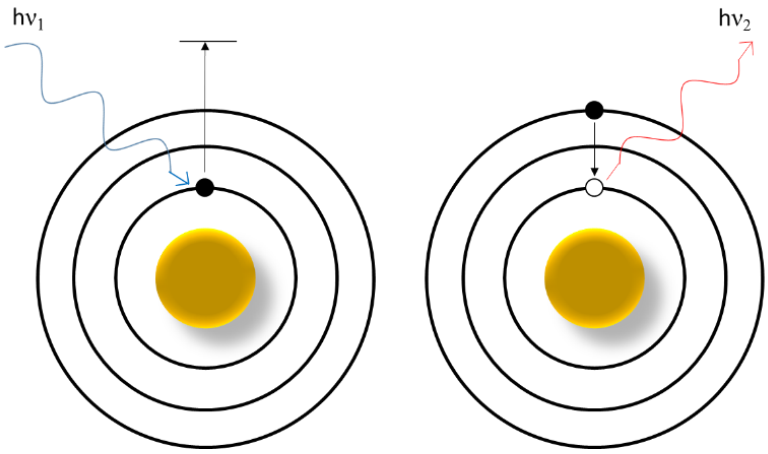

Figure 2.8: X-ray fluorescence

The energy of the photon is characteristic of the energy difference between the initial and final orbitals involved in this process. The emitted x-ray fluorescence radiation is characteristic for element. The spectrometer can discriminate between the fluorescent radiation by sorting the energies of the photons (energy dispersive analysis – EDXRF) or

by separating the wavelengths of the radiation (wavelength dispersive analysis – WDXRF). Depending on the method of analysis, the energy or wavelength of the fluorescent radiation can be calculated using Planck's constant, see equation 2.16.

$$\lambda = \frac{h \cdot c}{E}$$

Equation 2.16 (where λ is the wavelength, h isPlancks constant, c is the speed of light and E is the energy)

An energy dispersive spectrometer can determine the energy of the photon that it detected as well as measuring the intensity. The emitted fluorescent x-rays are directed towards a solid state detector (silicon drift detectors), producing continuous distribution of pulses of which the voltage is proportional to the incoming energy of the photon. A multichannel analyser (MCA) produces an accumulated digital spectrum from the number of pulses which when processed gives analytical information. The silicon detector consists of a highly resistive silicon chip where electrons are collected at the anode. Advantages to this detector type are that it has fast analytical capabilities, high processing and count rates, operates at high temperatures (no need for cooling with liquid nitrogen), lowers dead time (time spent on processing an event) and has high resolution compared to traditional Si(Li) detectors.

A wavelength dispersive x-ray fluorescence spectrometer (WDXRF) measures only the intensity of the emitted photons. The fluorescent x-rays that are emitted from the sample of interest are directed towards a single crystal monochromator via a collimator, which ensures that only a parallel beam of photons from the sample are diffracted from the monochromator, to produce a beam of single wavelength radiation. The angle at which these x-rays are diffracted are recorded by a goniometer before reaching the detector. As only photons of a single wavelength hit the detector, WDXRF has greater resolution compared to EDXRF.

As with PXRD, x-ray tubes are used as the source of x-rays (radiation) in x-ray fluorescence spectroscopy. In this case, rhodium (Rh) is used as the anode material as the energies of Rh are sufficient for the excitation of both heavy and light elements. Other elements such as chromium and molybdenum can also be used for the anode material. However, using rhodium as the anode material results in the appearance of Rh peaks in the emission spectrum. If the analysis of Rh was required in the sample of interest, radiation from the Rh tube must be absorbed by the primary beam filter before it reaches the sample. This is located in between the x-ray tube and the sample and is also used to improve the signal to noise ratio. A DuraBeryllium shield is used as protection for the x-ray tubes window. Using a robotic arm, the sample is loaded into the instruments entry position. The sample chamber (x-ray tube → sample → detector) is maintained under vacuum as the secondary radiation from light elements is low in energy and has low penetrating power so the beam is severely attenuated if it passes through the air at any distance. For this reason it is extremely difficult to quantify elements which are lighter than sodium. Being under vacuum prevents air from absorbing the fluorescent x-rays. For the elemental analysis of solid samples, measurements are performed under vacuum but for liquid samples or loose powders the samples are measured in a helium atmosphere. The vacuum seal protects the goniometer chamber so that the systems components are well protected from samples breakages or leaks. A mask is in place in the sample chamber to prevent any unwanted radiation specifically from the sample holder once the sample is exposed to the x-rays.

In WDXRF, the detectors require high processing speeds in order to deal with high count rates of photons. The energy resolution must also be sufficient to filter out any noise form the background or photons form the incident beam. For the detection of light elements a proportional counter is used but for heavier elements, a scintillation counter

is required. There are two types of proportional counter, gas flow and sealed proportional counters. The key feature of a proportional counter is that it is used to measure the intensity of the incident radiation. A gas flow counter is a metallic tube (cathode) with a tungsten or nichrome wire in the centre (anode) which is the counters device for the detection of photons. The gas typically used in proportional counters is a mixture of argon and methane (90 %:10 %). The incoming photons penetrate the conductive window ionising the Ar atoms resulting in the creation of ion pairs. The presence of methane suppresses the fluorescent photons caused by the recombination of Ar^+ atoms with the free electrons. The free electrons move towards the anode where the field strength is highest producing a current. The positive ions drift towards the cathode. The field strength in the chamber is sufficient to cause avalanches; a large cloud of electrons at the anode as a result of the electrons having sufficient energy to undergo further ionisation. The number of ion pairs created in this process is proportional to the energy of the photon. The conductive window must effectively transmit the x-rays but needs to be of sufficient thickness to minimise the diffusion of the detector gas into the vacuum chamber.

A sealed proportional counter works in the same way as a gas flow proportional counter except that it does not have a continual gas flow running through, instead it is of fixed volume and needs to be replaced once the gas inside has become permanently ionised.

Scintillation counters are used to measure both the energy and the intensity of the incident radiation. The fluorescent radiation from the sample is incident on the scintillator. This consists of a phosphor, which is a transparent crystal that fluoresces (emits a photon) when struck by the ionising radiation. The photon released from the fluorescence event is directed towards the photocathode, which emits a photoelectron

of the same energy as the incident photon on the photocathode, as per the photoelectric effect. The electron passes through a photomultiplier tube which generates an output pulse at the anode. The composition of phosphor materials that are typically used in XRF spectrometers are sodium iodide crystals doped with thallium. Subsequent to measurements on the sample of interest, an x-ray spectrum will be produced. This consists of multiple peaks, all with differing intensities. The peak positions identify the elements present in the sample whilst the intensities relate to the quantity of the element present.

Undoubtedly, there will be random errors associated with the measurements due to instrument errors (x-ray tube stability and counting statistics). However, errors in the measurements can be introduced from the sample itself, these are known as matrix effects. This can have a significant effect on the analysis and the results obtained. Sample preparation is of utmost importance in XRF spectroscopy as it is vital to choose the best method of preparation for the samples in order to obtain the most accurate results. XRF has the capability of analysing samples in various forms; liquids, loose powders, pressed pellets and fused beads. A summary of these sample preparation methods are outlined in table 2.3.

Table 2.3 Sample preparation methods for XRF spectroscopy[13]

Preparation Method	Apparatus	Advantages	Disadvantages
Liquid	Plastic sample cups Mylar film	Overcome many matrix effects Easy to prepare samples	Mylar film and solvent can introduce problems
Loose powders	Plastic sample cups Mylar film	Easy to prepare samples	Mylar film can introduce problems Issues with the size of particles
Pressed pellets	Sample press Binding agent	Pellets of equal density, and size Smooth, flat and clean surface	Difficult to produce a homogenous sample Non-representative sample surface – inaccurate results Choice of binding agent is vital, incorrect choice can introduce problems
Fused beads	Inert, heat resistant crucible Furnace Flux Non-wetting agent	Minimise matrix effects Homogenous mixture Beads can be stored in a desiccator and re-used	High temperatures required Expensive Time consuming

Certain criteria must be met when preparing samples for analysis as variations in composition can produce results which are not representative of the entire sample. Therefore it is important to ensure that samples are homogenous, have a smooth, flat surface and the size of the particles are small. The best preparation method to ensure that these criteria are met is the fused bead method.

2.6.1 Fused Bead Procedure

In this work, all samples were prepared as fused beads using the following procedure. In a 10:1 ratio, 3.50 g of flux and 0.35 g of sample were ground together using a pestle and mortar for a few minutes. The mixture is then transferred into the

Pt/Au crucible and placed into a furnace at 1250 °C for 6 minutes. The crucible is then removed and a small amount of Ammonium Iodide (approximately 15 mg) is added before placing the crucible back into the furnace for a further 6 minutes. This time upon removal from the furnace the molten mixture is swirled to remove the presence of air bubbles in the mixture. For a final time, the crucible was placed back into the furnace for a further 30 seconds before being taken out and being allowed to cool. Once cooled, the crucible was tapped against a hard surface to release the glass bead (28 mm diameter and 3-4 mm thick). All elements in the sample are oxidised into their most stable form.

Measurements were performed on a Bruker AXS S8 Tiger wavelength dispersive XRF instrument and analysed using the spectra plus software version 2.0. High purity reagents were used to produce two calibrations, providing accurate data from which the ratio between our M^{2+} cation and the phosphorus (Ca/Sr:P) can be calculated.

2.6.2 Calibration

A calibration can be used in conjunction with sample preparation in order to ensure more reliable results are obtained. Whilst sample preparation can remove the majority of the matrix effects present in the data collected, some effect will still persist. Therefore, a calibration curve can be used to account for any remaining effects. A calibration curve is generated from known standards, using the same sample preparation method as the sample of interest. The concentration range in which the calibration is produced extends below and beyond the estimated (if known) concentrations within the sample. As the fluorescence intensity is proportional to the concentration in the form a linear relationship at low concentrations, the concentration of the elements within the sample can be determined.

The standards for the calibrations were produced using the compounds stated in table 2.4 and made up to the appropriate concentrations. These standards were then

prepared as fused beads following the procedure described in section 2.7.1 and the subsequent calibration curves were produced. The resulting calibration curves for both calibrations can be found in sections 2.6.2.1 and 2.6.2.2 respectively. Sodium and potassium salts are present from a NaCl by-product and trace amounts of potassium in the sodium fluorophosphate starting material respectively.

Table 2.4 Composition of standards for two XRF calibrations

Calibration	Compounds required to make standards	Oxidation Products
Strontium fluorophosphate	$SrCO_3$ $NH_4H_2PO_4$ NaCl KCl	SrO P_2O_5 Na_2O K_2O
Calcium fluorophosphate	$CaCO_3$ $NH_4H_2PO_4$ NaCl KCl	CaO P_2O_5 Na_2O K_2O

2.6.2.1 Strontium Fluorophosphate Calibration Curves

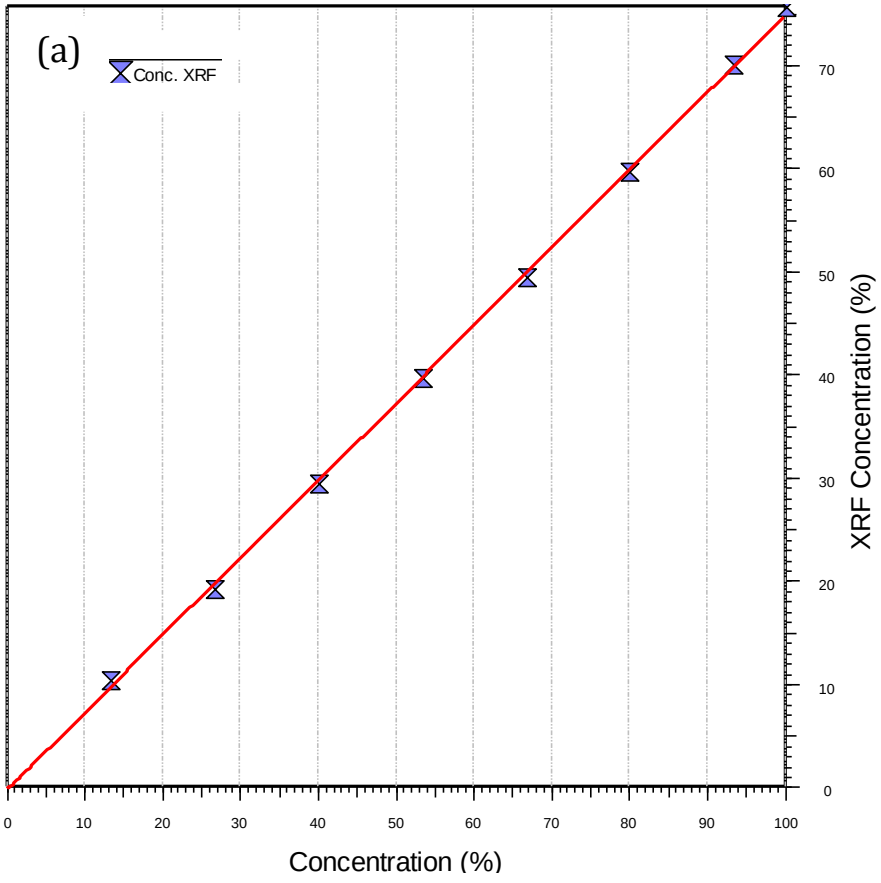

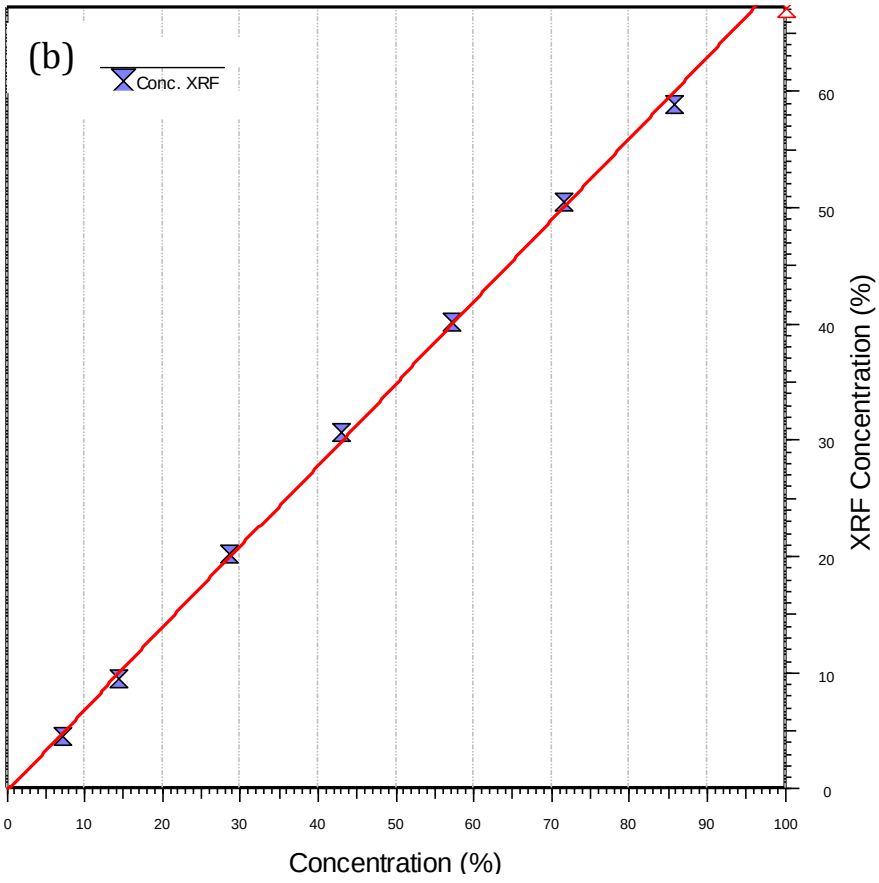
(b)
Conc. XRF
XRF Concentration (%)
Concentration (%)
0
10
20
30
40
50
60
70
80
90
100

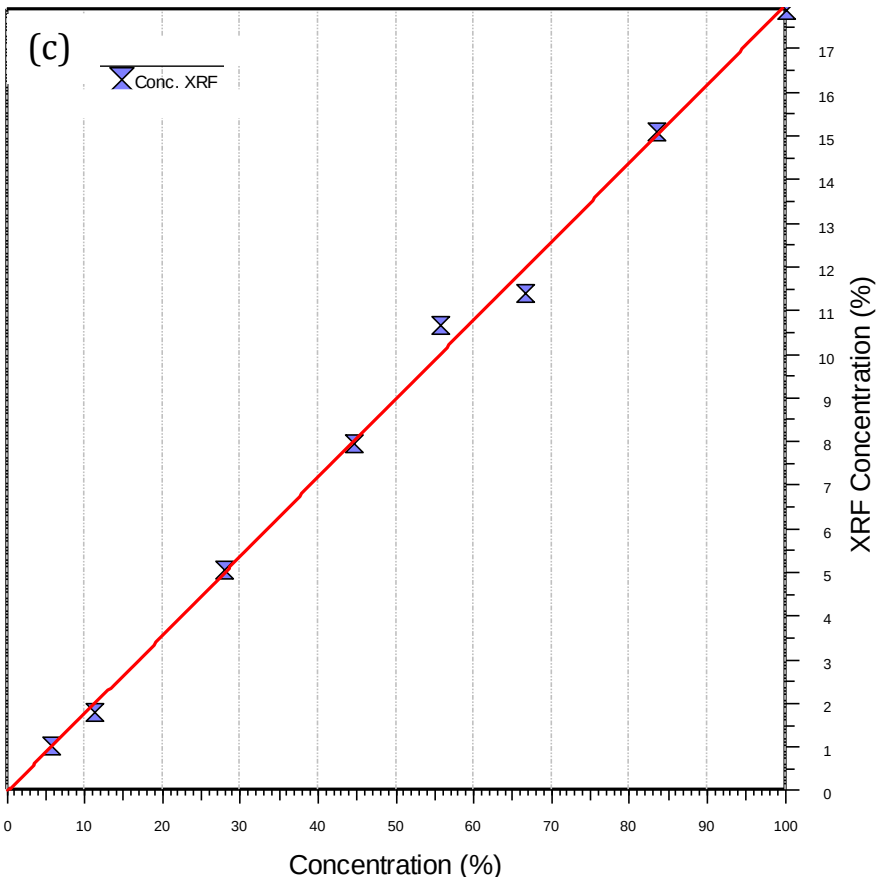
(c)
Conc. XRF
XRF Concentration (%)
Concentration (%)
0
1
2
3
4
5
6
7
8
9
10
11
12
13
14
15
16
17
0
10
20
30
40
50
60
70
80
90
100

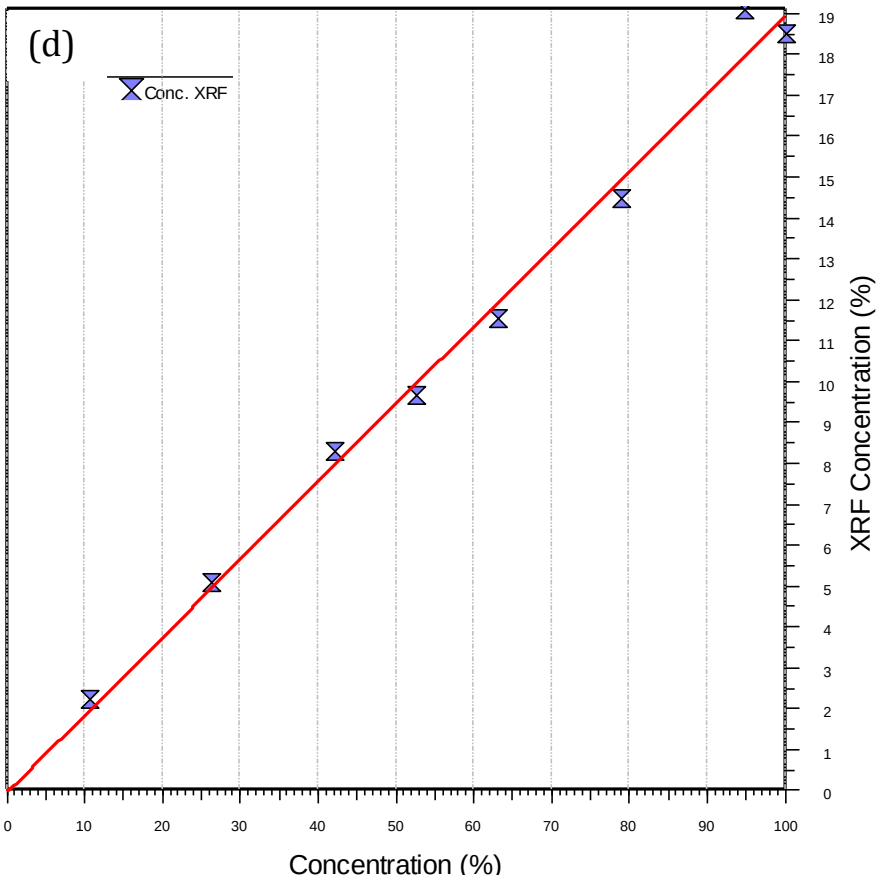

Figure 2.9: XRF calibration curves for the strontium fluorophosphate calibration; Sr (a), P (b), Na (c) and K (d)

2.6.2.2 Calcium Fluorophosphate Calibration Curves

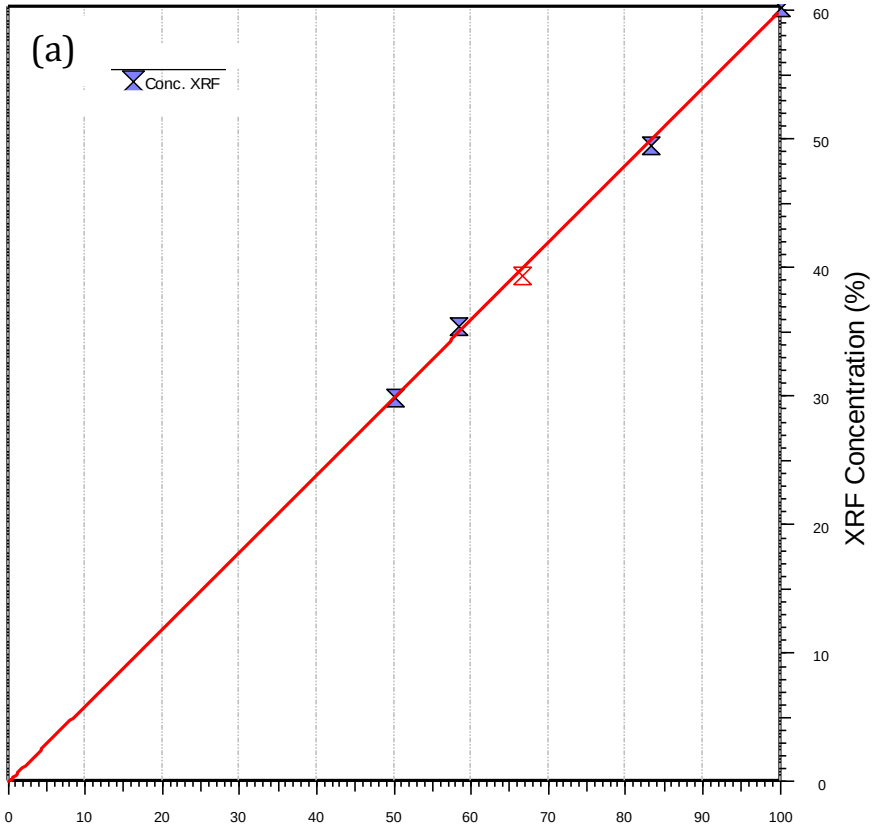

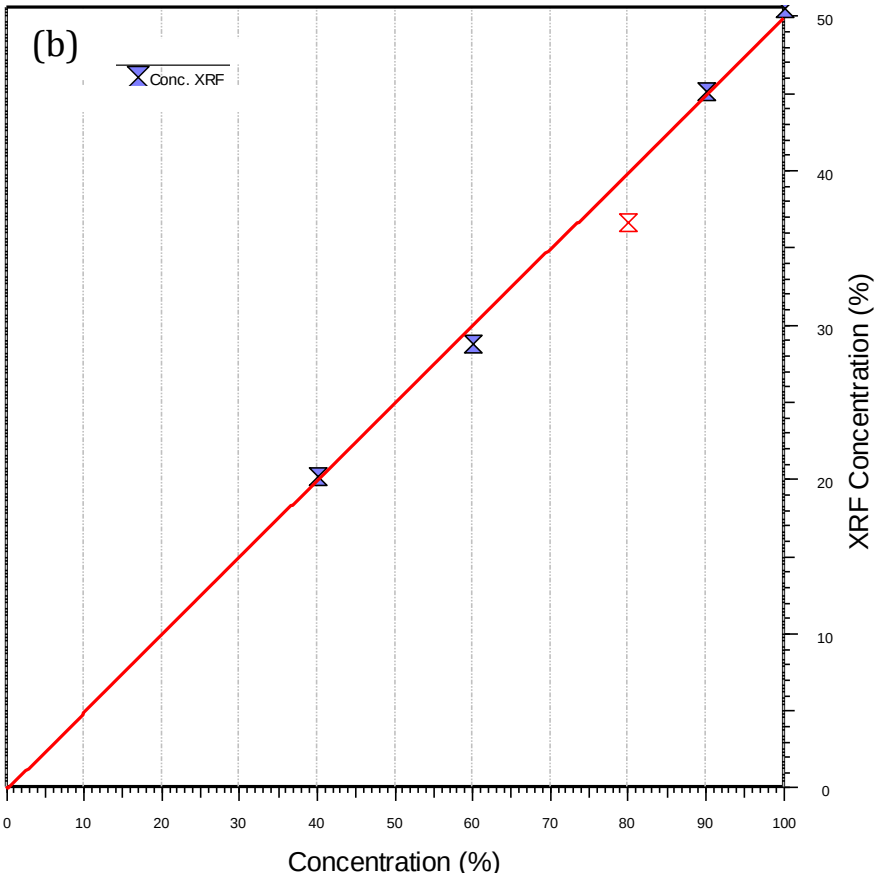

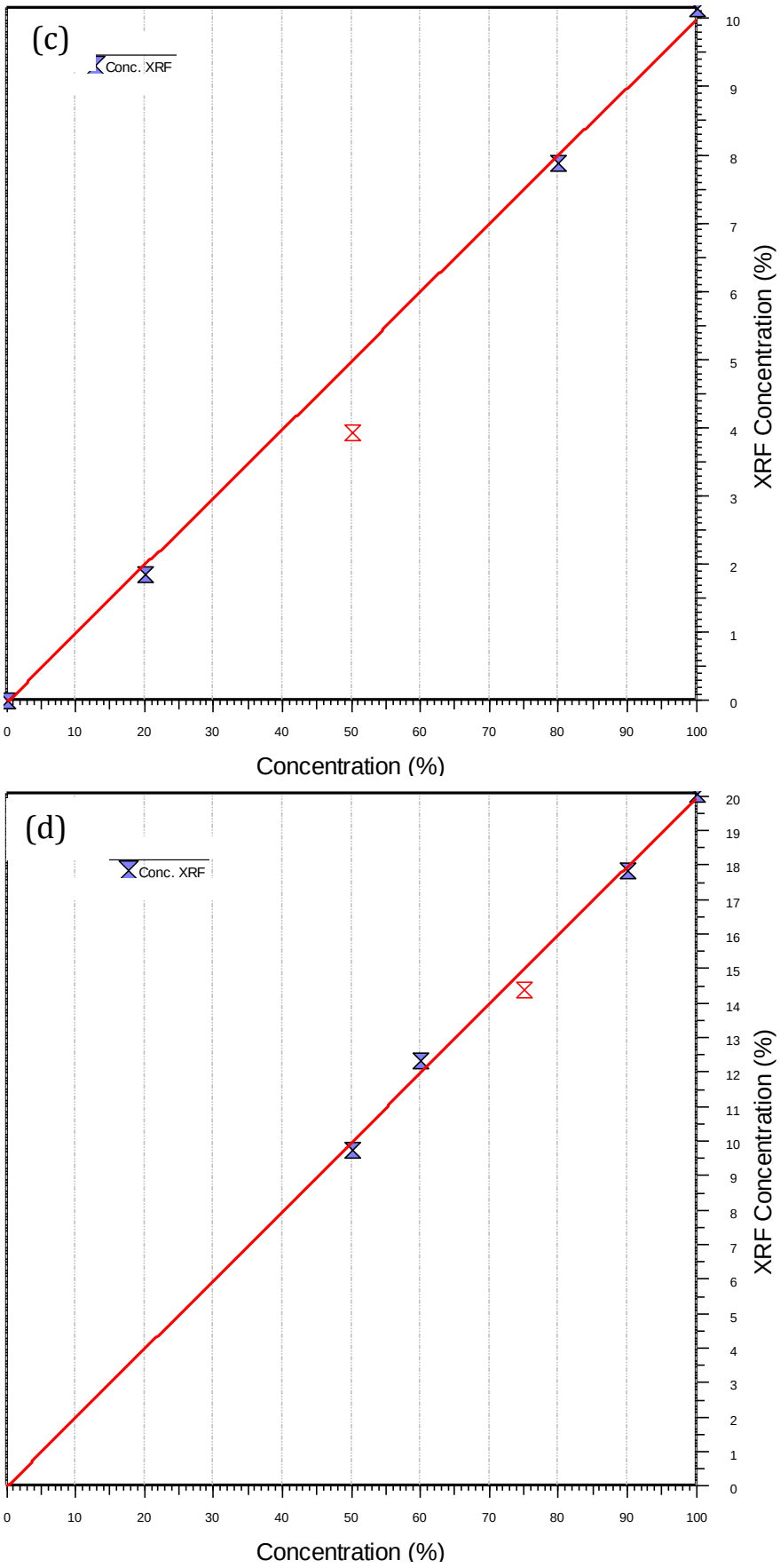

Figure 2.10: XRF calibration curves for the calcium fluorophosphate calibration; Ca (a), P (b), Na (c) and K (d)

2.6.3 Immediate Measurements

As the detection of fluorine following fused bead analysis is not possible due to the expulsion of fluorine at high temperatures (1250 °C), so the presence of fluorine can only be inferred from this analysis. However, in order to confirm the presence of fluorine, samples of both strontium fluorophosphate systems can be prepared as pressed pellets (13 mm diameter pellets using 1 g of sample) and an immediate measurement can be performed of the sample whereby the fluorine $K\alpha_1$ line is selected and only the emission signal from that line is detected. Although the amount of fluorine cannot be quantified using this method, it does however provide evidence as to whether fluorine is present in the sample of interest.

2.7 References

1. S.-T. Liu and G. H. Nancollas, *Journal of Crystal Growth*, 1970, **6**, 281-289.
2. N. Koga, Y. Z. Nakagoe and H. Tanaka, *Thermochim. Acta*, 1998, **318**, 239-244.
3. V. K. Pecharsky and P. Y. Zavalij, *Fundamentals of powder diffraction and structural characterisation of materials*, 2nd Edition, Springer, 2009.
4. R. E. Dinnebier and S. J. L. Billinge, *Powder diffraction theory and practice*, RSC Publishing, 2008.
5. A. R.West, *Basic Solid State Chemistry* Second Edition.
6. Rutherford Appleton Laboratory ISIS http://www.isis.stfc.ac.uk/instruments/polaris/polaris4643.html.
7. R. A. Young, *The Rietveld Method*, Oxford University Press, Oxford, 1995.
8. H. M. Rietveld, *Acta Crystallographica.*, 1967, **22**.
9. H. M. Rietveld, J*ournal of Applied Crysallography*, 1969, **2**.
10. A.C.Larson and R. B. V. Dreele, 1994, General Structure Analysis System (GSAS)
11. B. H. Toby, J*ournal of Applied Crysallography* 2001, **34**, 210-213.
12. P. J. Hore, *Nuclear Magnetic Resonance*, Oxford Science Publications, Oxford, 1997.
13. Bruker,http://www.bruker.com/fileadmin/user_upload/8-PDF_Docs/XrayDiffraction_ElementalAnalysis/XRF/Brochures/S8_TIGER_Brochure_DOC-B80-EXS009_en_low.pdf.

CHAPTER 3

Strontium Fluorophosphate Materials

3.1 Introduction

As highlighted in chapter 1, fluorophosphate materials have not been widely studied and certainly not as potential biomaterials. This is despite Na_2PO_3F being used as an additive in toothpaste[1] and investigated as a treatment of osteoporosis.[2-3] In both these applications the fluoride is considered to be the active ingredient; preventing dental caries and providing potential for stimulating bone formation. In light of this, this thesis reports investigations into the synthesis and characterisation of a range of monofluorophosphate materials. Of particular interest as potential biomaterials are materials containing key elements linked to bone and those with proven influence on bone function. For this reason the combination of Sr^{2+} and F^- in strontium fluorophosphates is appealing. Structural characterisation of the calcium fluorophosphates system has previously been reported by Perloff *et al*.[4] but although the a strontium fluorophosphate system is known ($SrPO_3F{\cdot}H_2O$),[5] there appears to be no reports regarding the structure of the strontium fluorophosphate phase. This chapter will focus on the strontium system, particularly attempts to isolate new materials. Whilst many of the reported fluorophosphates materials have been synthesised using $(NH_4)_2PO_3F$ as the source of fluorophosphate (section 1.5.3), this work reports the use of the commercially available sodium fluorophosphate as a reagent. This chapter reports the formation of two new strontium fluorophosphate phases and details the synthesis and structures of these materials and their stability.

3.2 Synthesis of Strontium Fluorophosphate Phases

The strontium fluorophosphate phases, $SrPO_3F \cdot H_2O$ and $SrPO_3F$ were synthesised *via* precipitation reactions as described in section 2.1.1. The hydrated phase was found to form at temperatures between room temperature and 40 °C whilst the anhydrous phase was formed at 80 °C. The solution of sodium fluorophosphate was heated to the desired temperature and to this a solution of strontium chloride hexahydrate was added drop-wise. A white precipitate was obtained and was collected by vacuum filtration, washed thoroughly with deionised water and left to dry in air overnight.

3.2.1 Heat Treatments of Strontium fluorophosphate Phases

Samples of $SrPO_3F \cdot H_2O$ and $SrPO_3F$ were heated in an alumina crucible to temperatures between 100-750 °C for a duration of 2 hours in a muffle furnace. After each temperature treatment, the samples were allowed to cool before a small amount of the each sample was removed in order to analyse using PXRD.

For the analysis of fluorine using XRF spectroscopy, multiple strontium fluorophosphate samples were required in order to form a large and sufficiently dense pellet in order to perform the measurement. The samples were heated to various temperatures for the same duration as stated above.

3.2.2 X-Ray Fluorescence Measurement

3.2.2.1 Calibration Curves for the strontium fluorophosphate calibration

Calibration curves were constructed following the procedure described in section 2.7.2. The resulting calibration curves (shown in appendix 1 section 1.4.1) were used to determine the concentration of the unknown samples ($SrPO_3F \cdot H_2O$ and $SrPO_3F$).

3.3 Results and Discussion

3.3.1 Synthesis of the strontium fluorophosphate phases

Many of the currently known monofluorophosphate materials have been synthesised *via* a metathesis reaction. This method for the formation of fluorophosphate materials avoids many problems which can arise from using other synthetic methods (refer to section 1.5.3). The common source of fluorophosphate used in these reactions was ammonium salt $(NH_4)_2PO_3F$, prepared from a mixture $(NH_4)_2HPO_4$ and $NH_4 \cdot HF$ in a urea melt at 180 °C, with the addition of the appropriate metal salt to form the corresponding fluorophosphate material. In this study, attempts were made to synthesise strontium fluorophosphate using the ammonium fluorophosphate as the fluorophosphate source. However, generating the initial source of fluorophosphate proved to be more problematic than expected, with the reaction proving to have a very low success rate and many of the products obtained appeared to contain two phases, the desired ammonium fluorophosphate phase and some un-reacted starting material in the form of urea phosphate. Attempts were made to rectify this problem but a reliable solution could not be identified. Due to the problems arising from the formation of the ammonium salt, it was decided that the synthesis for the formation of strontium fluorophosphate would be performed but using the commercially available sodium

fluorophosphate salt as the source of PO_3F^{2-} ions. The reaction scheme for the modified reaction is shown in equation 3.1.

Equation 3.1: Reaction scheme for the formation of the intended strontium fluorophosphate phases

$$Na_2PO_3F + SrCl_2 \cdot 6H_2O \longrightarrow SrPO_3F \cdot xH_2O + 2NaCl$$

Although sodium chloride would likely form as a by-product of the reaction, it was envisioned that washing the product thoroughly with deionised water would remove this phase.

3.3.2 Effects of Synthesis Temperature

Attempts at synthesising strontium fluorophosphate were carried out as described in section 3.1.1. As details regarding the synthesis temperature of the previously reported hydrated strontium fluorophosphate phase ($SrPO_3F \cdot H_2O$)[5] were unknown, the reactions were performed at a range of temperatures from room temperature through to 95 °C. It was found that varying the reaction temperature influenced the products which were formed, as the PXRD patterns of the resultant products were markedly different.

It was evident from the PXRD patterns that there were two products formed during strontium fluorophosphate precipitation reactions: one formed at low temperatures between room temperature and 70 °C (phase 1), the other between 75-95 °C (phase 2), for which the PXRD patterns are shown in figures 3.1(a) and 3.1(b) respectively. These were initially labelled as phase 1 and phase 2, as it was not possible to match the patterns to any contained on the JCPDS database,[6] which suggested that two new

strontium fluorophosphates had been formed. The slightly raised background in both PXRD patterns may be suggestive of some amorphous content in both of these samples.

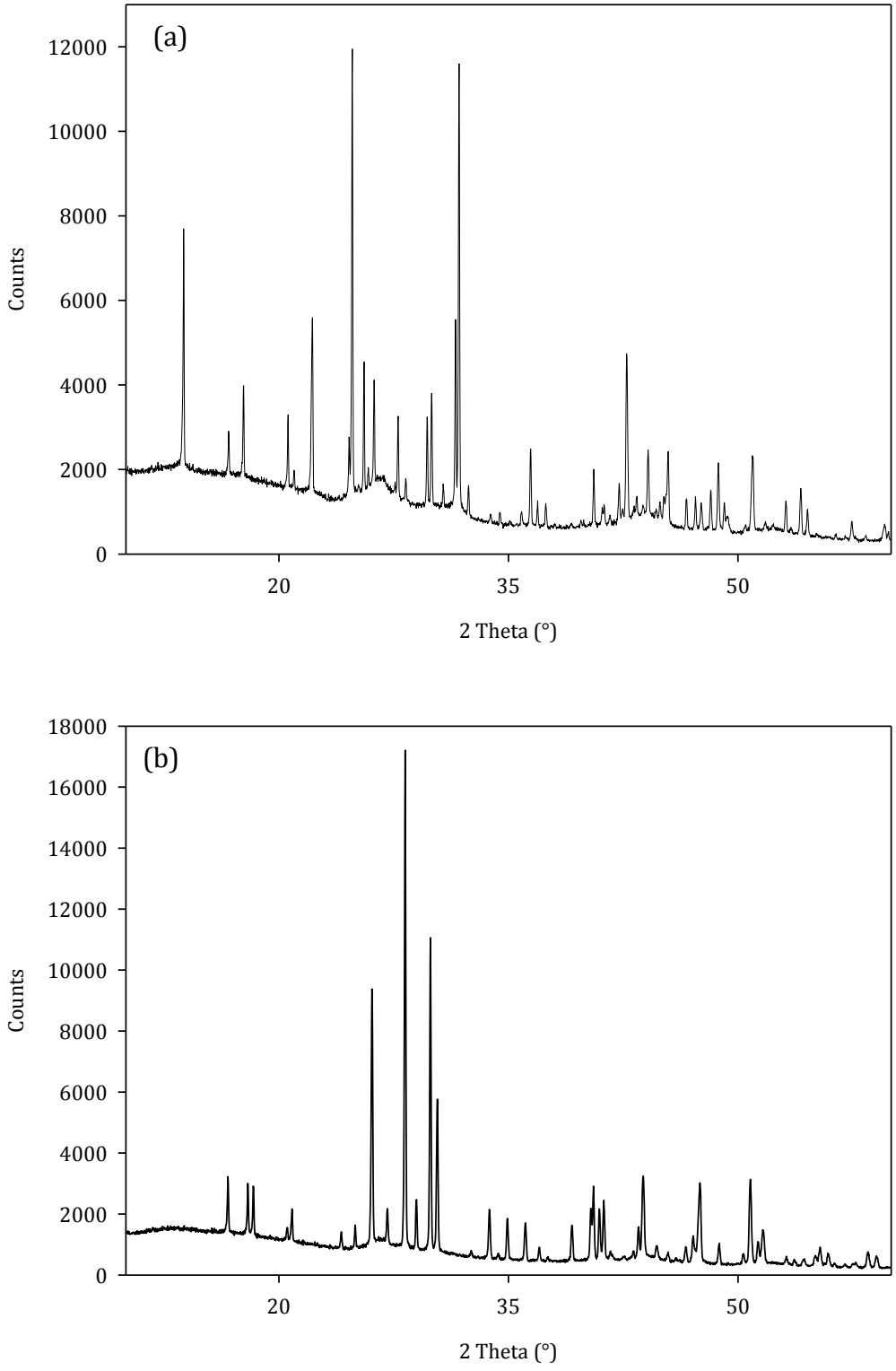

Figure 3.1: PXRD patterns of the products obtained from the precipitation reaction:- Phase 1 (a) and Phase 2 (b)

Whilst performing the precipitation reactions, it was observed that temperature was not the only influential factor in determining which products formed but also the speed at which the solutions were added together (approximately one drop per second). In some experiments, mixed phase products were observed at temperatures between 60-75 °C (consisting of phase 1 and phase 2) and 75-95 °C (consisting of phase 2 and $SrPO_3F{\cdot}H_2O$).[5] However, these were not consistently reproducible and may be attributed to variations in the time taken to heat the solutions, the dropping rate or a fluctuation in the temperature. A schematic representation of the products of the reactions as a function of temperature is outlined in figure 3.2.

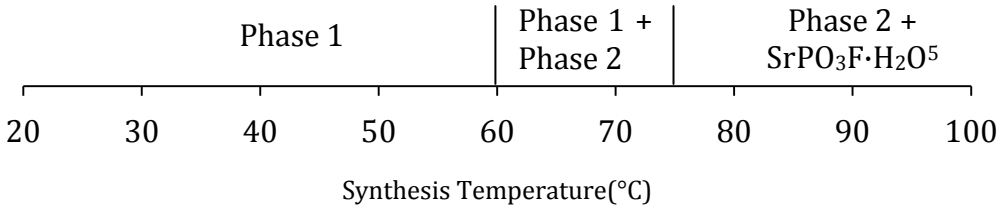

Figure 3.2: Reaction products formed from initial attempts at the precipitation reaction stated in equation 3.1

3.3.3 Powder diffraction indexing

In order to establish whether both phase 1 and phase 2 were indeed single phase, attempts were made to index the PXRD patterns using CRYSFIRE.[7] This process involved extracting the 2θ values of the twenty most intense reflections and indexing using DICVOL and TREOR programs within CRYSFIRE to identify potential unit cells. From a list of the suggested unit cells (see appendix 1 section 1.1), the number of peaks indexed and the figure of merit for each unit cell were assessed to rank likely cells. Following this, cells indexing twenty reflections were identified for both phases, an orthorhombic

unit cell for the low temperature phase (phase 1) and a monoclinic unit cell for phase 2. With the suggested unit cell parameters, the assignments of additional reflections was then possible using D-SPACE.[8] This was followed by cell parameter refinements using CELL[9] (see appendix 1 section 1.2). In addition to this, the CHECKCELL[10] program was used to suggest a potential space groups using the refined unit cell parameters obtained from CELL. The results obtained from CELL and CHECKCELL for both phases are shown in table 3.1.

Table 3.1: A summary of the unit cell parameters and space group identified for both phase 1 and phase 2

Products	Temperature Formed (°C)	Unit Cell Parameters (Å)						Space Group
Phase 1	RT-75	12.815(9)	8.441(4)	7.992(4)	90	90	90	*Pbca*
Phase 2	75-95	6.720(1)	7.1212(9)	6.972(1)	90	101.755(6)	90	$P2_1/n$

Attempts to find a suitable structural model were then undertaken by conducting a search on the ICSD database.[11] This involved comparing the unit cells of each phase to known structures which closely resembled strontium fluorophosphate in terms of unit cell size, space groups and similar motifs within the structure. In particular, materials which were of interest were those which consisted of a cation and tetrahedral unit present in a 1:1 ratio, which might be expected for Sr^{2+}—PO_3F^{2-} phases. As a result of this search, potential models were found for both phases, with the unit cell of phase 1 resembling that of the orthorhombic $CaCrO_4 \cdot H_2O$[12] structure and a potential model was found in the monazite structure of lanthanum phosphate, $LaPO_4$[13] for phase 2. To initially establish if either of these models were suitable structures for the strontium fluorophosphate materials, simulated diffraction patterns were generated using modified versions of both $CaCrO_4 \cdot H_2O$ and $LaPO_4$ structures. In doing so, both simulated PXRD patterns generated were similar to those of the PXRD patterns of both phase 1 and

phase 2. This inferred that the stoichiometry of the strontium fluorophosphate materials were likely to be $SrPO_3F \cdot H_2O$ for phase 1 and $SrPO_3F$ for phase 2, but further characterisation was necessary to confirm the stoichiometry of these materials.

3.3.4 Structural Characterisation of $SrPO_3F \cdot H_2O$

3.3.4.1 Rietveld Refinement

Neutron powder diffraction data collected on POLARIS were used for the Rietveld refinement of a deuterated sample of the hydrated strontium fluorophosphate phase (phase 1). The sample was deuterated in order to eliminate the high background which would be obtained from the presence of the protons from the associated water molecules. The plots obtained from the Rietveld refinement are shown in figures 3.3(a) and 3.3(b) and the final refined structural parameters are shown in table 3.2 and a selection of bond lengths and angles summarised in table 3.3.

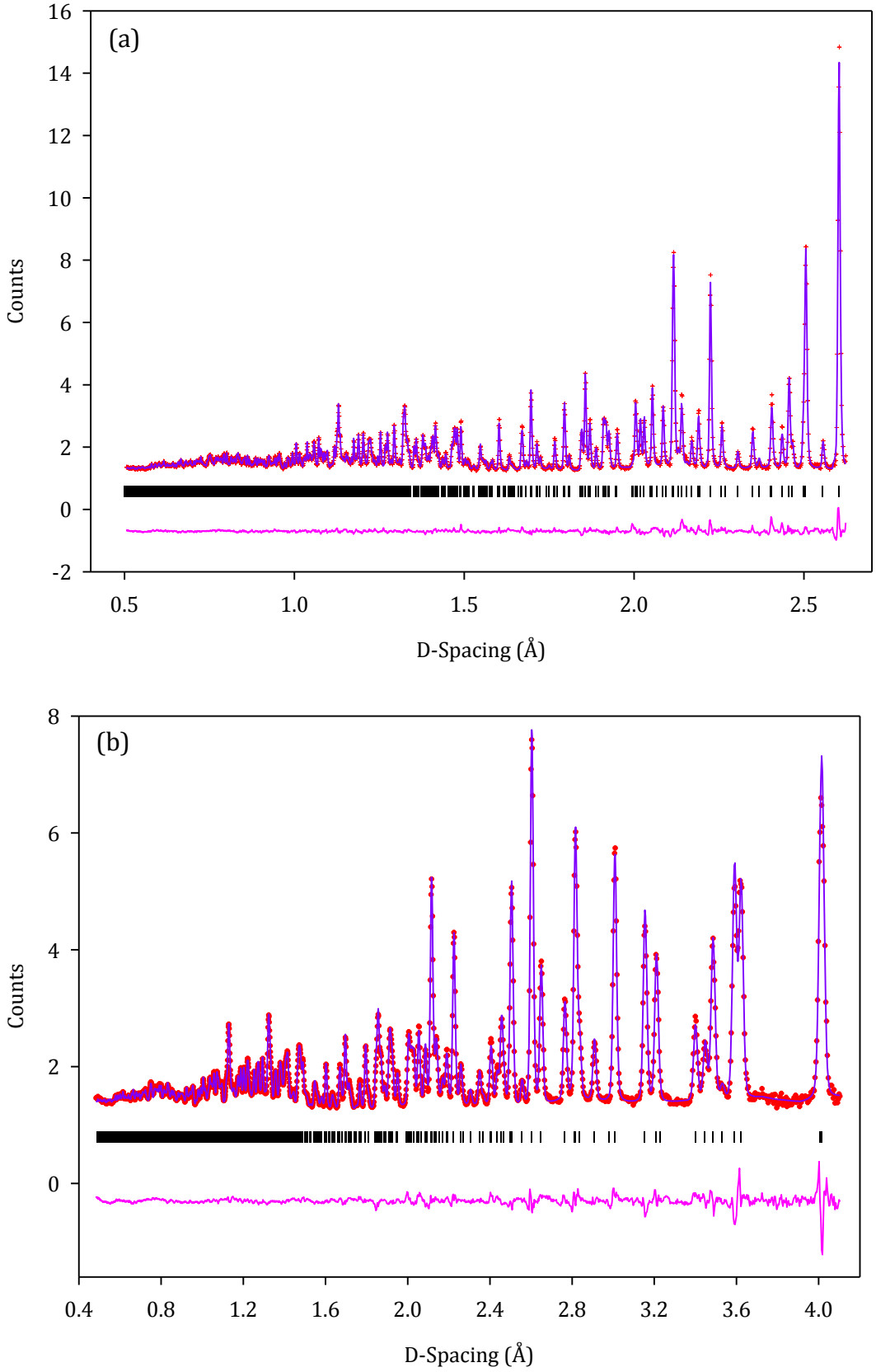

Figure 3.3: Final observed (red), calculated (purple) and difference profiles of the NPD refinement of $SrPO_3F{\cdot}D_2O$: (a) back scattering bank (b) 90° bank

From the apparent low background in the refinement, it appears that the amorphous content for this sample of SrPO3FH2O synthesised in D2O appears to be less compared to the suggested amorphous content in figure 3.1a. The refinement confirmed that $SrPO_3F{\cdot}H_2O$ adopts the structure of the suggested $CaCrO_4{\cdot}H_2O$ model with space group P*bca* and unit cell parameters a = 8.0131(1) Å, b = 8.4504(1) Å, c = 12.8350(2) Å, χ^2 = 7.1 and R_{wp} = 1.54 and 1.72 % for plots 3.3 (a and b) respectively.

Table 3.2: Structural parameters obtained from NPD Rietveld refinement of $SrPO_3F{\cdot}D_2O$

Atom	Multiplicity	x	y	z	Uiso* 100/Å^2	Fractional Occupancy
Sr	8	0.2641(2)	0.1071(2)	0.3202(1)	0.71(3)	1
P	8	0.1256(3)	0.3779(3)	0.1310(2)	0.68(4)	1
F	8	0.2051(3)	0.4289(3)	0.0208(2)	1.71(5)	1
O2	8	0.0196(3)	0.2364(3)	0.1064(2)	1.81(5)	1
O3	8	0.2758(3)	0.3472(3)	0.1988(2)	1.27(4)	1
O4	8	0.0329(3)	0.5233(2)	0.1695(2)	0.94(4)	1
O5	8	0.0850(3)	0.3583(3)	0.3985(2)	1.54(5)	1
D1	8	-0.0265(3)	0.3472(3)	0.3658(2)	3.06(9)	0.964(6)
D1	8	0.0676(4)	0.3397(4)	0.4725(2)	2.82(9)	0.942(6)
H1	8	-0.0265(3)	0.3472(3)	0.3658(2)	3.06(9)	0.036(6)
H2	8	0.0676(4)	0.3397(4)	0.4725(2)	2.82(9)	0.058(6)

Table 3.3: Selected bond lengths and angles obtained from the NPD Rietveld refinement of $SrPO_3F{\cdot}D_2O$

Sr-O1	2.635(3)	Sr-O4	2.625(3)
Sr-O2	2.505(3)	Sr-O4	2.486(3)
Sr-O3	2.560(3)	Sr-O5w	2.751(3)
Sr-O3	2.712(3)	Sr-O5w	2.626(3)
P-F	1.610(3)	P-O3	1.507(3)
P-O2	1.500(3)	P-O4	1.518(3)
O3-D1/H1	1.788(3)	O2-D2/H2	1.876(4)
O5-D1/H1	0.992(3)	O5-D2/H2	0.972(3)
F-P-O2	104.6(2)	O2-P-O3	115.9(2)
F-P-O3	103.7(2)	O2-P-O4	115.9(2)
F-P-O4	105.3(2)	O3-P-O4	110.0(2)
D1/H1-O5-D2/H2	105.6(3)	D2/H2-O5-D1/H1	105.6(3)

Despite the sample being deuterated, protons were included in the refinement. These were constrained with the deuterium atoms to have the same atomic co-ordinates, temperature factors and the fractional occupancies were refined to sum to 1. The fractional occupancies of the shared deuterium and hydrogen sites suggest that the deuteration procedure stated in section 2.1.2.1 was highly successful.

Although the structural model of $CaCrO_4 \cdot H_2O$ was confirmed as being a suitable model for the refinement, it contained four oxygen atoms whereas one of the oxygens has been replaced for a fluorine atom in the fluorophosphate unit PO_3F^{2-}, therefore it was deemed necessary to attempt to locate the position of the fluorine atom. However, distinguishing between an oxygen and fluorine atom via x-rays scattering is not usually possible, as the scattering lengths of oxygen and fluorine are very similar. Usually, neutron diffraction can be used to distinguish between atoms with similar atomic numbers as there is no linear dependence on the scattering power of neutrons with the atomic number with neutron diffraction but by coincidence the scattering lengths of both oxygen and fluorine are very similar so differentiating between them using neutron diffraction may also be difficult. However, based on the literature of other known fluorophosphate systems,[14-17] the lengthening of one of the tetrahedral bond lengths was indicative of the P-F bond, resulting in tetrahedral unit consisting of three shorter and one elongated bond which causes a distortion of the tetrahedral unit. Analysis of the refinements suggest that there is one longer tetrahedral bond (1.610(3) Å compared to three bonds between 1.510(3) and 1.518(3) and this can sensibly assigned to a P-F bond, hence locating the position of the fluorine atom.

The structure of $SrPO_3F \cdot H_2O$ is based on that of $CaCrO_4 \cdot H_2O$ which belongs to a family of monohydrates with the general formula of $MM'O_4 \cdot H_2O$ for which there appear to be

eight different structure types.[18] $SrPO_3F \cdot H_2O$ follows the 3rd structure type of this series, whereby strontium has a co-ordination number of eight, with the strontium atom bound to five oxygen atoms and a fluorine atom from the fluorophosphate units and two oxygen atoms from water molecules. The SrO_7F polyhedra link together by corner sharing to form chains along the *a* direction. The SrO_7F polyhedral units are linked to other SrO_7F units in an adjacent layer by edge sharing with oxygen and a fluorine atom from a neighbouring PO_3F^{2-} tetrahedral unit as shown in figure 3.4.

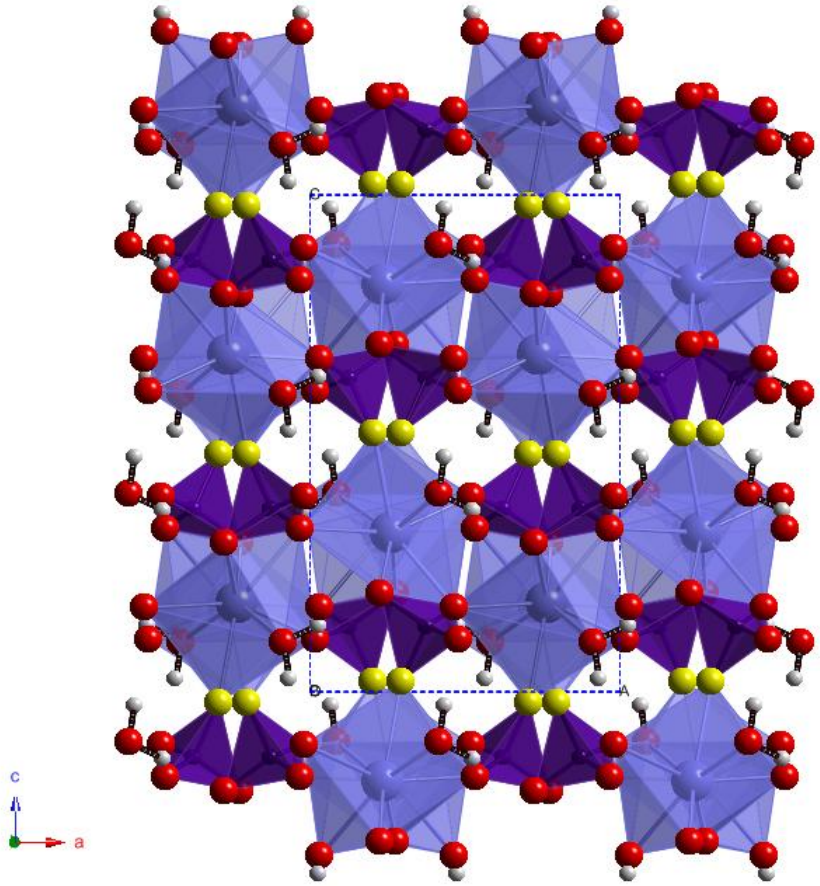

Figure 3.4: Structure of $SrPO_3F \cdot D_2O$ viewed down the *b* axis
SrO_7Fpolyhedra (lilac), PO_3F^{2-} tetrahedra (purple), oxygen atoms (red), fluorine atoms (yellow) hydrogen atoms from water molecules (white)

The water molecules orientate themselves towards the channels and utilise both hydrogen atoms in hydrogen bonding. Due to the orientation of the water molecules, there is a zig-zag hydrogen bonding network throughout the structure which is formed from hydrogen bonds between D1/H1-D2/H2 to oxygen atoms O2 and O3 of the PO_3F^{2-} tetrahedral units. This is illustrated in figure 3.5.

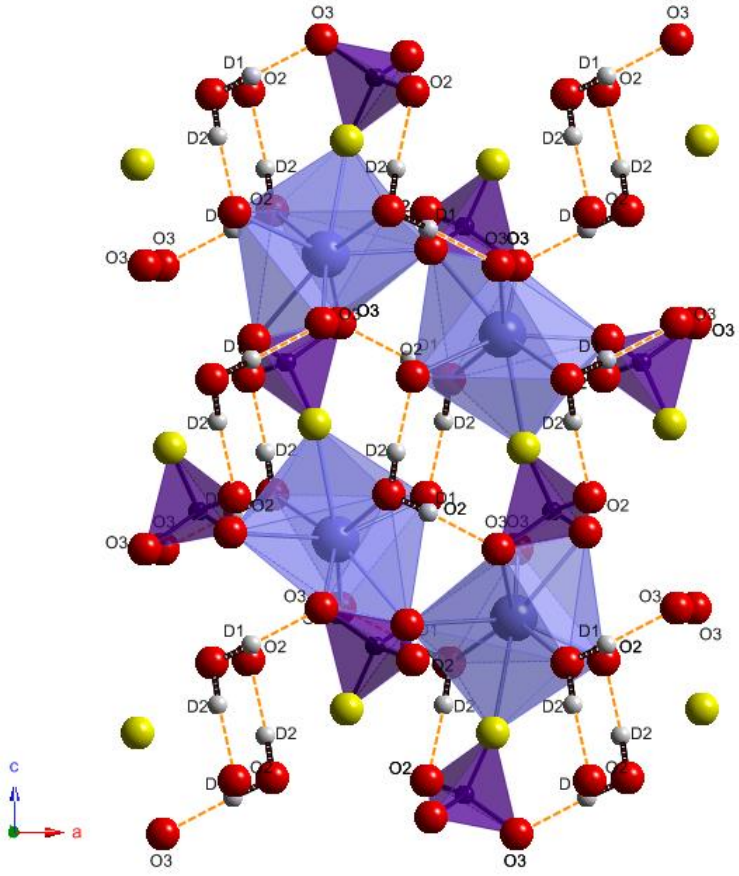

Figure 3.5: Hydrogen bonding network (orange) within the $SrPO_3F{\cdot}D_2O$ structure viewed down the *b* axis
SrO_7F polyhedra (lilac), PO_3F^{2-} tetrahedra (purple), oxygen atoms (red), fluorine atoms (yellow) hydrogen atoms from water molecules (white)

From the bonds lengths and angles shown in table 3.3, unsurprisingly the tetrahedral PO_3F^{2-} unit appears to deviate away from those expected for an ideal tetrahedron, with the tetrahedral unit consisting of three shorter and one longer bond (1.610 Å) as oppose

to four equivalent bond lengths with a mean length of ~ 1.5 Å for a PO_4^{3-} tetrahedral unit. The elongation of one of the PO_3F^{2-} bond lengths is due to the presence of fluorine which causes a distortion of the tetrahedral unit. The PO_3F^{2-} tetrahedral units form layers throughout the structure, with chains of the tetrahedral units existing both parallel and perpendicular to the *c* axis. The chains of PO_3F^{2-} tetrahedral units parallel to the *c* axis appear to exhibit an ordering of the P-F bond, where all of the P-F bonds are aligned (figure 3.4). This fluorine ordering can be inferred from the differing bond lengths observed for the tetrahedral unit (table 3.3). The presence of one lengthened bond, identified as the P-F bond, indicates that the fluorine must be largely ordered in one site within the structure as oppose to being randomly located, where a single average P-O/P-F bond length would likely exist.

For different fluorophosphate systems the bonding of fluorine was found to differ. In this system, fluorine was found to bind to the alkali metal centre (Sr^{2+}) as was the case with anhydrous monofluorophosphates (Ag_2PO_3F,[14] Hg_2PO_3F[15]) hydrogen monofluorophosphates ($CsHPO_3F$[19]) and systems consisting of one water of hydration ($(NH_4)_2PO_3F{\cdot}H_2O$[4]). This was not reported to be the case in monofluorophosphate systems containing two or more water molecules.[4, 16] However, in hydrated fluorophosphate systems such as $SrPO_3F{\cdot}H_2O$ (this work), $CaPO_3F{\cdot}2H_2O$, $(NH_4)_2PO_3F{\cdot}H_2O$[4] $Na_2PO_3F{\cdot}2.5H_2O$,[16] and $CuPO_3F{\cdot}2H_2O$,[20] fluorine was found to not be involved in the hydrogen bonding of these materials. The exception to this was for the heavily hydrated system, $Na_2PO_3F{\cdot}10H_2O$[16] which was found to participate in hydrogen bonding networks. These observations confirm that the level of hydration of fluorophosphates influences the hydrogen bond forming capability of the fluorine atom.

Usually calculations of the bond valence sums are helpful in indicating the likelihood of a structure existing given the bond lengths suggested and the likely oxidation states of the ions involved. However, as no empirical values for Sr-F or P-F were available, and therefore based on a purely oxygen coordination, the bond valence sum calculations are only able to provide limited guidance in this case. The bond valence sum (BVS) were calculated based on the r_0 distances for the cation-anion pair reported by Brown[21] for Sr-O (r_0 = 2.118 Å) and an updated version of the paper by Brown for the P-O distance (r_0 = 1.615 Å).[22] The BVS values obtained for strontium and phosphorus were +2.16 and +5.02, therefore close to the +2 and +5 values for expected for strontium and phosphorus respectively. (Calculations of the bond valence sums can be found in appendix 1 section 1.3).

3.3.4.2 XRF Spectroscopy Results

Multiple samples of $SrPO_3F{\cdot}H_2O$ were analysed using XRF spectroscopy in order to determine the elemental composition, principally focusing on the important Sr:P ratio of the materials. Each sample was measured three times in order to check the reproducibility of the results and to estimate the error associated with the values generated. In order to obtain the most accurate results, the samples were prepared as fused beads to eliminate matrix effects. An appropriate calibration was performed using a series of strontium phosphate fused beads. The calibrated results showed a Sr:P ratio of 0.99(2) which is in excellent agreement with that expected for the suggested stoichiometry of $SrPO_3F{\cdot}H_2O$. The table of the results obtained from the calibration can be seen in appendix 1 section 1.4.2.

As fluorine is unable to be detected following a fused bead analysis due to the expulsion of fluorine at the fusion temperature of 1250 °C, the presence of fluorine could only be

inferred from the Sr:P ratio and therefore a quantitative analysis of fluorine could not be performed. However, the presence of fluorine can be confirmed by measuring the emission signal from the fluorine Kα_1 from a pressed pellet of $SrPO_3F{\cdot}H_2O$. This indicated that a significant amount of fluorine is present in the as synthesised material (figure 3.6). For details of this measurement see section 2.7.3.

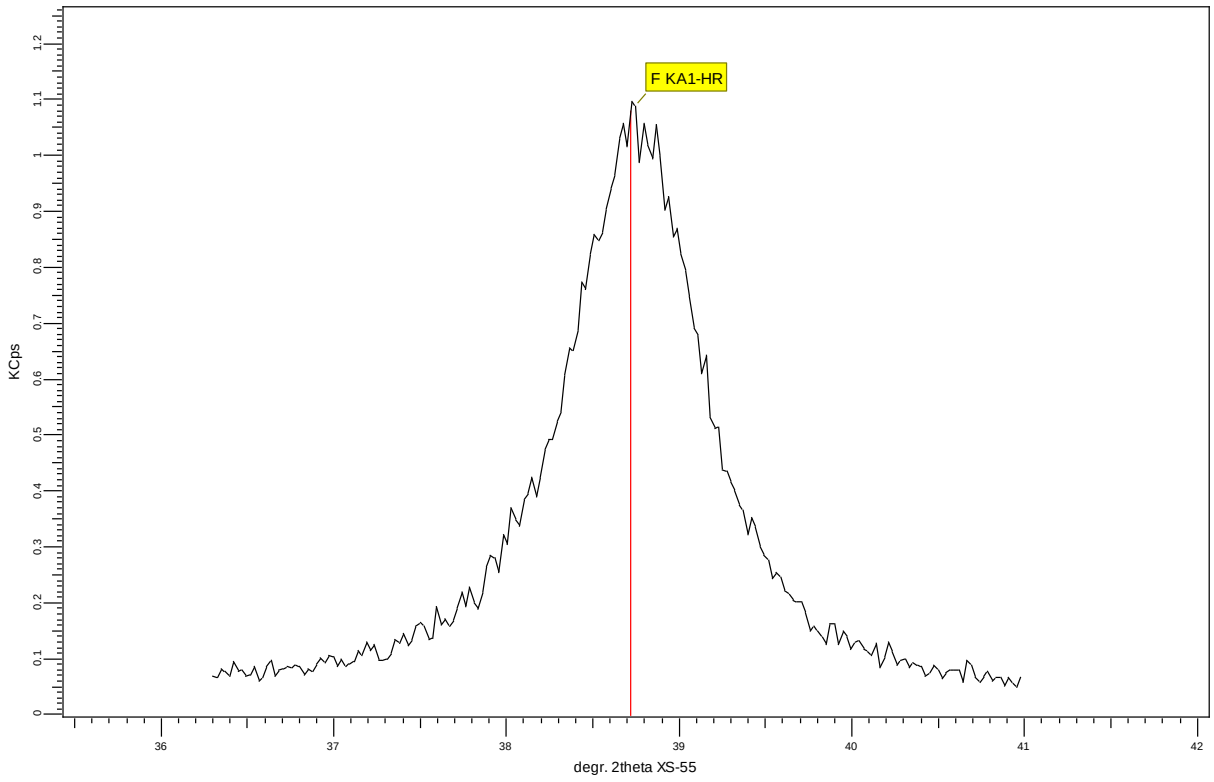

Figure 3.6: Emission signal obtained from the fluorine Kα_1 line of the as synthesised $SrPO_3F{\cdot}H_2O$ material

3.3.4.3 Raman Spectroscopy

The Raman spectra and assignments for $SrPO_3F{\cdot}H_2O$ are shown in figure 3.7 and table 3.4. Assignments of the observed vibrations were made based on those reported for similar monofluorophosphate systems, although there appeared to be very few literature sources which have reported Raman spectra of fluorophosphates.

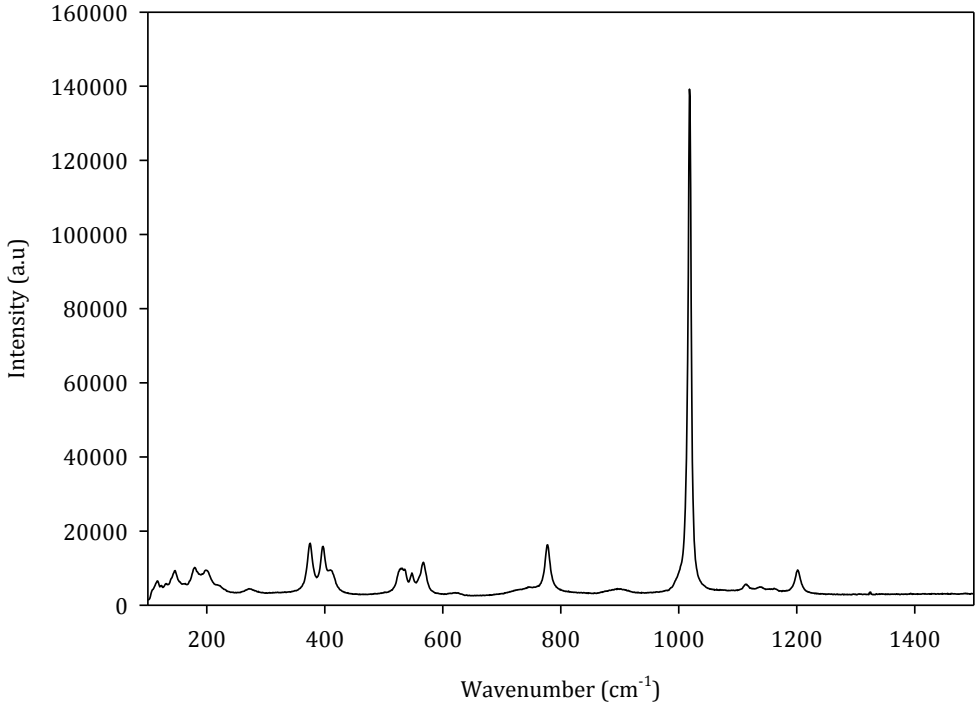

Figure 3.7: Raman Spectra of $SrPO_3F \cdot H_2O$

Table 3.4: Assignments of the vibrations observed in the Raman spectra of $SrPO_3F \cdot H_2O$

Vibrations (cm^{-1})	Assignments
1202	ν_{as} (PO_3)
1114	ν_{as} (PO_3)
1020	ν_s (PO_3)
898	unassigned
778	P-F
568, 548, 536 529	δ (PO_3)
412, 398, 376	ρ (PO_3)

Evidence of the fluorophosphate unit can be found at 778cm^{-1}, which is reported to be indicative of the P-F bond.[14-15] The most intense vibration is that of the ν_s (PO_3) stretch, which lies at 1020 cm^{-1}, with the corresponding asymmetric stretch apparent at 1114 cm^{-1}. Vibrations present in the region of 570-370 cm^{-1} appear to be in the correct region for the δ (PO_3) and ρ (PO_3) vibrations. The majority of the vibrations observed can be

attributed to hydrated strontium fluorophosphate system but there are some uncertainties assignments of the vibrations at 1202 and 898 cm^{-1}. It is unclear as to whether the band present at 1202 cm^{-1} also corresponds to another vibration relating to the asymmetric stretch of the fluorophosphate unit, as the frequency at which this vibration appears at a higher frequency than the vibrations observed for this particular mode in similar monofluorophosphate systems. It is unclear as to the assignment of the weak vibration evident at 898 cm^{-1}.

3.3.4.4 SEM-EDAX

SEM Images and EDAX measurements were collected in order to give an insight into the morphology and composition of these systems, given that many of the structurally characterised fluorophosphate materials have not been investigated in much detail. Figure 3.9 shows that $SrPO_3F \cdot H_2O$ consists of flat plate like crystals with some small aggregated particles. It is unclear as to whether these aggregated particles belong to the hydrated phase or whether they may be indicative of some amorphous material.

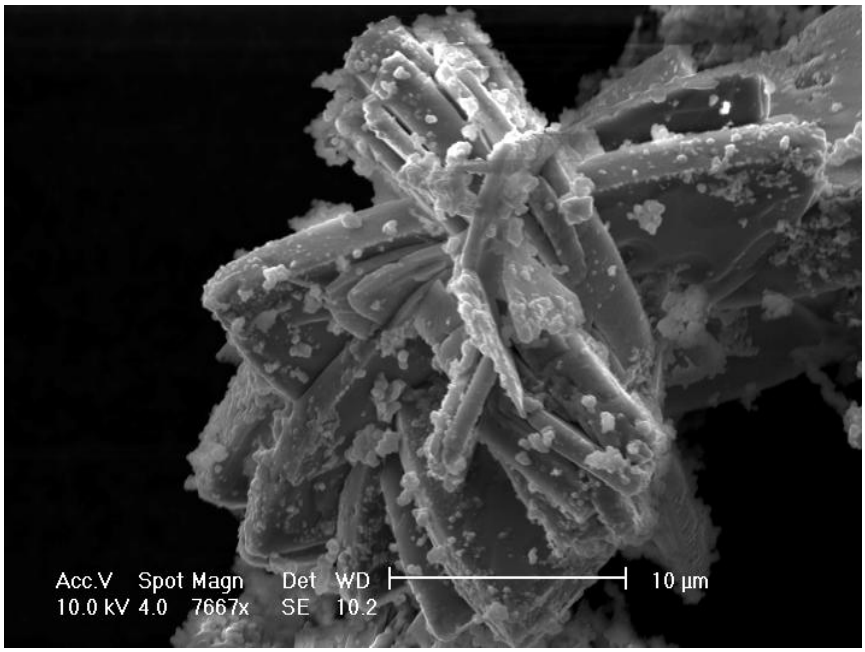

Figure 3.8: SEM Image of $SrPO_3F \cdot H_2O$

A number of EDAX measurements across the images of the samples demonstrated the homogeneity of the samples. The sample of $SrPO_3F \cdot H_2O$ (figure 3.8) appears to be homogeneous throughout and the elemental composition (from EDAX) is close to that expected. The absolute accuracy of EDAX is likely to be less than the calibrated WD-XRF results presented earlier, but the values were found to be similar (see appendix 1 section 1.5.1).

3.3.4.5 Solid State NMR

Solid state NMR proves to be a useful tool as it studies the local environments around the nuclei of interest, which for the strontium fluorophosphate samples are primarily the ^{31}P and ^{19}F nuclei. A table summarising the experimental data obtained from the one pulse and decoupled experiments can be seen in appendix 1 section 1.6.

For the ^{31}P nuclei, the spectra obtained from the one pulse, ^{1}H and ^{19}F decoupled experiments are shown in figure 3.10 (a, b, and c) respectively. The ^{31}P one pulse experiment shows a doublet peak due to the coupling between the ^{31}P and the ^{19}F nuclei (figure 3.9(a)). However, the shape of the doublet is unusual, as it is asymmetrical as oppose to being symmetrical which is what would normally be expected. This asymmetry is a result of there being an additional phosphorus site present at -4.66 ppm which is unexpected, as the structural model only predicts one phosphorus environment for this system. This additional phosphorus site, likely from the impurity phase, lies underneath the most intense side of the doublet peak (right hand side). The spectra for decoupling of ^{1}H from the ^{31}P nucleus (figure 3.9(b)) looks very similar to that of the one pulse experiment but some of the broadening has been removed as there is no P-H coupling present due to the ^{1}H decoupling which results in the narrowing of the line. Decoupling of the ^{19}F nuclei resulted in one peak in the NMR spectra due to the removal of the doublet peak present in figure 3.9(a) arising from the coupling between ^{31}P and ^{19}F nuclei (figure 3.9(c)).

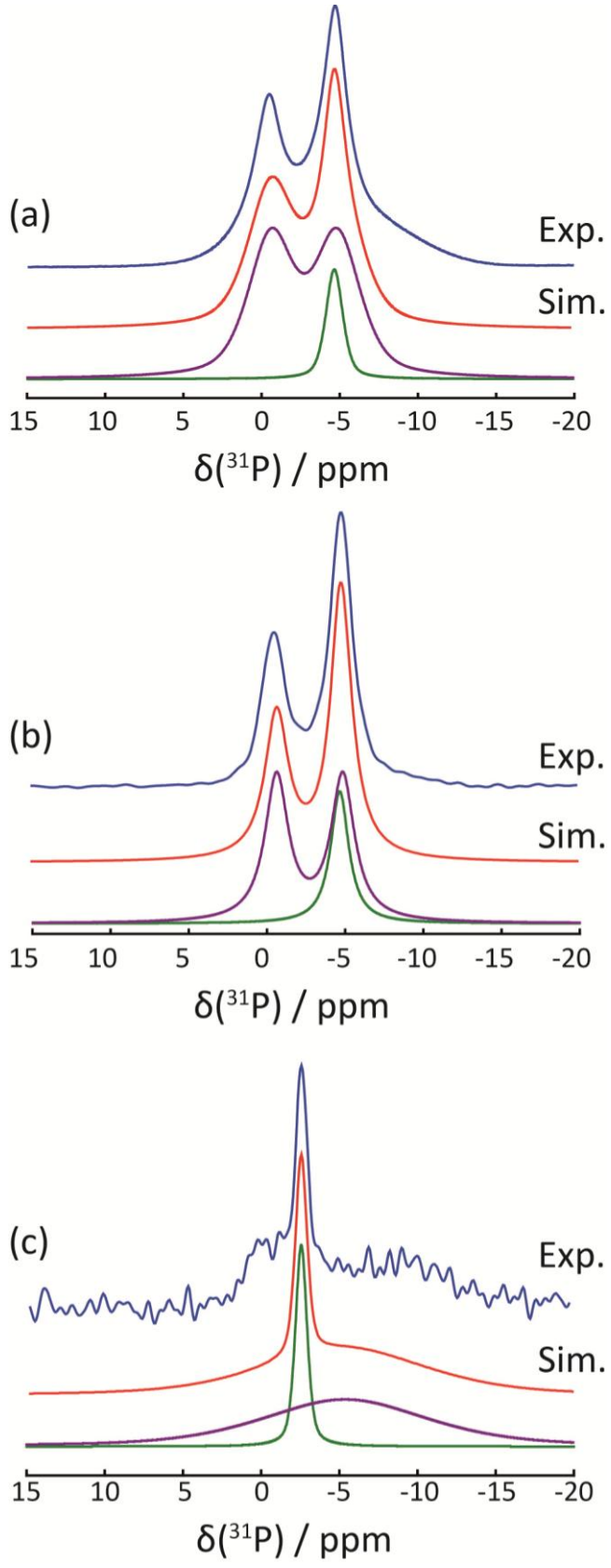

Figure 3.9: ^{31}P Experimental (blue) and simulated (red) NMR spectra for the one pulse (a), ^{1}H decoupled spectra (b) and ^{19}F decoupled spectra of $SrPO_3F \cdot H_2O$ (c). Deconvoluted peaks (green and purple)

Figure 3.10(a and b) shows the spectra from the un-decoupled (one pulse) and decoupled experiment for the ^{19}F nuclei. A doublet peak is observed in the one pulse spectra owing to the coupling with the ^{31}P nuclei. As with the ^{31}P one pulse spectra, the doublet is shown to be asymmetric in shape but this time the left hand side of the doublet is more intense than the right hand side. This asymmetry can once again be attributed to an impurity peak phase indicated by the peak at -71.87 ppm. The percentage intensity of this impurity has been estimated to be approximately 25 %. However, it is unclear at present as to what the impurities in the ^{31}P and the ^{19}F NMR spectra could be and whether they correspond to the same impurity material. There appears to be evidence for a small amount of SrF_2 (alkali metal fluorides are a well-known decomposition product of fluorophosphates[5, 14-15] with an additional peak in the NMR spectra at -87.87 ppm which is present in approximately 3 %. This could suggest that that very a low level of the original fluorophosphate material has decomposed during synthesis, despite the synthesis temperature being relatively low. As with the ^{31}P fluorine decoupled spectra, only one peak is observed for the ^{19}F spectra with ^{31}P decoupling due to the coupling between ^{19}F and ^{31}P nucleus being removed. The J coupling values generated from both the ^{31}P and ^{19}F one pulse spectrum are consistent with one another, with $J_{P\text{-}F}$ values of 855±2 Hz. Until the solid state NMR studies were performed, there had been no indication that the $SrPO_3F{\cdot}H_2O$ phase contained any impurities. Given that the Rietveld refinement on PXRD and NPD data do not indicate any substantial additional phases, we must assume that the impurity phase is likely to be present as an amorphous phase.

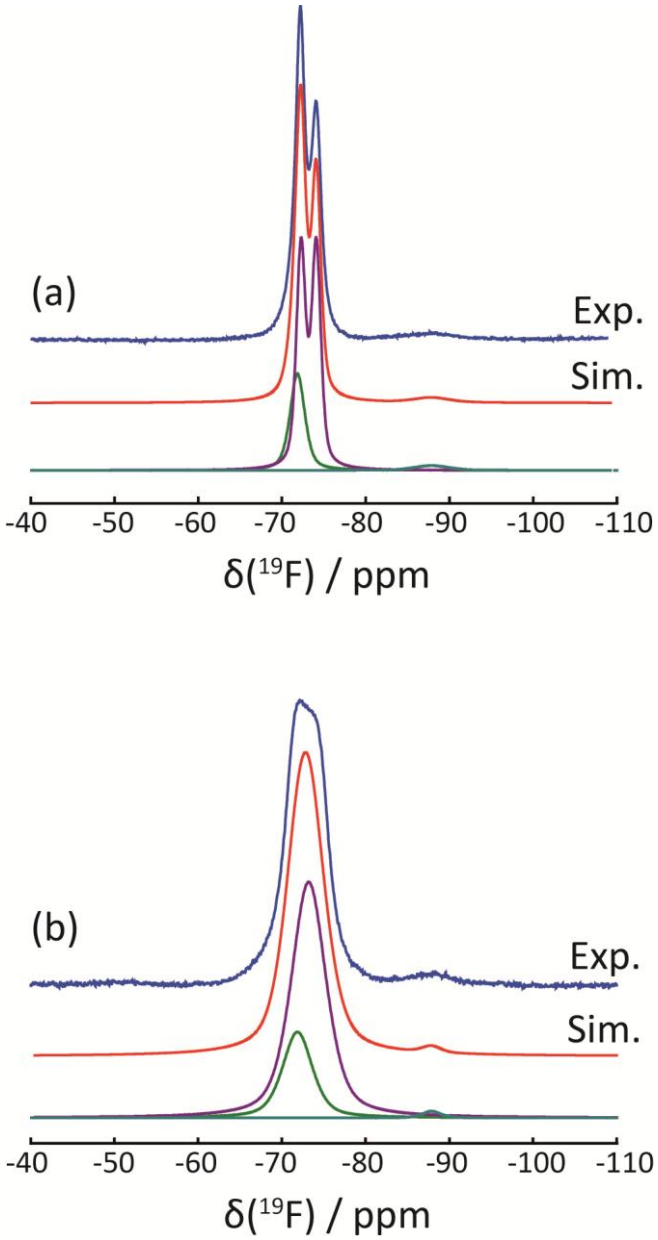

Figure 3.10: ^{19}F experimental (blue) and simulated (red) NMR spectra for the one pulse (a) and ^{31}P decoupling (b) for $SrPO_3F{\cdot}H_2O$. Deconvoluted peaks (green and purple)

3.3.4.6 Assessing the Amorphous Content within $SrPO_3F{\cdot}H_2O$

The suggestion from solid state NMR results from both ^{31}P and ^{19}F spectra, that $SrPO_3F{\cdot}H_2O$ was likely to contain poorly crystalline or amorphous entities warranted further study. In order to confirm whether the sample contains any amorphous material, a two phase Rietveld refinement was performed on $SrPO_3F{\cdot}H_2O$ with a known amount of

a highly crystalline material, TiO_2 (details of the amounts of $SrPO_3F{\cdot}H_2O$ and TiO_2 used are stated in appendix 1 section 1.7.1). The refinement was carried out in an identical manner to all other refinements. The phase fraction percentages obtained were used to estimate the level of amorphous content present in the sample. The value generated by this analysis would only provide an indication as to the level of amorphous material present in the sample. The calculations suggested that the hydrated strontium fluorophosphate phase did indeed contain some amorphous material and that the amorphous material was present in approximately 21 wt % which is good agreement with the predicted percentage of the impurity phase/phases for from the solid state NMR results. See appendix 1 section 1.7 for the two phase Rietveld refinement plot, the results from the refinement and calculated level amorphous material.

3.3.5 Structural Characterisation of $SrPO_3F$

3.3.5.1 Rietveld Refinement

High resolution NPD were collected on the higher temperature product, previously assigned as having the monazite structure. A Rietveld refinement of these data collected on HRPD at ISIS was performed using the monazite structure of $LaPO_4$ as the starting model.[13] Datasets from only the backscattering banks and the 90 bank were used in the refinement of $SrPO_3F$. The Rietveld profiles shown in figure 3.11 (a and b) show very good agreement between the experimental data and the calculated pattern, with the refinement yielding $\chi^2 = 3.177$ and R_{wp} values of, 1.23 (90° detector bank) and 2.21 % (back scatter detector bank) respectively. This indeed confirmed that $SrPO_3F$ adopts the monazite structure with space group $P2_1/n$ and unit cell parameters of a = 6.97294(7), b = 7.11856(7), c = 6.72009(6) and β = 101.7626(9).

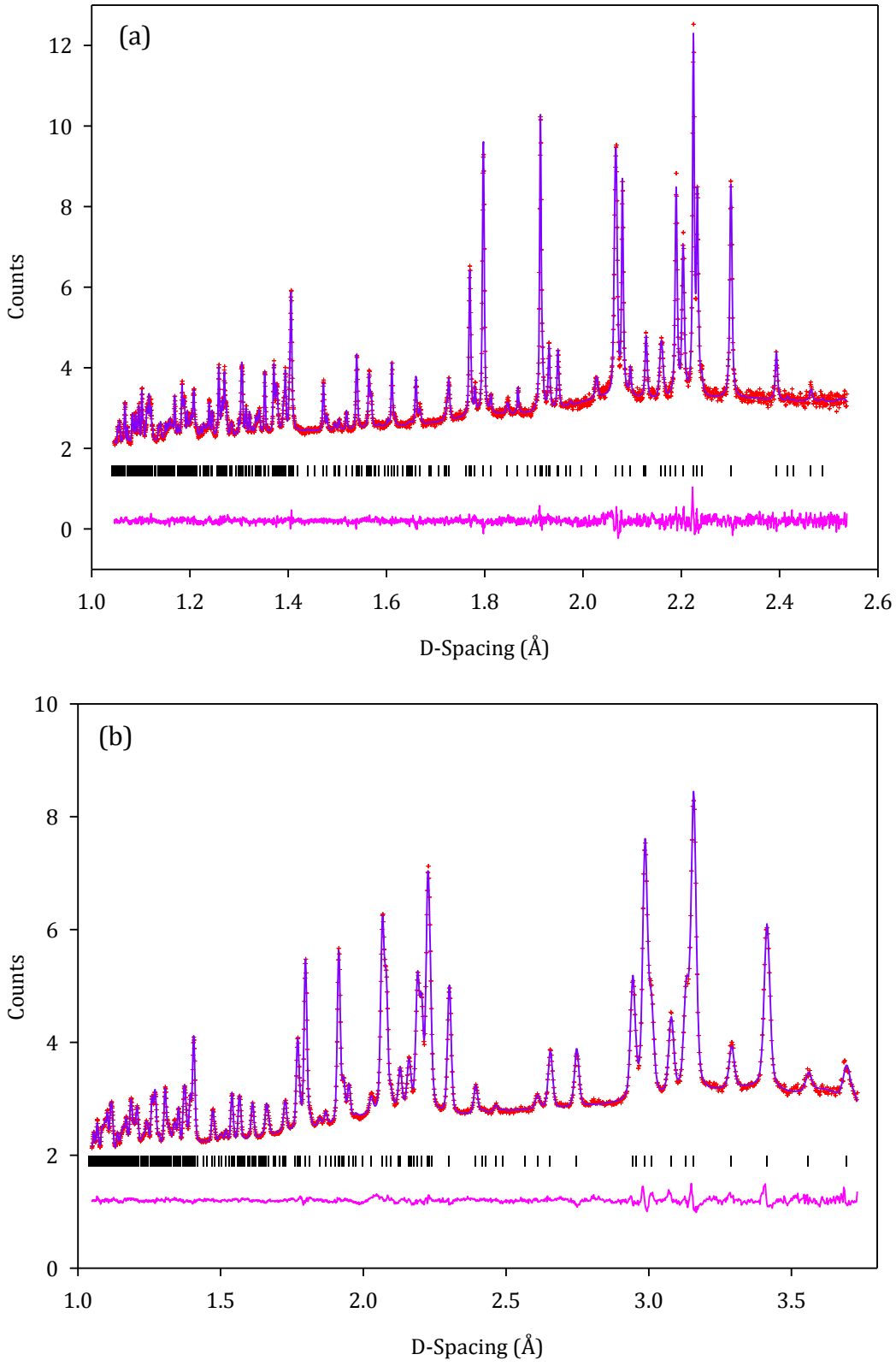

Figure 3.11: Final observed (red), calculated (purple) and difference profiles of the NPD refinement of $SrPO_3F$ (a) back scattering bank (b) 90° bank

During the refinement, no constraints were used for the oxygen/fluorine temperature factors as the refinement appeared to be stable, generating sensible values for the temperature factors. The temperature factors were refined isotropically as a refinement of $SrPO_3F$ with anisotropic temperature factors did not show any significant anisotropic displacement. The final refined atomic co-ordinates and temperature factors are shown in tables 3.5, with the selected bond lengths and angles from the refinement shown in table 3.6.

Based on an X-ray refinement of $SrPO_3F$, the distance between P and O4 was identified as being the longest bond in the tetrahedral unit, which indicated that this was the likely P-F bond. Therefore, position O4 was labelled as fluorine in the neutron refinement. The lengthening of the P-O4 (P-F) bond was also observed with the bond lengths neutron diffraction data (table 3.6).

Table 3.5: Structural parameters obtained from NPD Rietveld refinement of $SrPO_3F$

Atom	Multiplicity	x	y	z	Uiso*100/Å^2
Sr	4	0.2694(2)	0.1392(2)	0.1029(2)	1.15(5)
P	4	0.3150(3)	0.1468(3)	0.6037(4)	1.99(5)
O1	4	0.2528(3)	-0.0133(3)	0.4525(3)	2.23(6)
O2	4	0.3841(3)	0.3175(3)	0.4988(3)	1.40(5)
O3	4	0.4516(3)	0.0997(3)	0.8009(4)	2.60(7)
F	4	0.1248(3)	0.2038(3)	0.6803(3)	2.55(7)

Table 3.6: Selected bond lengths and angles obtained from the NPD Rietveld refinement of $SrPO_3F$

Sr-O1	2.612(3)	Sr-O3	2.620(3)
Sr-O1	2.502(2)	Sr-O3	2.566(3)
Sr-O2	2.909(3)	Sr-F	2.851(3)
Sr-O2	2.561(3)	Sr-F	2.672(3)
Sr-O2	2.653(2)		
P-O1	1.530(3)	P-O3	1.504 (3)
P-O2	1.531(3)	P-F	1.570(3)
O1-P-O2	111.0(2)	O2-P-O3	112.4(2)
O1-P-O3	117.5(2)	O2-P-F	108.2(2)
O1-P-F	105.5(2)	O3-P-F	101.2(2)

3.3.5.2 Monazite Structure

The structural arrangement of many rare earth monazite systems have previously been discussed in some detail but there appeared to be no previously reported monazite structure which contained the monofluorophosphate anion, PO_3F^{2-}.

The monazite system reported here consists of a 9 co-ordinate Sr^{2+} atom which has seven oxygen atoms and two fluorine atoms in its co-ordination sphere. The structure consists of SrO_7F_2 polyhedra, which edge-share with the PO_3F^{2-} units, linking the polyhedra to other SrO_7F_2 polyhedra in adjacent chains to form interlocked chains (figure 3.12).

The PO_3F^{2-} tetrahedral units form layers throughout the structure, with chains of the tetrahedral units existing both parallel and perpendicular to the *a* axis. The chains of PO_3F^{2-} tetrahedral units parallel to the *a* axis appear to exhibit an ordering of the P-F bond, where all of the P-F bonds are aligned (figure 3.13), as previously observed with the hydrated phase (section 3.2.4.1.). This degree of ordering can be inferred from the bong lengths of the tetrahedral unit (table 3.6), where there is an apparent elongation of one of the tetrahedral bonds. This lengthened bond can be identified as the P-F bond and indicates that the fluorine must be largely ordered in one site within the structure as oppose to being randomly located, as discussed earlier.

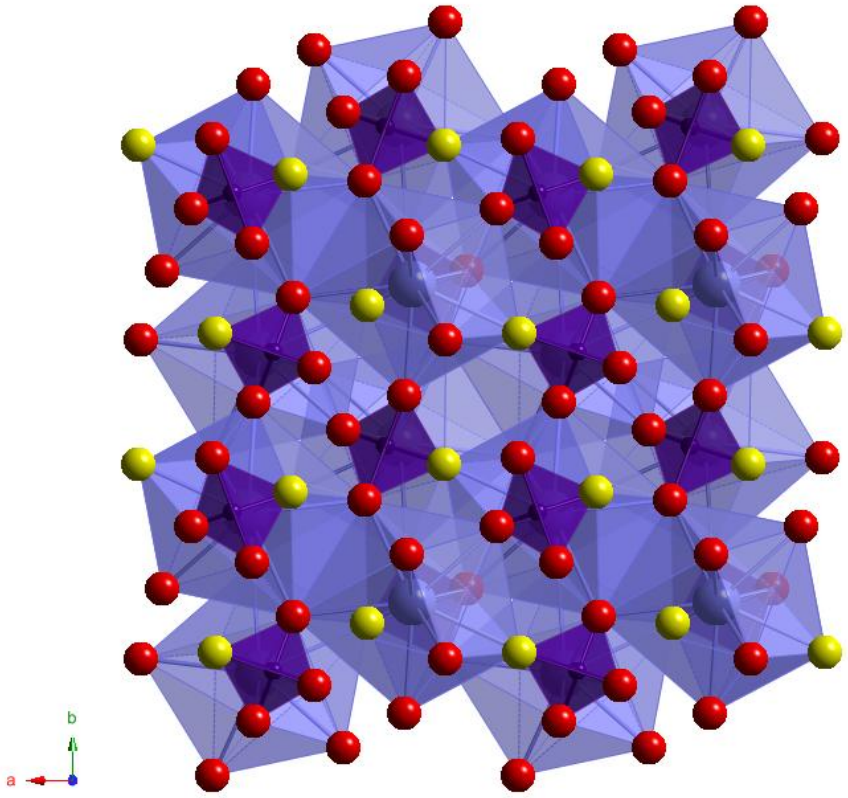

Figure 3.12: Structure of $SrPO_3F$ viewed down the *b* axis.
SrO_7F_2 polyhedra (lilac), PO_3F^{2-} tetrahedra (purple), oxygen atoms (red), fluorine atoms (yellow)

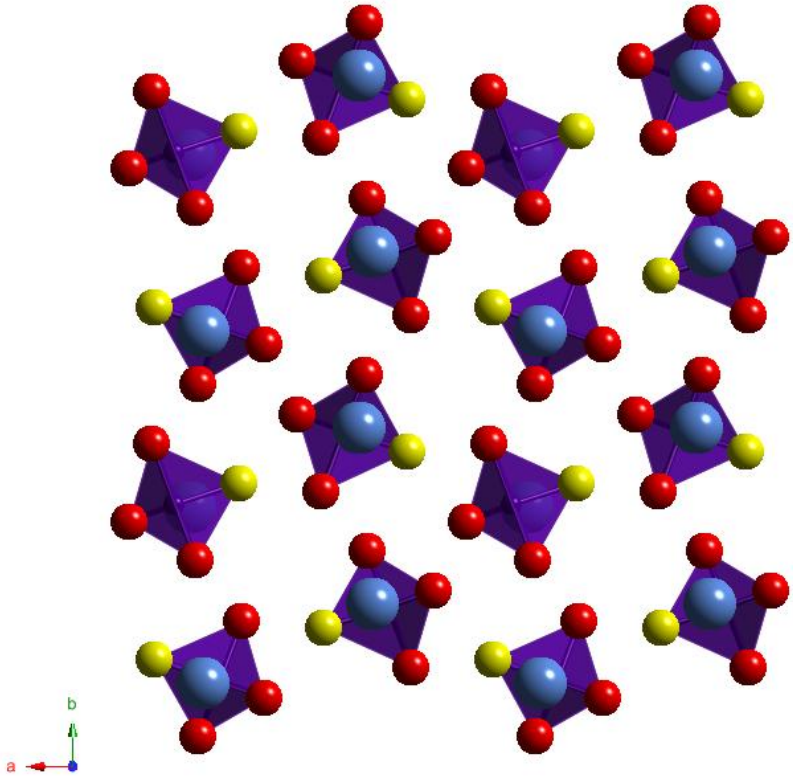

Figure 3.13: Structure of $SrPO_3F$ showing the ordering of the P-F bond (viewed down the *c* axis)

As with the hydrated phase, calculations of the BVS for strontium and phosphorus were performed and produced values of +2.18 and +5.08 respectively. These values were very similar to those calculated for the hydrated phase, $SrPO_3F{\cdot}H_2O$. Both values were slightly higher than the expected values but once again the calculations were only able to provide a limited guidance based the calculations based on a purely oxygen co-ordination environment. Full details of the bond valence sum calculation are shown in appendix 1 section 1.3.

Strontium fluorophosphate differs from that of any of the previously reported monazite structure as this appears to be the first example of a monazite system formed solely from divalent cations. To date, most reported monazite systems contain rare earth phosphates, which possess trivalent cations. Also, for monazite system containing PO_4^{3-},

the bond lengths associated with the tetrahedral units are all of a similar length, with an average length of 1.53(1) Å.[13] However, for fluorophosphate the replacement of an oxygen atom for fluorine in the tetrahedral unit results in a significant increase in one of the tetrahedral bond lengths to 1.575(3) Å compared to three shorter P-O bonds which results in a distortion of the tetrahedral unit.

When comparing other reported monazite systems, the general trend observed in crossing the orthophosphate systems $LaPO_4$-$EuPO_4$, shows a decrease in the unit cell size and the M-O bond lengths (figure 3.14 and 3.15 respectively). This is as a result of the decrease in ionic radius of the metal cation as you move across the period due to an increase in the charge density, which results in a contraction of the unit cell and shorter M-O distance. However, in $LaVO_4$ a larger unit cell size and longer M-O bond distances are observed compared to $LaPO_4$ due to the relative size of the phosphorous and vanadium cations (0.17 and 0.355 respectively).[23-24] When replacing an oxygen with fluorine and comparing the equivalent M-O/M-F bond lengths, it can be seen that the M-F bond is substantially longer than the M-O bond would be for a purely oxygen co-ordinated system and as a result $SrPO_3F$ does not fit with the trend across the series. However, the other M-O bond lengths follow the same trend as was observed for the orthophosphate series (La-Eu). This is due to the difference in bonding character.

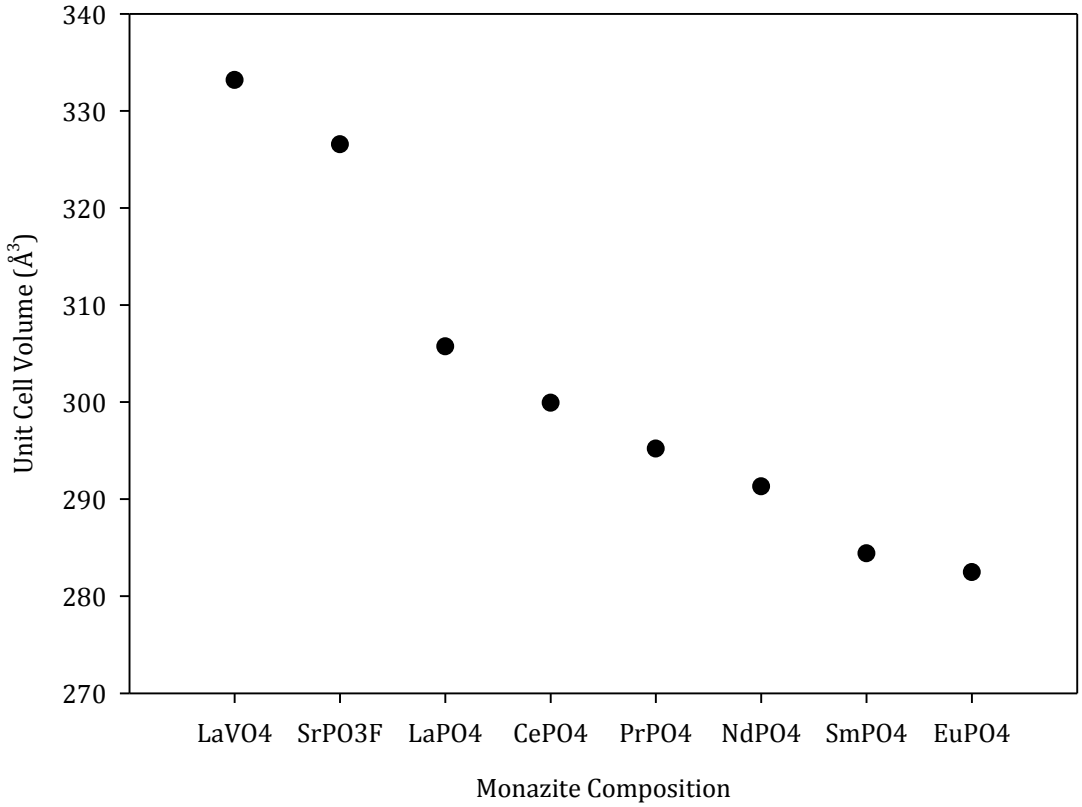

Figure 3.14: A comparison of the unit cell size for various monazite systems

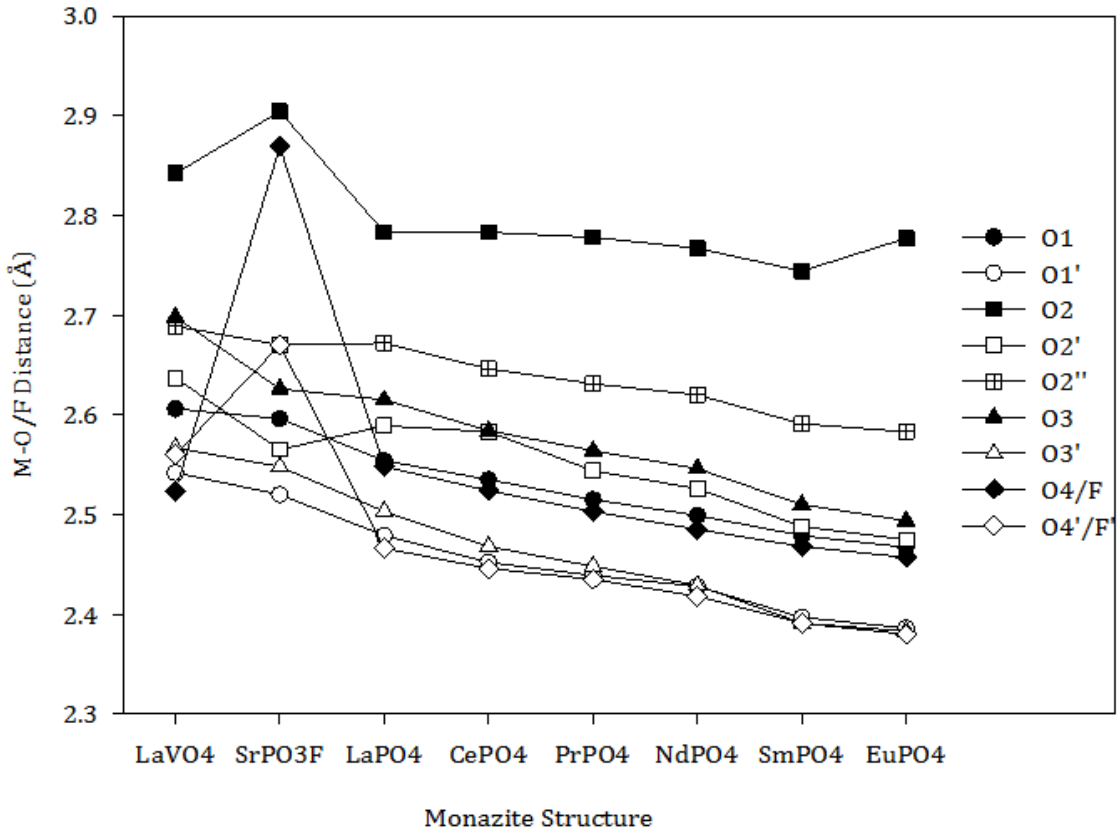

Figure 3.15: M-O/F bond distances for various monazite systems

3.3.5.3 XRF Spectroscopy Results

As with the hydrated phase, x-ray fluorescence spectroscopy was used to investigate the elemental composition of multiple $SrPO_3F$ samples, which have determined from calibrated XRF measurements. The Sr:P molar ratio for samples of $SrPO_3F$ was found to be 0.98(2), which is in excellent agreement with the expected $SrPO_3F$ stoichiometry. Full details of the elemental analysis of the $SrPO_3F$ samples can be found in appendix 1 section 1.4.3. As the presence of fluorine can only be inferred from the Sr:P ratio, it was possible to confirm a significant amount fluorine was present due to the emission from the fluorine Kα_1 line (Fig. 3.16).

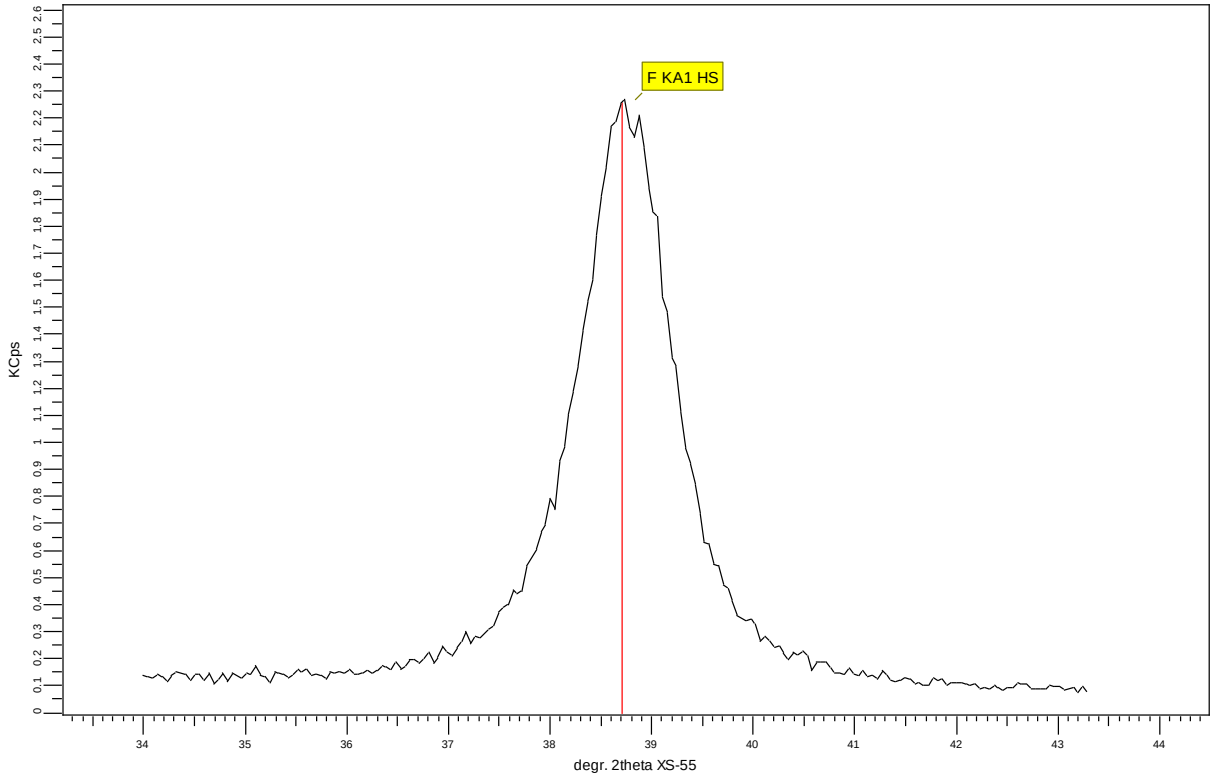

Figure 3.16: Emission signal obtained from the Fluorine Kα_1 line of the as synthesised monazite phase, $SrPO_3F$.

3.3.5.4 Raman Spectroscopy

The Raman spectra obtained for $SrPO_3F$ is shown in figure 3.17 with the assignments outlined in table 3.7.

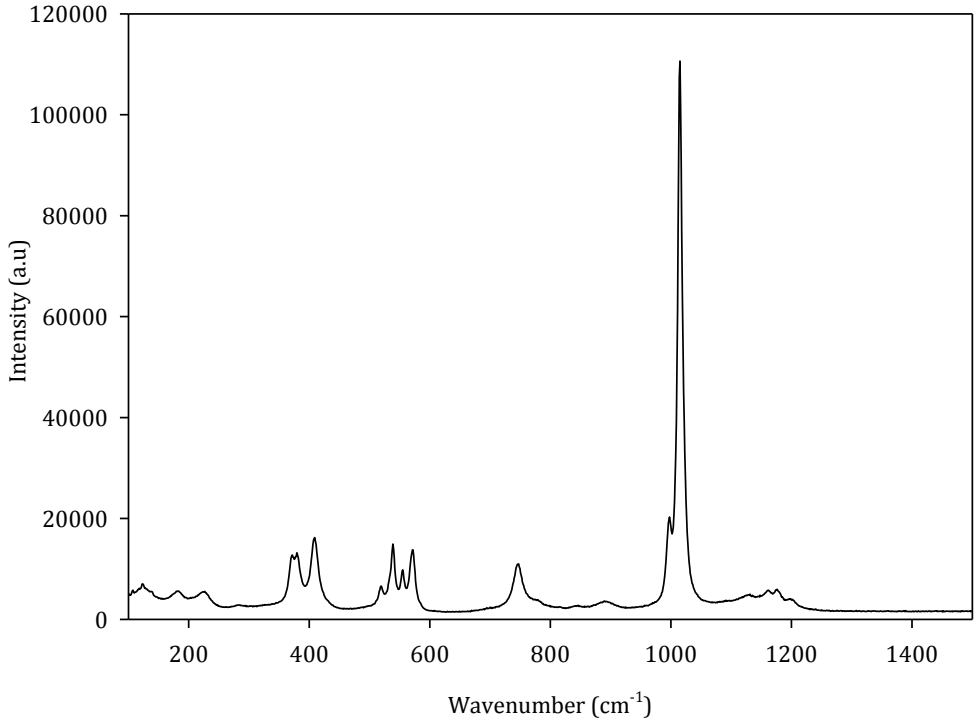

Figure 3.17: Raman spectra of $SrPO_3F$

Table 3.7: Assignment of the vibrations observed in the Raman spectra of $SrPO_3F$

Vibrations (cm^{-1})	Assignments
1176	ν_{as} (PO_3)
1014, 997	ν_s (PO_3)
746	P-F
571, 555, 538 519	δ (PO_3)
372, 381, 409	ρ (PO_3)

Further confirmation of the presence of PO_3F^{2-} was evident from the band observed at 746 cm^{-1} which is indicative of a P-F bond (although appearing at a slightly lower

frequency than the value measured in solution).[25] The phosphate vibrations are apparent in the regions 1200-800 cm^{-1} and 580-520 cm^{-1}, with the bands relating to the presence of the anti-symmetric (ν_{as}) and symmmetric (ν_s) stretches and $\delta(PO_3)$ vibrations respectively.

3.3.5.5 SEM-EDAX

Figure 3.18 shows the SEM image of anhydrous strontium fluorophosphate. As with the hydrated phase, a number of EDAX measurements were performed across the images of the sample which suggested that the sample of SrPO3F was indeed homogenous. The results from EDAX (appendix 1 section 1.5.2) were found to differ from the WD-XRF results presented earlier, with the Sr:P ratio determined from EDAX considerably higher than that determined from WD-XRF (1.35 and 0.98 respectively). This may be as a result of the low phosphorus content suggested from EDAX analysis.

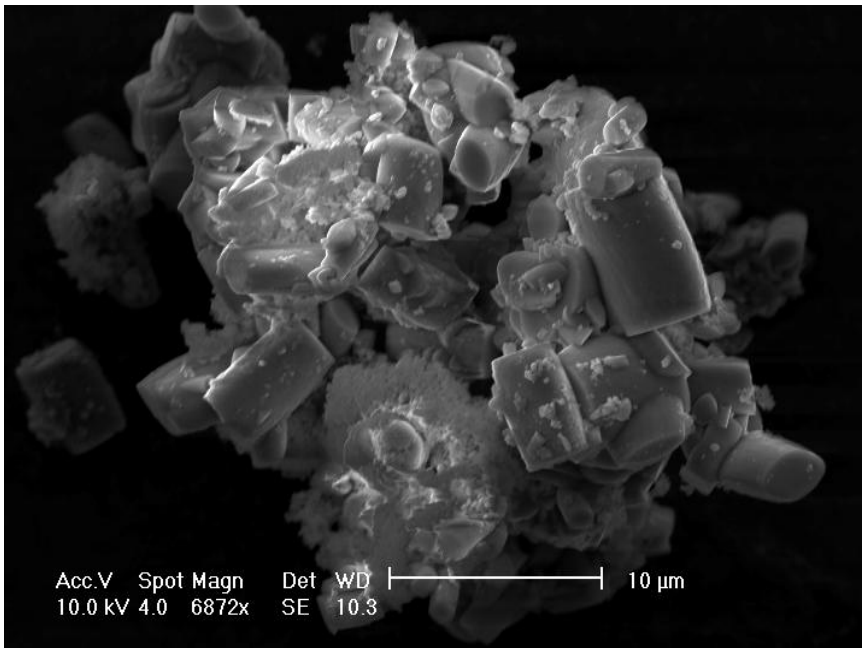

Figure 3.18: SEM Image of $SrPO_3F$

3.3.5.6 Solid State NMR

The simulated and one pulse experimental results for the ^{31}P and ^{19}F nuclei of $SrPO_3F$ are shown in figures 3.19 and 3.20 respectively. A table of the experimental results stating the chemical shifts, percentage intensities and the J coupling values can be found in appendix 1 section 1.6.

The ^{31}P NMR spectra (figure 3.19(a)) shows a doublet which is what would be expected due to the coupling between the ^{31}P and ^{19}F nuclei. However, the doublet appears to be asymmetrical, which implies that another phosphorus site may be present and lies directly underneath one side of the doublet, causing the asymmetric shape of the doublet. The presence of an additional phosphorus peak is confirmed by the decoupling of ^{19}F from the ^{31}P which results in two peaks, one which we identify as the expected phosphorus site in $SrPO_3F$ and another peak at about 0.14 ppm, whose presence is unexplained as the structural model only consists of one phosphorus site (figure 3.19(b). As there appears to be no J splitting for this phosphorus site, it is assumed that there is no bonding to fluorine, which implies that either the impurity phase either does not contain fluorine or that fluorine is not in close enough proximity to bond to the phosphorus site in the impurity phase. As the presence of the additional phosphorus site was unexpected, this suggests that the sample of $SrPO_3F$ contains an impurity phase which was not evident in PXRD or NPD patterns. Based on this, the impurity phase may likely be of an amorphous nature.

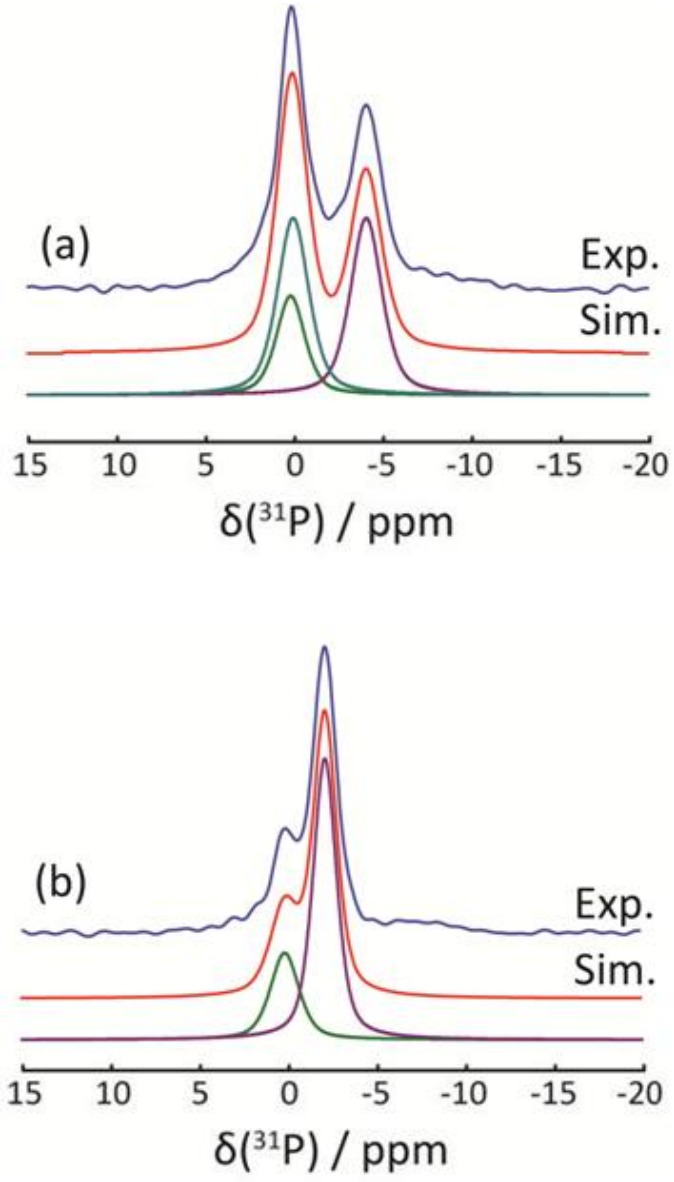

Figure 3.19: ^{31}P Experimental (blue) and simulated (red) NMR spectra for the one pulse (a), ^{19}F decoupled spectra (b) of $SrPO_3F$. Deconvoluted peaks (green and purple).

Figure 3.20(a) shows the one pulse ^{19}F NMR spectra which appears to be more complicated than the ^{31}P spectra as there appears to be more resonances than expected. Some aspects of the ^{19}F NMR spectra appear to be very similar to the ^{31}P one pulse spectra in that both spectra consist of an asymmetric doublet peak, implying that the ^{19}F NMR spectra also contains an impurity phase, where the peak due to the impurity phase

lies under one side of the doublet. The chemical shifts values appear to be consistent throughout and show good agreement between the un-decoupled and decoupled spectra (see appendix 1 section 1.6). The J coupling values for produced from the ^{31}P and the ^{19}F experiments are consistent with one another, producing values of 667 and 664±2 Hz respectively. However, the J coupling size for $SrPO_3F$ are considerably smaller than those for the hydrated system, which has a J coupling value of 855±2 Hz. The peak present at -88 ppm can be attributed to the presence of SrF_2 in the as synthesised $SrPO_3F$ monazite phase which was also found to be present in the ^{19}F NMR spectra of the hydrated phase as discussed in section 3.2.5.6. The presence of SrF_2 is more apparent in the ^{19}F (^{31}P decoupled) NMR spectra (figure 3.20(b), as this was a sample of monazite which was heat treated at 180 °C, which contained significantly more SrF_2 due to some thermal decomposition of the fluorophosphate anion. Evidence for the presence of a small amount of SrF_2 in the as synthesised material may be inferred from the slightly raised background in the PXRD pattern which occurs at $\sim 25°\ 2\theta$ which lies in the appropriate region for SrF_2 reflections to be observed. However, as there are no well defined peaks apparent for SrF_2 in the diffraction pattern, it likely that any SrF_2 present is either poorly crystalline or in an amorphous form. From the NMR results obtained, identification of the impurity phase(s) in both the ^{19}F and ^{31}P cannot be established.

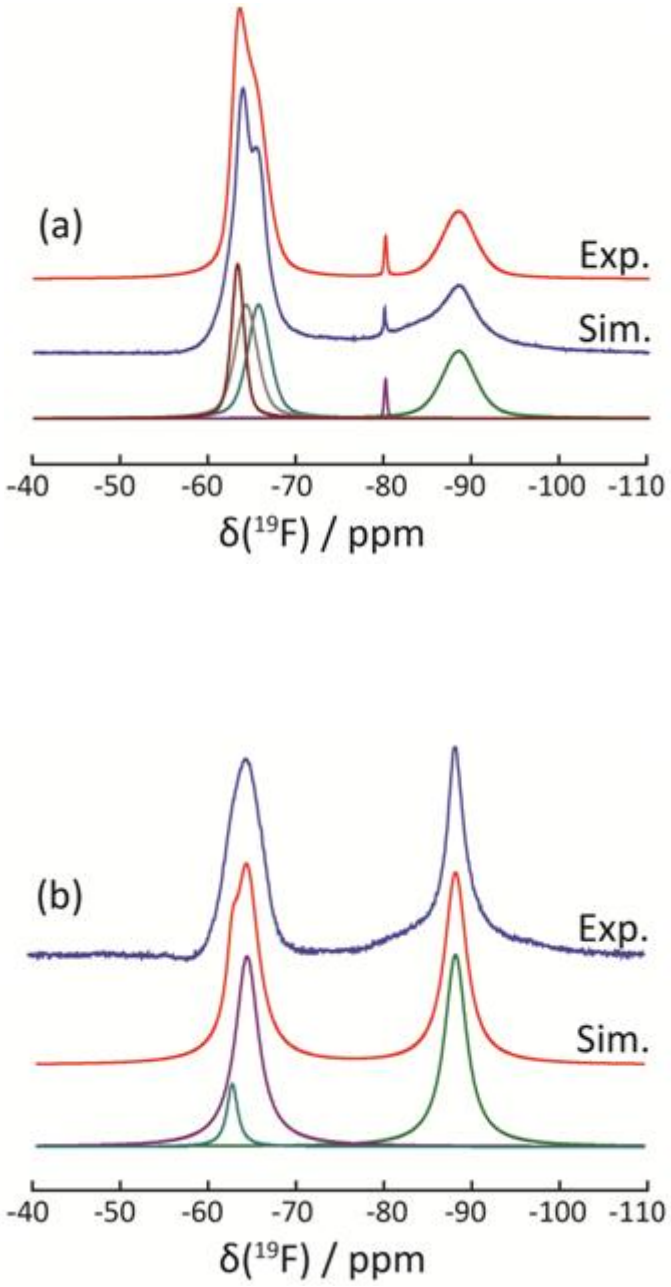

Figure 3.20: ^{19}F Experimental (blue) and simulated (red) NMR spectra for the one pulse (a) and ^{31}Pdecoupled spectra of $SrPO_3F$ (b). Deconvoluted peaks (green and purple).

3.3.5.7 Assessing the Amorphous Content within $SrPO_3F$

Given the suggested presence of an additional amorphous component from the NMR studies, a similar analysis was undertaken to that of the hydrated phase $SrPO_3F{\cdot}H_2O$, involving a two phase refinement using both $SrPO_3F$ and added TiO_2

(details of the amounts of $SrPO_3F$ and TiO_2 used are stated in appendix 1 section 1.7.2). The Rietveld refinement showed very good agreement between the experimental and calculated patterns for both phases, producing low χ^2 and R_{wp} values of 2.377 and 7.28 %. The phase fractions generated from the refinement for $SrPO_3F$ and TiO_2 were 52.50 % and 47.50 % respectively. The Rietveld plot and further results from the refinement are provided in appendix 1 section 1.7. Calculations based on using the actual weight % of TiO_2 present estimated an amorphous content of approximately 25 wt % which was slightly higher than the amorphous content calculated for $SrPO_3F{\cdot}H_2O$. However, the level of amorphous material estimated from the Rietveld refinement is in close agreement with the level of amorphous material predicted from the solid state NMR results. The confirmation that $SrPO_3F$ consists of some amorphous material may offer an explanation to the small aggregated particles observed on the surface of the well defined crystals of $SrPO_3F$.

3.3.6 Thermal Decomposition of $SrPO_3F{\cdot}H_2O$ and $SrPO_3F$

Assessing the thermal stability of these fluorophosphates phases is important in evaluating their potential for applications. Some decomposition studies have previously been reported for a limited number of fluorophosphate materials[14-15, 26] but the one which is of most interest is that reported by Menz *et al*.[5] which details the decomposition of a hydrated strontium fluorophosphate material (a polymorph of the hydrated phase reported in this work).

3.3.6.1 Ex-situ Temperature Treatments

The decomposition of both $SrPO_3F{\cdot}H_2O$ and $SrPO_3F$ were investigated by performing various heat treatments on each sample at temperatures between 100-750

°C (measurements were taken at room temperature, every 50 °C from 100-750 °C). The resulting products were analysed by powder XRD, XRF and Raman spectroscopy.

3.3.6.1.1 Decomposition of $SrPO_3F \cdot H_2O$

3.3.6.1.1.1 PXRD

Initial heat treatments to 100 °C resulted in the loss of water causing the structure to collapse and leading to the formation of a poorly crystalline material as indicated from the broad features/peaks on the PXRD pattern (figure 3.21).

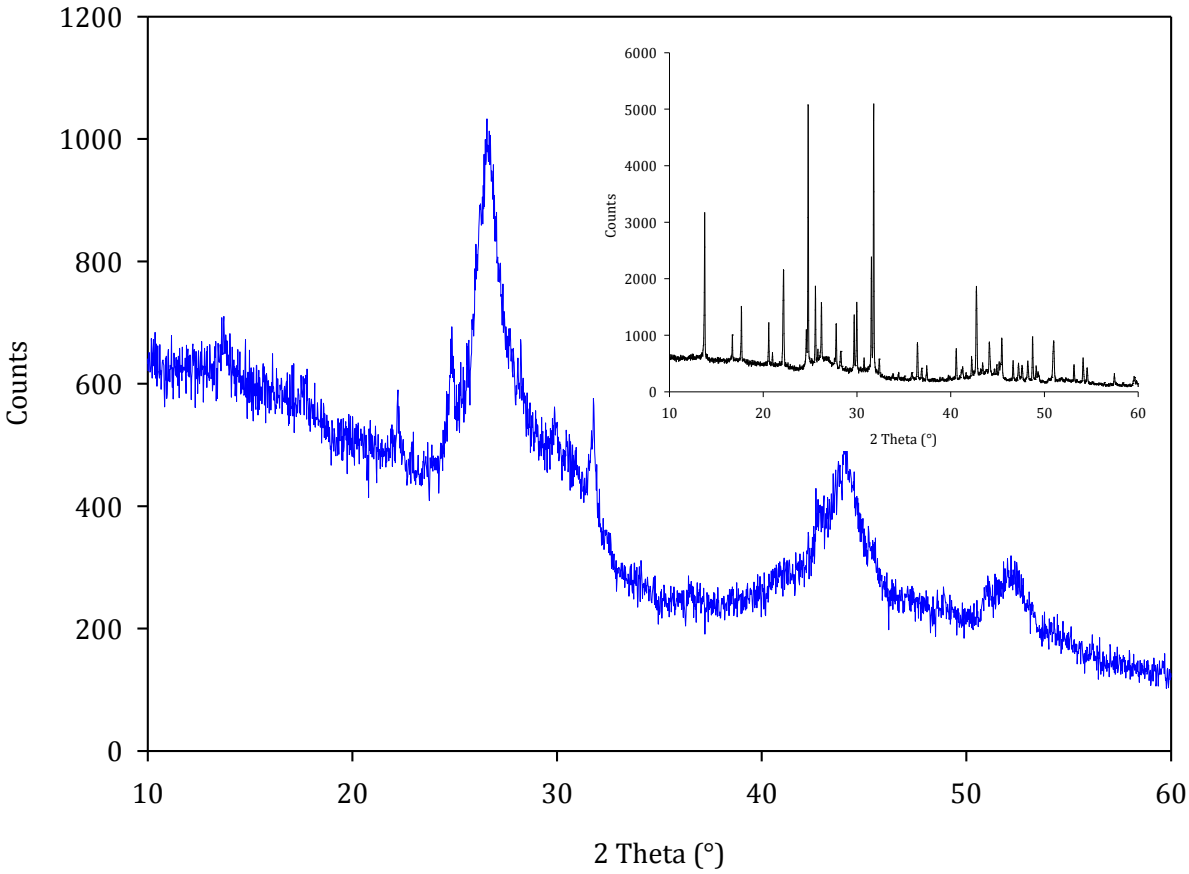

Figure 3.21: PXRD pattern obtained after dehydration of $SrPO_3F \cdot H_2O$ at 100 °C (Inset: PXRD pattern of the as synthesised $SrPO_3F \cdot H_2O$ material).

Figure 3.22 shows the PXRD patterns obtained beyond these temperatures whereby the crystallinity of the material is shown to improve significantly with increasing the temperature, as the broad features/peaks are no longer apparent and the PXRD pattern

resembles that of a crystalline form α-$Sr_2P_2O_7$ (PDF: 00-024-1011) In addition to α-$Sr_2P_2O_7$, presence of another phase becomes evident at 600 °C which corresponds to the that of an apatitic material, either $Sr_5(PO_4)_3OH$ (PDF: 00-033-1348) or $Sr_5(PO_4)_3F$ (PDF: 04-015-2310). From the PXRD data alone, differentiating between the two phases is difficult due to the similarity in the lattice parameters of both phases and therefore further analyses of these phases are required to establish the identity of the apatite material formed.

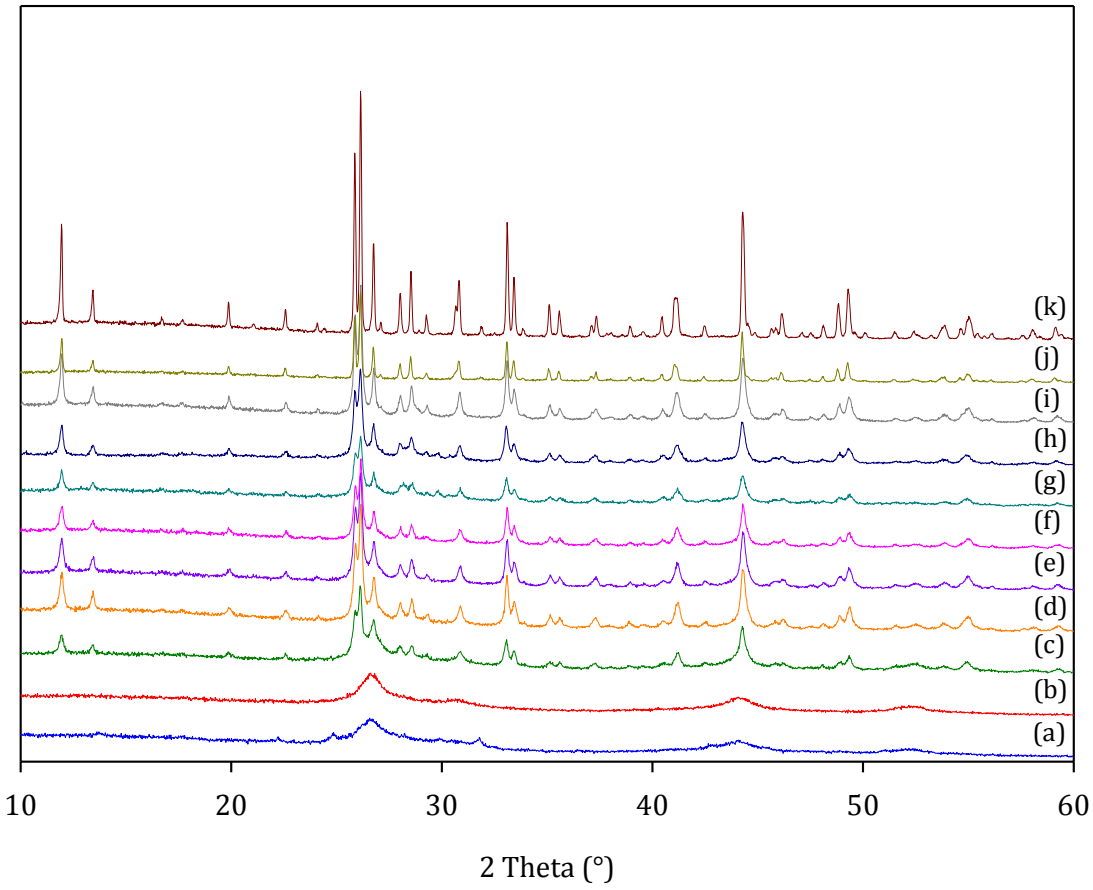

Figure 3.22: A stack plot of PXRD patterns obtained from heat treated samples of $SrPO_3F{\cdot}H_2O$ 100-500 °C (a-i), 600 °C (j) and 750 °C (k)

In order to determine the nature of the apatitic phase, XRF spectroscopy was utilised to establish whether the sample heated to 750 °C contained fluorine. For this, samples

were prepared as pressed pellets and were measurements were undertaken as stated in section 2.7.3.

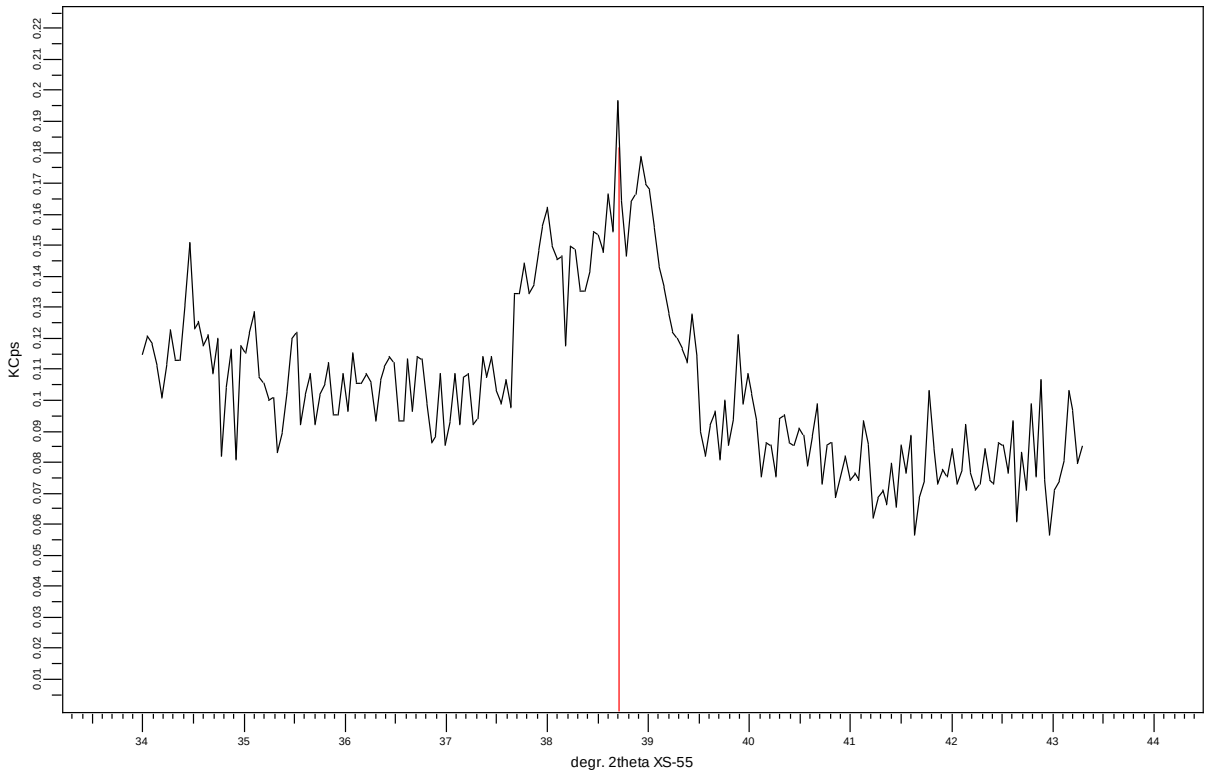

Figure 3.23: Emission signal from the fluorine Kα_1 line obtained from a sample of $SPO_3F{\cdot}H_2O$ heated to 750°C

Figure 3.23 confirms that the sample of interest does indeed contain fluorine, albeit only a low level as suggested from the intensity of the emission signal from the F Kα_1 peak. This infers that the apatite phase present with α-$Sr_2P_2O_7$ could possibly be $Sr_5(PO_4)_3F$. However, it is still unclear as to whether this apatite phase is solely present as fluorapatite or whether there is a mixture of the fluorine/non-fluorine containing apatites are present in the sample.

The decomposition of $SrPO_3F{\cdot}H_2O$ was monitored using Raman spectroscopy, where *ex-situ* measurements were carried out on each of the heated samples. However,

for the samples which were heated between 400-600 °C no valid spectra could be obtained due to problems with fluorescence, resulting in a significantly high and rising background in the spectra. Fluorescence appeared to also be an issue in some of the lower temperature treated samples but reasonable spectra could be obtained. Attempts were made to rectify this but the problem could not be overcome. Figure 3.24 (a,b,c and d) show the Raman spectra for $SrPO_3F \cdot H_2O$ after heating to temperatures of 100 °C, 250 °C, 600 °C and 750 °C which summarise the key decomposition events. The full assignment of the Raman spectrum for these heat treatments is summarised in table 3.9.

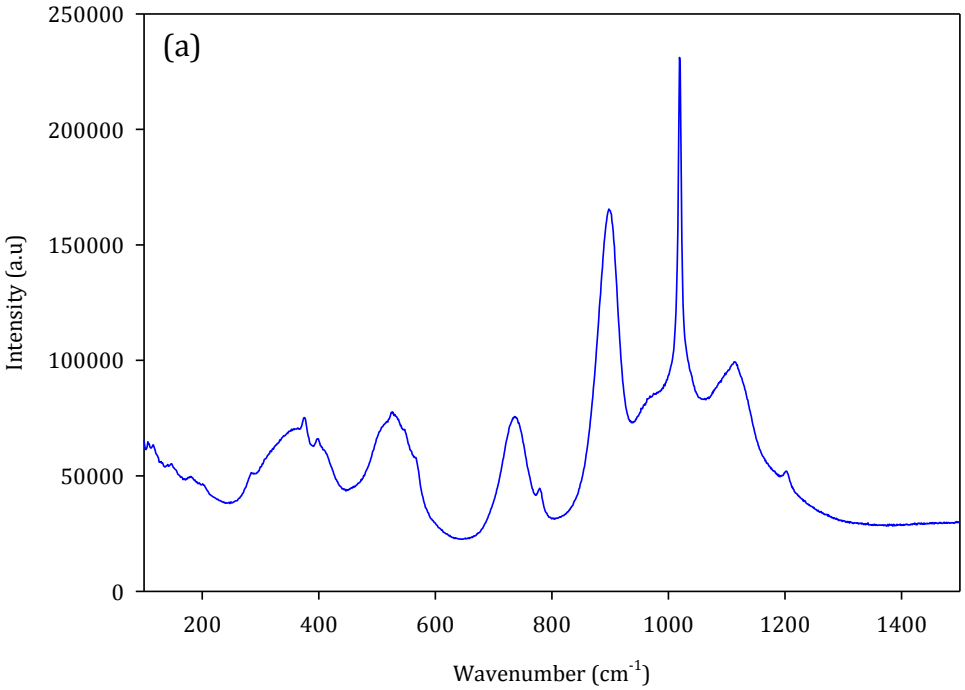
(a)
250000
200000
150000
100000
50000
0
Intensity (a.u)
200
400
600
800
1000
1200
1400
Wavenumber (cm-1)

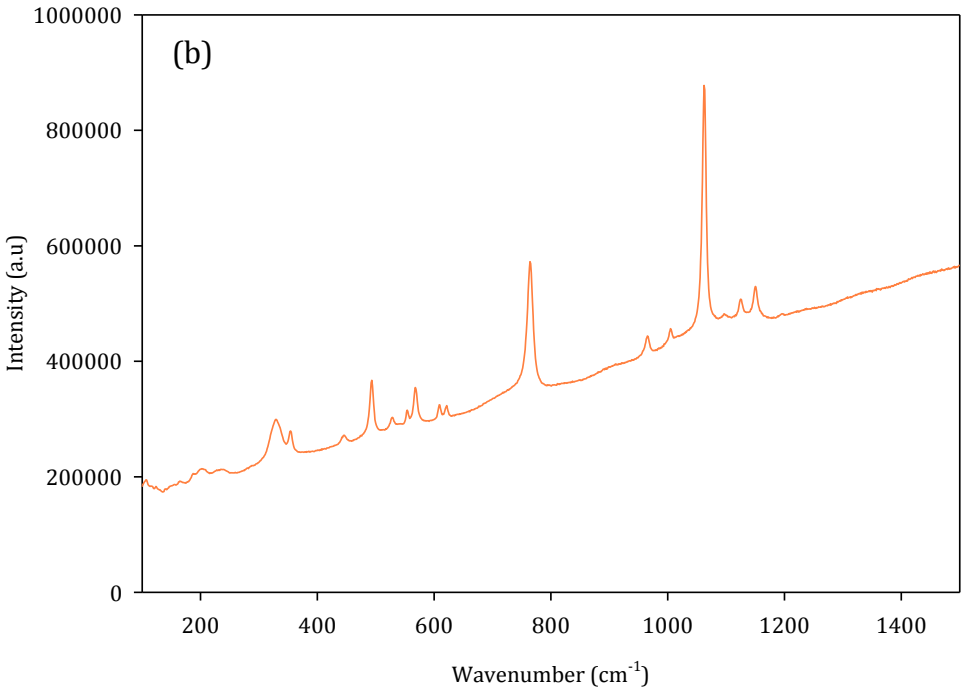
(b)
1000000
800000
600000
400000
200000
0
Intensity (a.u)
200
400
600
800
1000
1200
1400
Wavenumber (cm-1)

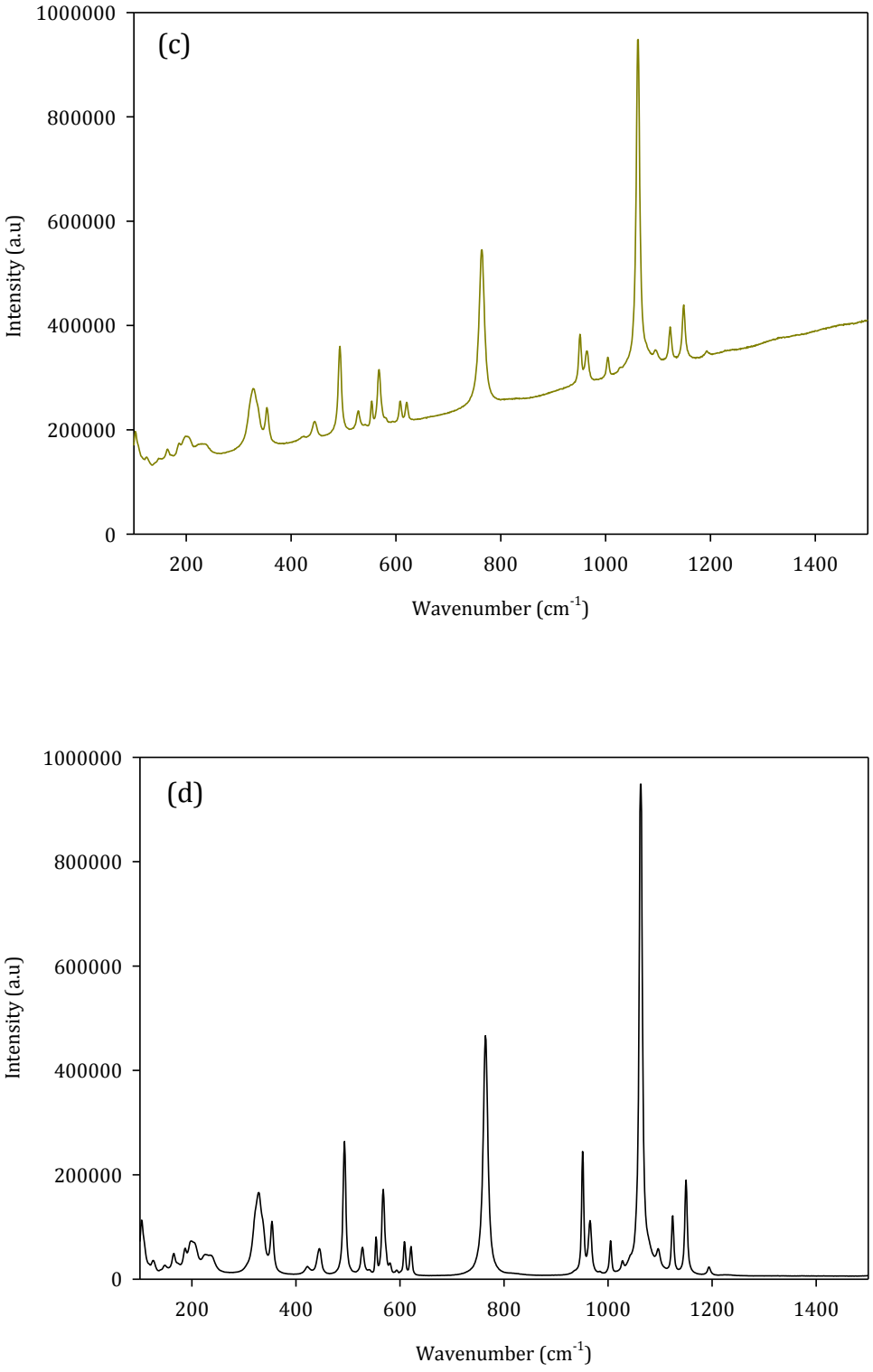

Figure 3.24: Raman spectra obtained from $SrPO_3F{\cdot}H_2O$ heat treated to 100 °C (a), 250 °C (b), 600 °C (c) and 750 °C (d)

Table 3.8: Assignments of the vibrations observed in the Raman spectra for heat treated samples of $SrPO_3F{\cdot}H_2O$

Region (cm^{-1})	Temperature of Heat Treatment (°C)				Assignments			
	100	250	600	750	$SrPO_3F{\cdot}H_2O$	α-$Sr_2P_2O_7$[27]	$Sr_5(PO_4)_3(OH)_2$[28]	$Sr_5(PO_4)_3F_2$[29]
900-1300	1203	-	-	-	ν_{as} (PO_3)	-	-	-
	-	-	-	1194	ν_{as} (PO_3)	-	-	-
	-	1150	1149	1150	-	ν_a (PO_3)1153	-	-
	-	1125	1123	1124	-	ν_a (PO_3)1128	-	-
	1116	-	-	-	ν_{as} (PO_3)	-	-	-
	-	-	1096	1097	unassigned	-	-	-
	-	1063	1062	1063	-	ν_s (PO_3)1068	-	-
	-	-	-	1028	-	-	ν_3 1028	ν_3 1023
	1020	-	-	-	ν_s (PO_3)	-	-	-
	-	1005	1004	1005	-	ν_a (PO_3)1009	-	-
	-	965	965	965	-	ν_a POP 968	-	-
	-	-	951	951	-	-	ν_1 951	ν_1 951
700-900	897	-	-	-	unassigned	-	-	-
	780	-	-	-	P-F	-	-	-
	-	764	764	764	-	ν_s POP 768	-	-
	735	-	-	-	unassigned	-	-	-
300-700	-	621	621	621	-	δ (PO_2) 623	-	-
	-	609	608	609	-	δ (PO_2) 609	-	-
	-	568	568	568	-	δ (PO_2) 571	ν_4 573	ν_4 572
	-	554	554	554	-	δ (PO_2) 556	-	-
	529	528	528	528	δ (PO_3)	δ (PO_2) 531	-	-
	-	493	493	493	-	δ (PO_2) 493	-	-
	-	446	445	445	-	δ (PO_2) 447	ν_2 442	ν_2 442
	-	-	-	422	unassigned	-	-	
	399	-	-	-	ρ (PO_3)	-	-	-
	376	-	-	-	ρ (PO_3)	-	-	-
	-	354	354	354	-	δ (PO_2) 360	-	-
	335	-	-	-	unassigned	-	-	-
	-	328	327	327	-	δ (PO_2) 336	-	-

The results obtained from Raman spectroscopy supported the findings from the pxrd data. The poorly crystalline product formed at 100 °C (figure 3.24(a)) shows very broad peaks in the Raman spectrum which is not uncommon and the frequencies at which these vibrations occur resemble those vibrations present in the parent $SrPO_3F{\cdot}H_2O$ material prior to heating, albeit with a few additional peaks in the heat treated sample. This could suggest that the amorphous material is an amorphous form of $SrPO_3F{\cdot}H_2O$ given the similarity of the frequencies observed in the Raman spectra. The unidentified vibration at 897 cm^{-1} in the untreated sample, is now more pronounced in the Raman spectra following the heat treatments. Decomposition of the fluorophosphate into crystalline form of α-$Sr_2P_2O_7$ was confirmed from the Raman spectrum at 250 °C (figure 3.24(b)), as all of the vibrations observed can be attributed to those vibrations previously reported for α-$Sr_2P_2O_7$. Along with the pyrophosphate phase, additional vibrations owing to the presence of the apatitic phase first becomes apparent in the Raman spectra at 600 °C (figure 3.24(c)) and becomes more apparent upon heating to higher temperatures, as more vibrations corresponding to the apatitic phase are observed in the 750 °C spectrum (figure 3.24(d)).

3.3.6.1.2 $SrPO_3F$

3.3.6.1.2.1 PXRD

Figure 3.25 shows the PXRD stack plot for the various heat treatments of $SrPO_3F$. Although the final decomposition products for anhydrous strontium fluorophosphate are the same as those for stated hydrated phase (section 3.2.6.1.1.1), the decomposition pathway appeared to be different.

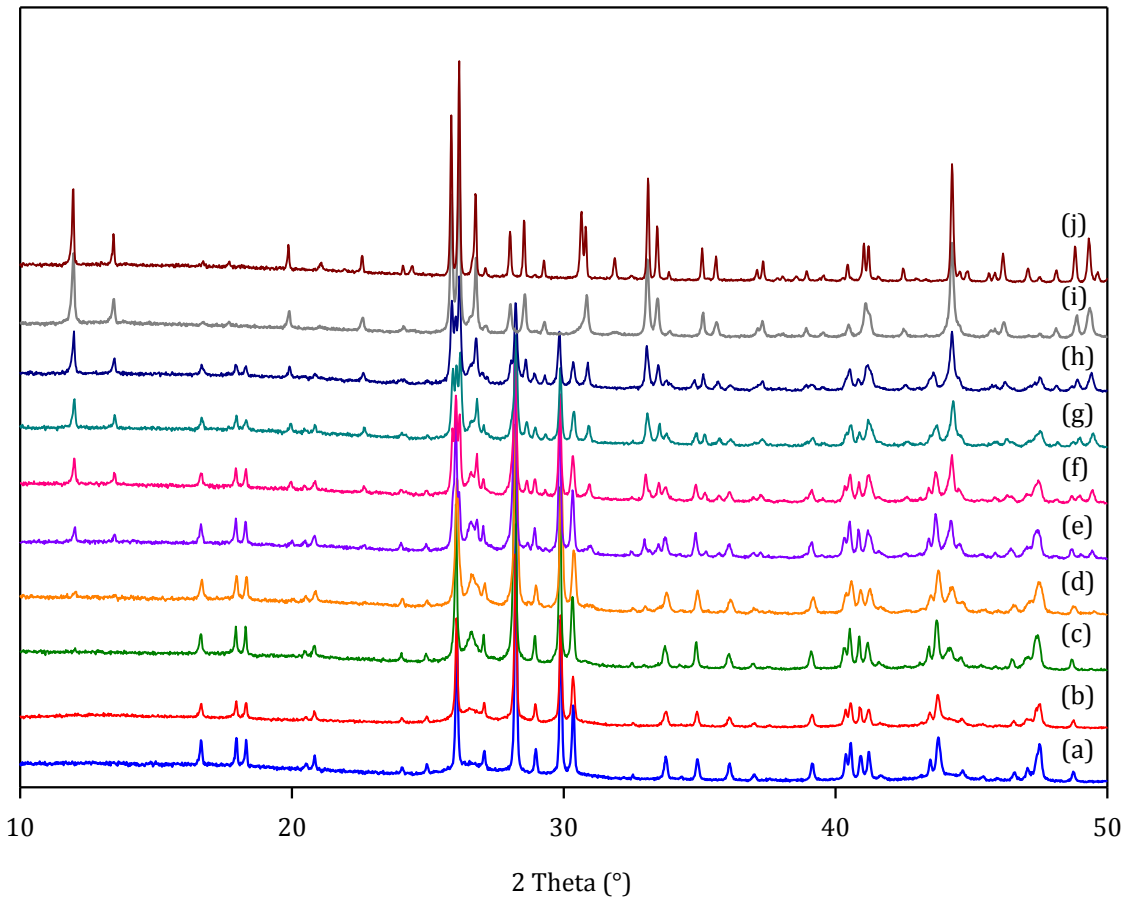

Figure 3.25: A stack plot of PXRD patterns obtained from heat treated samples of $SrPO_3F$ 100-500 °C in increments of 50 °C (a-i) and 750 °C (j)

Evidence of decomposition first becomes apparent at 150 °C with the presence of a peak at 25.2° 2θ in the diffraction pattern, originating from the presence of SrF_2. As with the hydrated phase, the results from the one pulse ^{19}F NMR experiments indicated that SrF_2 was already present in the as synthesised material (section 3.2.5.6). This suggested that some of the fluorophosphate had already decomposed but this could not be confirmed from diffraction experiments, as they could only imply that any SrF_2 in the as synthesised sample of $SrPO_3F$ was present either in low levels (< 3 wt %) or in an amorphous form. Further heating resulted in the diffraction peaks of SrF_2 became more

pronounced until 500 °C, where the peaks were no longer apparent. Further breakdown of fluorophosphate occurred between 200-250 °C, where the initial formation of α-$Sr_2P_2O_7$ was observed, confirmed by the appearance of some additional peaks in the diffraction pattern which became more apparent at subsequent temperatures. Additional heat treatments using smaller temperature increments of 10 °C were carried out between 200-250 °C and it was found that the decomposition of $SrPO_3F$ to the corresponding pyrophosphate phase occurred at 230°C. From this point, the co-existence of $SrPO_3F$, SrF_2 and α-$Sr_2P_2O_7$ were observed in the PXRD patterns until a temperature of 500 °C was reached, at which point there was no longer evidence for the original fluorophosphate material or SrF_2, suggesting complete decomposition of the original strontium fluorophosphate material. However, in addition to the presence of α-$Sr_2P_2O_7$, formation of an additional phase was observed in the diffraction pattern at 500 °C which corresponds to that of an apatitic phase, thought to be that of either $Sr_5(PO_4)_3OH$ or $Sr_5(PO_4)_3F$. Similarly, the presence of both the pyrophosphate and apatite materials were also observed in the diffraction patterns for the heated samples of $SrPO_3F{\cdot}H_2O$ but the decomposition into the apatite phase occurred at a higher temperature (600 °C) for the hydrated phase, this was when it was first apparent in the PXRD pattern.

The level of fluorine of the four heated samples that were discussed in the previous section were monitored using XRF spectroscopy, where measurements were carried out as stated in section 2.7.3. The intensities of the emission signal from the fluorine Kα_1 lines of each sample were plotted against temperature which showed that the level of fluorine decreased significantly upon heating which was expected (figure 3.26).

However, the results also confirmed that some fluorine remained present in the samples which were heated beyond 500 °C.

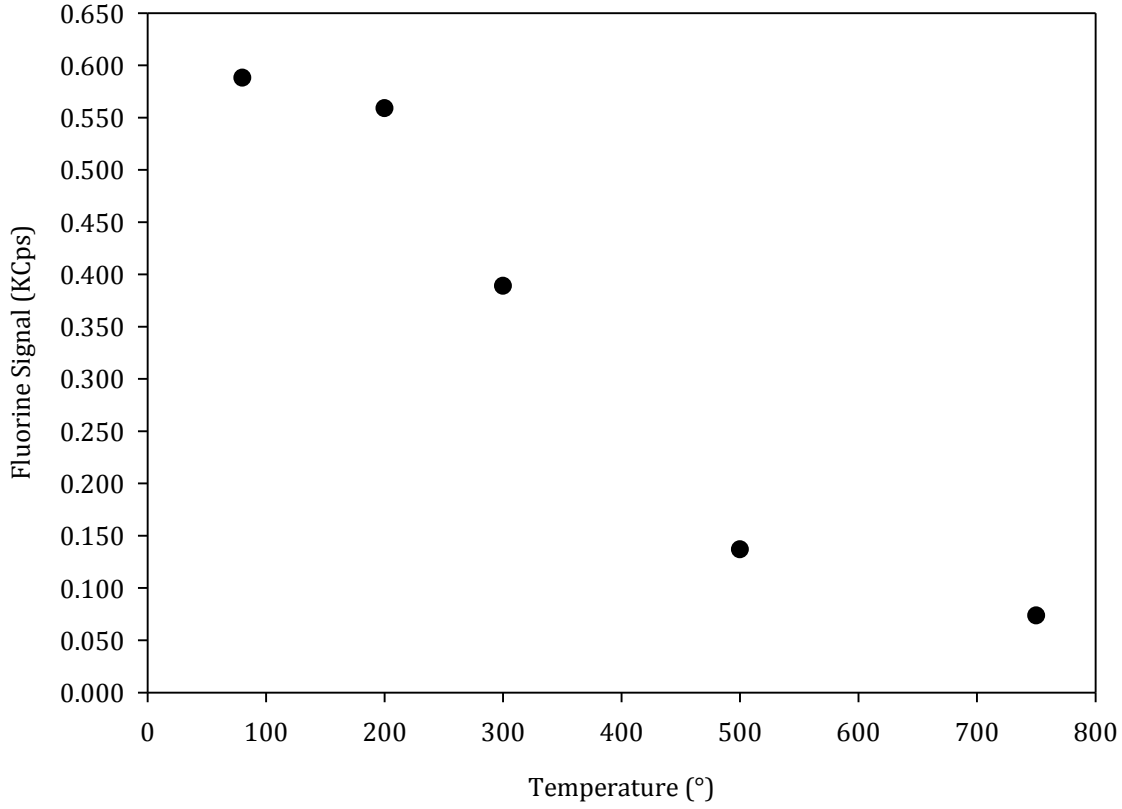

Figure 3.26: A plot of intensity from the fluorine Kα_1 line *vs* temperature for $SrPO_3F$ and samples of $SrPO_3F$ heated to 200°C, 300°C, 500°C and 750°C

The results were in agreement with the those obtained for $SrPO_3F{\cdot}H_2O$ which also suggested that not all fluorine was lost during the decomposition and that the apatitic phase apparent in the xrd patterns at both temperatures could be fluorapatite, $Sr_5(PO_4)_3F$ owing to the presence of fluorine in these samples. However, the amount of fluorine appeared to be limited once heated to 500 °C which could suggest that a mixture of the non fluorine containing apatite and fluorapatite was present in the

sample. The spectra of the F Kα_1 emission signal for each the four heat treated samples can be found in the appendix 1 section 1.8.

In addition to this, Raman spectroscopy was utilised in order to confirm the structural transitions observed in the PXRD patterns. Similarly, the Raman spectrum for every heat treated sample of $SrPO_3F$ were obtained but the spectra shown in figures 3.27 (a,b,c and d) were those corresponding to heat treatments of $SrPO_3F$ to 200 °C, 350 °C, 500 °C and 750 °C. These were chosen, as these clearly show the structural changes and provide further evidence for the decomposition of anhydrous strontium fluorophosphate. The spectra of the samples heated to 350 °C, 400 °C and 450 °C exhibited very high, rising background which is thought to be the result of fluorescence. Attempts were made to rectify this issue but no improvement to the spectra was possible. Assignments of the vibrations observed at the four key transition temperatures were made based on those in the literature of known fluorophosphate materials, alkaline metal earth pyrophosphates and strontium apatite materials and these are shown in table 3.12.

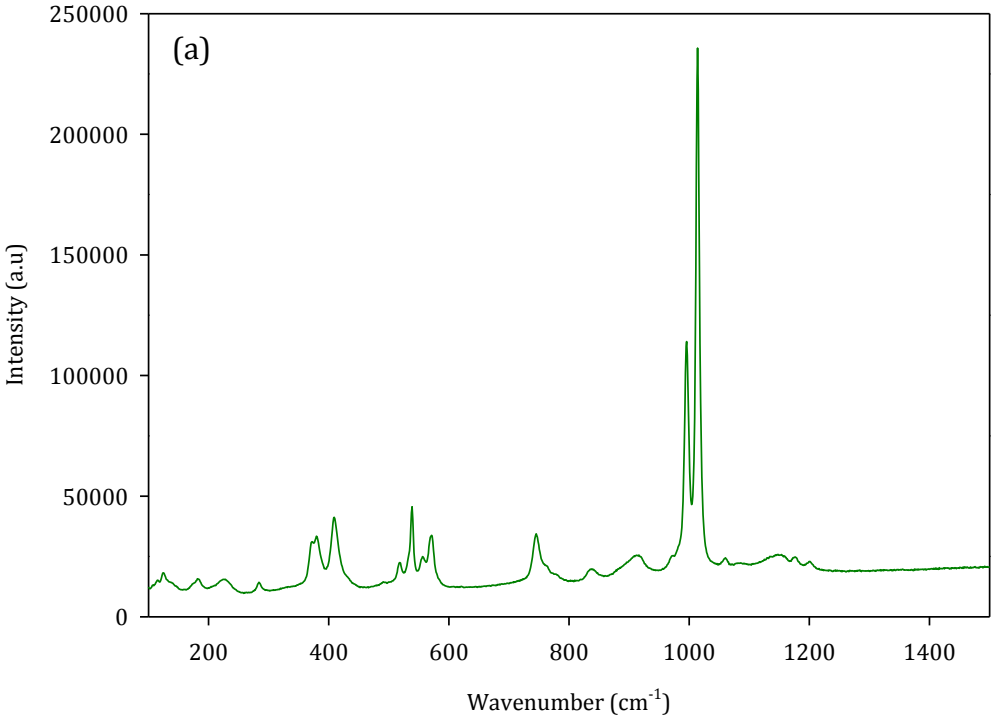
(a)
250000
200000
150000
100000
50000
0
Intensity (a.u)
200
400
600
800
1000
1200
1400
Wavenumber (cm-1)

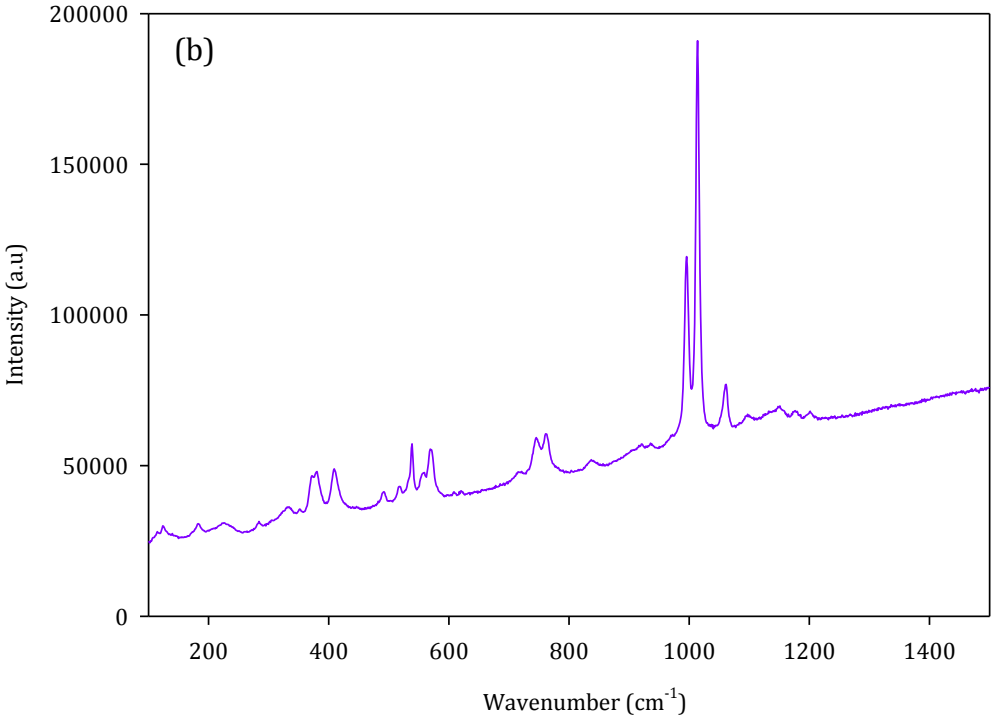
(b)
200000
150000
100000
50000
0
Intensity (a.u)
200
400
600
800
1000
1200
1400
Wavenumber (cm-1)

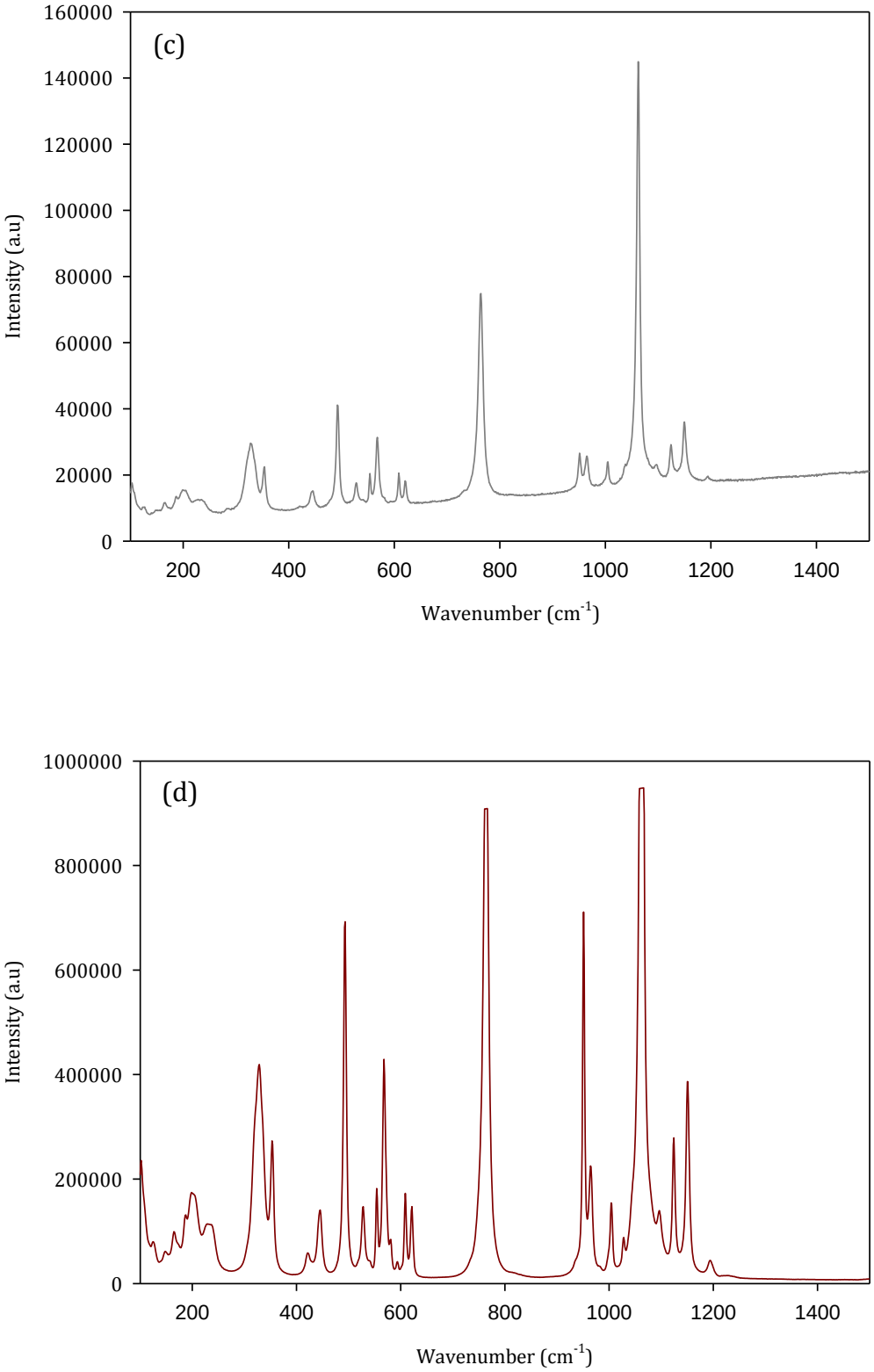

Figure 3.27: Raman spectra obtained from $SrPO_3F$ heat treated to 200 °C (a), 300 °C (b), 500 °C (c) and 750 °C (d)

Table 3.9: Assignments of the vibrations observed in the Raman spectra for heat treated samples of $SrPO_3F$

Region (cm^{-1})	Temperature of Heat Treatment (°C)				Assignments			
	200	300	500	750	$SrPO_3F$	α-$Sr_2P_2O_7$[27]	$Sr_5(PO_4)_3(OH)_2$ [28]	$Sr_5(PO_4)_3F_2$[29]
900 - 1200	1176	1176	-	-	$\nu_{as}(PO_3)$	-	-	-
	-	-	1150	1151	-	$\nu_a(PO_3)$1153	-	-
	-	-	1124	1124	-	$\nu_a(PO_3)$1128	-	-
	-	1060	1062	1063	-	$\nu_s(PO_3)$1068	-	-
	-	-	-	1028	-	-	ν_3 1028	ν_3 1023
	1014	1014	-	-	$\nu_s(PO_3)$	-	-	-
	-	-	1004	1005	-	$\nu_a(PO_3)$1009	-	-
	996	996	-	-	$\nu_s(PO_3)$	-	-	-
	-	-	965	965	-	ν_a POP 968	-	-
	-	-	951	951	-	-	ν_1 951	ν_1 951
700-800		763	764	764	-	ν_s POP 768	-	-
	746	746	-	-	P-F	-	-	-
300-700	-	-	621	622	-	δ (PO_2) 623	-	-
			609	609	-	δ (PO_2) 609	-	-
	-	-	-	581	-	-	ν_4 581	ν_4 580
	571	570			δ (PO_3)	δ (PO_2) 571	-	-
	-	-	568	568	-	-	ν_4 573	ν_4 572
	556	556	554	554	δ (PO_3)	δ (PO_2) 556	-	-
	539	539	-	-	δ (PO_3)	-	-	-
	-	-	528	528	-	δ (PO_2) 531	-	-
	518	518	-	-	δ (PO_3)	-	-	-
	-	491	493	493	-	δ (PO_2) 493	-	-
	-	-	445	445	-	δ (PO_2) 447	ν_2 442	ν_2 442
	-	-	-	442	unassigned	-	-	-
	410	410	-	-	ρ (PO_3)	-	-	-
	380	380	-	-	ρ (PO_3)	-	-	-
	372	372	-	-	ρ (PO_3)	-	-	-
	-	-	354	354	-	δ (PO_2) 360	-	-
	-	-	327	327	-	δ (PO_2) 336	-	-

The identification of the phases present in each of the Raman spectra was in agreement with those suggested from PXRD patterns. However, no vibrations owing to the presence of SrF_2 could be identified in the spectra, including in the spectra of the samples heated to both 200°C and 300°C, where the presence of SrF_2 is most prominent in the PXRD patterns.

Upon heating to 200 °C, the Raman spectrum looks almost identical to that of the parent $SrPO_3F$ material. Additional vibrations become apparent at 300 °C, which correspond to α-$Sr_2P_2O_7$ as suggested from the PXRD patterns. The co-existence of $SrPO_3F$ and α-$Sr_2P_2O_7$ are observed until 500 °C, at which point the vibration relating to the P-F bond is no longer apparent, suggesting total decomposition of the original fluorophosphate material. Simultaneously, the formation of an apatitic phase becomes evident in the Raman spectrum, with vibrations occurring at 951 cm^{-1} and 445 cm^{-1} corresponding to the v_1 and v_2 vibrations of an apatitic material. The v_3 and v_4 modes become apparent upon further heating, as these vibrations are present in the spectra for the sample heated to 750 °C. Although the presence of fluorine has been confirmed in the 750 °C sample, as with PXRD, it is inconclusive as to whether the apatite material is solely fluorapatite based on the vibrations observed in the Raman spectrum as the similarity between the frequencies of a fluorine containing and non-fluorine containing apatite material are very similar.

The assignments of the vibrations which relate to the apatite phase are very similar for a fluorine containing and a non-fluorine containing strontium apatite material. The main difference appears to be position of the v_3 band, with the fluorine containing apatite lying at a lower frequency compared to the non fluorine containing apatite (table 3.12).

However, it appears inconclusive as to whether the apatite phase is solely fluorapatite or a mixture of the two apatite materials.

3.3.7 Fluorine Sensitive Electrode Measurements

Although the presence of fluorine has been proven in both strontium fluorophosphate systems, a quantitative analysis for the fluorine content within each sample could not be achieved. Attempts were made to quantify the fluorine content by using a fluorine sensitive electrode. This required the sample to be soluble in a solvent with a pH between 5 and 7 to avoid the formation of complexes with hydrogen ions and interference from hydroxyl ions. As the electrode only has the capability of measuring the concentration of F^- ions in solution, it requires full dissociation of the fluoride from the complex (in this case PO_3F^{2-}) to obtain an accurate concentration of fluoride in solution. Based on these criteria, attempts were made to prepare a range of fluorophosphate samples of: $SrPO_3F{\cdot}H_2O$, $SrPO_3F$, $CaPO_3F{\cdot}2H_2O$ and Na_2PO_3F. Initial attempts were made to dissolve a known amount of the samples in water, but only the sodium analogue proved to be soluble. Dissolution of the strontium and calcium fluorophosphates in a dilute KOH solution was possible but caused the pH of the solutions to be less than 5.

3.4 Conclusions

Two new strontium fluorophosphate materials, $SrPO_3F{\cdot}H_2O$ and $SrPO_3F$ have been successfully synthesised and the formation of these products were found to be strongly influenced by the reaction temperature, with the anhydrous phase found to be isolated at higher temperatures compared to the hydrated phase. Both materials were structurally characterised using NPD, Raman and X-ray fluorescence Spectroscopy

which all confirmed the expected stoichiometry of these materials. Qualitative evidence for the presence of fluorine in both materials was obtained from Raman spectroscopy, through the identification of the P-F bond, and by XRF spectroscopy, from the emission signal obtained from the F Kα_1 line. Upon investigating the local structure with solid state NMR, the results proved to be more complicated than first thought, with both nuclei of interest ^{31}P and ^{19}F indicating multiple environments present for each nucleus in both systems as oppose to one phosphorus and fluorine environment suggested in the structural model. From this, it was suggested that both materials contained some impurities which were likely to be present as an amorphous entity which would explain why they were not detected by PXRD and NPD. The amorphous content for both $SrPO_3F{\cdot}H_2O$ and $SrPO_3F$ was estimated by performing a two phase refinement with each strontium fluorophosphate material and an added amounted of highly crystalline TiO_2. Both materials were subsequently confirmed to contain an amorphous component close that suggested from the NMR results of 21 wt % and 25 wt % for the hydrated and the anhydrous phase respectively. Decomposition of the fluorophosphate had also been inferred from the NMR results due to the presence of a small amount of SrF_2 present in ^{19}F NMR spectra in the as synthesised materials, despite the temperature of the reactions being relatively low. The composition of the amorphous material has yet to be confirmed but it most likely to match that of the crystalline components given that the overall Sr:P molar ratio is 1, An investigation into the stability of these materials has shown that the hydrated phase is not stable after dehydration at 100 °C, with the loss of water causing a collapse of the structure. However, the anhydrous phase remains stable to slightly higher temperatures of ~ 150 °C, where upon the decomposition is first evident from the presence of SrF_2 in the diffraction patterns. However, some SrF_2 may

be present following synthesis and not solely as a result of the decomposition, as heating may just have improved the crystallinity of SrF_2 making it more visible in the diffraction data. The decomposition products were largely in agreement with the few previously reported in the literature for other fluorophosphate materials and were identified as being α-$Sr_2P_2O_7$ and an apatitic phase suggested as being either $Sr(PO_4)_3F$ or $Sr(PO_4)_3OH$,[5] but the precise identity of the apatitic material is currently unknown.

3.5 References

1. W. Lange, Dentifrice Preparation containing sodium monofluorophosphate, *Great Britain Pat.*, 1965.
2. J. D. P.D.Delmas, F. Deboeuf, M.C.Chapuy, P.J.Meunier, *Journal of Bone and Mineral Research*, 1990, **5**, 143-147.
3. F. José López, *Current Opinion in Chemical Biology*, 2000, **4**, 383-393.
4. A. Perloff, *Acta Crystallographica Section B-Structural Crystallography and Crystal Chemistry*, 1972, **B 28**, 2183-2191.
5. D. H. Menz, K. Heide, C. Kunert, C. Mensing and L. Kolditz, *Zeitschrift Fur Anorganische Und Allgemeine Chemie*, 1986, **541**, 191-197.
6. P. L. JCPDS International centre for diffraction data, Swarthmore, Pensylvania, PA 19081, USA 1990,
7. R. Shirley, The Crysfire 2002 System for Automatic Powder Indexing: User's Manual", The Lattice Press, 41 Guildford Park Avenue, Surrey GU2 7NL, 2002
8. C. Greaves, D-SPACE, The School of Chemistry, University of Birmingham, 1982
9. CELL, based on the original code by M.F.Pye, I.C.L, Oxford
10. J. Laugier and B. Bochy, http://www.ccp2014.ac.uk/tutorial/lmgp/ LMGP Suite of Programs, Grenoble, France, 2000.
11. ICSD:http://www.cds.dl.ac.uk/cds/datasets/crys/icsd/llicsd.html.
12. O. Bars, J. Y. Lemarouille and D. Grandjean, *Acta Crystallographica Section B-Structural Science*, 1977, **33**, 3751-3755.
13. D. F. Mullica, W. O. Milligan, D. A. Grossie, G. W. Beall and L. A. Boatner, *Inorganica Chimica Acta-F-Block Elements Articles and Letters*, 1984, **95**, 231-236.
14. M. Weil, M. Puchberger, E. Fuglein, E. J. Baran, J. Vannahme, H. J. Jakobsen and J. Skibsted, *Inorganic Chemistry*, 2007, **46**, 801-808.
15. M. Weil, M. Puchberger and E. J. Baran, *Inorganic Chemistry*, 2004, **43**, 8330-8335.
16. H. A. Prescott, S. I. Troyanov and E. Kemnitz, *Journal of Solid State Chemistry*, 2001, **156**, 415-421.
17. J. Durand, L. Cot and J. L. Galigne, *Acta Crystallographica Section B-Structural Science*, 1974, **B 30**, 1565-1569.
18. O. Bars, J. Y. Le Marouille and D. Grandjean, *Acta Crystallographica Section B*, 1981, **37**, 2143-2147.
19. E. K. H.A. Prescott, S.I.Troyanov, *Zeitschrift Fur Kristallographie*, 2000, **215**, 240.
20. M. Zeibig, B. Wallis, F. Mowius and M. Meisel, *Zeitschrift Fur Anorganische Und Allgemeine Chemie*, 1991, **600**, 231-238.
21. I. D. Brown and D. Altermatt, *Acta Crystallographica Section B-Structural Science*, 1985, **41**, 244-247.
22. I. D. Brown, *Chemical Reviews*, 2009, **109**, 6858-6919.
23. R. D. Shannon and C. T. Prewitt, *Acta Crystallographica Section B*, 1969, **25**, 925-946.
24. R. D. Shannon, *Acta Crystallographica Section A*, 1976, **32**, 751-767.
25. H. Siebert, *Anwendungen der Schwingungsspektroskopie in der Anorganischen Chemie; Springer-Verlag: Berlin*, 1966.
26. K. Heide, D. H. Menz, C. Schmidt and L. Kolditz, *Zeitschrift Fur Anorganische Und Allgemeine Chemie*, 1985, **520**, 32-38.
27. B. C. Cornilsen and R. A. Condrate, *Journal of Solid State Chemistry*, 1978, **23**, 375-382.

28. M. D. O'Donnell, Y. Fredholm, A. de Rouffignac and R. G. Hill, *Acta Biomaterialia*, 2008, **4**, 1455-1464.
29. C. Meegoda, C. E. Bonner, G. Loutts, S. Stefanos and G. E. Miller Iii, *Journal of Luminescence*, 1999, **81**, 101-109.

CHAPTER 4

Cation and Anion Substitutions within Strontium Fluorophosphate Systems

4.1 Introduction

The formation of two new strontium fluorophosphate systems has been achieved and described in chapter 3 and both systems were found to adopt known structure types, $MM'XO_4 \cdot H_2O$ for $SrPO_3F \cdot H_2O$ and monazite for $SrPO_3F$. Monazite is an important structure type, particularly for rare earth phosphates. The stability of monazite has been extensively studied by investigating the substitutional capabilities of the structure, largely through cationic substitutions with the reported incorporation of monovalent, divalent and tetravalent cations into the structure.[1] Further compositional changes within the system have been achieved via anionic substitutions, by changing the XO_4 tetrahedral unit to other tetrahedral units, such as AsO_4,[2-5] VO_4[6-7] and CrO_4[8-9]. The manipulation of the monazite structure has been shown to change the chemical properties of the material and make monazite a suitable candidate for many applications such as a matrix for radioactive waste material,[10-11] coatings,[12-13] laser, light emitters and luminophors[14-16] and ionic conductors.[17-19] Monazite systems normally consist of trivalent cations as these systems are found to be more commonly adopted by rare earth phosphate materials and few other systems. Therefore the isolation in this work of a purely divalent monazite system is rare and offers an opportunity to further expand the range of monazite compositions. The key aspect of this work is the incorporation of the

fluorophosphate ion, PO_3F^{2-}, as a replacement for the generic phosphate unit from which monazite is usually formed. In doing so, the charge of the system is reduced and must be compensated for through the use of a divalent counterion (in this case Sr^{2+}). The ability to manipulate the composition of well known materials has ultimately led to the formation of two new materials $SrPO_3F{\cdot}H_2O$ and $SrPO_3F$, both of which contain fluorine within the system which is advantageous if considering these materials as potential candidates in biomaterial applications.

The focus of this chapter will centre on determining the stability of both strontium fluorophosphate systems towards doping. Compositional variations of both structures will be explored, primarily via cationic substitutions using other alkaline earth metals and lanthanides (Ca^{2+}, Ba^{2+} and Eu^{2+}) for potential applications of bioceramic materials (Ca^{2+}) and optical material (Eu^{2+}). Also, a co-precipitation reaction will be considered in an attempt to simultaneous cation and anion substitute the monazite structure $SrPO_3F$ with $LaPO_4$. The drive for such a material is the potential to develop an improved proton conductor material.[17-19] By such substitutions the compositional variability of the monazite structure will be explored and such knowledge will allow for new monazite compositions to be isolated and comparisons made with known monazite systems to better understand the potential of this structure type.

4.2 Synthesis of chemically modified strontium fluorophosphate systems

A range of fluorophosphates materials were synthesised and characterised following the experimental procedure described in section 2.1.1 with the modification that for the $Sr_{1-x}La_x(PO_3F)_{1-x}(PO_4)_x$ phases, a 1 M cation containing solution was used.

The target materials were achieved by modifying the cation and anion solutions to contain the appropriate quantities of the constituent elements required, as described in table 4.1.

Table 4.1: Summary of reaction conditions employed for the synthesis of various mixed metal strontium phosphates

Target Material	x	Cation Containing Solution	Anion Containing Solution	Temperature of reaction (°C)	Synthesis Success
$Sr_{1-x}Ca_xPO_3F$	0.1	$SrCl_2 \cdot 6H_2O$:$CaCl_2$	Na_2PO_3F	80	✓
	0.2	$SrCl_2 \cdot 6H_2O$:$CaCl_2$	Na_2PO_3F	80	✓
	0.3	$SrCl_2 \cdot 6H_2O$:$CaCl_2$	Na_2PO_3F	70	✓
	0.4	$SrCl_2 \cdot 6H_2O$:$CaCl_2$	Na_2PO_3F	70	✓
$Sr_{1-x}Ba_xPO_3F$	0.01	$SrCl_2 \cdot 6H_2O$:$BaCl_2 \cdot 2H_2O$	Na_2PO_3F	75, 70	×
	0.02	$SrCl_2 \cdot 6H_2O$:$BaCl_2 \cdot 2H_2O$	Na_2PO_3F	75, 70	×
	0.03	$SrCl_2 \cdot 6H_2O$:$BaCl_2 \cdot 2H_2O$	Na_2PO_3F	75, 70	✓
	0.1	$SrCl_2 \cdot 6H_2O$:$BaCl_2 \cdot 2H_2O$	Na_2PO_3F	80	✓
	0.2	$SrCl_2 \cdot 6H_2O$:$BaCl_2 \cdot 2H_2O$	Na_2PO_3F	80, 75	×
	0.3	$SrCl_2 \cdot 6H_2O$:$BaCl_2 \cdot 2H_2O$	Na_2PO_3F	80, 75	×
$Sr_{1-x}Eu_xPO_3F$	0.05	$SrCl_2 \cdot 6H_2O$: $EuCl_2$	Na_2PO_3F	80	×
	0.1	$SrCl_2 \cdot 6H_2O$: $EuCl_2$	Na_2PO_3F	75	×
	0.1	$SrCl_2 \cdot 6H_2O$: $EuCl_2$ (0.03M)	Na_2PO_3F (0.03M)	75	×
$Sr_{1-x}La_x(PO_3F)_{1-x}(PO_4)_x$	0.1	$SrCl_2 \cdot 6H_2O$:$La(NO_3)_2 \cdot H_2O$	Na_2PO_3F:$NH_4H_2PO_4$	80, 50	✓
	0.2	$SrCl_2 \cdot 6H_2O$: $La(NO_3)_2 \cdot H_2O$	Na_2PO_3F:$NH_4H_2PO_4$	80, 50	✓
	0.3	$SrCl_2 \cdot 6H_2O$: $La(NO_3)_2 \cdot H_2O$	Na_2PO_3F:$NH_4H_2PO_4$	80, 50	×
	0.4	$SrCl_2 \cdot 6H_2O$: $La(NO_3)_2 \cdot H_2O$	Na_2PO_3F:$NH_4H_2PO_4$	80, 50	×
	0.5	$SrCl_2 \cdot 6H_2O$: $La(NO_3)_2 \cdot H_2O$	Na_2PO_3F:$NH_4H_2PO_4$	80, 50	×
	0.6	$SrCl_2 \cdot 6H_2O$: $La(NO_3)_2 \cdot H_2O$	Na_2PO_3F:$NH_4H_2PO_4$	80, 50	×
	0.7	$SrCl_2 \cdot 6H_2O$: $La(NO_3)_2 \cdot H_2O$	Na_2PO_3F:$NH_4H_2PO_4$	80, 50	×
	0.8	$SrCl_2 \cdot 6H_2O$: $La(NO_3)_2 \cdot H_2O$	Na_2PO_3F:$NH_4H_2PO_4$	80, 50	×
	0.9	$SrCl_2 \cdot 6H_2O$: $La(NO_3)_2 \cdot H_2O$	Na_2PO_3F:$NH_4H_2PO_4$	80, 50	×
	1	$La(NO_3)_2 \cdot H_2O$	$NH_4H_2PO_4$	80, 50	×
$Sr_{1-x}Ca_xPO_3F \cdot H_2O$	0.1	$SrCl_2 \cdot 6H_2O$:$CaCl_2$	Na_2PO_3F	40	✓
	0.2	$SrCl_2 \cdot 6H_2O$:$CaCl_2$	Na_2PO_3F	40	✓
	0.3	$SrCl_2 \cdot 6H_2O$:$CaCl_2$	Na_2PO_3F	40	✓
	0.5	$SrCl_2 \cdot 6H_2O$:$CaCl_2$	Na_2PO_3F	40	✓
	0.6	$SrCl_2 \cdot 6H_2O$:$CaCl_2$	Na_2PO_3F	40	✓
	0.7	$SrCl_2 \cdot 6H_2O$:$CaCl_2$	Na_2PO_3F	40	✓

4.3 Results and Discussion

4.3.1 Substitutions in $SrPO_3F$ (Monazite)

4.3.1.1 $Sr_{1-x}Ca_xPO_3F$

Materials from the $Sr_{1-x}Ca_xPO_3F$ series where $0<x<0.4$ were successfully synthesised with the monazite structure. This was confirmed using PXRD. Up to x = 0.2 phases were formed using the reaction temperature (80 °C) that was used to synthesise the parent monazite phase, $SrPO_3F$. This temperature proved not to be suitable for the formation of both x = 0.3 and 0.4 members as poorly crystalline versions of monazite were observed. However, a significant improvement in these phases was achieved when the reaction temperature was lowered to 70 °C. Attempts to synthesise x = 0.5 at both 70 °C and 80 °C were unsuccessful and yielded the formation of a very poorly crystalline material resembling monazite. Attempts to further increase the level of calcium substituted beyond 50 mol % yielded products that no longer favoured the monazite structure but instead adopted the $CaPO_3F \cdot 2H_2O$ structure.[20]

A comparison of the PXRD patterns obtained for $0 \leq x \leq 0.4$ (see figure 4.1) shows a number of significant trends. Firstly, the crystallinity of the materials significantly decreases as x increases as evidenced by increasing peak broadness. Also, importantly, the substitution of Ca^{2+} was supported by decreases in the unit cell parameters causing a shift in the peak positions. As a result of the substantial decrease in the crystallinity of the calcium doped systems, particularly with the x = 0.3 and 0.4 members, the intensity of the PXRD data were normalised to allow a direct comparison of the $Sr_{1-x}Ca_xPO_3F$ systems to be made.

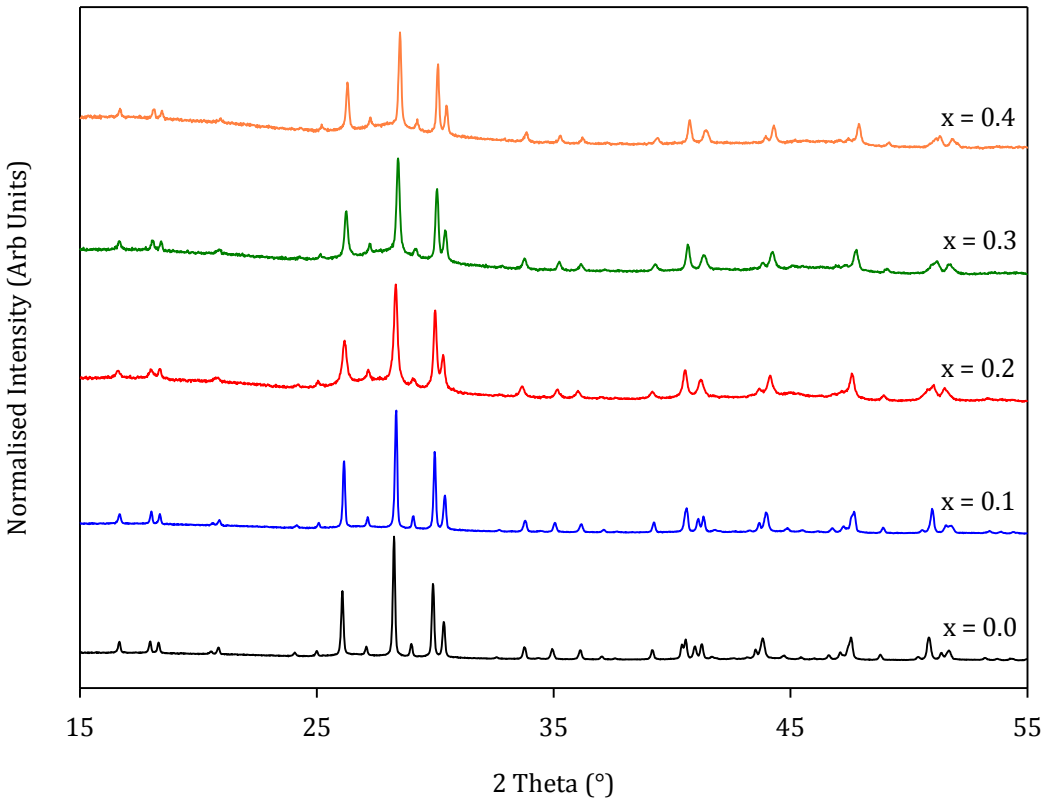

Figure 4.1: A stack plot of the PXRD patterns obtained from members of the $Sr_{1-x}Ca_xPO_3F$ series (x = 0-0.4)

A comparison of the PXRD patterns for both low (x = 0.1) and high levels (x = 0.4) of Ca^{2+} shows an apparent increase in the background of the x = 0.4 system (figure 4.2 a and b) which is indicative of the presence of increased levels of amorphous materials found in addition to the parent monazite phase (discussed in section 3.2.5.7).

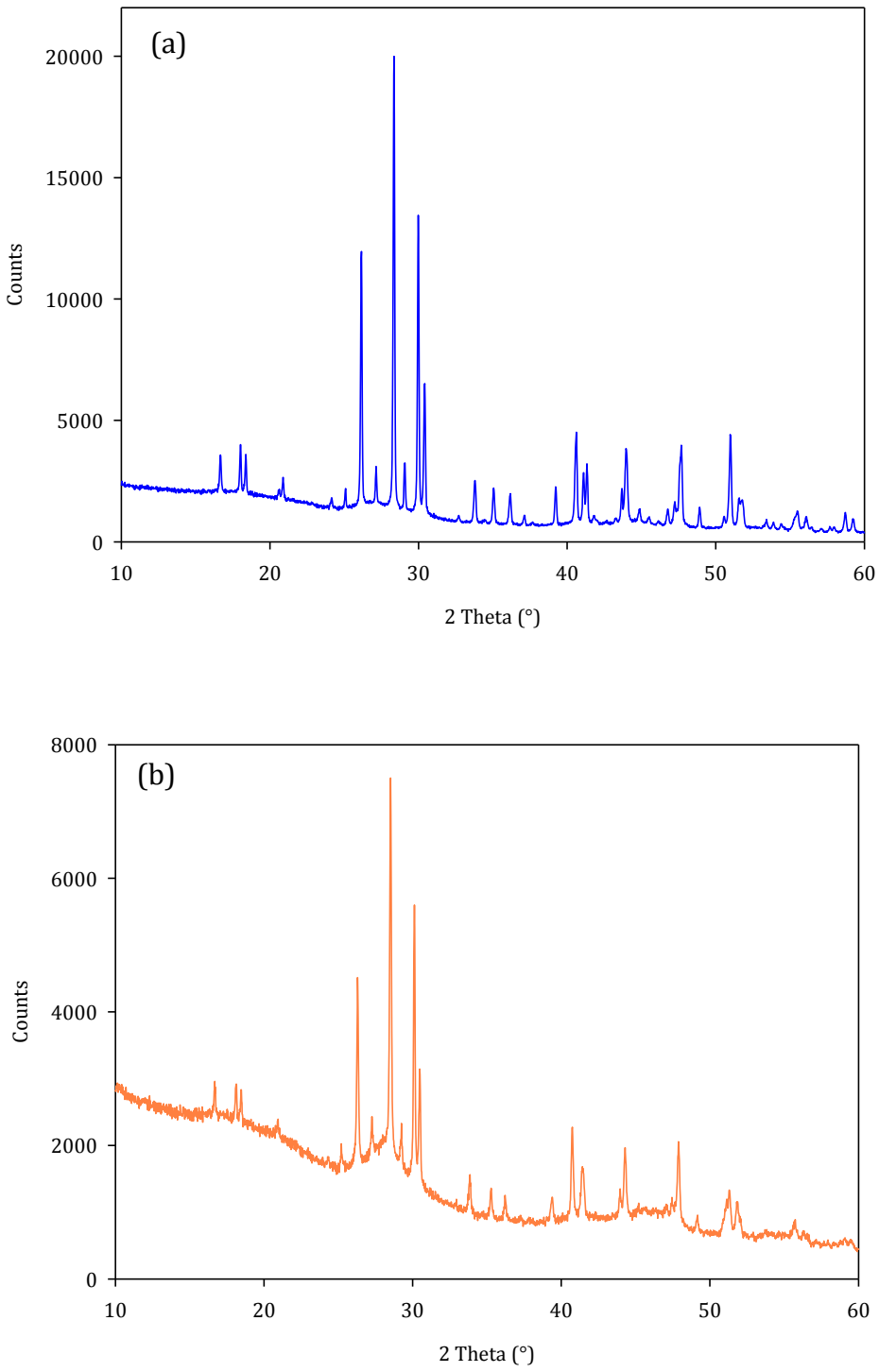

Figure 4.2: PXRD patterns of the x = 0.1 (a) and x = 0.4 (b) systems from the $Sr_{1-x}Ca_xPO_3F$ series

The level of amorphous component present within each member of the $Sr_{1-x}Ca_xPO_3F$ series was estimated by a two phase refinement following the addition of a known

amount of highly crystalline material (TiO_2). The resulting phase fractions were used to estimate the amount of amorphous material present within each sample (as described previously). The refinements for each member of the series can be found in appendix 2 section 2.1.1. Table 4.2 shows the calculated percentage of amorphous component for each member of the series. The full tabulated data of results obtained is shown in appendix 2 section 2.1.1. The level of amorphous material present in members of the $Sr_{1-x}Ca_xPO_3F$ system was found to increase as the level of incorporated Ca^{2+} increased, particularly for systems with Ca^{2+} content of $x \geq 0.2$, where over 50 weight % of the material was suggested as being amorphous.

Table 4.2: Calculated amorphous content obtained from the two phase Rietveld refinements of the $Sr_{1-x}Ca_xPO_3F$ series and TiO_2

	Calcium Doped Systems				
	$SrPO_3F$	$Sr_{0.9}Ca_{0.1}PO_3F$	$Sr_{0.8}Ca_{0.2}PO_3F$	$Sr_{0.7}Ca_{0.3}PO_3F$	$Sr_{0.6}Ca_{0.4}PO_3F$
Mass Monazite phase (g)	1.00	0.30	0.30	0.30	0.30
Mass of TiO_2 (g)	0.55	0.18	0.09	0.09	0.06
Calculated Amorphous Content (wt %)	25	27	56	53	59

Rietveld refinements of the NPD and PXRD data were performed on all members of the $Sr_{1-x}Ca_xPO_3F$ series. Whilst NPD data were obtained, they were not of a sufficiently high quality to allow accurate determination of the occupancies of both Ca^{2+} and Sr^{2+} within the $Sr_{1-x}Ca_xPO_3F$ system (figure 4.3). The high background and poor crystallinity limits the amount of information which can reliably be extracted from these refinements. As a result, it has not been possible to refine the Sr;Ca ratio, these have been fixed at stoichiometric values to aid the stability of the refinement. The Rietveld refinements for all other members of the $Sr_{1-x}Ca_xPO_3F$ series and the refined parameters

of the NPD refinements can be found in appendix 2 section 2.1.2. Therefore, the discussion regarding the lattice parameters and structure are based on the results from the PXRD refinements.

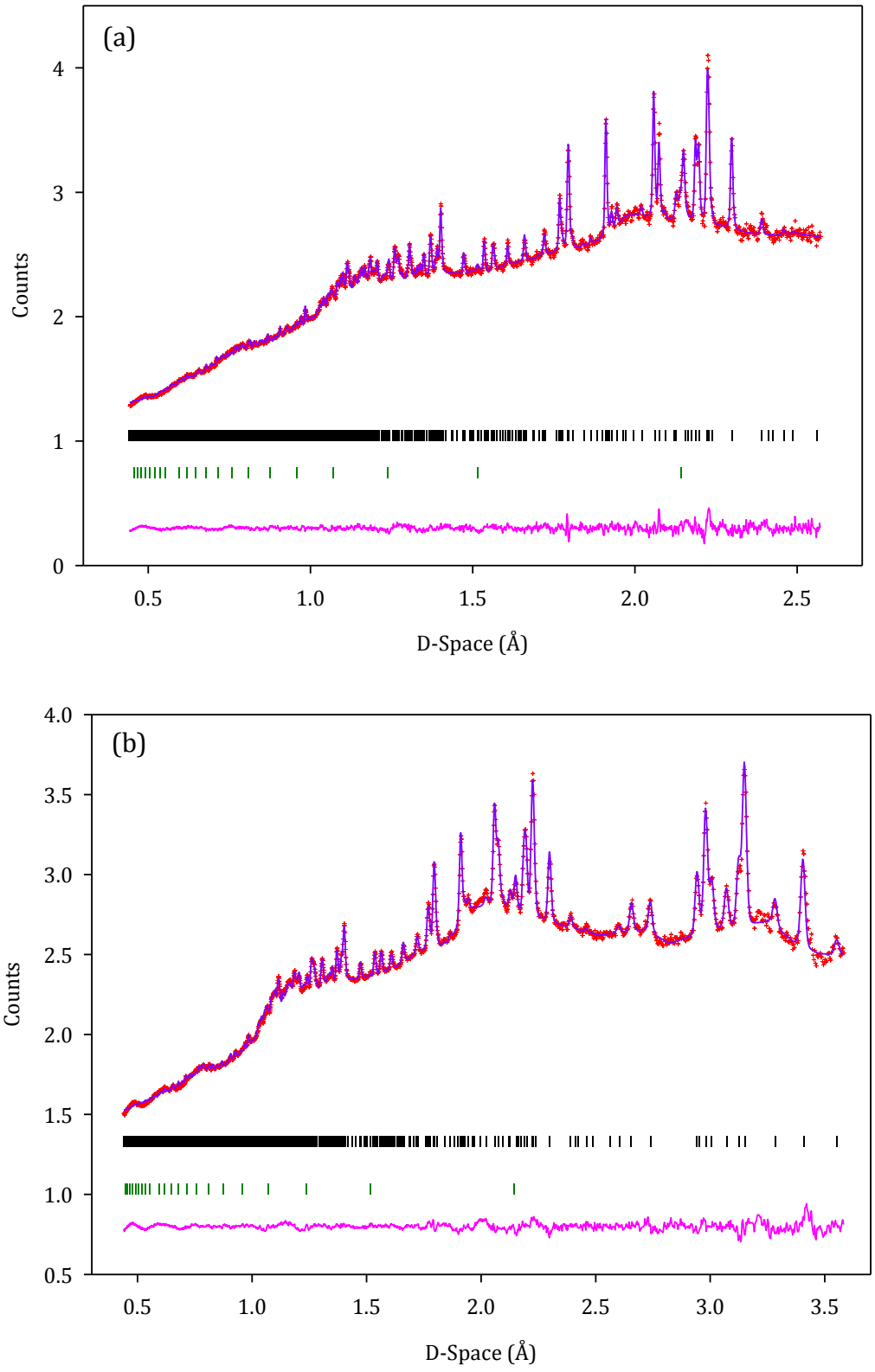

Figure 4.3: Final observed (red), calculated (purple) and difference profiles (pink) of the NPD refinement of $Sr_{0.8}Ca_{0.2}PO_3F$ (a) back scattering bank (b) 90° bank. Reflections positions for $Sr_{0.8}Ca_{0.2}PO_3F$ and the impurity from the vanadium can are shown as vertical tick marks (black and green respectively)

The plots obtained from the PXRD refinements of a low and high calcium doped systems (x = 0.1 and x = 0.4) are shown in figures 4.4 a and b respectively. Refinements for the x = 0.2 and 0.3 systems are shown in appendix 2 section 2.1.3.

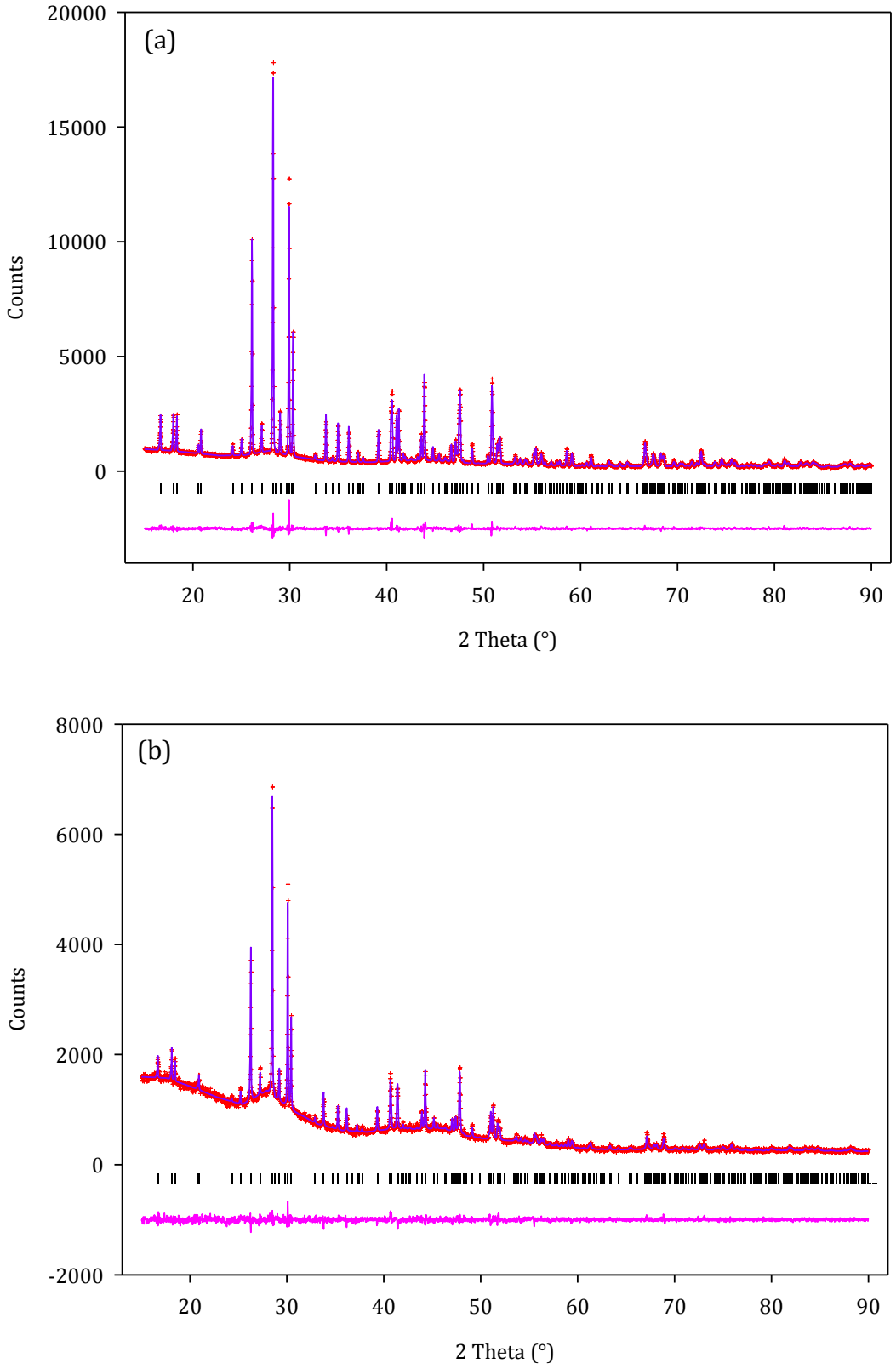

Figure 4.4: Final observed (red), calculated (purple) and difference profiles (pink) of the PXRD refinements of the x = 0.1 (a) and x = 0.4 (b) systems from the $Sr_{1-x}Ca_xPO_3F$ series. Reflection positions are shown as vertical tick marks (black)

For these refinements the temperature factors for all O/F positions were refined but constrained to be equivalent and the occupancies of both strontium and calcium were fixed to the stoichiometric values to aid the stability of the refinements. The refined lattice and structural parameters are shown in table 4.3 and 4.4 respectively.

From the refinements, it is clear that the substitution of increasing levels of Ca^{2+} into the structure causes a decrease in the lattice parameters and the unit cell volume (figure 4.5) of the system compared to that of the parent monazite phase $SrPO_3F$, (table 4.3). This linear decrease in volume with increasing calcium follows Vegard's law and is expected due to differences in the ionic radii of the two cations (1.31 and 1.18 Å for Sr^{2+} and Ca^{2+}respectively in IX-fold co-ordination).[21-22] This provides strong evidence that the substitution of Ca^{2+} into the structure has indeed been successful.

Table 4.3: Refined lattice parameters obtained from the PXRD refinements of the $Sr_{1-x}Ca_xPO_3F$ systems

$Sr_{1-x}Ca_xPO_3F$ Series					
	x = 0	**x = 0.1**	**x =0.2**	**x = 0.3**	**x = 0.4**
***a* (Å)**	6.9674(1)	6.9592(1)	6.9443(1)	6.9355(2)	6.9222(2)
***b* (Å)**	7.1154(1)	7.0990(1)	7.0859(2)	7.0631(2)	7.0447(2)
***c* (Å)**	6.7146(1)	6.70716(8)	6.6960(2)	6.6907(1)	6.6833(2)
***α, γ* (°)**	90	90	90	90	90
***β* (°)**	101.745(1)	101.882(8)	102.022(2)	102.114(1)	102.271(2)
Volume (Å³)	325.91(1)	324.254(8)	322.26(2)	320.45(1)	318.47(2)
χ^2	2.296	1.931	2.284	2.162	1.369
R_{wp} (%)	5.48	5.78	5.75	5.51	4.44

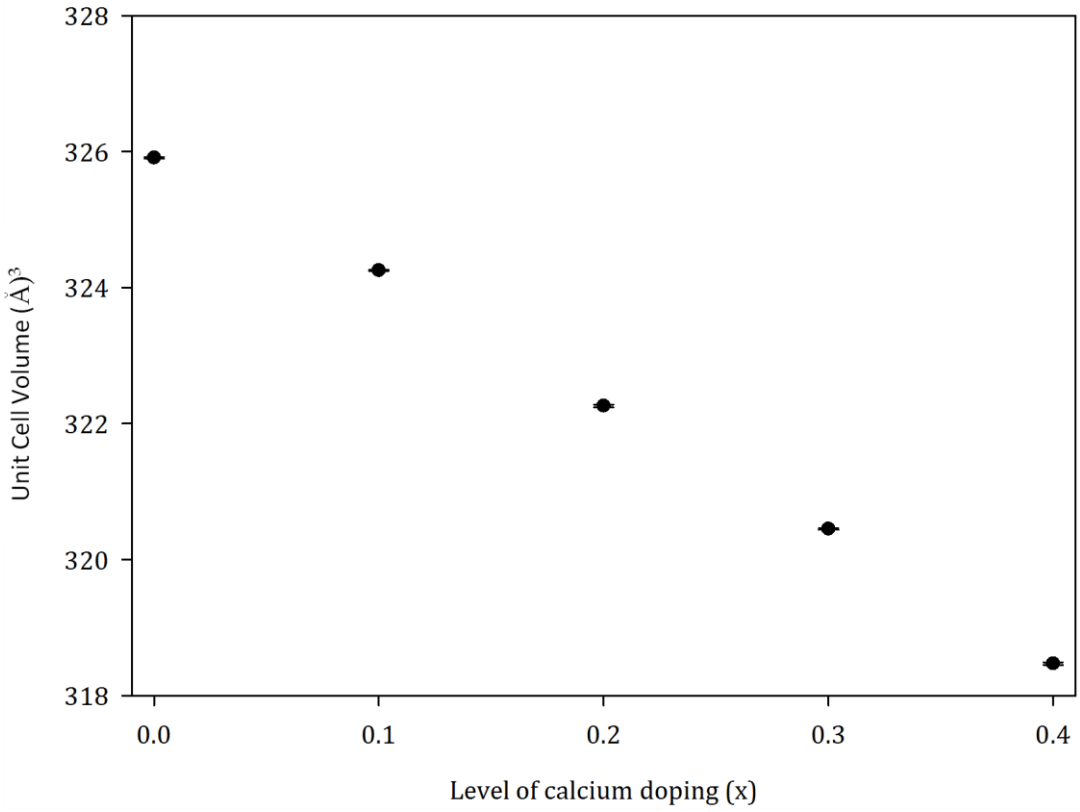

Figure 4.5: A plot of the volume for all members of the $Sr_{1-x}Ca_xPO_3F$ series

Table 4.4 shows the refined structural parameters for each member of the $Sr_{1-x}Ca_xPO_3F$ series. All of the refinements in this series are shown to have good fits, by producing χ^2 values < 2.5 and R_{wp} values less than 6 %, with only a few minor discrepancies with the peak shape on some of the more pronounced peaks.

Table 4.4: Refined structural parameters obtained from the PXRD refinements of the $Sr_{1-x}Ca_xPO_3F$ systems

			x = 0			
Atom	**Multiplicity**	**x**	**y**	**z**	**Uiso*100 (Å²)**	**Fractional Occupancy**
Sr	4	0.2698(2)	0.1384(2)	0.1032(2)	1.9(1)	1
P	4	0.3133(6)	0.1467(7)	0.6009(7)	2.6(1)	1
O1	4	0.252(1)	-0.0131(9)	0.451(1)	0.1(1)	1
O2	4	0.385(1)	0.318(1)	0.499(1)	0.1(1)	1
O3	4	0.450(1)	0.090(1)	0.799(1)	0.1(1)	1
F	4	0.121(1)	0.202(1)	0.673(1)	0.1(1)	1
			x = 0.1			
Atom	**Multiplicity**	**x**	**y**	**z**	**Uiso*100 (Å²)**	
Sr	4	0.2705(2)	0.1386(2)	0.1033(2)	1.8(1)	0.90
Ca	4	0.2705(2)	0.1386(2)	0.1033(2)	1.8(1)	0.10
P	4	0.3151(5)	0.1459(6)	0.6009(6)	2.9(1)	1
O1	4	0.255(1)	-0.0140(8)	0.449(1)	2.0(1)	1
O2	4	0.3846(8)	0.3278(9)	0.4956(9)	2.0(1)	1
O3	4	0.4512(9)	0.098(1)	0.799(1)	2.0(1)	1
F	4	0.1215(7)	0.2060(8)	0.6749(8)	2.0(1)	1
			x = 0.2			
Atom	**Multiplicity**	**x**	**y**	**z**	**Uiso*100 (Å²)**	
Sr	4	0.2698(4)	0.1390(4)	0.1034(4)	1.7(1)	0.8
Ca	4	0.2698(4)	0.1390(4)	0.1034(4)	1.7(1)	0.2
P	4	0.311(1)	0.150(1)	0.598(1)	4.7(3)	1
O1	4	0.257(2)	-0.014(2)	0.449(2)	3.3(3)	1
O2	4	0.390(2)	0.329(2)	0.501(2)	3.3(3)	1
O3	4	0.445(2)	0.090(3)	0.804(2)	3.3(3)	1
F	4	0.119(2)	0.205(2)	0.672(2)	3.3(3)	1
			x = 0.3			
Atom	**Multiplicity**	**x**	**y**	**z**	**Uiso*100 (Å²)**	
Sr	4	0.2707(3)	0.1403(4)	0.1036(4)	2.1(1)	0.7
Ca	4	0.2707(3)	0.1403(4)	0.1036(4)	2.1(1)	0.3
P	4	0.3138(9)	0.147(1)	0.602(1)	4.8(2)	1
O1	4	0.252(2)	-0.008(2)	0.440(2)	3.9(2)	1
O2	4	0.389(2)	0.326(2)	0.495(2)	3.9(2)	1
O3	4	0.454(2)	0.086(2)	0.803(2)	3.9(2)	1
F	4	0.118(2)	0.207(2)	0.672(2)	3.9(2)	1
			x = 0.4			
Atom	**Multiplicity**	**x**	**y**	**Z**	**Uiso*100 (Å²)**	
Sr	4	0.2698(5)	0.1400(5)	0.1029(6)	2.2(1)	0.6
Ca	4	0.2698(5)	0.1400(5)	0.1029(6)	2.1(1)	0.4
P	4	0.314(1)	0.1489(16)	0.602(2)	5.3(3)	1
O1	4	0.250(3)	-0.011(12)	0.442(3)	4.9(3)	1
O2	4	0.399(2)	0.324(2)	0.501(2)	4.9(3)	1
O3	4	0.450(2)	0.080(2)	0.804(3)	4.9(3)	1
F	4	0.113(2)	0.205(2)	0.674(2)	4.9(3)	1

At each increasing level of calcium doping, the temperature factors, particularly for the oxygens, tend to increase, in keeping with a system becoming increasingly disordered as the structure accommodates the inclusion of increasing levels of Ca^{2+}. This also results in the bond lengths and angles (table 2.7 in appendix 2 section 2.1.3) generated from the refinements deviating slightly from those of the parent system (x = 0). The refinements also show some uncertainty in the location of the fluorine atom due to variations in the location of the longest P-O/F bonds. However, this variation is not seen in the refinements of the NPD data, as this indicates that the longer bond (assigned as the P-F bond) is present in a specific direction, suggesting a degree of ordering of the fluorine on a specific site (see appendix 2 section 2.1.3). The presence of the P-F bond was also identified using Raman spectroscopy, with an observed vibration apparent in the region of 740-750 cm^{-1} for the monazite system (table 4.5).

Table 4.5: Assignments of the vibrations observed in the Raman spectra of the $Sr_{1-x}Ca_xPO_3F$ systems

$Sr_{1-x}Ca_xPO_3F$						
Region (cm^{-1})	**x = 0**	**x = 0.1**	**x = 0.2**	**x = 0.3**	**x = 0.4**	**Assignments**
1200-900	1162	1162	-	-	-	v_{as} (PO_3)
	1018	1016	1016	1017	1018	v_s (PO_3)
	996	998	998	998		
	-	894	898	896	894	unassigned
900-700	747	748	747	747	749	P-F
700-350	572	572	572	573	573	δ(PO_3)
	555	556	556	557	557	
	539	539	539	539	540	
	520	520	510	520	520	
	409	409	410	410	410	ρ(PO_3)
	381	382	381	380	380	
	372	372	373	376	376	

The positions of the other vibrations observed in the Raman spectra were in close agreement with those observed in the un-doped monazite system. However, an additional unidentified vibration at just below ~ 900 cm^{-1} became evident in the spectra

of the doped systems. The spectra for all members of the series can be found in appendix 2 section 2.1.4.

4.3.1.2 $Sr_{1-x}Ba_xPO_3F$

Initial attempts to incorporate Ba^{2+} into $SrPO_3F$ to form materials of composition $Sr_{1-x}Ba_xPO_3F$ were carried out with the level of Ba^{2+} up to x = 0.3. From the PXRD diffraction patterns of the products obtained, it was evident that the maximum level of x = 0.1 barium could be successfully substituted using the reaction conditions stated in section 4.2. At higher levels the samples no longer adopted the monazite structure (figure 4.6).

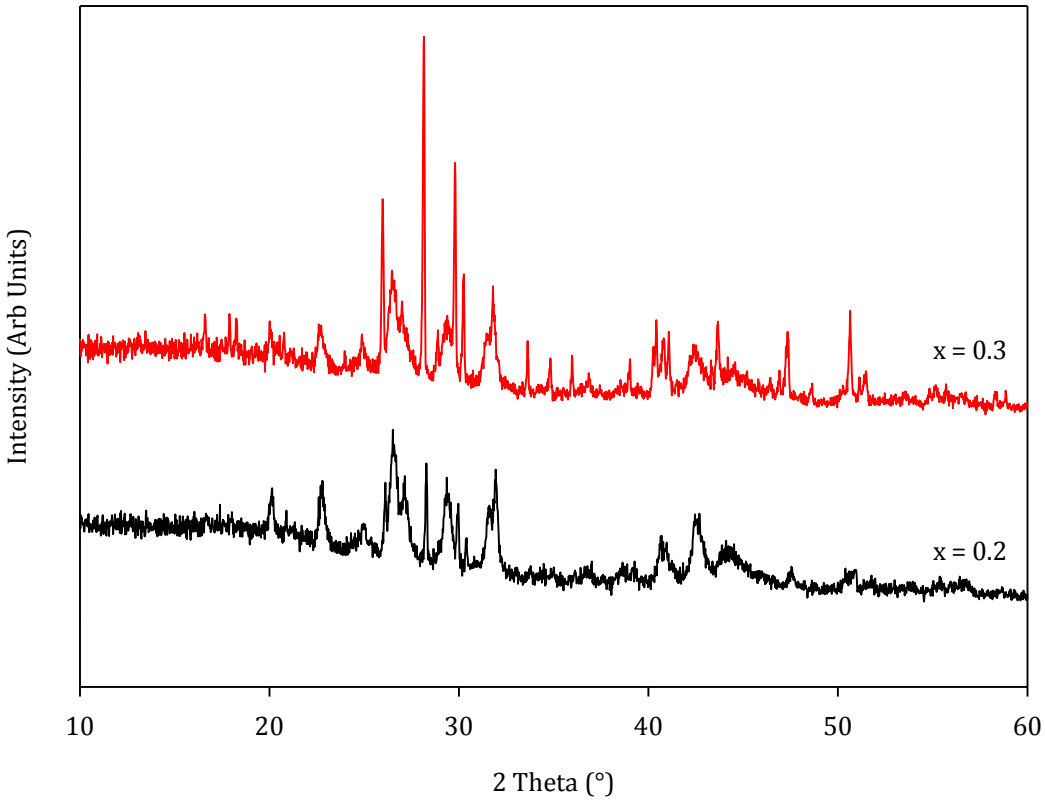

Figure 4.6: A stack plot of the PXRD patterns obtained from the attempting to synthesise members of the $Sr_{1-x}Ba_xPO_3F$ series (x = 0.2-0.3)

Evidence of the incorporation of small levels ($x < 0.1$) of Ba^{2+} into $SrPO_3F$ was provided by PXRD as the resulting products retain the parent monazite phase, but with an observable shift and broadening of the peaks (figure 4.7). Although both of these systems largely resembled the monazite structure, both contained some additional peaks due to the presence of barium containing impurity phases. Whilst the observed shift in the peak positions for these systems is indicative of barium substitution, the presence of these impurity phases indicates that it is unlikely that the maximum level of barium substitution has actually been achieved. In order to investigate this, Rietveld analyses were performed on both x = 0.0 and 0.1 systems.

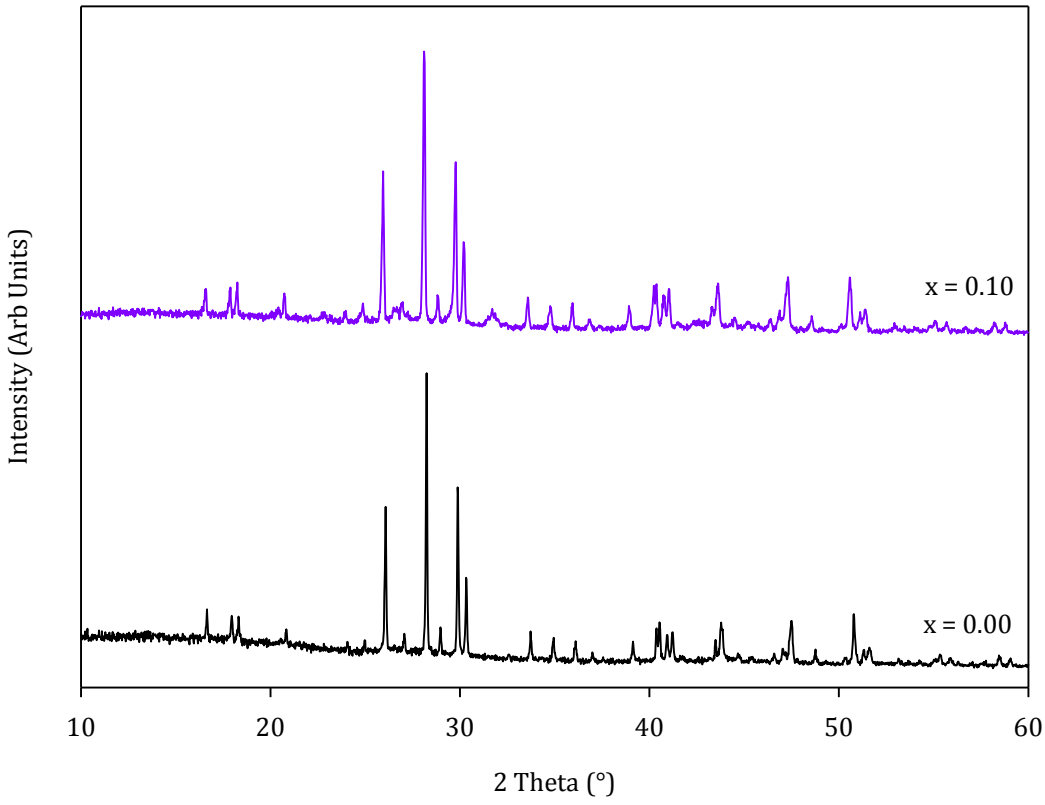

Figure 4.7: A stack plot of the PXRD patterns obtained from the successful synthesis of the x = 0 and 0.1 members of the $Sr_{1-x}Ba_xPO_3F$ series

For x = 0.1, it would be expected that the unit cell size would increase due to the observed shift in the peak positions to lower 2θ as a result of the partial substitution of a larger cation (in this case Ba^{2+}) on to the Sr^{2+} site in the monazite system (figure 4.8).

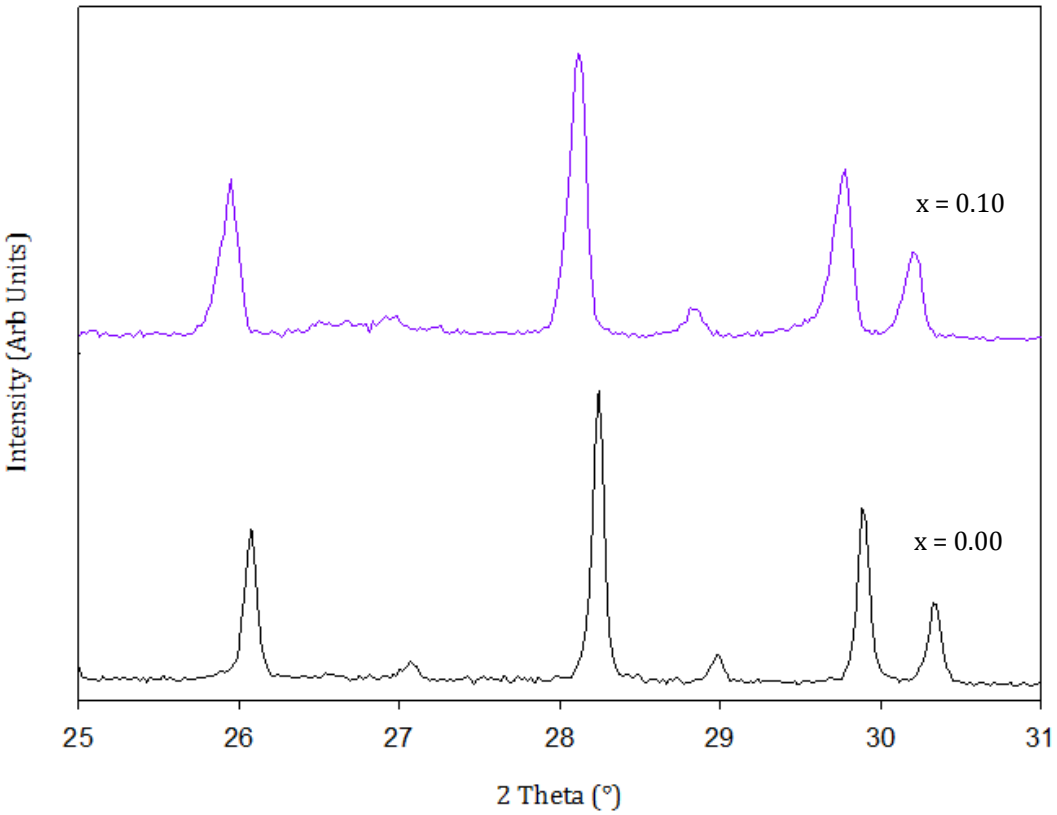

Figure 4.8: A stack plot of the PXRD patterns obtained from the successful synthesis of the x = 0 and 0.1 members of the $Sr_{1-x}Ba_xPO_3F$ series for the region of interest 25-31° 2θ

The Rietveld refinements presented in figures 4.9 a and b show a relatively good fit between observed and calculated data. However, there are some discrepancies with the peak shape and the clear presence of an additional, as yet unidentified, impurity phase which undoubtedly affect the quality of the fit. The refined structural parameters and a table of the bond lengths and angles for both x = 0 and x = 0.1 can be found in appendix 2 section 2.2.1. The results obtained from the Rietveld refinements of these systems

appear to show the small but expected increase in lattice parameters following inclusion of Ba^{2+} into monazite (table 4.6)

Table 4.6: Refined lattice parameters obtained from the PXRD refinements of the x = 0 and x = 0.1 members of the $Sr_{1-x}Ba_xPO_3F$ series

$Sr_{1-x}Ba_xPO_3F$		
	x = 0	**x = 0.1**
***a* (Å)**	6.9674(1)	6.9844(3)
***b* (Å)**	7.1154(1)	7.1281(3)
***c* (Å)**	6.7146(1)	6.7278(2)
***α, γ* (°)**	90	90
***β* (°)**	101.745(1)	101.762(8)
Volume (Å³)	325.91(1)	327.92(2)
χ^2	2.295	4.625
R_{wp} **(%)**	5.48	8.72

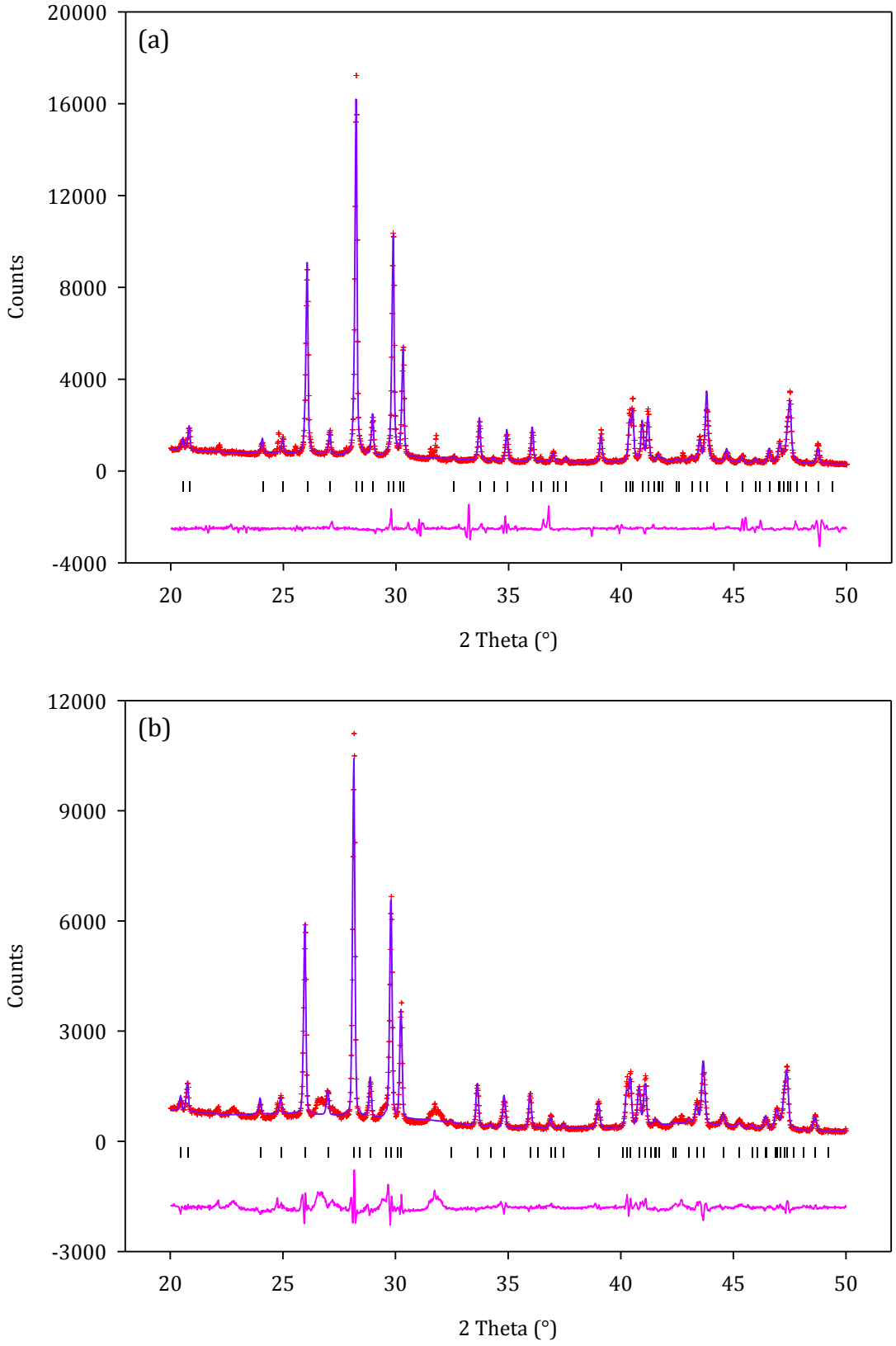

Figure 4.9: Final observed (red), calculated (purple) and difference profiles (pink) of the PXRD refinements of the x = 0.03 (a) and x = 0.01 (b) systems from the $Sr_{1-x}Ba_xPO_3F$ series. Reflection positions are shown as vertical tick marks (black)

Attempts to vary the Sr^{2+}/Ba^{2+} site occupancy to establish the relative content of these ions proved unsuccessful as the levels were too small to provide reliable results. However, the increase in the lattice parameters observed provides good evidence for the substitution of barium into the monazite lattice. The likely presence of Ba^{2+} impurities suggests the real level of barium incorporation is lower than stated.

4.3.1.3 $Sr_{1-x}La_x(PO_3F)_{1-x}(PO_4)_x$

The interest in the ionic conductivity properties of $LaPO_4$ doped with low levels of strontium prompted an investigation into the potential of fluorophosphate allowing much higher Sr^{2+} incorporation than the current ~ 3 mol %.[17] in these materials it is believed that the presence of strontium is responsible for the inclusion of OH^- into the monazite structure resulting in significant proton conductivity.[17-19] The aim of this investigation was to attempt to synthesise a higher Sr^{2+} content monazite phase to encourage greater OH^- formation and potential for improved conductivity. By isolating a mixed Sr^{2+}/La^{3+} – PO_3F^{2-}/PO_4^{3-} system, it was hoped that subsequent topotactic replacement of F^- with OH^- might be possible. From the synthetic method described in section 4.2, a simultaneous cation and anion substitution into the monazite $SrPO_3F$ was attempted using mixed cation and anion solutions, containing divalent and trivalent species.

Materials with composition $Sr_{1-x}La_x(PO_3F)_{1-x}(PO_4)_x$ were attempted across the full range $0 < x < 1$. From the PXRD patterns it was clear that only those where $x \leq 0.2$ resembled the monazite structure (figure 4.10), with the materials with $x > 0.3$ resembling that of hexagonal $LaPO_4$ (PDf- 00-004-0635). This was also confirmed by Raman spectroscopy (see appendix 2 section 2.3.1).

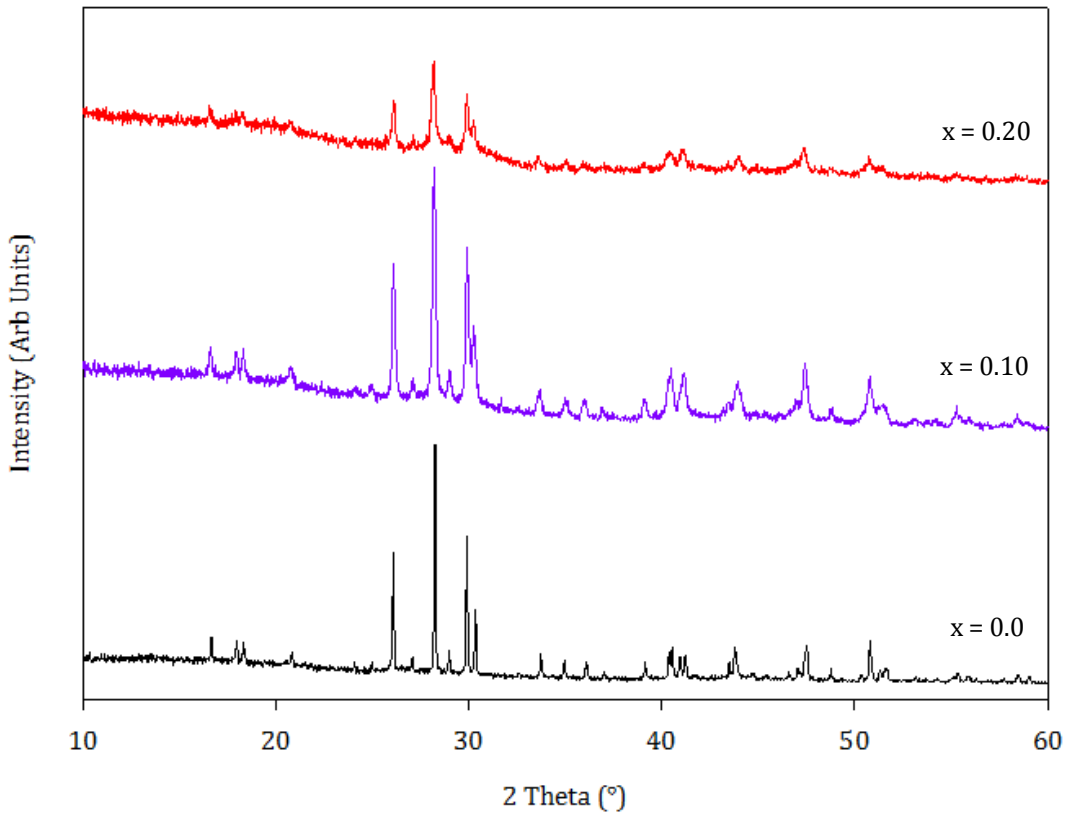

Figure 4.10: A stack plot of the PXRD patterns obtained from the successful synthesis of the x = 0.0, 0.1, 0.3 members of the $Sr_{1-x}La_x(PO_3F)_{1-x}(PO_4)_x$ series

It was evident from the PXRD patterns that as the proposed level of La^{3+} and PO_4^{3-} increased, the crystallinity reduced and an increased background would suggest that the level of amorphous content had significantly increased. Changes to the reaction temperatures were attempted in order to try to improve the crystallinity of these phases but no improvement was observed.

Upon closer inspection of the PXRD patterns in the region of 25-31° 2θ (figure 4.11), there was little evidence to support the incorporation of lanthanum and phosphate ions into the monazite structure, as no discernible shift in the peak positions were evident.

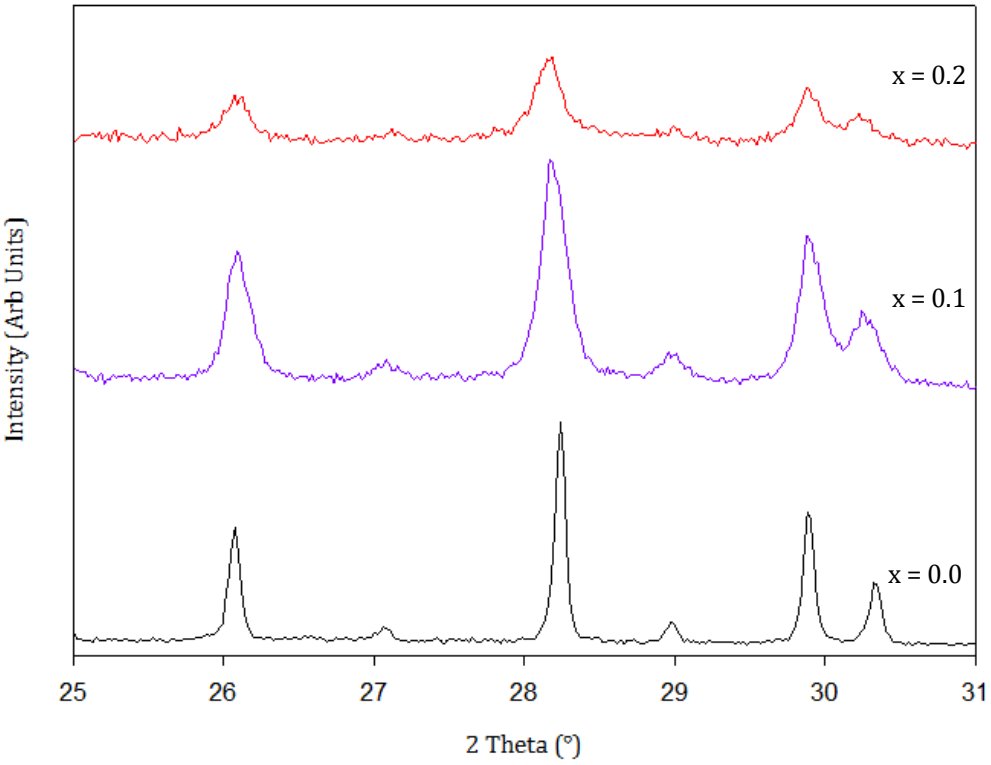

Figure 4.11: A stack plot of the PXRD patterns obtained from the successful synthesis of the x = 0.0, 0.1, 0.3 members of the $Sr_{1-x}La_x(PO_3F)_{1-x}(PO_4)_x$ series for the region of interest 25-31° 2θ

However, given the limited differences in ionic radii of the ions in this system (Sr^{2+}/La^{3+} and PO_4^{3-}/PO_3F^{2-} units), only very subtle changes in the unit cell parameters would likely be expected with such a substitution. The presence of broadening of some of the peaks may suggest some doping had occurred. In order to establish whether the successful substitution of La^{3+} had been achieved, a Rietveld refinements of the x = 0.1 system was performed. Although the x = 0.2 system was also seen to adopted the monazite structure, a Rietveld refinement to assess the structural changes of this system was not performed due to the poor crystallinity of this phase.

Figure 4.12 a and b shows the plots obtained from the NPD Rietveld refinement of the x = 0.1 system, with the refined atomic co-ordinates and selected bond lengths and bond angles shown in tables 4.7 and 4.8 respectively.

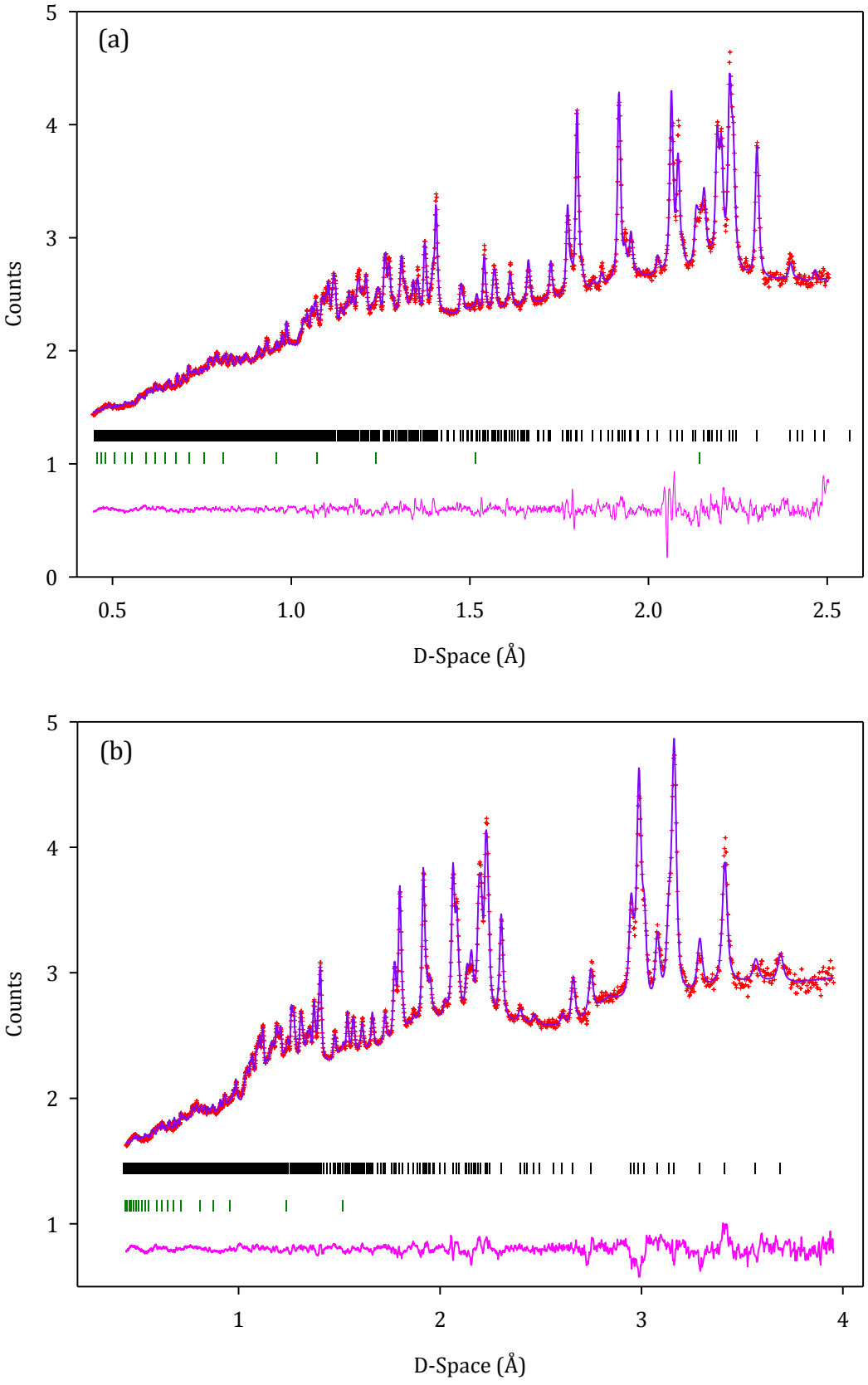

Figure 4.12: Final observed (red), calculated (purple) and difference profiles (pink) of the NPD refinement of $Sr_{0.9}La_{0.1}(PO_3F)_{0.9}(PO_4)_{0.1}$ (a) back scattering bank (b) 90° bank. Reflections positions for $Sr_{0.9}La_{0.1}(PO_3F)_{0.9}(PO_4)_{0.1}$ and the impurity from the vanadium can are shown as vertical tick marks (black and green respectively)

Table 4.7: Refined structural parameters obtained from the NPD refinements of the $Sr_{0.9}La_{0.1}(PO_3F)_{0.9}(PO_4)_{0.1}$ system

Atom	Multiplicity	x	y	z	Uiso*100(Å²)	Fractional Occupancy
Sr	4	0.2715(3)	0.1380(3)	0.0992(4)	0.65(4)	0.9
La	4	0.2715(3)	0.1380(3)	0.0992(4)	0.65(4)	0.1
P	4	0.3138(5)	0.1486(5)	0.6039(5)	0.70(5)	1
O1	4	0.2570(4)	-0.0650(4)	0.4534(4)	0.73(5)	1
O2	4	0.3878(4)	0.3194(5)	0.5010(4)	0.65(5)	1
O3	4	0.4514(6)	0.1022(6)	0.8033(5)	1.24(6)	1
F	4	0.1183(6)	0.2139(5)	0.6675(5)	1.82(7)	1

Table 4.8: Selected bond lengths and angles obtained from the NPD Rietveld refinement of the $Sr_{0.9}La_{0.1}(PO_3F)_{0.9}(PO_4)_{0.1}$ system

Sr-O1	2.615(4)	Sr-O3	2.575(4)
Sr-O1	2.561(4)	Sr-O3	2.564(4)
Sr-O2	2.952(4)	Sr-F	2.927(4)
Sr-O2	2.557(4)	Sr-F	2.591(4)
Sr-O2	2.638(4)		
P-O1	1.496(4)	P-O3	1.515(5)
P-O2	1.541(5)	P-F	1.582(4)
O1-P-O2	110.3(3)	O2-P-O3	111.1(3)
O1-P-O3	117.9(3)	O2-P-F	106.0(2)
O1-P-F	106.2(3)	O3-P-F	104.4(2)

The plots obtained for the x = 0.1 system indicate a good agreement between the experimental and the calculated data. As previously suggested by the PXRD patterns, the high amorphous content is also evident in the neutron data.

A comparison of the lattice parameters from the NPD refinements of the x = 0.1 and the parent $SrPO_3F$ phase is shown in table 4.9. The small increase in the unit cell parameters of the x = 0.1 system might suggest that some of the La^{3+} ions may have been substituted into the monazite system, however this could not be verified in the refinement as attempts to vary the occupancies of Sr^{2+} and La^{3+} caused the refinement to become unstable. As result, fractional occupancies of Sr^{2+} and La^{3+} were constrained to

0.9 and 0.1 respectively for this refinement, but this was based on the target stoichiometry rather than any evident from the product obtained and therefore the successful doping could not be confirmed by this refinement.

Table 4.9: Refined lattice parameters obtained from the NPD refinement of the x = 0 and 0.1 members of the $Sr_{1-x}La_x(PO_3F)_{1-x}(PO_4)_x$ series

$Sr_{1-x}La_x(PO_3F)_{1-x}(PO_4)_x$		
	x = 0	x = 0.1
***a* (Å)**	6.97292(6)	6.9751(6)
***b* (Å)**	7.11850(5)	7.1306(6)
***c* (Å)**	6.71991(5)	6.7213(6)
α, ɣ (°)	90	90
β (°)	101.763(1)	101.967(4)
Volume (Å³)	326.550(5)	327.03(5)
χ^2	2.223	5.281
R_{wp} histogram 1 (%)	0.99	0.94
R_{wp} histogram 2 (%)	1.91	0.88

The presence of both lanthanum and phosphorus in the x = 0.1 system were suggested by XRF spectroscopy (table 4.10), along with all samples of the $Sr_{1-x}La_x(PO_3F)_{1-x}(PO_4)_x$ series (see appendix 2 section 2.3.2).

Table 4.10: XRF pressed pellet results obtained from samples of the $Sr_{1-x}La_x(PO_3F)_{1-x}(PO_4)_x$ series. The expected values are shown below the experimental results obtained

$Sr_{1-x}La_x(PO_3F)_{1-x}(PO_4)_x$			
Elements (Wt %)	x = 0	x = 0.1	x = 0.2
Sr (actual)	42.10	32.56	25.63
Sr (expected)	47.20	41.41	35.90
La (actual)	-	11.17	25.70
La (expected)	-	7.295	14.23
P (actual)	10.60	10.50	10.86
P (expected)	16.69	16.27	15.86
Na	0.59	0.62	0.62
Cl	0.48	0.56	0.46

The XRF analysis of $Sr_{1-x}La_x(PO_3F)_{1-x}(PO_4)_x$ series (table 4.10 & appendix 2 section 2.3.2) suggest the presence of lanthanum in the sample but it is not possible to confirm whether it is present in the monazite structure or in an amorphous phase.

4.3.1.4 $Sr_{1-x}Eu_xPO_3F$

Trivalent lanthanides are commonly form monazite structures such as $LaPO_4$.[23-24] Here attempts were made to discover whether a divalent lanthanide could be incorporated within the monazite structure. The formation of $Sr_{1-x}Ln_xPO_3F$ was attempted with Ln = Eu^{2+} given its similar ionic radii to Sr^{2+}. Despite this, the synthesis of the target materials $Sr_{0.95}Eu_{0.05}PO_3F$ and $Sr_{0.90}Eu_{0.1}PO_3F$ could not be achieved, which was thought to be largely due to the solubility problems of Eu^{2+} salt ($EuCl_2$) in water. Initially, the $EuCl_2$ salt dissolved upon stirring but a precipitate was apparent in the mixed Sr^{2+}:Eu^{2+} solution whilst waiting for the fluorophosphate solution to heat. In an attempt to rectify this problem, some minor adjustments to the reaction procedure were made. However, a lower concentration of the mixed cation solution yielded the same problem. As it was unclear as to whether the presence of Sr^{2+} ions in the solution were affecting the solubility of $EuCl_2$, dissolution of a solely Eu^{2+} solution was attempted. This also experienced the same problems suggesting the limited usefulness of $EuCl_2$ in these reactions. Further work is required, particularly to identify alternative sources of a Europium (II) in solution.

4.3.1.5 Comparison of Monazite Systems

It was found the incorporation of varying levels of both Ca^{2+} and Ba^{2+} within the monazite structure were possible. Therefore, a comparison between the unit cell size of these cation substituted systems and other well known monazite systems can be made (figure 4.13).

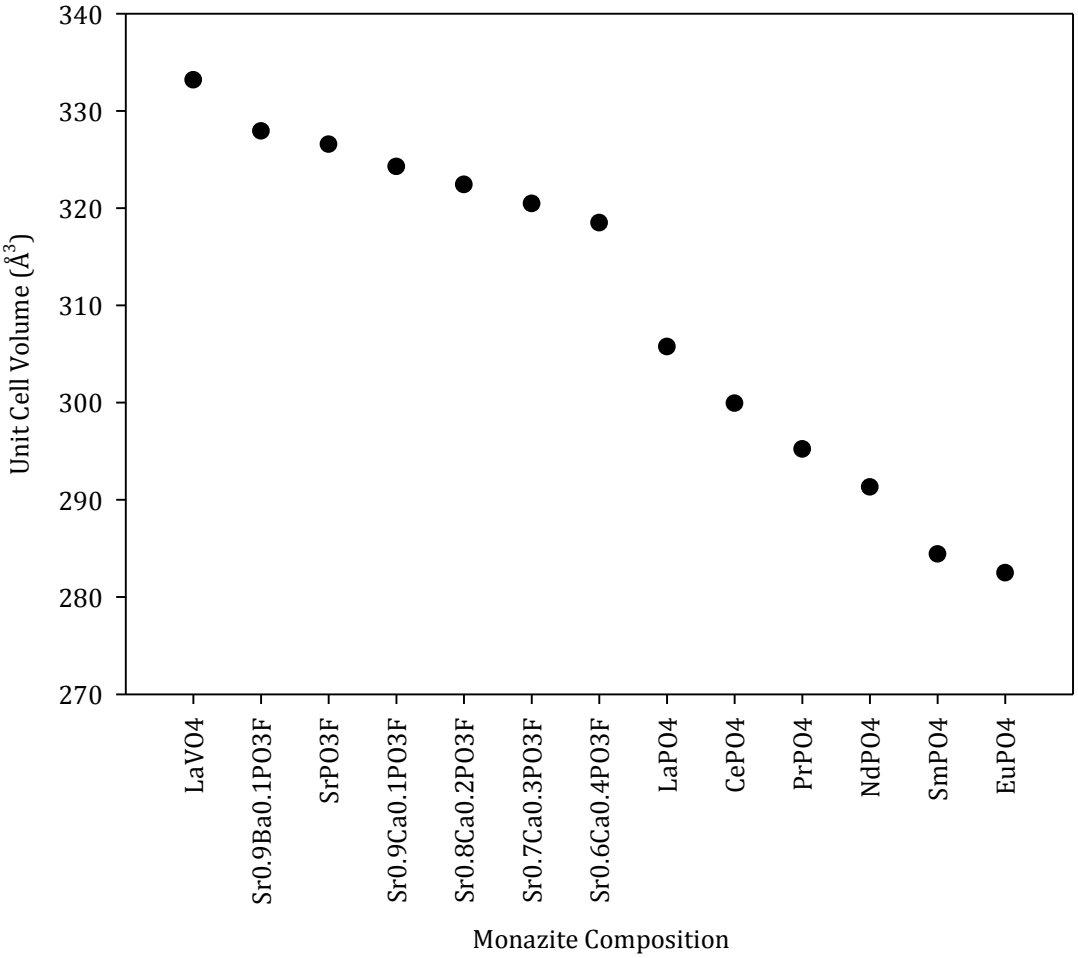

Figure 4.13: A comparison of the unit cell size for various monazite systems

As previously described in section 3.2.5.2, the parent $SrPO_3F$ was found to have a larger unit cell size compared to that of $LaPO_4$, despite the ionic radii of both Sr^{2+} and La^{3+} being very similar. Of the reported monazite phases, $LaVO_4$ possesses the largest unit cell volume due to the greater ionic radius of vanadium compared with phosphorus.

4.3.2 Substitutions in $SrPO_3F \cdot H_2O$

4.3.2.1 $Sr_{1-x}Ca_xPO_3F \cdot H_2O$

All samples of the $Sr_{1-x}Ca_xPO_3F \cdot H_2O$ series were prepared as described in section 4.2. It was found from PXRD patterns that samples with Ca^{2+} content of $x \leq 0.3$ resembled that of the parent material, $SrPO_3F \cdot H_2O$, with a shift in peak position, suggesting that Ca^{2+} had successfully been substituted (figure 4.14).

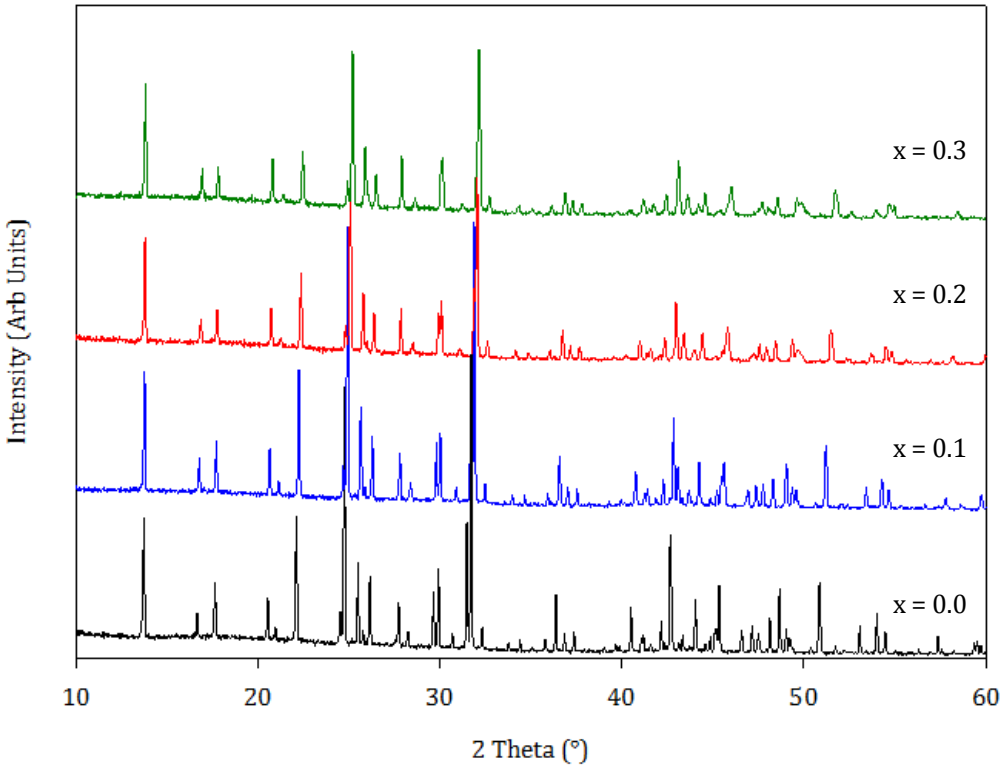

Figure 4.14: A stack plot of the PXRD patterns obtained from members of the $Sr_{1-x}Ca_xPO_3F \cdot H_2O$ series (x = 0.0-0.3)

Beyond this level of attempted calcium incorporation, a preference for the $CaPO_3F \cdot 2H_2O$ structure[25] was observed (figure 4.15).

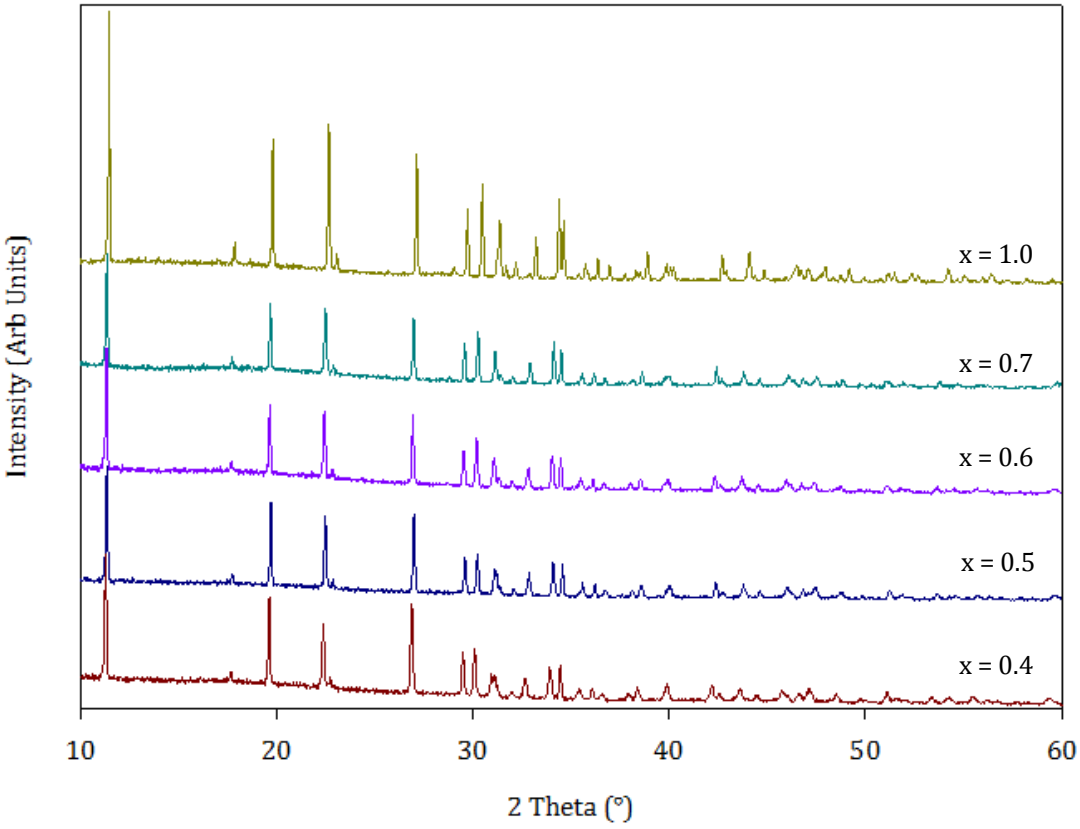

Figure 4.15: A stack plot of the PXRD patterns obtained from members of the $Sr_{1-x}Ca_xPO_3F{\cdot}H_2O$ series where x = 0.4-0.7 and 1.0

. These results were supported by Raman spectroscopy which showed no additional vibrations observed in the Raman spectra compared to those of the parent $SrPO_3F{\cdot}H_2O$ phase and also a change in structural preference from $SrPO_3F{\cdot}H_2O$ to $CaPO_3F{\cdot}2H_2O$ between x = 0.3 and x = 0.4 respectively (see appendix 2 section 2.4.1).

From the PXRD patterns obtained for each member of the $Sr_{1-x}Ca_xPO_3F{\cdot}H_2O$ series, apparent shifts in the position of the peaks are observed. In the x = 0.1-0.3 systems, the shifts in the peak positions are more pronounced compared to the shifts observed in the x = 0.4-0.7 materials, as shown in figures 4.16 and 4.17. This indicates that the structure of $SrPO_3F{\cdot}H_2O$ is more susceptible to changes in the unit cell parameters with increased level of doping compared to the materials which adopt the

$CaPO_3F \cdot 2H_2O$ structure. The resultant shift in the peak positions for the x = 0.1-0.3 systems to higher values of 2θ would suggest a decrease in the unit cell parameters of the systems due to the incorporation of a smaller cation (in this case Ca^{2+}).

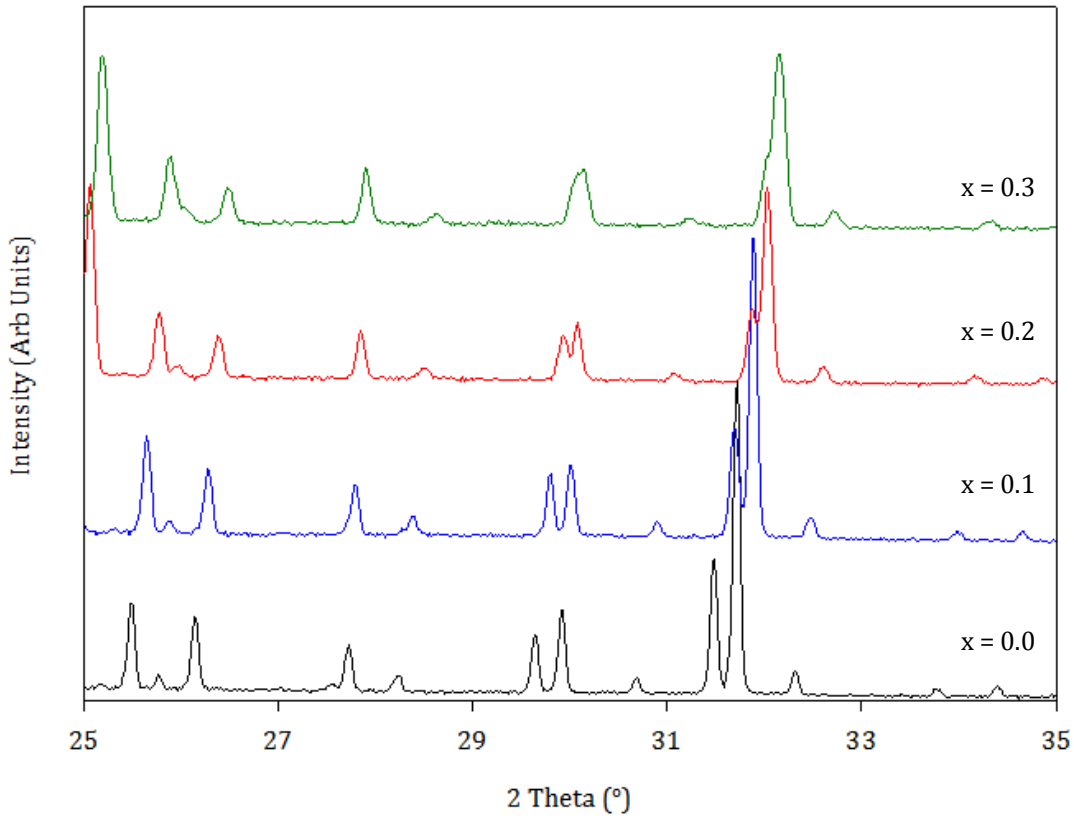

Figure 4.16: A stack plot of the PXRD patterns obtained from members of the $Sr_{1-x}Ca_xPO_3F \cdot H_2O$ series (x = 0.0-0.3) for the region of interest 25-35° 2θ

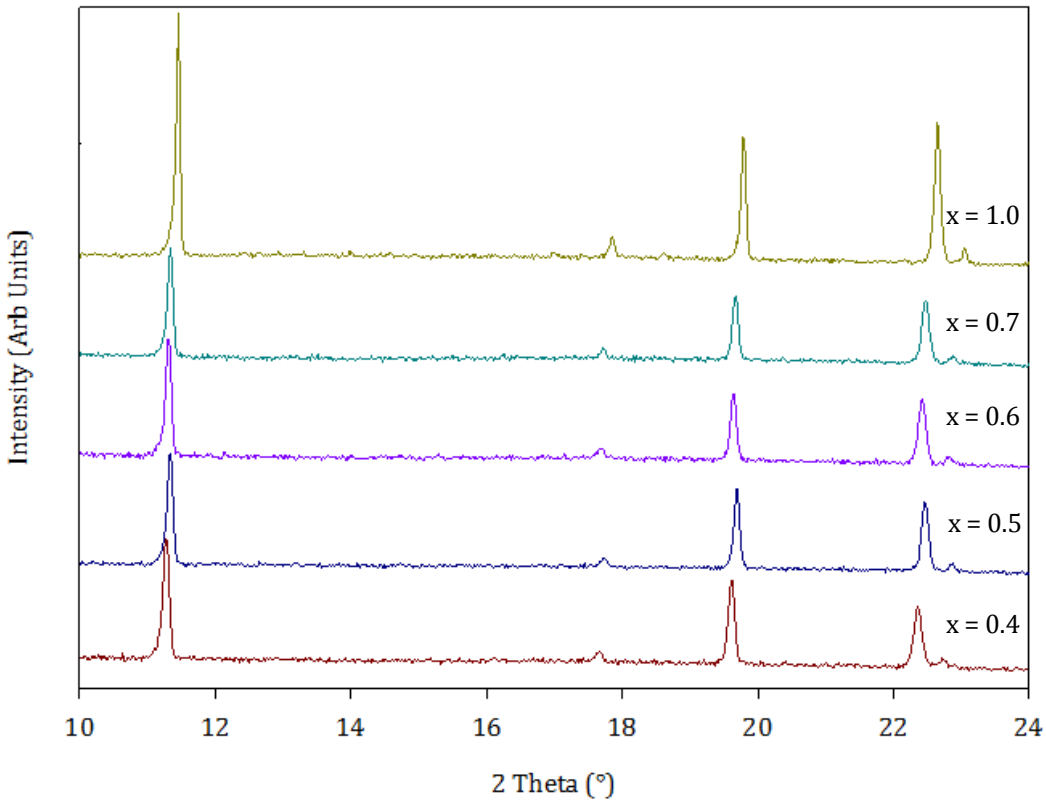

Figure 4.17: A stack plot of the PXRD patterns obtained from members of the $Sr_{1-x}Ca_xPO_3F{\cdot}H_2O$ series (x = 0.4-0.7 and 1.0) for the region of interest 10-24° 2θ

To investigate the inferred structural changes within the x = 0.1-0.3 systems as a result of the incorporation of calcium, Rietveld refinements based on the PXRD data for these systems were performed. The refinement of the x = 0.1 system is shown in figure 4.18). Similarly to the $Sr_{1-x}Ca_xPO_3F$ series, the quality of the data did not allow fractional occupancies of the Sr^{2+} and Ca^{2+} cations to be refined freely. Instead they were constrained to the target doping level. All refinements were shown to have good agreement between the experimental and calculated data, generating relatively low values of χ^2 and R_{wp} (see table 4.11 and figure 4.20). The remainder of the plots obtained from the final refinements, tables of the refined atomic co-ordinates and selected bond lengths and angles are shown in appendix 2 section 2.4.2.

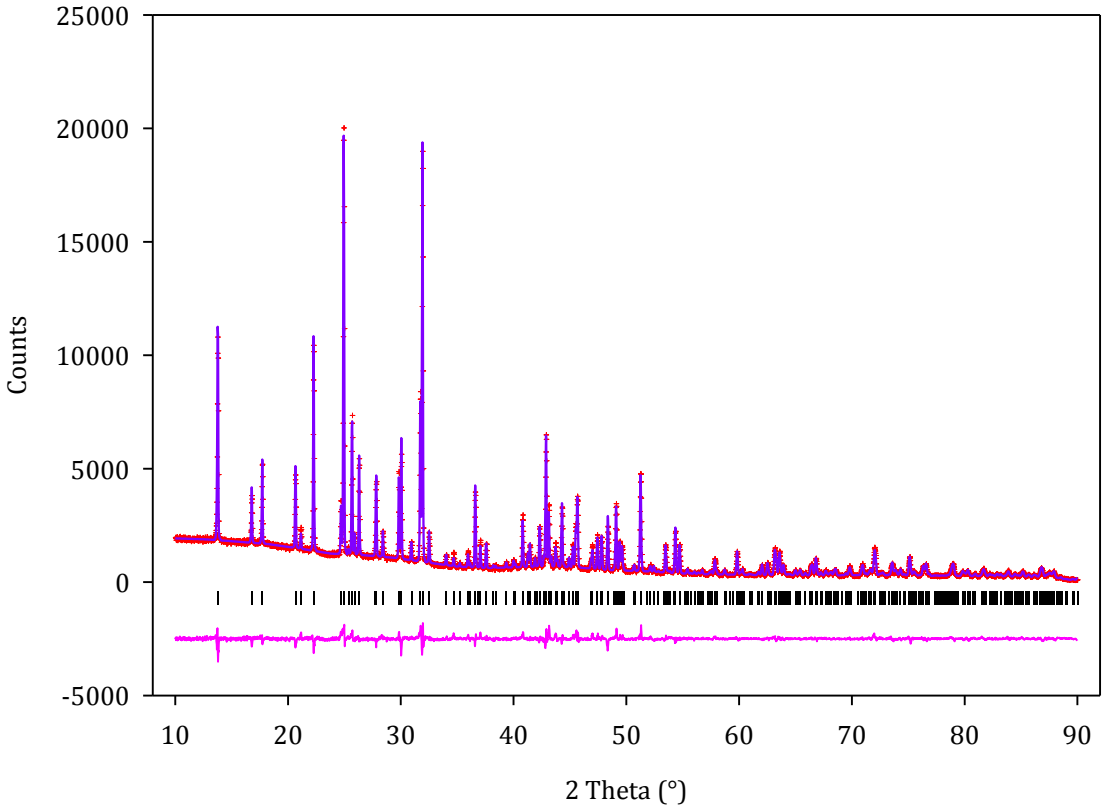

Figure 4.18: Final observed (red), calculated (purple) and difference profiles (pink) of the PXRD refinement of the x = 0.1 system from the $Sr_{1-x}Ca_xPO_3F{\cdot}H_2O$ series. Reflections position are shown as vertical tick marks (black)

Table 4.11 shows the refined lattice parameters and unit cell volumes for the x = 0.1-0.3 systems. The results from the refinement showed an overall decrease in the unit cell parameters a result of increasing x, with the exception of the *c* parameter of the x = 0.3 system, which was found to show a slight increase. However, as a result of the increasing calcium incorporation into the $SrPO_3F{\cdot}H_2O$ structure, the unit cell volumes of all systems were found to decrease linearly up to x =0.3 (figure 4.19). This may suggest that a limit of calcium doping has been reached.

Table 4.11: Refined lattice parameters obtained from the PXRD refinements of the $Sr_{1-x}Ca_xPO_3F{\cdot}H_2O$ systems

$Sr_{1-x}Ca_xPO_3F{\cdot}H_2O$ Series				
	x = 0	x = 0.1	x =0.2	x = 0.3
***a* (Å)**	8.00940(5)	7.95416(9)	7.9100(1)	7.8991(2)
***b* (Å)**	8.44643(6)	8.3744(1)	8.3120(2)	8.2889(2)
***c* (Å)**	12.83400(8)	12.7892(1)	12.7540(2)	12.7656(3)
***α,β,γ* (°)**	90	90	90	90
Volume (Å³)	868.23(1)	851.91(2)	838.55(3)	835.82(4)
χ^2	2.893	3.225	2.249	3.955
R_{wp} (%)	5.20	5.64	4.67	6.16

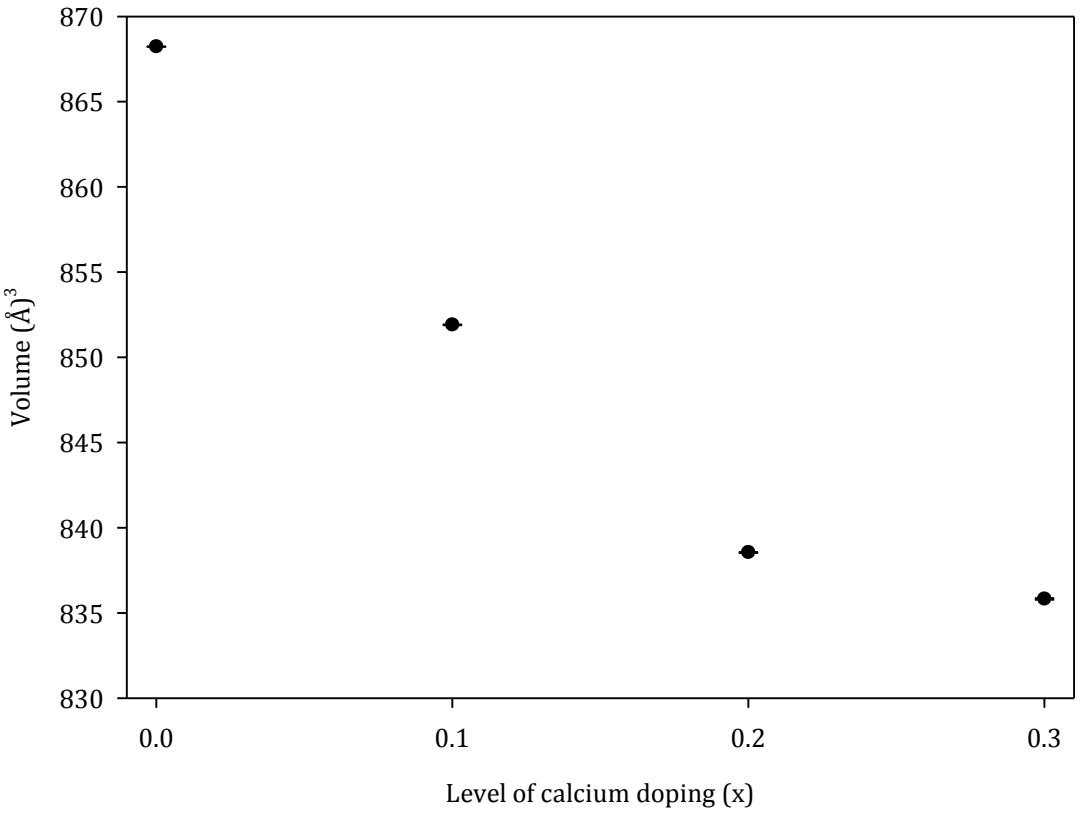

Figure 4.19: A plot of the volume for all members of the $Sr_{1-x}Ca_xPO_3F{\cdot}H_2O$ series

Although the background levels observed in the Rietveld refinements of this $Sr_{1-x}Ca_xPO_3F{\cdot}H_2O$ system do not appear to be significant, it is very likely that these phases contain significant amorphous material given the amorphous content of the parent material $SrPO_3F{\cdot}H_2O$ (discussed in section 3.2.4.6). The background does appear to increase with increasing x, a feature which was observed with the both the PXRD

patterns and the Rietveld plots for the $Sr_{1-x}Ca_xPO_3F$ systems. Further work is required to confirm the presence of an amorphous component along with the determining the actual level of Ca^{2+} successfully substituted.

4.4 Conclusions

To conclude, it was found that the partial substitution of other alkali earth metals (Ba^{2+} and Ca^{2+}) into the monazite system was possible. As expected given the contrasting ionic radii, the substitution of Ba^{2+} for Sr^{2+} resulted in an expansion of the unit cell volume, whereas substituting Ca^{2+} resulted in the contraction of the unit cell. The investigation into the maximum level of substitution within the monazite system, under the experimental conditions employed, showed that nominal levels of x = 0.1 and x = 0.4 could be achieved for the $Sr_{1-x}Ba_xPO_3F$ and $Sr_{1-x}Ca_xPO_3F$ systems respectively before both systems no longer adopted the monazite structure. As with the parent material, the $Sr_{1-x}Ca_xPO_3F$ system was found to contain an amorphous component which has yet to be identified. The level of amorphous material within these systems was found to increase with increasing Ca^{2+}, particularly with the systems containing Ca^{2+} levels $\geq$ 0.2 where the amorphous content was estimated at $\sim$ 50 %. Attempts to substitute Eu^{2+} into the $SrPO_3F$ system were inconclusive at best, but likely to have been unsuccessful. These experiments were hampered by solubility issues with the Eu(II) salt reagent. Attempts to co-substitute La^{3+} and PO_4^{3-} into $SrPO_3F$ were also inconclusive, despite a small expansion of the lattice parameters.

Preliminary studies into the substitution of Ca^{2+} within the hydrated system to form products of composition $Sr_{1-x}Ca_xPO_3F{\cdot}H_2O$ have shown that a maximum level close to x = 0.3 can be achieved, before a preference for the structure of $CaPO_3F{\cdot}2H_2O$ occurs at higher levels. However, the level of Ca^{2+} actually incorporated into the structure could

not be determined from the Rietveld refinement, as the fractional occupancies of the cation sites were too unstable to allow to refinement. Although the presence of an amorphous component has not yet been established within these materials, it is likely that members of the $Sr_{1-x}Ca_xPO_3F \cdot H_2O$ series will contain significant amorphous material due to the nature of the reaction and in light of the fact that the parent material was found to contain ~ 21 weight % amorphous content.

4.5 References

1. N. Clavier, R. Podor and N. Dacheux, *Journal of the European Ceramic Society*, 2011, **31**, 941-976.
2. R. Cabella, G. Lucchetti and P. Marescotti, *Canadian Mineralogist*, 1999, **37**, 961-972.
3. S. Graeser and H. Schwander, *Schweizerische Mineralogische und Petrographische Mitteilungen*, 1987, **67**, 103-113.
4. I. L. Botto and E. J. Baran, *Journal of The Less-Common Metals*, 1982, **83**, 255-261.
5. R. N. P. Choudhary, *Journal of Materials Science Letters*, 1991, **10**, 432-434.
6. J. Bashir and M. N. Khan, *Materials Letters*, 2006, **60**, 470-473.
7. S. Mahapatra, G. Madras and Row, *The Journal of Physical Chemistry C*, 2007, **111**, 6505-6511.
8. H. Konno, H. Tachikawa, A. Furusaki and R. Furuichi, *Analytical Sciences*, 1992, **8**, 641-646.
9. Y. Aoki, H. Habazaki and H. Konno, *Chemistry of Materials*, 2003, **15**, 2419-2428.
10. L. A. Boatner, G. W. Beall, M. M. Abraham, C. B. Finch, P. G. Huray and M. Rappaz, *Monazite and other lanthanide orthophosphates as alternate actinide waste forms* Plenum Publishing Corporation, New York, 1980.
11. E. H. Oelkers and J. M. Montel, *Elements* 2008, **4**, 113-116.
12. D. H. Kuo and W. M. Kruen, *Materials Science and Engineering A*, 1996, **210**, 123-134.
13. K. Sueng-Ho, T. Sekino, T. Kusunose and A. T. Hirvonen, *Materials Science Forum*, 2007, **554-555**, 909-912.
14. M. Ferhi, K. Horchani-Naifer and M. Férid, *Journal of Rare Earths*, 2009, **27**, 182-186.
15. J. Dexpert-Ghys, R. Mauricot and M. D. Faucher, *Journal of Luminescence*, 1996, **69**, 203-215.
16. G. Chen, J. Holsa and J. R. Peterson, *J. Phys Chem*, 1997, **58**, 2031-2037.
17. K. Amezawa, Y. Tomii and N. Yamamoto, *Solid State Ionics*, 2005, **176**, 143-148.
18. K. Amezawa, H. Maekawa, Y. Tomii and N. Yamamoto, *Solid State Ionics*, 2001, **145**, 233-240.
19. K. Amezawa, Y. Tomii and N. Yamamoto, *Solid State Ionics*, 2005, **176**, 135-141.
20. J. Potts, The University of Birmingham, Birmingham, 2013.
21. R. D. Shannon, *Acta Crystallographica Section A*, 1976, **32**, 751-767.
22. R. D. Shannon and C. T. Prewitt, *Acta Crystallographica Section B*, 1969, **25**, 925-946.
23. S. Jaulmes, *Bulletin De La Societe Francaise Mineralogie Et De Cristallographie*, 1972, **95**, 42.
24. D. F. Mullica, W. O. Milligan, D. A. Grossie, G. W. Beall and L. A. Boatner, *Inorganica Chimica Acta-F-Block Elements Articles and Letters*, 1984, **95**, 231-236.
25. A. Perloff, *Acta Crystallographica Section B-Structural Crystallography and Crystal Chemistry*, 1972, **B 28**, 2183-2191.

CHAPTER 5:

Synthesis and Characterisation of Modified Gypsum Systems

5.1 Introduction

Calcium sulphate materials have been considered for use as biomaterials in many applications, with its first reported use in dentistry in 1892[1] and have been most extensively used as bone replacement materials, where gypsum (calcium sulphate dihydrate, $CaSO_4 \cdot 2H_2O$), formed from a reaction with calcium sulphate hemihydrates and water ($CaSO_4 \cdot \frac{1}{2}H_2O$) was used to fill the voids in the bone of tuberculosis patients.[2-3] Further investigations were carried out between the 1950s and 1970s which found that calcium sulphate materials could be used as a filler for various defect sites, as the material was found to be safe, encouraged bone re-growth and was completely resorbed by the body.[4-5] However, *in vivo* studies have shown that its relatively rapid rate of resorption to be problematic,[6] as it does not allow sufficient time for native bone re-growth to occur before the implant is lost.[7] For example, Wright Medical Technology commercialised Osteoset which is a brand of calcium sulphate pellets[8] but these were found to completely resorbed in 3-8 weeks[9], meaning the rate of resorption of the implant is faster than the rate of formation of new bone. In light of this, calcium sulphate biomaterials are still considered to assist the repair of stable fractures on non-load bearing bone defects.[10] Indeed, gypsum has greater compressive strength than

cancellous bone but a weaker tensile strength in a dry environment, however once damp, it becomes brittle and can therefore not be used for major repairs *in vivo*.[11]

In this work, the aim is to address the issue of solubility by modifying gypsum through doping with fluorophosphate in hope of reducing solubility and so making an improved bone replacement material. To date, there have been no reports of fluorophosphate substitutions in gypsum. However, previous work by Vlad *et al*.[12] in 2010 have shown that producing a biphasic material by combining an iron-modified calcium phosphate material with sulphate has led to improved resorbability. Some other examples of biphasic materials have been investigated. An example of which is PRO-DENSE®,[13] which is an example of calcium phosphate-sulphate materials. Other compositions using various forms of calcium phosphate have been explored.

As fluorophosphate and sulphate are isovalent and of similar sizes, the concept of doping fluorophosphate into the gypsum structure appears feasible. As an added advantage fluorophosphate not only contains phosphate which is a key component of bone but it also contains fluorine, which is reported to promote bone growth. Therefore attempts will be made to synthesise and characterise a range of fluorophosphate doped gypsum systems for use as potential bone replacement materials.

5.2 Synthesis of Fluorophosphate doped Gypsum systems

The synthesis of calcium sulphate dihydrate, calcium fluorophosphate and a series of fluorophosphate doped gypsum systems were performed following the synthesis as described in section 2.1.2 using the appropriate anion containing solutions described in table 5.1. The reaction temperature, duration of stirring and the rate of addition of the $CaCl_2$ solution have also been investigated. Preliminary reactions were carried out at

both 40 °C and 60 °C with stirring and the $CaCl_2$ solution was added over a period of 30 minutes. Once all of the $CaCl_2$ solution had been added, the resulting white precipitate was collected by vacuum filtration, washed thoroughly with de-ionised water and left to dry in air overnight.

Table 5.1: A table to show the level of fluorophosphate incorporation into gypsum and the anion solutions used in these reactions

Target Material	x	Anion Containing Solution
$Ca(SO_4)_x(PO_3F)_{1-x}\cdot 2H_2O$	1.0	Na_2SO_4
$Ca(SO_4)_x(PO_3F)_{1-x}\cdot 2H_2O$	0.9	Na_2SO_4:Na_2PO_3F
$Ca(SO_4)_x(PO_3F)_{1-x}\cdot 2H_2O$	0.8	Na_2SO_4:Na_2PO_3F
$Ca(SO_4)_x(PO_3F)_{1-x}\cdot 2H_2O$	0.7	Na_2SO_4:Na_2PO_3F
$Ca(SO_4)_x(PO_3F)_{1-x}\cdot 2H_2O$	0.6	Na_2SO_4:Na_2PO_3F
$Ca(SO_4)_x(PO_3F)_{1-x}\cdot 2H_2O$	0.5	Na_2SO_4:Na_2PO_3F
$Ca(SO_4)_x(PO_3F)_{1-x}\cdot 2H_2O$	0.4	Na_2SO_4:Na_2PO_3F
$Ca(SO_4)_x(PO_3F)_{1-x}\cdot 2H_2O$	0.3	Na_2SO_4:Na_2PO_3F
$Ca(SO_4)_x(PO_3F)_{1-x}\cdot 2H_2O$	0.2	Na_2SO_4:Na_2PO_3F
$Ca(SO_4)_x(PO_3F)_{1-x}\cdot 2H_2O$	0.1	Na_2SO_4:Na_2PO_3F
$Ca(SO_4)_x(PO_3F)_{1-x}\cdot 2H_2O$	0.0	Na_2PO_3F

5.2.1 Deuteration

A series of samples from the fluorophosphate doped gypsum series were deuterated as described in Chapter 2 section 2.1.2.1.

5.2.2 Cement Formation

In order to form cements from samples of calcium fluorophosphate, calcium sulphate dihydrate and fluorophosphate doped gypsum, it required each of the samples to first be dehydrated and then rehydrated. The temperature at which the samples were dehydrated was determined by Thermogravimetric Analysis.

A known amount of sample was placed into individual alumina boats and heated in a muffle furnace to temperatures between 170-180 °C for 1 hour. The weights of the samples were recorded before rehydrating. To rehydrate, water was added to the

samples dropwise and the mixture was stirred to form a paste. The paste was transferred into a mould and left to set overnight.

5.3 Results and Discussion

5.3.1 Initial Sample Formation and Characterisation

The synthesis conditions of the two end members of the series calcium fluorophosphate and calcium sulphate dihydrate (gypsum) were established prior to proceeding with any doping experiments. Analysis of the X-ray diffraction patterns obtained of the parent calcium fluorophosphate phase (x = 0) precipitated at both 40 °C and 60 °C confirmed that the intended phase had been successfully synthesised at both temperatures. Peaks present in the PXRD pattern matched the pattern corresponding to calcium fluorophosphate dihydrate ($CaPO_3F{\cdot}2H_2O$ PDF; 00-029-0323) on the International Center for Diffraction Data (ICDD) database, suggesting that the products formed at both temperatures were single phase. From the PXRD patterns shown in figure 5.1(a and b), it was evident that the calcium fluorophosphate sample synthesised at 40 °C not only showed a higher degree of crystallinity but also a significantly lower background. The increased background that was observed was thought to occur due to there being a higher level of amorphous content, which is commonly found in fluorophosphate syntheses. The effect of temperature on the reaction products formed when synthesising calcium fluorophosphate, was evident in the formation of strontium fluorophosphate phases mentioned in Chapter 3.

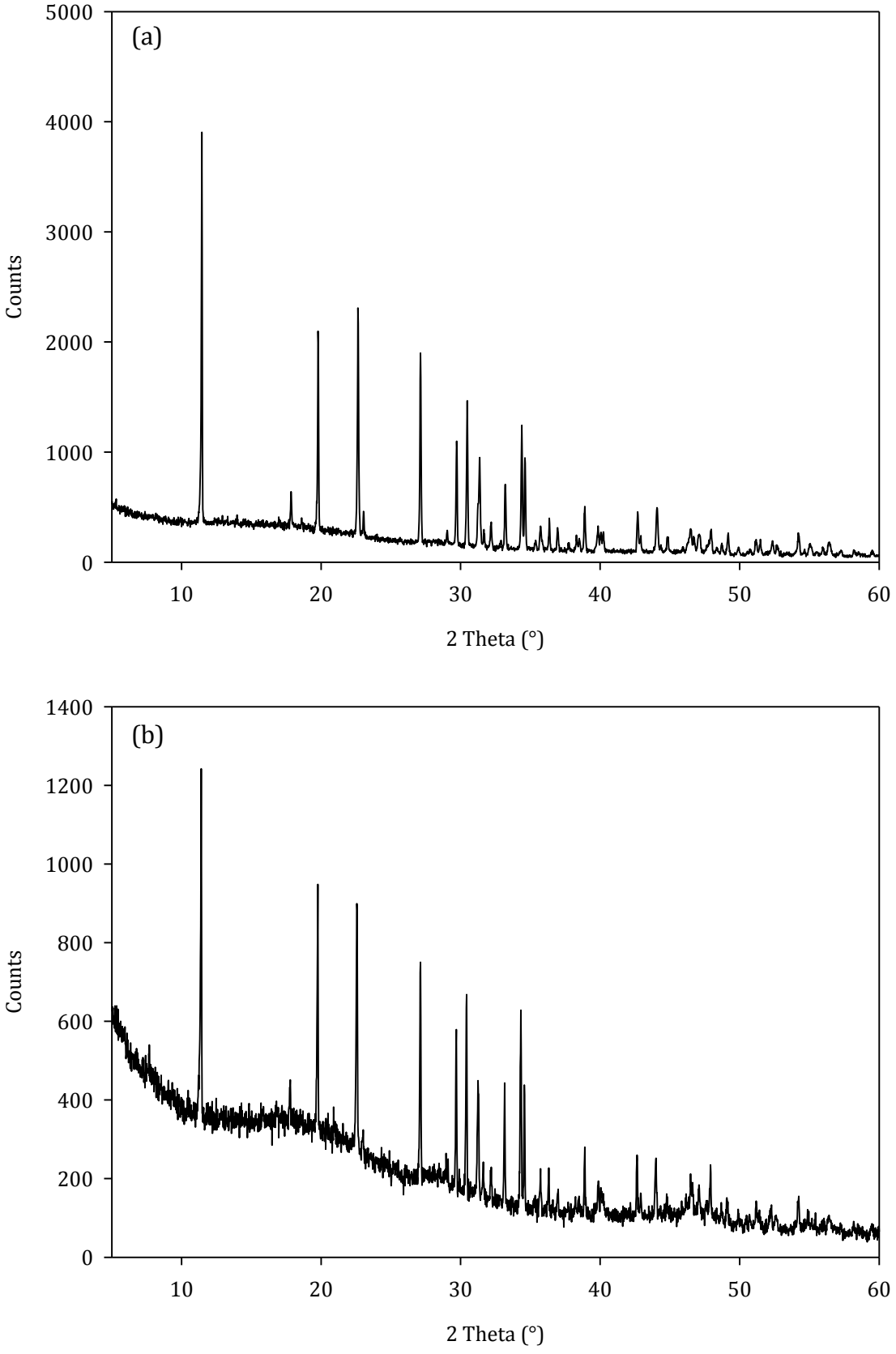

Figure 5.1: PXRD patterns of $CaPO_3F{\cdot}2H_2O$ synthesised at 40 °C (a) and 60 °C (b)

It was found that the products obtained from the reactions performed at a range of temperatures between RT-70 °C were largely crystalline but the synthesis at 80 °C led to the formation of an amorphous product only. Therefore, it was to be expected that the calcium fluorophosphate samples precipitated at 60 °C, and possibly even at 40 °C, might contain some amorphous content as well as the crystalline component of $CaPO_3F{\cdot}2H_2O$.

Rietveld refinements were employed to estimate the amount of amorphous content present within both samples. This was achieved by adding known amounts of a highly crystalline material (here TiO_2). Following the refinements of both the fluorophosphate and TiO_2 components, it was possible to estimate amorphous content from the calculated phase fractions.

The Rietveld plots obtained from the refinements of the mixed $CaPO_3F{\cdot}2H_2O$ and TiO_2 samples are shown in Figure 5.2 a and b. It is evident from the refinements that there is very good agreement between the experimental and calculated data, with both refinements producing fits with low χ^2 values of 1.81 (CaFP-40 °C) and 1.70 (CaFP-60 °C) respectively.

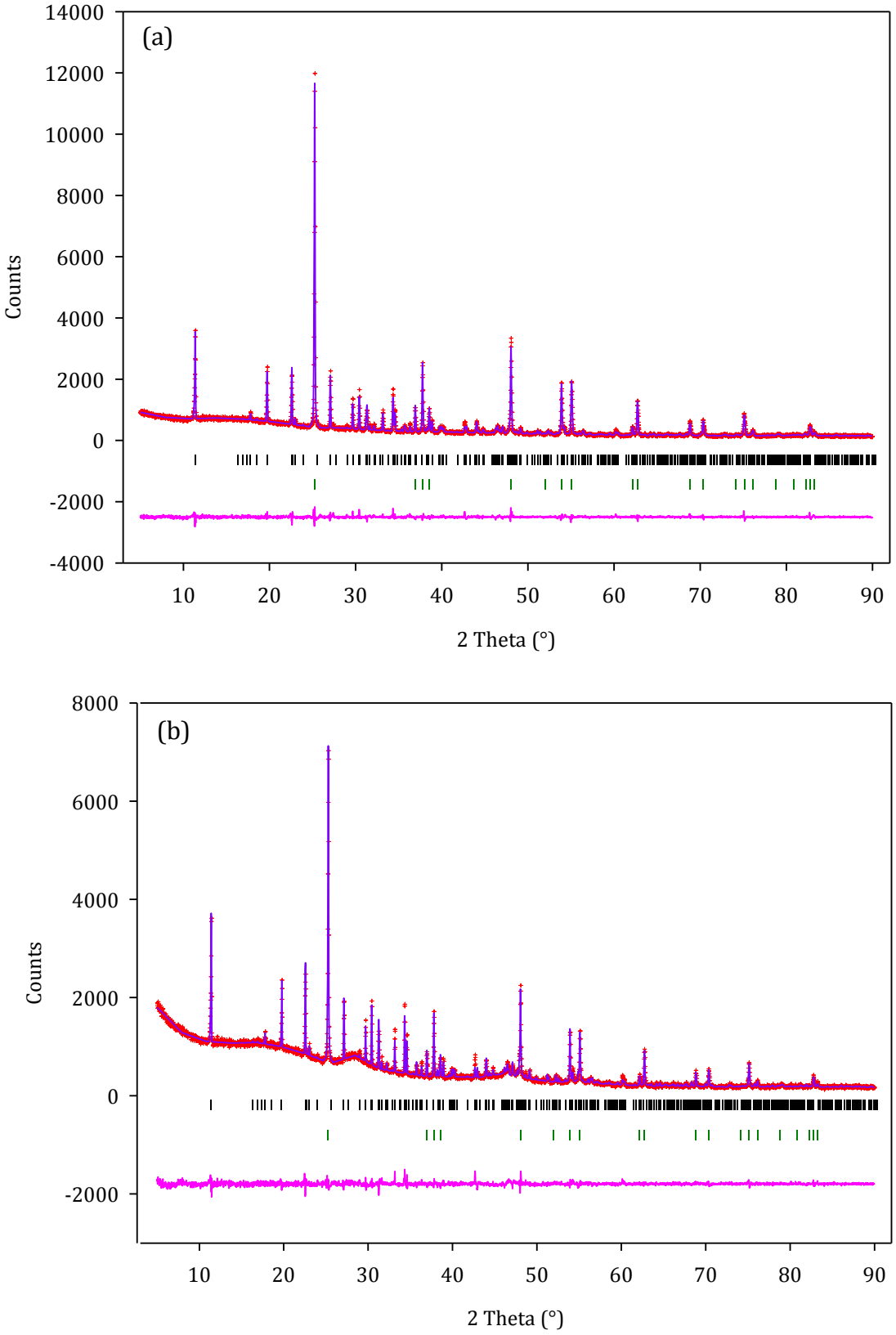

Figure 5.2: Final observed (red), calculated (purple) and difference line (pink) X-ray diffraction refinements of $CaPO_3F{\cdot}2H_2O$ (40 °C) (a) and $CaPO_3F{\cdot}2H_2O$ (60 °C) with TiO_2 (b). Reflection positions for $CaPO_3F{\cdot}2H_2O$ and TiO_2 are shown as vertical tick marks (black and green respectively)

The calculations were made based on the relative amounts of both crystalline components and the phase fraction values generated from the refinement. The results from each refinement and the calculated level of amorphous are summarised in table 5.2.

Table 5.2: Summarised data obtained from the two phase Rietveld refinements of $CaPO_3F{\cdot}2H_2O$ and TiO_2

	$CaPO_3F{\cdot}2H_2O$ (synthesis at 40 °C) + TiO_2 refinement	**$CaPO_3F{\cdot}2H_2O$ (synthesis at 60 °C) + TiO_2 refinement**
Mass of $CaPO_3F{\cdot}2H_2O$ (g)	1.00	0.50
Mass of TiO_2 (g)	0.60	0.13
Total mass of $CaPO_3F{\cdot}2H_2O/TiO_2$ sample (g)	1.60	0.63
Actual wt % of $CaPO_3F{\cdot}2H_2O$ in sample	62.50	79.40
Actual wt % of TiO_2 in sample	37.50	20.6
Wt % of $CaPO_3F{\cdot}2H_2O$ from Rietveld analysis	49.09	57.69
Wt % of TiO_2 from Rietveld analysis	50.91	42.31
Calculated amorphous content (wt %)	26	51

As expected, the calculations confirmed that the level of amorphous material present in the calcium fluorophosphate samples was significantly increased upon raising the reaction temperature from 40 to 60 °C. The sample produced at 60 °C was estimated to contain approximately 50 % more amorphous content compared to the sample synthesised at 40 °C. Therefore, it can be suggested that the optimum temperature for the synthesis of calcium fluorophosphate was 40 °C. As the composition of the amorphous component is unknown, X-ray fluorescence spectroscopy was utilised to determine the calcium to phosphorus ratio. Should the amorphous material largely be based on the crystalline stoichiometry then this value should not deviate significantly from one. Fused glass beads of calcium fluorophosphate were measured against a

calibration, from which a series of fused glass beads were produced primarily containing varied amounts of calcium and phosphorus. Sodium was also included in the calibration as NaCl may be a by-product of the precipitation of the reaction. As with the calibration for strontium fluorophosphate phases, the inclusion of fluorine in this calibration was not considered for the reasons previously mentioned in Chapter 3. The calibration curves for each element can be found in section 2.7.2.

Values of 1.02(1) and 1.03(1) were obtained for the Ca:P ratio of calcium fluorophosphate synthesised at both 40 and 60 °C respectively. These values are close to the ideal value of 1 and so suggested that the amorphous phase stoichiometry also possessed an equivalent Ca:P ratio to the crystalline phase, and is likely to be an amorphous polymorph.

Similar conditions to those used for calcium fluorophosphate were adopted to synthesise calcium sulphate dihydrate. From the powder X-ray diffraction patterns it was evident that the crystalline products obtained were single phase and resembled that of calcium sulphate dihydrate ($CaSO_4 \cdot 2H_2O$ PDF; 00-021-0816) identified on the International Center for Diffraction Data (ICDD) database. In contrast to the $CaPO_3F \cdot 2H_2O$, the sample of gypsum prepared at 60 °C exhibited a higher degree of crystallinity compared to the sample synthesised at 40 °C.

Initial attempts to synthesise members of the $Ca(SO_4)_x(PO_3F)_{1-x} \cdot 2H_2O$ series were based on the experimental procedure described by Nancollas *et al.*[14] for the synthesis of calcium sulphate dihydrate crystals. The concentration of the reagents (0.2 M), reaction temperature (70 °C) and duration of the reaction (2 hrs) were all followed according to this method, but the volume of the solutions used initially were reduced to 50 cm^3, given

these were the initial attempts at synthesising members of the fluorophosphate doped calcium sulphate (gypsum) series. As the synthesis of the parent calcium sulphate dihydrate phase was successful under these conditions, subsequent reactions were carried out with the addition of fluorophosphate, where the level of fluorophosphate was increased in increments of 10 mole percent (mol %) for each reaction coupled to an appropriate reduction in SO_4^{2-} content. It was evident from the powder X-ray diffraction patterns that products formed above a nominal level of fluorophosphate doping of 30 mol % were amorphous under these conditions.

5.3.2 Optimising the Synthesis

To attempt to form all members of the intended $Ca(SO_4)_x(PO_3F)_{1-x}\cdot 2H_2O$ series in crystalline forms, increased concentration of reagents and lower reaction temperatures were attempted. The products from the precipitation reactions were formed at both 40 and 60 °C and characterised using powder X-ray diffraction. These temperatures had previously been shown to favour the formation of crystalline fluorophosphate phases described in Chapter 3. Indeed, the latter temperature has been reported for the synthesis of single crystal calcium sulphate (gypsum) crystals.[14]

Upon synthesising the intermediate compositions of the $Ca(SO_4)_x(PO_3F)_{1-x}\cdot 2H_2O$ series (x = 0.9-0.1), it was established that varying the reaction temperature appeared to have very little effect on the crystallinity of the products formed, even at for higher levels of fluorophosphate. Therefore, it was decided to proceed and synthesise these materials in an identical manner to that of calcium sulphate dihydrate with the addition of fluorophosphate, increasing the level of fluorophosphate by increments of 10 mol % for each composition. This method proved to be successful, with the PXRD patterns

showing that a complete solid solution of the fluorophosphate doped gypsum system had been achieved (figure 5.3).

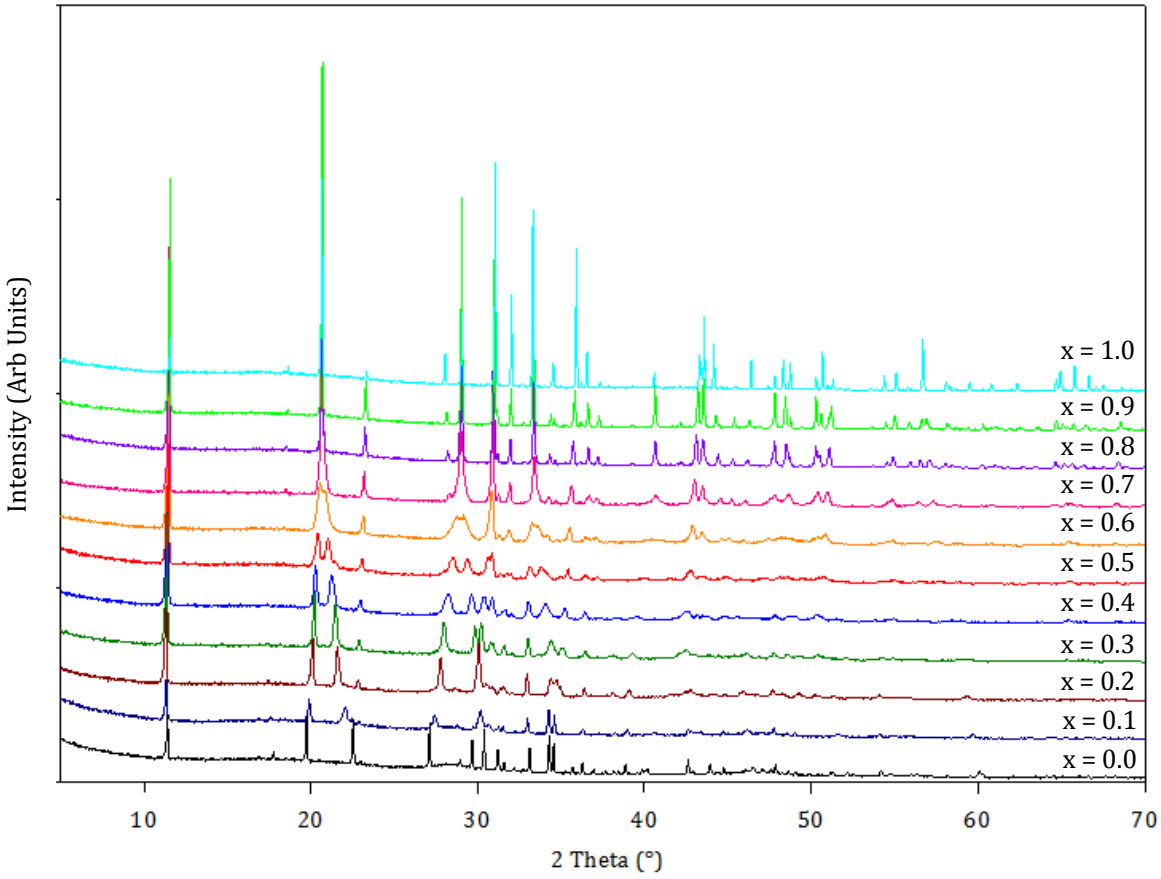

Figure 5.3: PXRD stack plot of all members of the $Ca(SO_4)_x(PO_3F)_{1-x}\cdot 2H_2O$ series where x =0.0-1.0 (incorporation of sulphate in increments of 0.1)

It is apparent from the PXRD stack plot, that those products containing relatively low levels of fluorophosphate (x = 0.9-0.7) strongly resemble the pattern of gypsum and show very small shifts in the peak positions compared to the parent gypsum material, indicating that small changes in the unit cell parameters. This would suggest that the inclusion of low levels (< 30 mol %) of PO_3F^{2-} retains the gypsum structure. For gypsum itself, a degree of preferred orientation is observed along the 010 direction, giving higher intensity for the Bragg peaks corresponding to that direction. This phenomenon is very common for calcium sulphate dihydrate as the growth of the crystals is favoured

in one direction, in this case along the *b* axis, which causes the crystallites to adopt a needle like appearance. Upon increasing the level of fluorophosphate incorporated into the gypsum structure, there is a clear transition in the crystal structure from a monoclinic to a triclinic system observed when the level of fluorophosphate incorporated is ≥ 30 mol %. Beyond this point, the PXRD patterns resemble that of calcium fluorophosphate although the samples containing 50 and 60 wt% fluorophosphate are poorly crystalline making analysis difficult. For compositions where x = 0.6-0.1, significant shifts in the peak positions are observed in the region of 20-27° 2θ compared to the pure fluorophosphate containing material. These shifts in the peak positions appear to be more prominent in the PXRD patterns of $CaPO_3F{\cdot}2H_2O$ and $Ca(SO_4)_{0.1}(PO_3F)_{0.9}{\cdot}2H_2O$, which contain 0 and 10 mole percent sulphate respectively. This indicates that the calcium fluorophosphate structure is more susceptible to undergo structural changes when low weight percentages of sulphate are incorporated into the structure. As it was difficult to map the progression of the peaks with doping, particularly for samples with high fluorophosphate content (low sulphate content), additional compositions within the x = 0-0.1 range were synthesised, targeting the compositions $Ca(SO_4)_{0.025}(PO_3F)_{0.975}{\cdot}2H_2O$, $Ca(SO_4)_{0.05}(PO_3F)_{0.95}{\cdot}2H_2O$, $Ca(SO_4)_{0.075}(PO_3F)_{0.925}{\cdot}2H_2O$.

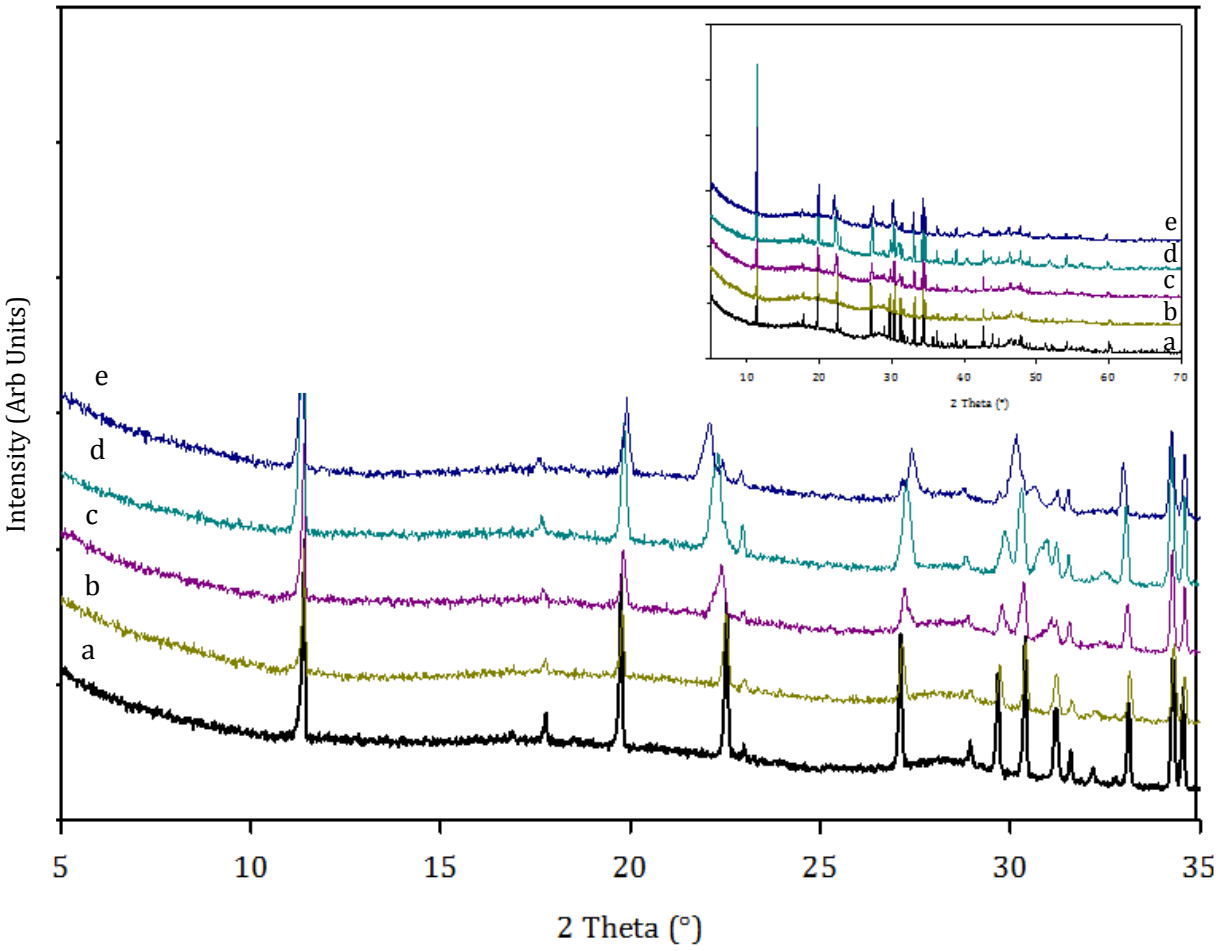

Figure 5.4: PXRD stack plot of $Ca(SO_4)_x(PO_3F)_{1-x}\cdot 2H_2O$ series where x = 0-0.1 (incorporation of sulphate in increments of 0.025 (a-e)) in the region of 5-35° 2θ
Inset: PXRD stack plot showing the full scan 5-70° 2θ

Figure 5.4 shows the PXRD patterns obtained for these additional samples. By doping with smaller increments of fluorophosphate it is possible to more readily identify shifts in the peak positions with doping within the main region of interest (19-35° 2θ). Not all peaks in this region appear to be affected by the presence of sulphate. The peak around 20° appears to be unaffected and, whilst the peak at 22° broadens and shifts to the left (lower 2θ) and the peak at 27° broadens and shift to the right. Despite doping in smaller increments, it is still difficult to monitor the changes in the peaks between 29-

33° but the overall changes in lattice parameters will be discussed in detail later in section 5.3.11.

Further analysis of the PXRD data collected on the fluorophosphate doped calcium sulphate series highlighted a broadening of certain peaks. On closer inspection, these peaks were those whose position was most sensitive to changes in PO_3F^{2-} content. A likely explanation might be the presence of inhomogeneity in the distribution of PO_3F^{2-} with the sample. Therefore, modifications to the synthesis were made in an attempt to reduce the inhomogeneity and if possible also improve the crystallinity of the samples in this series. This was particularly important so as to ensure that samples of the best quality were produced for the neutron diffraction study, which it was hoped would allow for a more detailed structural analysis of fluorophosphate doped calcium sulphate systems. The findings from the neutron diffraction experiments will be discussed in a subsequent section (5.3.10) of this chapter.

A range of different syntheses were carried out which involved changes to the reaction temperature, stirring time, addition time of $CaCl_2$ and increasing the volume of solutions and PXRD patterns of the resulting products were collected and analysed.

The effects of modifying various reaction conditions were only considered for the sample containing 10 mol % sulphate as this was the sample where the issue of inhomogeneity was first recognised. The peak intensities and the full width half maximum (FWHM) values for a selection of peaks in the region of 19-35° 2θ were taken into consideration in order to establish the best synthetic method. As the full width half maximum values can be used to assess the crystallinity of the sample, this was a key factor in determining which synthetic method was chosen. Once identified this method

would then be employed for all compositions in the range x = 0.1-0.6. The crystallinity of the samples outside of this range do not appear to be affected by changes in the reaction conditions and therefore the synthesis described in section 5.2.3 was employed for these higher sulphate contents.

For all reactions, the concentrations of the solutions were not varied and kept constant at 1M as the effects of reducing this were found to produce poorly crystalline products. As the synthesis of gypsum was found to be successful at 70 °C, the reaction was performed in an attempt to form calcium fluorophosphate. However, this proved to be unsuccessful as the product obtained from this reaction was amorphous and as a result this temperature was no longer considered as suitable for this reaction series. Identical synthetic methods were performed of 40 and 60 °C, temperatures which provided the best quality samples of the two end members of the fluorophosphate doped sulphate series. In total six different synthetic methods were investigated at each temperature and PXRD patterns were collected for each method over the 2θ range 19-35°.

5.3.3 Modifications at 40 °C

As the sample with fluorophosphate composition of x = 0.9 closely resembled that of calcium fluorophosphate, it was deemed reasonable to first of all attempt the modifications to the synthesis at the lower reaction temperature as this is the preferred temperature for the synthesis of the parent fluorophosphate material as discussed previously.

The PXRD patterns of the samples with the composition of $Ca(SO_4)_{0.1}(PO_3F)_{0.9}\cdot 2H_2O$ that were obtained from performing each synthetic method are shown in figure 5.5 with an

outline of the various synthetic methods undertaken to synthesise samples of $Ca(SO_4)_{0.1}(PO_3F)_{0.9}\cdot 2H_2O$ along with the corresponding FWHM values displayed in table 5.3.

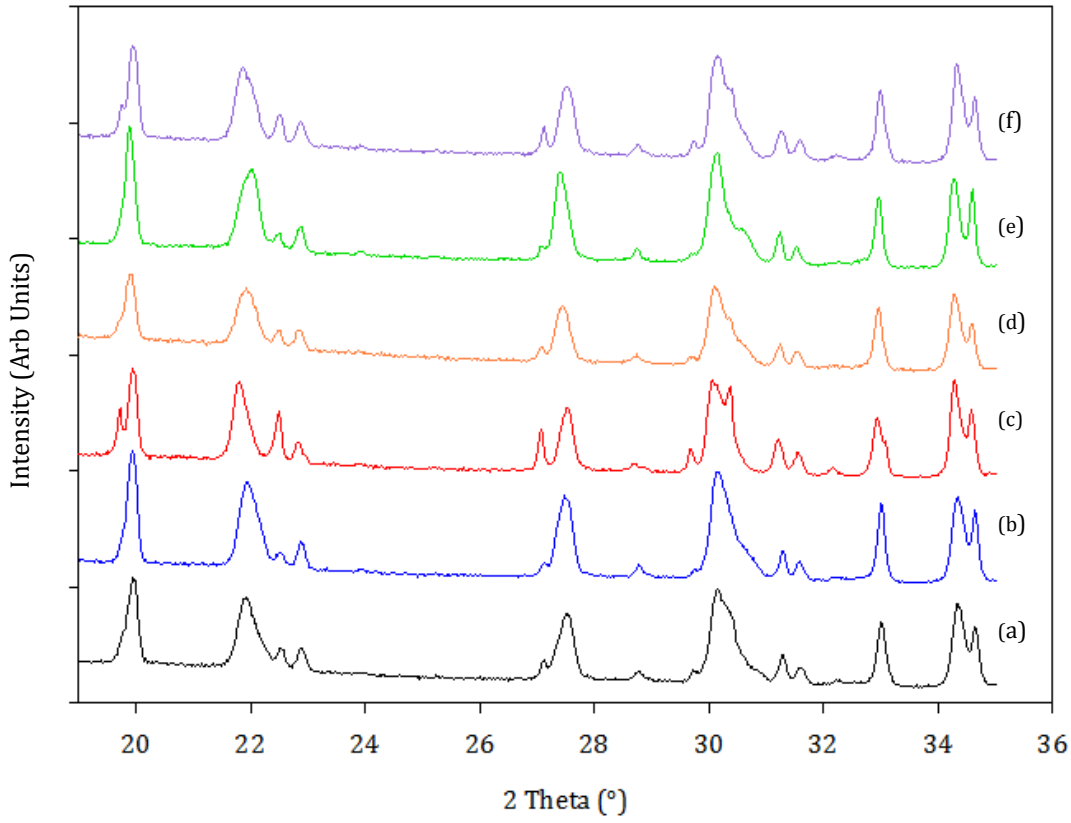

Figure 5.5: Products of $Ca(SO4)_{0.1}(PO_3F)_{0.9}\cdot 2H_2O$ from synthesis modification reactions performed at 40 °C which are described in table 5.3

Table 5.3: FWHM values of the peaks present in the PXRD pattern of $Ca(SO_4)_{0.1}(PO_3F)_{0.9}\cdot 2H_2O$ prepared *via* the different synthetic methods at 40 °C

Synthetic Methods (40 °C)	Volume (cm^3)	$CaCl_2$ Addition Time (minutes)	Stirring Time (minutes)	FWHM 2θ = 19.9°	FWHM 2θ = 21.8°	FWHM 2θ = 27.5°	FWHM 2θ = 32.9°	FWHM 2θ = 34.2°
a	20	30	30	0.214	0.349	0.280	0.167	0.195
b	20	30	-	0.194	0.374	0.298	0.139	0.209
c	50	Dropwise	-	0.157	0.255	0.242	0.242	0.135
d	50	30	-	0.197	0.369	0.264	0.414	0.151
e	50	60	60	0.177	0.372	0.244	0.140	0.181
f	50	60	-	0.169	0.379	0.282	0.158	0.171

The majority of the synthesis methods (*c-f*) were scaled up reactions of the original method (method *a*) which used 50 cm^3 volumes of the required solutions rather than the original 20 cm^3, this was also the case for the synthetic methods attempted at 60 °C). The reasoning behind the scale up of the reactions was so that large enough samples could be made for the neutron experiments but also to see whether the crystallinity of the samples could be improved. The latter was proven to be the possible, as the crystallinity for the products obtained from the scaled up reactions were an improvement on the samples synthesised from the original volume.

Analysis of the diffraction patterns obtained at 40 °C indicated an impurity at 20° 2θ and therefore eliminated synthetic methods *c*, *d*, and *f*, despite the method for the dropwise addition of calcium chloride (method *c*) producing the lowest FWHM values. From the FWHM values of the remaining synthetic methods (*a*, *b* and *e*), method *e* was slightly favoured as this method gave marginally lower FWHM values for the majority of peaks.

5.3.4 Modifications at 60 °C

To determine the influence of temperature, identical synthesis conditions to those carried out at 40 °C were replicated at 60 °C. However, data for only five of the intended six methods could be presented, as samples produced by method *k* produced an amorphous product. The diffraction data for these crystalline products are shown in figure 5.6.

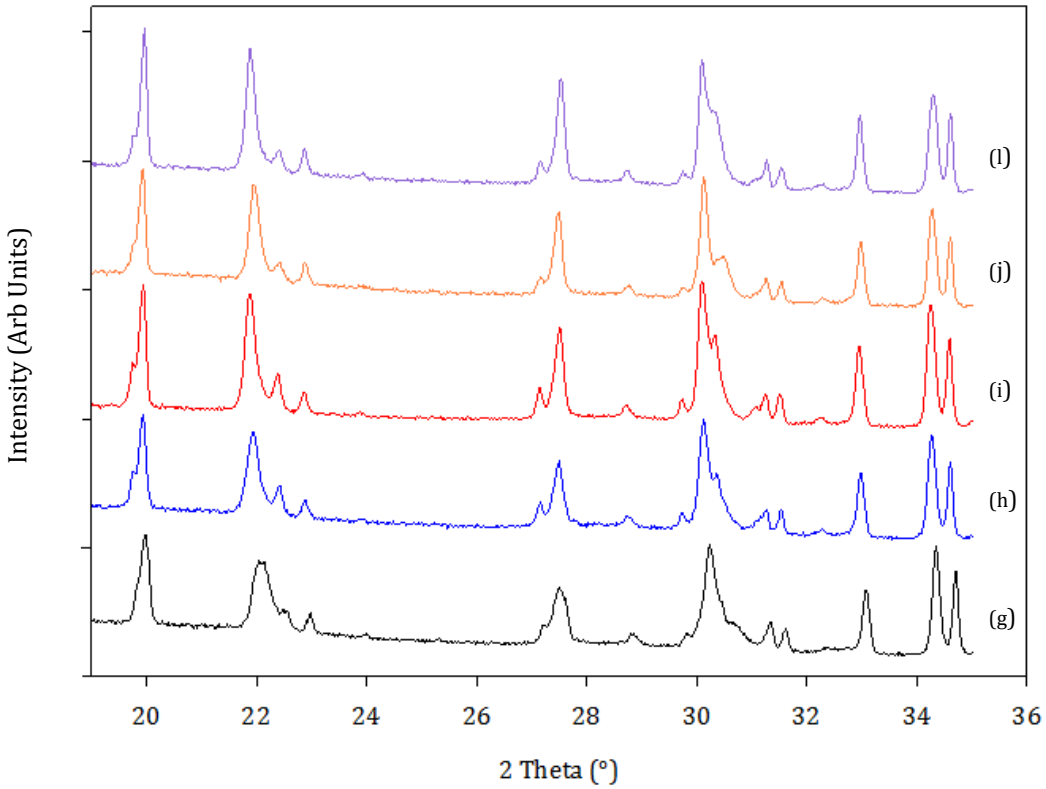

Figure 5.6: Products of $Ca(SO_4)_{0.1}(PO_3F)_{0.9}\cdot 2H_2O$ from synthesis modification reactions performed at 60 °C which are described in table 5.4

Table 5.4: FWHM values of the peaks present in the PXRD pattern of $Ca(SO_4)_{0.1}(PO_3F)_{0.9}\cdot 2H_2O$ prepared *via* the different synthetic methods at 60 °C

Synthetic Methods (60 °C)	Volume (cm^3)	$CaCl_2$ Addition Time (minutes)	Stirring Time (minutes)	FWHM 2θ = 19.9°	FWHM 2θ = 21.8°	FWHM 2θ = 27.5°	FWHM 2θ = 32.9°	FWHM 2θ = 34.2°
g	20	30	30	0.191	0.323	0.258	0.147	0.146
h	20	30	-	0.125	0.205	0.174	0.140	0.166
i	50	Dropwise	-	0.220	0.223	0.182	0.142	0.165
j	50	30	-	0.132	0.201	0.164	0.146	0.136
k	50	60	60	-	-	-	-	-
l	50	60	-	0.116	0.178	0.149	0.124	0.168

Upon inspection of the FWHM values (table 5.4), it was evident that the FWHM values of the peaks in the materials synthesised at 60 °C were considerably smaller compared with those synthesised at 40 °C, suggesting that the samples prepared at 60 °C were more crystalline. Therefore, the preferred synthesis temperature for these reactions was 60 °C. Further analysis was able to conclude that the lowest FWHM values were observed when the x = 0.1 sample was synthesised *via* method *l*.

Having chosen method *l* as the preferred synthetic method, samples with fluorophosphate content of 90-40 mol % (x = 0.1-0.6 in figure 5.3) were re-synthesised using this method and were shown to have improved crystallinity and appeared to be more homogenous. Some initial Rietveld refinements using the PXRD data were performed on these systems in order to establish the effect of fluorophosphate doping had on the lattice parameters.

5.3.5 Compositional Characterisation

Before a detailed structural analysis of the fluorophosphate doped sulphate systems was carried out, further evidence was required to confirm/establish the composition of the materials. Although it has been suggested by powder x-ray

diffraction that the majority of the materials in this series were indeed single phase, techniques such as Raman spectroscopy, XRF and TGA were utilised to further test this hypothesis.

5.3.6 Raman Spectroscopy

The vibrational modes of interest for the fluorophosphate doped sulphate series are those associated with the PO_3F^{2-} and SO_4^{2-} anions and the changes that could occur upon increasing the level of fluorophosphate incorporated/doped into the structure can be monitored. Raman spectra were recorded for all members of the $Ca(SO_4)_x(PO_3F)_{1-x}\cdot 2H_2O$ series and can be seen in figure 5.7.

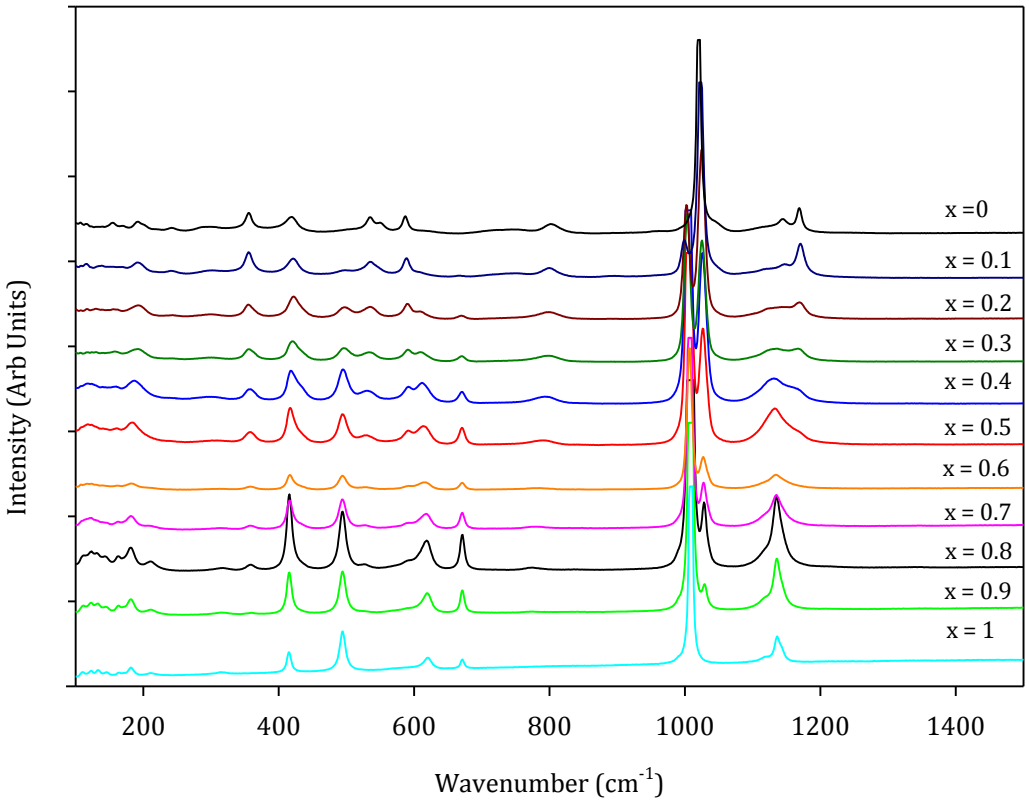

Figure 5.7: Raman Spectra for each member of the $Ca(SO_4)_x(PO_3F)_{1-x}\cdot 2H_2O$ series

All of the vibrations observed in the spectra for each composition of the fluorophosphate doped series correspond to the vibrations expected for both calcium sulphate dihydrate and calcium fluorophosphate, suggesting that fluorophosphate had been successfully doped into the structure of gypsum for which the assignments can be found in appendix 3 section 3.1. The assignments of the PO_3F^{2-} and SO_4^{2-} vibrations for all members of the series were made based on those reported in the literature for $CaSO_4 \cdot 2H_2O$[15] and for similar fluorophosphate materials,[16-17] as the Raman spectrum of calcium fluorophosphate has not previously been reported. The changes observed in the spectra for the fluorophosphate doped materials become evident at the lowest level of fluorophosphate doping (10 mol %, x = 0.9), where additional vibrations at 1029 and 494, 359 cm^{-1} first become apparent which are indicative of the v_2 symmetric stretch and the v_6 $\rho(PO_3)$ vibrational modes of the fluorophosphate unit. These bands are present in addition to the six vibrational modes relating to the sulphate group observed at frequencies of 1136 (v_3), 1013 (v_1), 671, 620 (v_4) 494, 415 (v_2) which are in excellent agreement with those previously reported for gypsum.[15, 18] The symmetric stretching mode of the fluorophosphate unit becomes more apparent as the level of fluorophosphate in the doped systems increases. This is illustrated in figure 5.10 which shows the normalised version of the Raman data in order to clearly show the changes in intensities of the most intense vibrations of both the sulphate (v_1) and fluorophosphate (v_2) units.

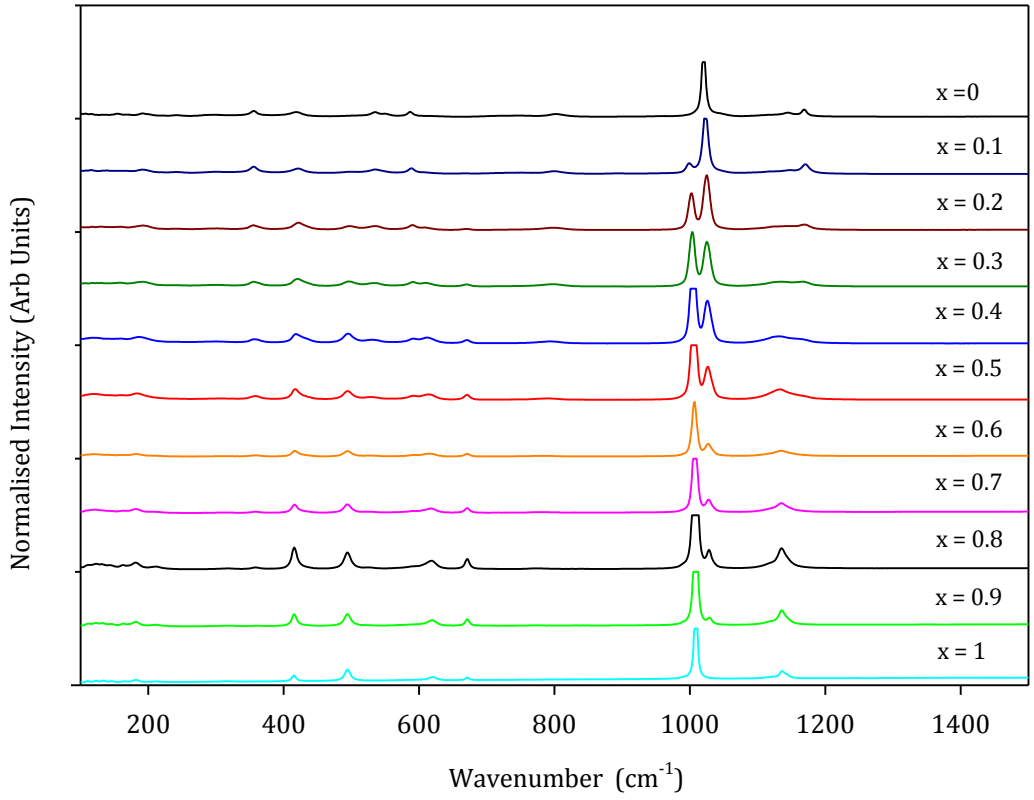

Figure 5.8: Normalised Raman spectroscopy data for each member of the $Ca(SO_4)_x(PO_3F)_{1-x}\cdot 2H_2O$ series

It is clear that the intensity of the v_2, v_s (PO_3) peak at 1029 cm^{-1} increases for all compositions simultaneously as the vibration at 1013 cm^{-1} relating to the v_1 (SO_4) decreases, which is to be expected as level of fluorophosphate is increased and as a result the amount of sulphate present decreases. However, a direct comparison of both the PO_3 and SO_4 vibrations observed in the Raman spectra cannot be made as the peaks appear to be truncated. Although, as the level of fluorophosphate increases the intensity of the PO_3 peak was found to increase whilst the intensity of the SO_4 vibrations decreased as a result of the reduced level of sulphate present. For the material with fluorophosphate content of 70 mol %, a switch in the intensity of the v_2 and v_1 bands is observed, where the v_2 (v_s PO_3) vibration is greater than the v_1 (SO_4). Further evidence to

confirm the presence of fluorophosphate within these materials can found in the region of 700-900 cm^{-1} in the Raman spectra, where the vibration associated with the P-F bond of the PO_3F^{2-} unit can be located at approximately 800 cm^{-1}. As the peak at corresponding to the P-F bond is relatively weak in the parent calcium fluorophosphate phase, identifying the P-F vibration on the stack plot of the doped systems is difficult as the peak becomes less intense as the level of fluorophosphate decreases. However, analysis of the individual spectra clearly shows the presence of the P-F vibration in the fluorophosphate doped materials for compositions where the PO_3F^{2-} content x= 0-0.5 which can be seen in table 2 in appendix 3 section 3.1. From the table, it is noticed that the positions of the peaks relating to both the PO_3 and SO_4 vibrations marginally shift throughout the fluorophosphate doped sulphate series which is thought to be a result of the changing environment.

5.3.7 X-Ray Fluorescence Spectroscopy (XRF)

Although both powder X-ray diffraction and Raman spectroscopy have indicated that fluorophosphate has been successfully doped into the gypsum structure, the actual amounts of fluorophosphate and sulphate present within these materials are yet to be established. For the fluorophosphate doped gypsum systems, the expected increase in levels of fluorophosphate as sulphate decreased was confirmed by Raman spectroscopy. To further support this, X-ray fluorescence can be utilised to investigate the fluorine content within these materials. The results obtained from this study are not quantitative, as the detection of elements lighter than sodium are extremely difficult to quantify using XRF. This is largely due to their relatively low energy X-ray fluorescence being absorbed prior to detection, either within the sample or on route to the detector. Samples were prepared as pressed pellets because loose powders require a mylar film

which absorbs the F^- X-rays and fused beads lose F^- in their preparation. The standard semi quantitative analysis routine on the spectrometer (Quant-Express measurement), which sweeps across the entire X-ray emission spectrum, would be unlikely to detect fluorine given the weakness of the signal. So for the purposes of this investigation the spectrometer was set to only collect data in the region of the emission signal from the fluorine Kα_1 line (34-43° 2θ). This was repeated for each member of the fluorophosphate doped sulphate series. The XRF spectrum obtained for the parent material calcium fluorophosphate is shown in figure 5.9. This method provides a semi-quantitative analysis by simply monitoring the F Kα_1 line intensity and assumes no significant change in the matrix across the dopant range. Given all samples contain the same Ca content and similar structures, this was deemed an acceptable assumption.

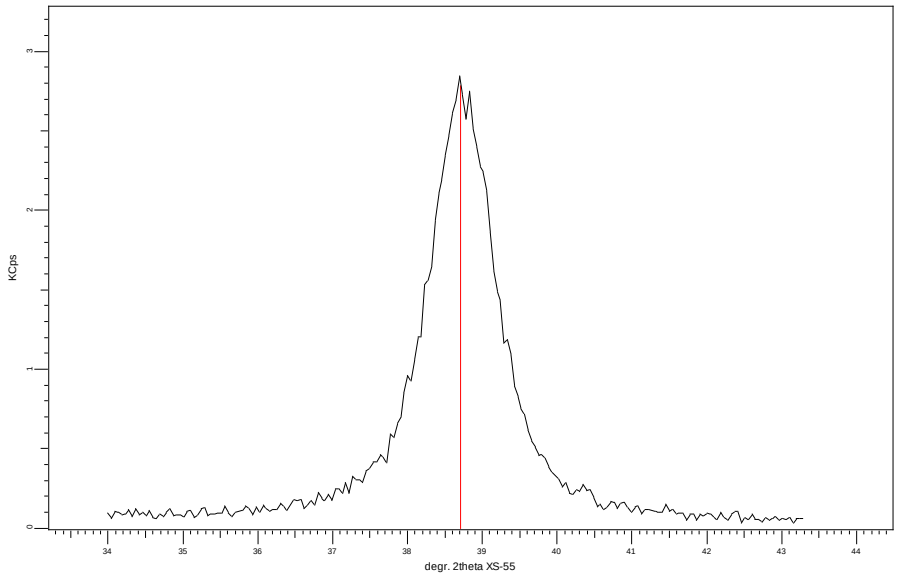

Figure 5.9: Fluorine signal obtained from the fluorine Kα_1 high sensitivity line for calcium fluorophosphate

The spectrum for all compositions were recorded in an identical manner to that of calcium fluorophosphate and the results can be found in appendix 3 section 3.2. From this data, the intensity of the peak corresponding to the fluorine Kα_1 line were plotted

against the weight percent of fluorophosphate used in the reaction mixture for each material (figure 5.10). The results show that there is a clear linear relationship between the relative amount fluorine detected and the expected level of fluorophosphate incorporated into the gypsum structure, as would be expected with a successful synthesis of this solid solution.

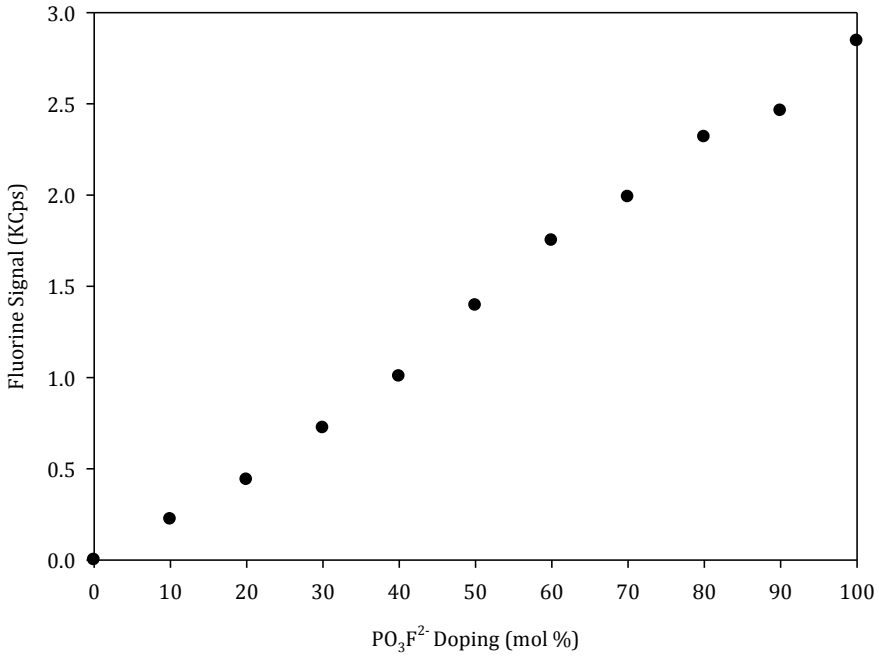

Figure 5.10: Fluorine signal obtained from XRF immediate measurement of fluorine Kα$_1$ high sensitivity line for all members of the Ca(SO$_4$)$_x$(PO$_3$F)$_{1-x}$·2H$_2$O series

5.3.8 Thermogravimetric Analysis (TGA-MS)

When determining the composition of the members of the fluorophosphate doped calcium sulphate series, it is important to consider the number of water molecules associated with these materials. The end members of the series, calcium sulphate dihydrate and calcium fluorophosphate are known to possess two waters of crystallisation and therefore it is likely for members of the doped series to also contain two water molecules. For calcium sulphate dihydrate it is known that under heating the

waters of hydration are lost *via* a two step process, however the process by which calcium fluorophosphate loses its water molecules is unknown. TGA was performed on each member of the $Ca(SO_4)_x(PO_3F)_{1-x}\cdot 2H_2O$ series in order to determine whether the number of waters of hydration and to establish the steps in the process of water loss. Samples with low levels of fluorophosphates of x = 0-0.2 were heated to 250 °C to achieve full dehydration, but members of the series containing fluorophosphate levels > 0.2 had to be heated to 300 °C in order to fully dehydrate the samples.

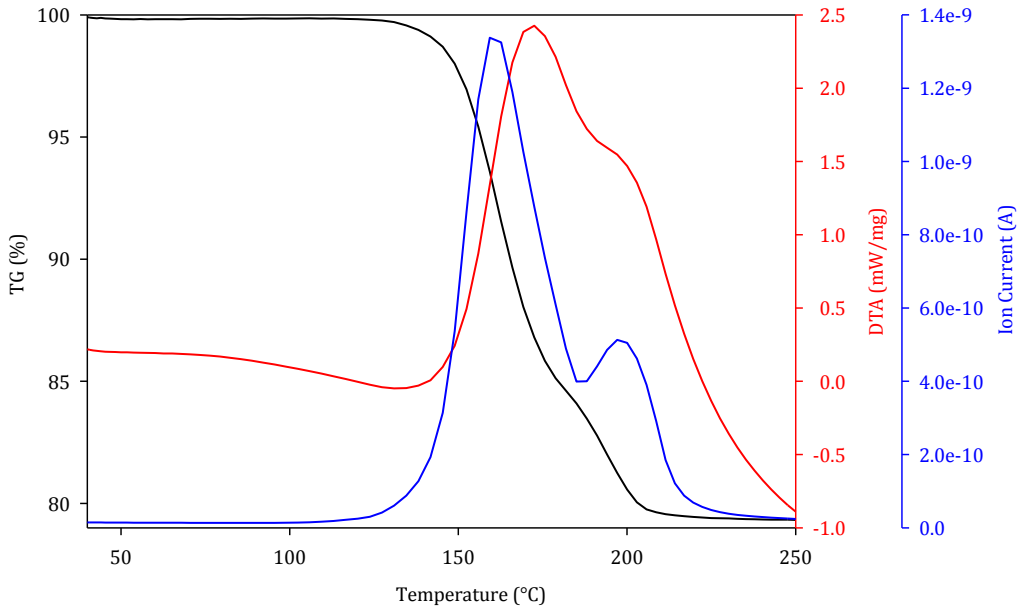

Figure 5.11: Thermogravimetric Analysis Data of Calcium Sulphate Dihydrate, $CaSO_4\cdot 2H_2O$, showing the mass loss (black), DTA (red) and the evolution of water (blue) as indicated by the mass spec data

Figure 5.11 shows the TGA plot of the pure gypsum system. The data shown represents the mass loss (black line), the DTA (red line) and the ion current (blue line) obtained from the mass spectrometer. There are two clear mass loss steps which are signified by a change in gradient of the mass loss line which occur between 120-220 °C until a plateau is observed, indicating that no more mass is being lost beyond this temperature.

The ion current signal of the fragments detected has a mass to charge ratio of 18 which corresponds to that of water. As the mass loss of the material coincides with a peak in the mass spec, this suggests that that the loss of mass can be attributed to the dehydration of gypsum, as no other signal is observed from the mass spectrometer. The DTA line shows the occurrence of an exothermic event at the same point as the mass loss corresponding to the loss of water. The overall mass loss of the system between 40-250 °C corresponds to a loss of 1.97 waters of hydration, a process which occurs in two steps. The first mass loss of 6.32 mg corresponds to a loss of 1.45 waters of hydration at 167 °C, with the remaining 0.52 moles of water lost at 212 °C calculated from a second mass loss of 2.28 mg. The two step process by which gypsum loses its associated water molecules is in keeping with that reported in the literature, which suggests that a loss of approximately 1.5 molecules of water are lost in the first step, this forms the hemihydrate before further losing the remaining 0.5 to form the fully dehydrated anhydrite system, $CaSO_4$.[15, 19] A similar analysis of the TGA data was carried out for each member of the fluorophosphate doped series to determine the overall water content of each material and the number of steps associated with the dehydration process for these systems. The TGA plots obtained for all members of the $Ca(SO_4)_x(PO_3F)_{1-x}\cdot 2H_2O$ series are shown in appendix 3 section 3.3. The numbers of steps associated with the loss of water in these materials are observed in the mass spec data, which suggests that all members of fluorophosphate doped calcium sulphate series predominantly lose water in a two step process. When plotting the ion current for fragments with m/z ratio 18 against temperature, it was possible to identify a trend in the dehydration process for the following compositions x = 1-0.8, 0.7-0.3 and 0.2-0, where the water losses for each occurred in a similar manner which is illustrated in figures 5.12 (a, b and c) respectively.

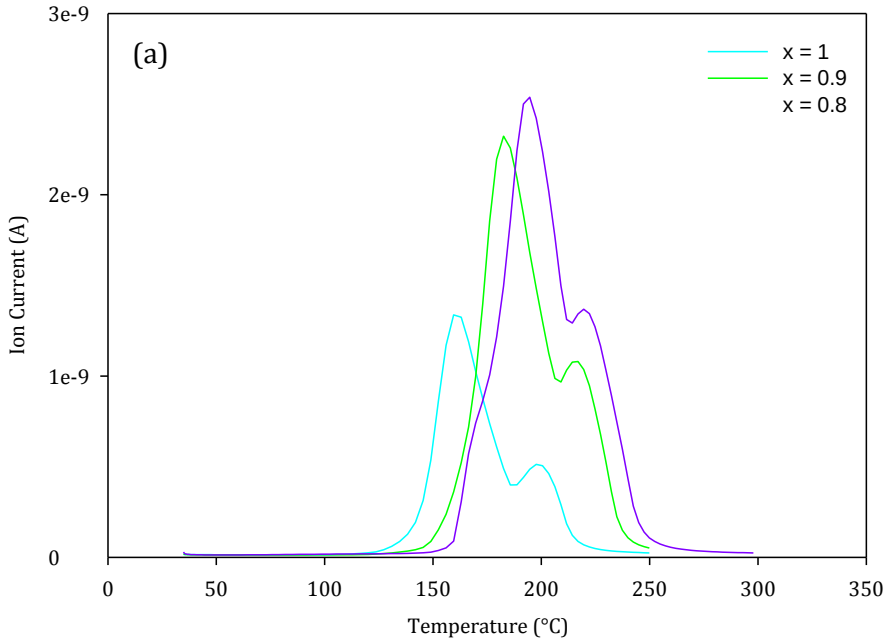
(a)
x = 1
x = 0.9
x = 0.8
Ion Current (A)
3e-9
2e-9
1e-9
0
0
50
100
150
200
250
300
350
Temperature (°C)

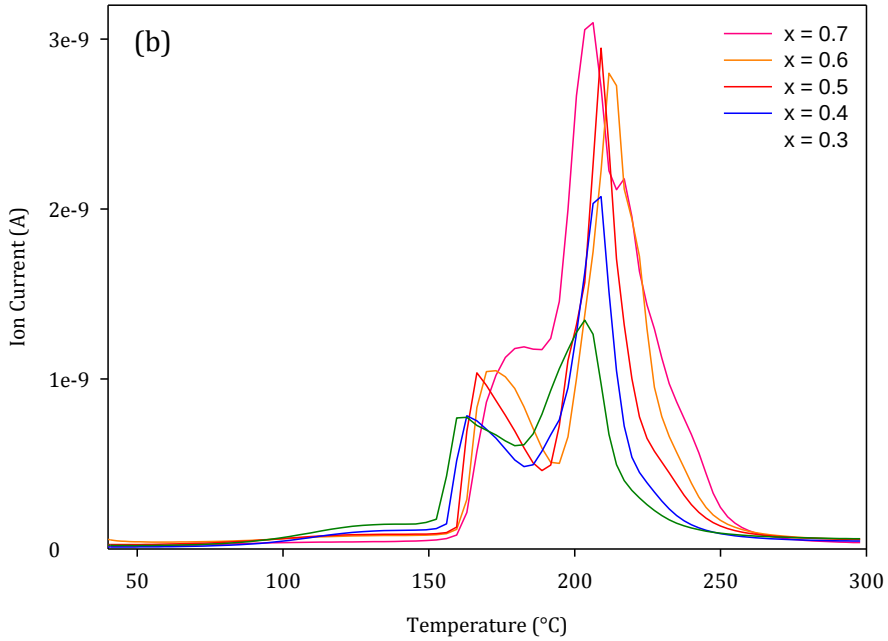
(b)
x = 0.7
x = 0.6
x = 0.5
x = 0.4
x = 0.3
Ion Current (A)
3e-9
2e-9
1e-9
0
50
100
150
200
250
300
Temperature (°C)

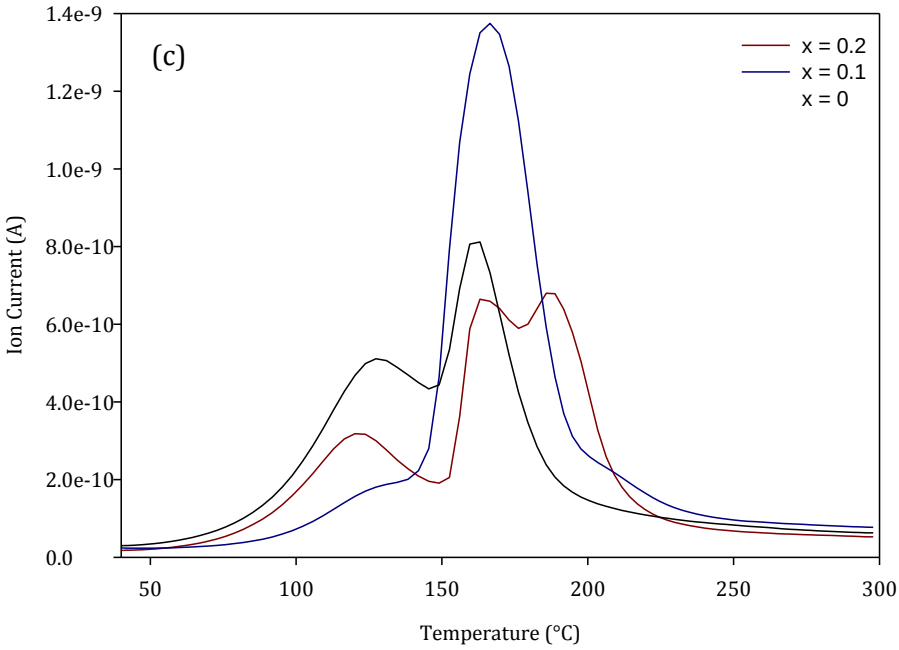

Figure 5.12 (a, b, c): Mass spectrometry data for m/z = 18 attributing to the presence of water in all samples in the fluorophosphate doped sulphate series

For compositions of x = 1-0.8 (figure 5.12 (a)), the first step appears to be the predominant water loss step. This confirmed what would be expected for these materials as they contain relatively low levels of fluorophosphate and the PXRD patterns of these materials confirm that their structures closely resemble that of gypsum. Therefore, the mechanism by which the water molecules are lost is similar to that of gypsum. However, the PXRD pattern of the sample with composition of $Ca(SO_4)_{0.7}(PO_3F)_{0.3}\cdot xH_2O$ also resembles that of gypsum, but the process by which this system loses water differs from that of gypsum. Instead, the water loss process for the x = 0.7 sample follows the trend observed for materials with composition x =0.6-0.3 (figure 5.12 (b)), where the second water loss stage is the dominant step. This is surprising as it would be expected that the waters of hydration for the x = 0.7 sample would be lost in a similar manner to that of gypsum. Materials which consists

predominantly of fluorophosphate (x = 0.2-0 and shown in figure 5.12 (c)), to a certain degree follows the same trend as the x=0.7-0.3 materials as the second peak observed in mass spec data is clearly larger for both x = 0.2-0.1 but for the pure calcium fluorophosphate material this feature is not quite so clear, suggesting that the loss of water in the second step may only be marginally greater than the water lost in the first. The addition of a shoulder peak on the mass spec data for the x = 0.2 sample suggests that the second loss of waters occurs in two stages rather than one as previously seen for the majority of the systems. It is unsurprising that the mass spec data for this sample deviates from what may be expected as this is the composition where the structural data suggests a possible transition between triclinic systems. The amount of water lost for each material was calculated and the results are illustrated in figure 5.13 and are shown table 3 in appendix 3 section 3.3 along with data for an identical batch of samples which TGA measurements were replicated. The data include the exact temperature each water loss occurred.

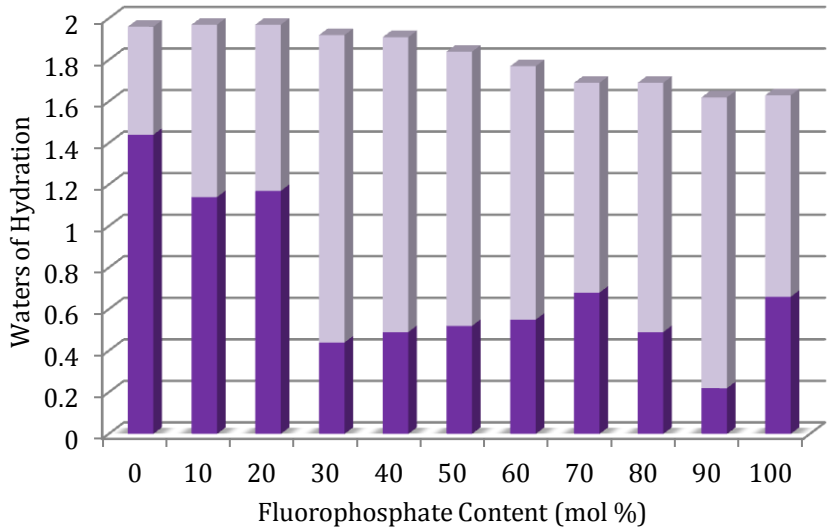

Figure 5.13: Summarised TGA data showing the overall water content and the waters of hydration lost during each water loss step (water loss 1 dark purple, water loss 2 light purple) for each member of the fluorophosphate doped sulphate series

The results show the materials with lower fluorophosphate content contained between 1.97-1.91 waters (batch 2) of hydration for x = 1-0.6 but as level of fluorophosphate increased, the overall number of water molecules associated with each material decreased. It is also interesting to note that the temperature required to fully dehydrate the samples decreased from gypsum to calcium fluorophosphate, suggesting that it is easier for calcium fluorophosphate to lose its waters of hydration than it is for gypsum. This can be explained by considering the structures of both systems.

5.3.9 Structural Implications

It is clear that incorporating fluorophosphate into the calcium sulphate dihydrate structure results in some significant structural changes as suggested by the changes in lattice parameters from the Rietveld refinement data. Not only is there a clear transition from the monoclinic gypsum system (x = 0.7) to the triclinic system (x = 0.6) adopted by calcium fluorophosphate, but a further transition between triclinic systems is suggested between x = 0.3 and 0.2, however the nature of these transitions appear very complex. The modification of gypsum system has proven to be successful, by replacing the tetrahedral SO_4^{2-} unit for the isoelectronic PO_3F^{2-} unit which is of a similar size. The structures of both calcium sulphate dihydrate and calcium fluorophosphate themselves are very similar and are shown in figure 5.14 (a and b) respectively.

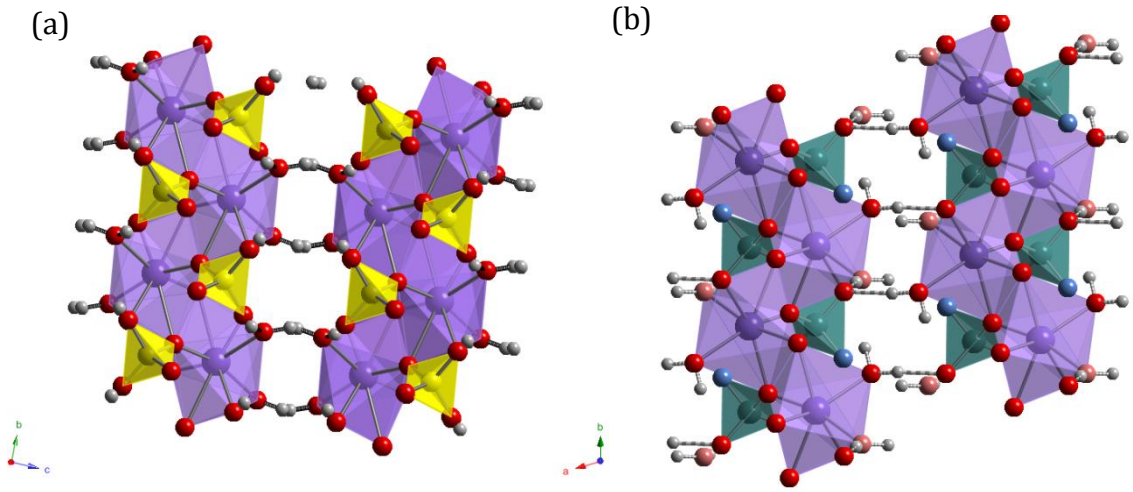

Figure 5.14: Structures of Calcium Sulphate Dihydrate (a) and Calcium Fluorophosphate (b) Calcium atoms (purple), Phosphorus atoms (teal), Sulphur atoms (yellow), Oxygen atoms (red), Fluorine atoms (blue) and Hydrogen atoms (pale grey)

The structure of calcium fluorophosphate is said to resemble that of calcium sulphate dihydrate (gypsum), as both systems contain calcium polyhedron and tetrahedral units of either the sulphate or fluorophosphate anions. In calcium sulphate dihydrate, the calcium binds to eight oxygen atoms, six of which are from four different sulphate groups and the remaining two are from water molecules. In contrast, calcium fluorophosphate consists of calcium atoms are bonded to seven oxygen atoms, five from four different PO_3F^{2-} groups and the other two from water molecules. The main difference in between these two structures, apart from the replacement of an oxygen atom for fluorine in the tetrahedral unit is the hydrogen bonding network. In calcium sulphate dihydrate, atom O1 acts as a hydrogen bond acceptor and can accept two hydrogen bonds utilising both of the hydrogen bonds on the water molecules. In calcium fluorophosphate, one of the O1 atoms from the sulphate tetrahedral unit is now replaced by fluorine, which does not participate in hydrogen bonding or cation bonding[20] and points away from the channels where the water molecules lie. As a result, the hydrogen bonding network of the system is reduced. As only one hydrogen bond is observed for

calcium fluorophosphate, the structure can be described as being less rigid compared to gypsum, as the molecule is less restricted and has more freedom to twist.

In order to attempt to understand the structural changes which occur, Neutron diffraction studies were performed to provide a more detailed structural analysis of these systems.

5.3.10 Rietveld Refinements

Rietveld refinements were performed on the NPD data obtained on all deuterated samples from the fluorophosphate doped calcium sulphate series with compositions x = 1, 0.8, 0.6, 0.4, 0.3, 0.2 and 0. The data collected from the 90° and the back scattering banks (90-170°) were used for the refinements which were carried out using background function 1 (shifted Chebyschev) and profile function 4.[21-22] The latter was used to correct for anisotropic line broadening which was a prominent feature in the refinements of the doped samples. Despite being known structures, refinements of both end members calcium sulphate and calcium fluorophosphate were performed for the aid of comparison to the doped members of the series. The structural parameters obtained from the refinements of both the pure calcium sulphate dihydrate and calcium fluorophosphate are in excellent agreement with those reported in the literature.[20,23] Given that the changes in the lattice parameters are quite significant upon increased doping with fluorophosphate, the doped samples could not be refined from the original starting models (gypsum and calcium fluorophosphate). In order to assess the level of deuteration, the refinements of calcium sulphate dihydrate and the x = 0.8 system included both deuterium and hydrogen atoms, constraining the atomic coordinates, temperature factors to be the same and setting the fractional occupancies to sum to 1. It

was suggested by the fractional occupancy values that the deuteration experiments were successful and that the level of deuteration was suggested as being between 92-97 %. Due to the success of the deuteration, subsequent refinements did not include protons. In the refinements of the doped samples, both phosphorus and sulphur were refined on the same site. The S terms relating to Stephens broadening were refined and were seen to improve the fit in many cases, however, there appeared to be little dependence on the broadening with certain *hkl* values, this appeared to be more random suggesting that the broadening occurred in random direction rather than in a specific direction. The temperature factors for the deuterium atoms were relatively high but were not unusual for water molecules. It was hoped that analysis of these systems would give an insight to the structural changes upon increasing the level of fluorophosphate. However, to date, it has not been possible to extract detailed structural information from the NPD refinements, as the quality of the fits for various members of the series are poor, which is particularly evident in the x = 0.6 system which is considered to be a highly disordered system due to the apparent broadening of the peaks. Therefore the discussion of the data will be limited to the extracted lattice parameters alone. Figure 5.15 a and b shows the NPD Rietveld refinement of the $Ca(SO_4)_{0.8}(PO_3F)_{0.2}\cdot 2H_2O$ system, which displays a reasonable agreement between the experimental and calculated data.

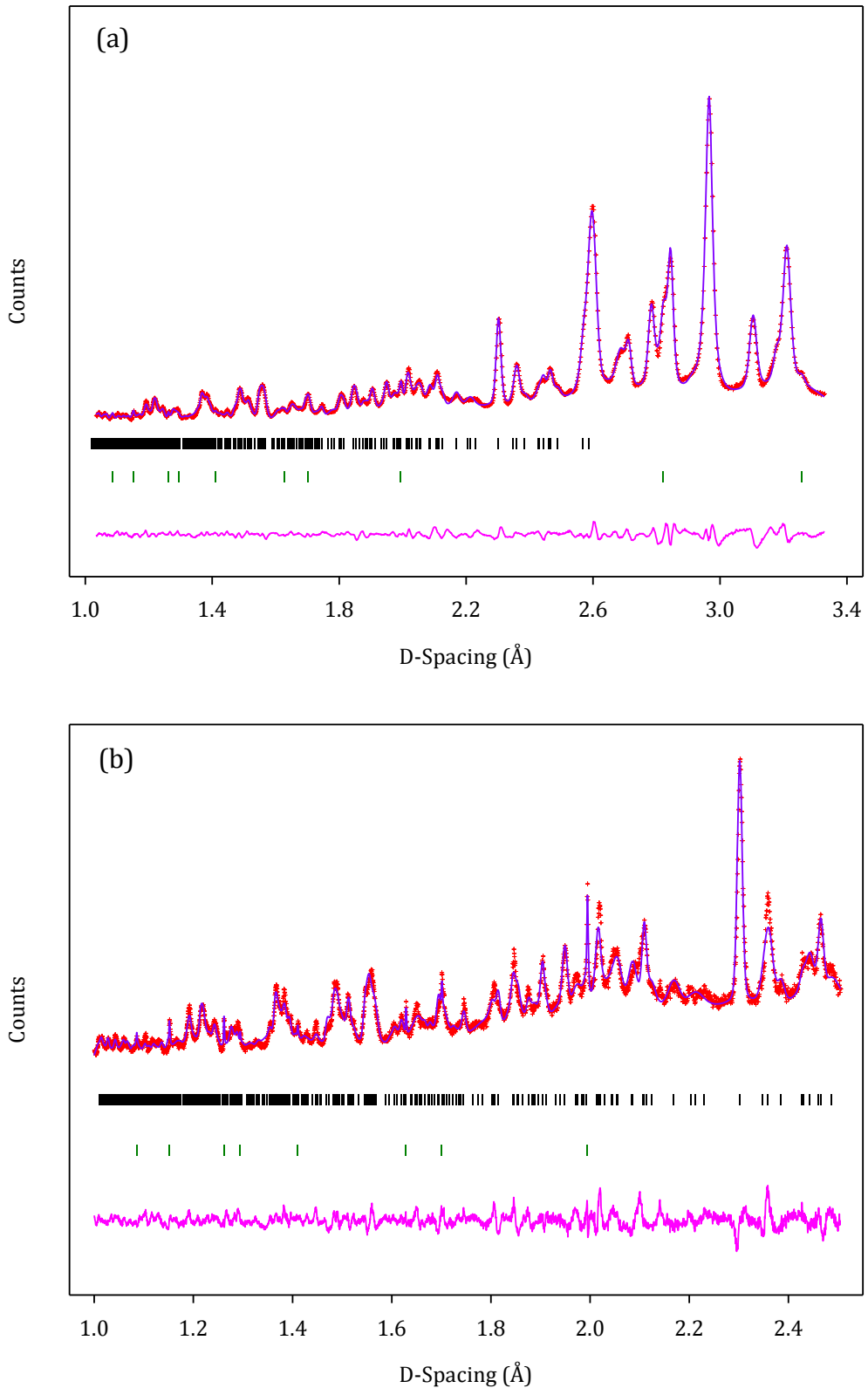

Figure 5.15: Final observed (red), calculated (purple) and difference profiles (pink) of the NPD refinement of $Ca(SO_4)_{0.2}(PO_3F)_{0.8}\cdot 2H_2O$(a) 90° bank (b) back scattering bank Reflection positions for $Ca(SO_4)_{0.2}(PO_3F)_{0.8}\cdot 2H_2O$ and NaCl are shown as vertical tickmarks (black and green respectively)

5.3.11 Converted Lattice Parameters

In order to appropriately compare the lattice parameters of all members of the fluorophosphate doped sulphate system, a common unit cell was established with the help of Kevin Knight ISIS station scientist for HRPD, which used a matrix transformation to convert the original triclinic unit cell ($P\bar{1}$) adopted by calcium fluorophosphate to a pseudo monoclinic unit cell with space group $I\bar{1}$, Details of the matrix, unit cell conversion and tabulated data of the original and converted lattice parameters are shown in appendix 3 section 3.5.

Figure 5.16 shows the lattice parameters for the NPD data of the fluorophosphate doped sulphate systems, which have been converted to a common unit cell $I\bar{1}$. These parameters are seen to vary upon increasing the level of fluorophosphate. The errors were calculated from the original error on the lattice parameters generated by GSAS, this gave the maximum and minimum values for that parameter which were then re-entered into the various equations for the unit cell conversion (see appendix 3 section 3.5) in order to find the maximum and minimum values possible for the errors from which the maximum error value was then used as the final error.

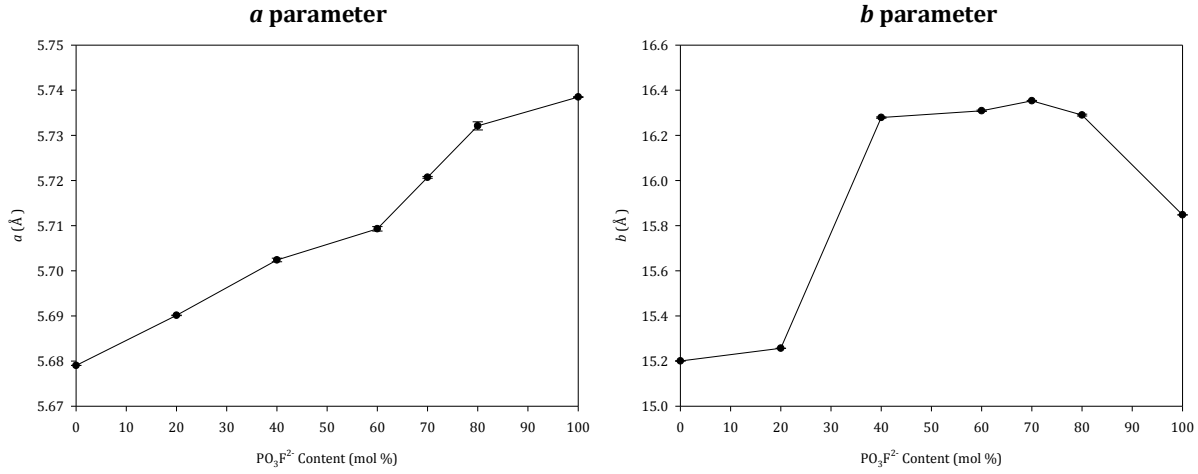

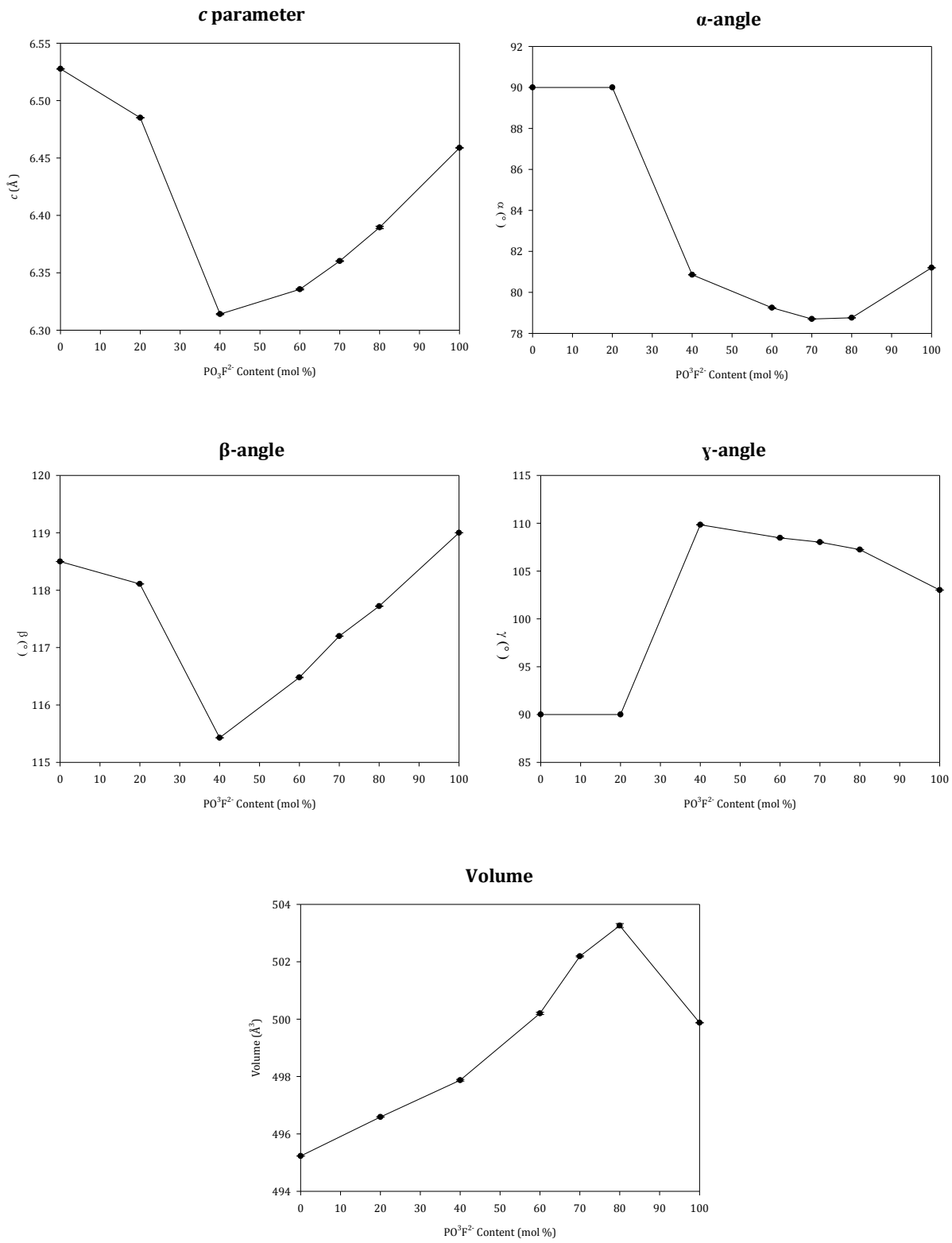

Figure 5.16: Refined unit cell parameters of fluorophosphate doped sulphate materials converted to a common unit cell $I\bar{1}$ (PO_3F^{2-} 0-100 mol %)

The unit cell parameters observed from the NPD data can be seen to have very small errors. The trends observed in the unit cell parameters from the NPD data confirm those findings from the PXRD patterns, that two structural transitions are observed within this solid solution series. The transitions are observed for compositions between 20-40 (x = 0.8-0.6) and 70-80 (x = 0.3-0.2) mol % fluorophosphate, which relate to the monoclinic to triclinic and the triclinic to triclinic transitions respectively. In the PXRD patterns the monoclinic to triclinic transition was evident for compositions containing 20-30 mol % fluorophosphate not between 20-40 mol % as suggested from the NPD lattice parameter plots (figure 5.16). This was due to time constraints with NPD time resulting in some samples within the series not being measured. The monoclinic to triclinic transition is most evident from the significant changes with the *b*, *c*, α and β unit cell parameters whilst a transition within the triclinic systems is indicated from the changes in the *a*, *b*, and γ parameters and also in the volume of the converted unit cell.

5.3.12 SEM

Images from various members of the $Ca(SO_4)_x(PO_3F)_{1-x}\cdot 2H_2O$ series with compositions with compositions x = 1, 0.75, 0.5, 0.25 and 0 were collected to compare how the morphologies of the materials change upon increasing the PO_3F^{2-} content. This range of samples was investigated in order to represent members over the whole range. Figure 5.17 shows the images of both end members of the series calcium sulphate (a) and calcium fluorophosphate (b).

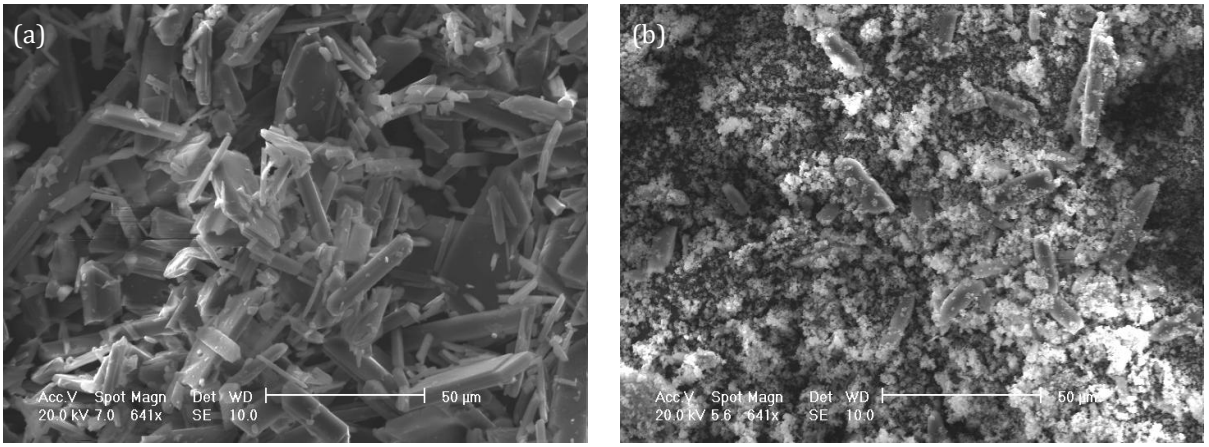

Figure 5.17: Scanning Electron Microscope Images of gypsum (a) and calcium fluorophosphate (b)

The needle like appearance shown in figure 5.17 (a) resembles that of the well known calcium sulphate dihydrate crystals.[24-26] The morphology of $CaPO_3F{\cdot}2H_2O$ observed in figure 5.17 (b) differs to that of calcium sulphate dihydrate and consists mainly of aggregated clusters of fine calcium fluorophosphate particles with a few needle like crystals. No literature regarding the morphology of calcium fluorophosphate has previously been reported. The morphology of the crystals in the doped systems is dependent on the level of fluorophosphate present. When the amount of fluorophosphate within the structure is increased, more of the small aggregated particles are observed, with the crystals being less defined compared to the plate like crystals observed in the systems which predominantly contain sulphate. Scanning electron images for the doped systems are shown in appendix 2 section 2.5.

5.3.13 Cements

To assess the potential of these doped gypsum systems to act as sustainable bone cements, some initial cement reactions were attempted. This involved the materials to be dehydrated and rehydrated to form the cements (Eqn. 5.1). The quality and integrity of the cements were assessed by the appearance of the cements. It is important that

during the rehydration process, just enough water is added in order to form a paste and the material is well mixed. If too much water is added, small air pockets can form and as a result can weaken the strength of the cement. On the other hand, if too little water is added, the cement will set too quickly. This is not an ideal property for bone cements, as the time between the formation and setting of the cement needs to be sufficient enough to allow the cement to be implanted into the defect site of the body. The formation of gypsum cements is well known but no previous studies have been carried out which explore the cementing reactions with fluorophosphate containing materials. The method described in section 5.2.5 was followed for the formation of the cements.

Equation 5.1: Formation of calcium sulphate dihydrate cements

$$CaSO_4 \cdot 2H_2O \xrightarrow{\text{Heat to } 170\ ^\circ C} CaSO_4 \cdot 0.5H_2O \xrightarrow{+\ H_2O} CaSO_4 \cdot 2H_2O$$

Cements of gypsum are formed from partially dehydrating the dihydrate material at 170 °C, losing one and a half waters of hydration to form the hemihydrate, $CaSO_4 \cdot 0.5H_2O$. Formation of the intermediate hemihydrate phase was confirmed by X-ray diffraction before the addition of water to rehydrate and reform the dihydrate in cement form. As there is no literature regarding cementing reactions of fluorophosphate materials, the dehydration of the cements relied heavily on the TGA data in order to establish at what temperatures the waters of hydration were lost for each member of the series. Analysis of the TGA data confirmed that the majority of the fluorophosphate doped series contained two water loss steps, except for samples with fluorophosphate content of x = 0.3 and 0.8, in which it appeared that three water loss steps had occurred For the fluorophosphate containing compounds, it was decided to dehydrate at

temperatures similar to that used for gypsum. Full dehydration occurred for samples containing high levels of fluorophosphate x = 0.8-1, as the product from PXRD was confirmed to be amorphous due to the loss of water causing a collapse of the structure, whilst materials with fluorophosphate content x = 0.7-1 would undergo partial dehydration, as the temperatures used would not be sufficient to fully dehydrate the samples. The corresponding PXRD patterns of these materials closely resembled those of the as synthesised materials.

The initial cement formation of each member of the $Ca(SO_4)_x(PO_3F)_{1-x}\cdot 2H_2O$ series proved to be successful on appearance. The strength of these cements were monitored by touch alone with the cement for calcium sulphate dihydrate proving to be the strongest, with calcium fluorophosphate also proving to be relatively strong along with the compositions close to both end members. Once removed from the mould, the intermediate systems in the series x = 0.5-0.6 immediately lost their integrity, suggesting that these cements were particularly weak, which is unsurprising given that these are the most disordered systems in the series. Many of the cements proved to have defects (holes) on the surface or within the cement itself caused by loading the cement paste into the mould. This problem would need to be addressed if these materials were to be considered for strength testing as these defects would weaken the cements and therefore the results of the test would be invalid.

5.3.14 Solubility

Another property which needs to be considered when investigating the properties of bone replacement materials is the resorbability. One of the main drawbacks with using calcium sulphate dihydrate as a bone replacement material is its high solubility *in vivo*. The cement form of $CaSO_4\cdot 2H_2O$ was found to resorb too quickly,

not giving the new bone sufficient time to grow in the defect site. As the solubility of fluorophosphates have not previously been investigated, it would be important to do so, particularly within the calcium sulphate-fluorophosphate systems in order to see whether the solubility of the fluorophosphate doped sulphate systems would be an improvement compared to gypsum. Initial studies were undertaken using cements of the parent materials, calcium sulphate dihydrate and calcium fluorophosphate where the appearance of the cements was monitored over a period of 4 weeks in a container of distilled water. It was found that the cement formed from calcium fluorophosphate had retained its shape and integrity whilst the calcium sulphate dihydrate cement had disintegrated and resembled the consistency of a powder. From the appearance of the cements, it could be suggested that calcium fluorophosphate appears less influenced by the water and therefore potentially less soluble than calcium sulphate dihydrate. The suggestion of better integrity towards water exposure is very encouraging. Much further work is necessary to further access this. These include performing identical experiments using the doped materials to understand how the solubility is affected by varying amounts of fluorophosphate. At present, these solubility results are very encouraging but still somewhat speculative.

5.4 Conclusions

To conclude, the formation of the $Ca(SO_4)_x(PO_3F)_{1-x}\cdot 2H_2O$ solid solution series was successfully synthesised *via* a precipitation reaction in which the reaction conditions were optimised in order to improve the crystallinity and reduce the inhomogeneity which was observed some of the fluorophosphate doped systems, in particular those compositions which contain high weight percentages of

fluorophosphate, $Ca(SO_4)_x(PO_3F)_{1-x}\cdot 2H_2O$. Confirmation that fluorophosphate had been directly doped into the calcium sulphate dihydrate structure was initially obtained from powder X-ray diffraction, where significant shifts in the positions of the peaks were observed, particularly for those systems which resemble the structure of calcium fluorophosphate, suggesting that the structure of calcium fluorophosphate is more susceptible to structural changes than calcium sulphate dihydrate. Data from both Raman spectroscopy and XRF provide further evidence to confirm fluorophosphate doping within the structure of calcium sulphate. Results from TGA measurements determined that the overall water content of these systems and showed that the majority of these materials lose water in a two step process. As expected, these materials contain approximately two waters of hydration, similarly to both parent materials. This appeared to be the case for the majority of these materials but those with high fluorophosphate content including calcium fluorophosphate itself proved to contain slightly lower water contents of x = 1.3 to 1.7. Initial Rietveld refinements of the PXRD suggested two structural transitions between compositions where x = 0.2-0.3 and 0.7-0.8 which relate to a monoclinic-triclinic and a triclinic-triclinic transition respectively. These transitions were later supported by NPD studies but they could not be confirmed as full structural analyses were not possible. This was due to the poor quality of the data, modelling of the anisotropic line broadening features and the complexity of the structures. The initial solubility study appeared to be encouraging as it was suggested that calcium fluorophosphate could potentially be less soluble than gypsum as it appeared to be less influenced by the presence of water and retained its structural integrity. This could indicate that other members of the $Ca(SO_4)_x(PO_3F)_{1-}$

$_x \cdot 2H_2O$ series could exhibit similar properties, particularly those with higher fluorophosphate content.

5.5 References

1. H. Dreesman, *Uber Knochrnplombierung. Beitr Klin Chir*, 1892, **9**, 804-810.
2. C. L. Peters, J. L. Hines, K. N. Bachus, M. A. Craig and R. D. Bloebaum, *Journal of Biomedical Materials Research Part A*, 2005, **76**, 456-462.
3. K. C. Boatright and S. D. Boden, *Biology of spine fusion: In Lieberman G.E. Friedlaender. Editors. Bone regeneration and repair: Biology and Clinical Applications*, Human Press New Jersey, 2005.
4. L. F. Peltier, *American ournal of Surgery* 1959, **97**, 311-315.
5. L. F. Peltier and R. H. Jones, *Bone Joint Surgergy American volume*, 1978, **60**, 820-822.
6. S. Jalota, S. B. Bhadin and A. Cunyet-Tas, *American Mineralogist*, 2008, **93**, 1530-1537.
7. A. F. Schilling, W. Linhart, S. Filke, M. Gebauer, T. Schinke, J. M. Reuger and M. Amling, *Biomaterials*, 2004, **25**, 3963-3972.
8. G. H. Lee, J. G. Khoury, J. Bell and J. A. Buckwater, *Iowa Orthopaedic Journal*, 2002, 35-38.
9. A. L. Ladd and A. T. Lee, *In R.H. Gelberman Editor. The wrist (master techniques in orthopaedic surgery) Lippinncott, Williams and Wilkins. Pennsylvania*, 2009.
10. A. Gisep and B. Rahn, *European Celsl Materials Journal*, 2004, **7**, 34-35.
11. W. R. Moore, S. E. Greaves and G. I. Bain, *ANZ Journal of Surgery*, 2001, **71**, 354-361.
12. M. D. Vlad, E. V. Sindilar, M. L. Marinoso, I. Poeata, R. Torres, J. Lopez, M. Barraco and E. Fernandez, *Acta Biomaterialia*, 2010, **2**, 607-616.
13. Wright Medical Technology, Product Overview http://www.wmt.com/prodense/product_overview.asp.
14. S.-T. Liu and G. H. Nancollas, *Journal of Crystal Growth*, 1970, **6**, 281-289.
15. H. Chang, P. Jane Huang and S. C. Hou, *Mater. Journal of Chemical Physics*, 1999, **58**, 12-19.
16. M. Weil, M. Puchberger and E. J. Baran, *Inorganic Chemistry*, 2004, **43**, 8330-8335.
17. M. Weil, M. Puchberger, E. Fuglein, E. J. Baran, J. Vannahme, H. J. Jakobsen and J. Skibsted, *Inorganic Chemistry*, 2007, **46**, 801-808.
18. B. J. Berenblut, P. Dawson and G. R. Wilkinson, *Spectrochimica Acta Part A: Molecular Spectroscopy*, 1973, **29**, 29-36.
19. C. A. Strydom, D. L. Hudson-Lamb, J. H. Potgieter and E. Dagg, *Thermochim. Acta*, 1995, **269–270**, 631-638.
20. A. Perloff, *Acta Crystallographica Section B-Structural Crystallography and Crystal Chemistry*, 1972, **B 28**, 2183-2191.
21. V. Dreele, 1990.
22. P. W. Stevens, *Jouranl of Applied Crystallography*, 1999, **32**, 281-287.
23. B. F. Pedersen, *Acta Crystallographica Section B-Structural Crystallography and Crystal Chemistry*, 1982, **B38**, 1074-1077.
24. M. G. Lioliou, C. A. Paraskeva, P. G. Koutsoukos and A. C. Payatakes, *Journal of Colloid and Interface Science*, 2006, **303**, 164-170.
25. M. R. Christoffersen, J. Christoffersen, M. P. C. Weijnen and G. M. Van Rosmalen, *Journal of Crystal Growth*, 1982, **58**, 585-595.
26. J. Zhang and G. H. Nancollas, *Journal of Crystal Growth*, 1992, **118**, 287-294.

CHAPTER 6:

Investigation into Phosphate Stabilised Amorphous Calcium Carbonate (ACC)

6.1 Introduction

As described in chapter 1, there are two types of amorphous calcium carbonate: biogenic and synthetic. The biogenic forms are often stabilised within the host organism, whilst the synthetic forms are highly unstable. Biogenic ACC is the common constituent of mineralised tissues in a number of organisms.[1] Biogenic samples of ACC can be further differentiated from one another by determining whether they have long term stability (remain as ACC) or are transient (subsequently transforming into a crystalline phase).[2] Stable phases of ACC are used in organisms to act as a mechanical stiffner of mineralised tissue and these are believed to contain one water molecule per carbonate unit compared to the transient form which is anhydrous. The first example which identified ACC acting as a transient precursor was in a species of sea urchin larval spicules (Paracentrotus lividus) during growth, where the transformation of ACC into calcite was observed.[3] Weiss et al[4] showed that ACC was used for a similar function in larvae of molluscan bivalves, where the product of crystallisation of ACC is not calcite but aragonite, another example of the stable $CaCO_3$ polymorphs. Through the analysis of other sea urchin species, the co-existence of two calcium polymorphs was found.[5-6] The separate layers of both calcite and ACC were identified through the use of powder x-ray diffraction and scanning electron microscopy. Although, in the case of the ascidian Pyura

Pachydermatina, its antler (body) spicules are entirely composed of ACC.[6] Despite all of these organisms forming ACC for a specific purpose, the polymorph of ACC that precipitates was found to vary for each species.

In order to further understand its role in the process of biomineralisation, there is an obvious need to produce ACC synthetically. ACC was first synthesised in vitro by Johnston et al.[7] using supersaturated solutions of calcium chloride ($CaCl_2$) and sodium carbonate (Na_2CO_3).[7] This is the simplest method for ACC formation but alternative/other methods have been used to produce different $CaCO_3$ polymorphs. One way of forming these is by the double injection method. This is where the simultaneous addition of Ca^{2+} and CO_3^{2-} ions from solution occurs.[8-11] An alternative method is via CO_2 diffusion.[12-14] Studies on this aqueous system (Na_2CO_3-NaOH-$CaCl_2$) have shown that ACC can successfully be precipitated from solution. Producing amorphous calcium carbonate on a laboratory scale presents a significant challenge as it is not straightforward to mimic the processes which occur naturally in several organisms. ACC's inherent instability and eagerness to form the thermodynamically more stable polymorph calcite requires complete control of the reactions and their outcomes. Subtle changes to the reaction conditions and the reagents can have significant effects on the overall reaction, influencing the morphology and the polymorph that is formed. Kojima et al showed that altering the pH of the Na_2CO_3-NaOH-$CaCl_2$ system affects the thermal behaviour of ACC.[15] When the pH of the mother solution is < 13, the crystallisation temperature of ACC is lower compared to crystallisation temperature of amorphous basic calcium carbonate phase, (ABCC) which is formed at higher pH (> 13.5).[16] This

demonstrates that both the crystallisation temperature and the amorphous phase are dependent on pH.

Temperature variation is one of the most influential factors in controlling the formation of a specific polymorph or a mixture of polymorphs.[17-18] At low temperatures, the formation of calcite and vaterite has been reported compared to the presence of calcite and aragonite formed at high temperatures. In the temperature range of 40-50 °C a mixed phase product of all three crystalline calcium carbonate polymorphs was observed.[19] Phase transitions between the different calcium carbonate polymorphs can be induced through stainless steel ball milling.[20] As with biogenic ACC, multiple techniques such as NMR,[21] EXAFS, Raman, Infrared and PDF have been used to identify in order to characterise the various calcium carbonate polymorphs including the structure of synthetic ACC.[22-23] Whilst PXRD provides no information regarding the structure, it is useful for identifying crystalline polymorphs of calcium carbonate. For synthetic ACC, results have concluded that there is no long range order beyond 15 Å rendering the resulting product as amorphous.[23]

It is well known that exposure of synthetic ACC to water causes the immediate transformation to calcite (or other crystalline forms). However, the exposure of ACC to some chemical species has been reported to inhibit the formation of the crystalline materials. Controlling this reactivity could be a potential route to explore new materials and to further understand ACC's role in naturally occurring biological mechanisms, including biomineralisation. In order to achieve this, ACC will be synthetically produced and will be used as a reactant and so allowing potential to explore the role that ACC may play in different reactions. Of particular interest will be reactions with different

phosphate species, as biogenic ACC has been reported to contain traces of simple inorganic species such as phosphate ions, which potentially inhibit the crystallisation of ACC.[2, 24] A previous investigation by the Wright group has observed that synthetic ACC exposed to phosphate ions from Na_2HPO_4, leads to the formation of poorly crystalline carbonated apatite type material.[25] It would therefore be of interest to establish whether other phases could be produced from reactions of ACC and different types of phosphate such as fluorophosphates and pyrophosphate, both of which appear to have a propensity to form stable amorphous phases and therefore are potentially attractive stabilising agents for ACC. Given the inherent instability of ACC, this study seeks to systematically establish and optimise reaction parameters (e.g. temperature, concentration, pH), often by repeated reactions to obtain reliable and repeatable conclusions.

6.2 Reactions of ACC with Various Phosphate Species

6.2.1 Reaction Procedure

The synthesis of amorphous calcium carbonate was performed as described in section 2.1.3. Known amounts of ACC were then immersed in various phosphate solutions of differing concentrations summarised in table 6.1 with the source of phosphate being Na_2HPO_4 (Fisher), $Na_4P_2O_7$ (Sigma Aldrich) and Na_2PO_3F (Sigma Aldrich). Typically concentrations 0.01-1mol dm^{-3} of the phosphate solutions was used in these reactions. Samples of ACC were immersed in the phosphate solutions for a duration of 30 minutes before vaccum filtering and washing with de-ionised water. Once any excess solution had been removed, the samples were placed into desiccators overnight to continue drying. The pH of the phosphate solutions were monitored before and after the addition of ACC.

Table 6.1: A summary of the reaction conditions employed for the reactions between ACC and the various phosphate solutions. * Concentration for pyrophosphate is moles per $P_2O_7^{4-}$ unit

Mass of ACC (g)	Concentration of phosphate solution (mol dm^{-3})*	Volume of phosphate solution (dm^3)	Molar ratio ACC:Phosphate formula	Reaction time (mins)
Na_2HPO_4				
0.175	0.1	0.05833	0.25	30
0.175	0.3	0.05833	0.08	30
0.175	0.5	0.05833	0.05	30
Na_2PO_3F				
0.175	0.1	0.05833	0.12	30
0.175	0.2	0.05833	0.08	30
0.175	0.3	0.05833	0.07	30
0.175	0.35	0.05833	0.07	30
0.175	0.375	0.05833	0.06	30
0.175	0.4	0.05833	0.05	30
0.175	0.5	0.05833	0.12	30
$Na_4P_2O_7$				
0.175	0.0125	0.05833	1.97	30
0.175	0.025	0.05833	0.99	30
0.175	0.03	0.05833	0.82	30
0.175	0.04	0.05833	0.62	30
0.175	0.05	0.05833	0.49	30
0.175	0.075	0.05833	0.33	30
0.175	0.1	0.05833	0.25	30
0.175	0.2	0.05833	0.12	30

6.3 Results and Discussion

6.3.1 Synthesis and Characterisation of ACC

The synthesis of the parent ACC material was followed as described in section 2.1.2 which was based on the method by Koga *et al.*[26] whereby ACC was formed from highly supersaturated solutions in an alkaline environment where the pH of the aqueous system (Na_2CO_3-NaOH and $CaCl_2$) was maintained between 11.2-13.5, producing compositions of the form $CaCO_3 \cdot xH_2O$ (a pH above this threshold (> 13.5) led to the

formation of amorphous basic calcium carbonate (ABCC)).[15, 26] Despite no modifications to the stated synthesis of ACC, reliable formation has proven to be very challenging due to its inherent instability. The synthesis proved extremely susceptible to slight deviations to the reaction conditions leading to calcite formation. Clearly in this metastable state there is a strong thermodynamic driving force to crystallise into the more stable polymorph calcite.[12, 27] Due to its instability, volumes no greater than 50cm^3 for each solution could be used for the reactions and therefore no scale up synthesis for the formation of ACC could be identified. As a result of this, approximately 0.2 g per sample of ACC could be synthesised using the method stated in section 2.1.2. Therefore, in order to investigate the reactivity of ACC towards various phosphate species, multiple samples of ACC were synthesised and combined in order to perform each reaction and characterise the products formed. The reactions of ACC with phosphate will be discussed later in section 6.2.3.

6.3.1.1 PXRD

Initial confirmation that the 'as synthesised' material was amorphous was provided by PXRD. Figure 6.1 shows the PXRD pattern of one of the products from the ACC reaction. The diffraction pattern contained no apparent Bragg peaks, this indicates that the as synthesised calcium carbonate material was indeed amorphous with no evidence of the presence of any significant crystalline forms of calcium carbonate unlike the product (calcite) shown in figure 6.2 which was formed from soaking a sample of ACC in water for 30 minutes. This reaction was then used as the control experiments for the reactions of ACC with phosphate discussed in section 6.3.2.

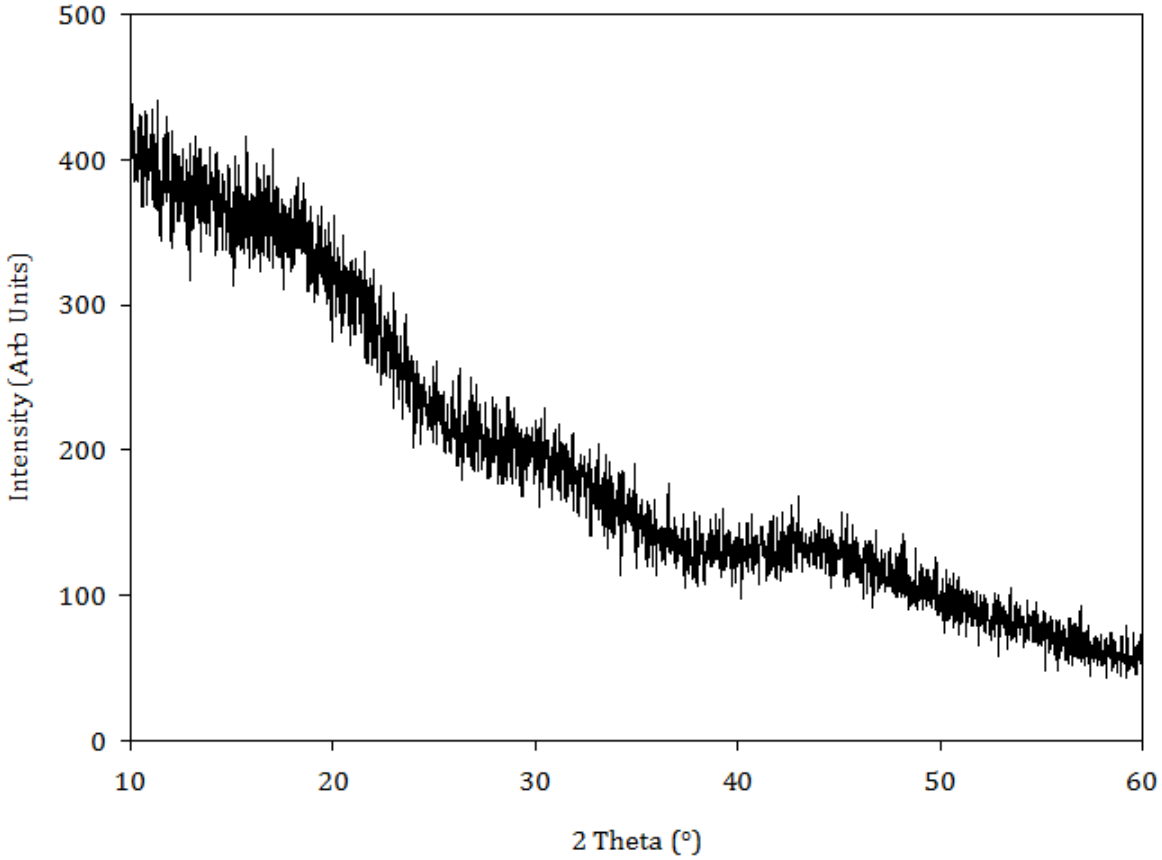

Figure 6.1: PXRD pattern of amorphous calcium carbonate (ACC)

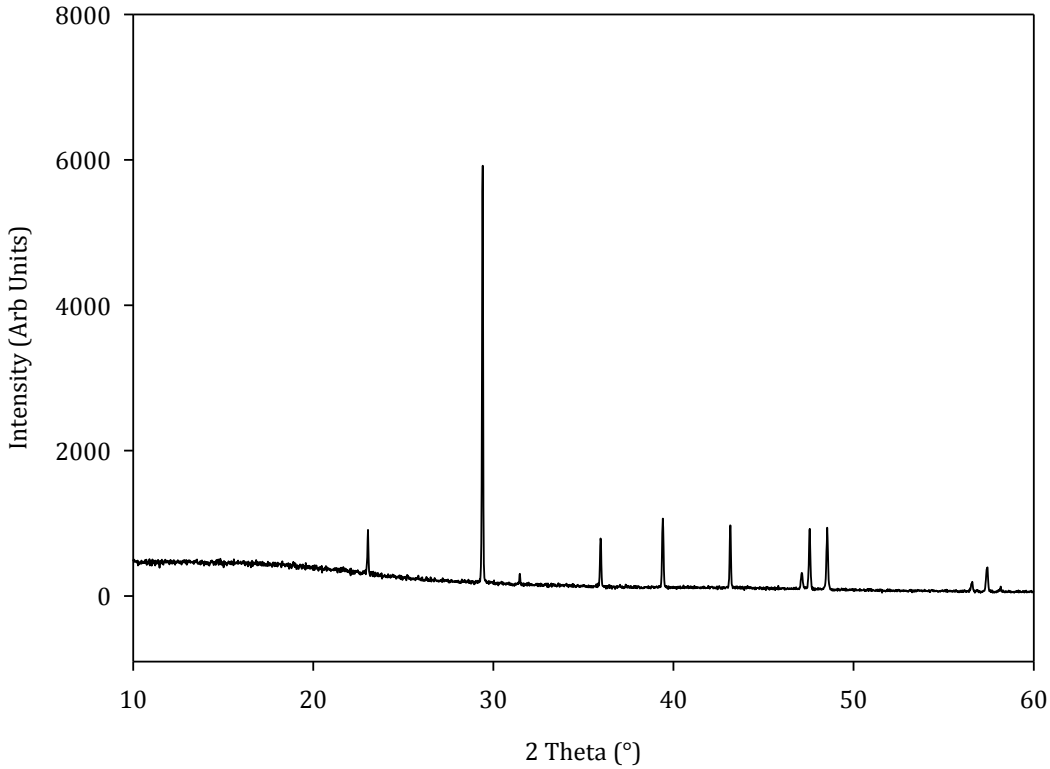

Figure 6.2: PXRD pattern of calcite (PDF: 04-007-8659), the thermodynamically most stable calcium carbonate polymorph

6.3.1.2 Raman Spectroscopy

Given the starting materials, it can be assumed that the amorphous product formed is calcium carbonate, but as this cannot be determined from PXRD, Raman spectroscopy of the amorphous product was performed. The Raman spectra of synthetic ACC (figure 6.3) shows a broad vibration at a frequency of 1087 cm^{-1}, which corresponds to the v_1 symmetric stretch of CO_3^{2-}. This spectrum resembles the reported Raman spectra of synthetic ACC and biogenic ACC.[2, 28] In contrast to this, more vibrations are observed in the Raman spectra of the crystalline polymorph calcite which can be attributed to the v_1 (1089), v_3 (1436), v_4 (715) vibrations and the lattice modes at 155 and 281 cm^{-1} from the CO_3^{2-} group (figure 6.4). It is also evident that the vibrations are significantly broader in ACC than in calcite, again suggesting the amorphous nature of the ACC product.

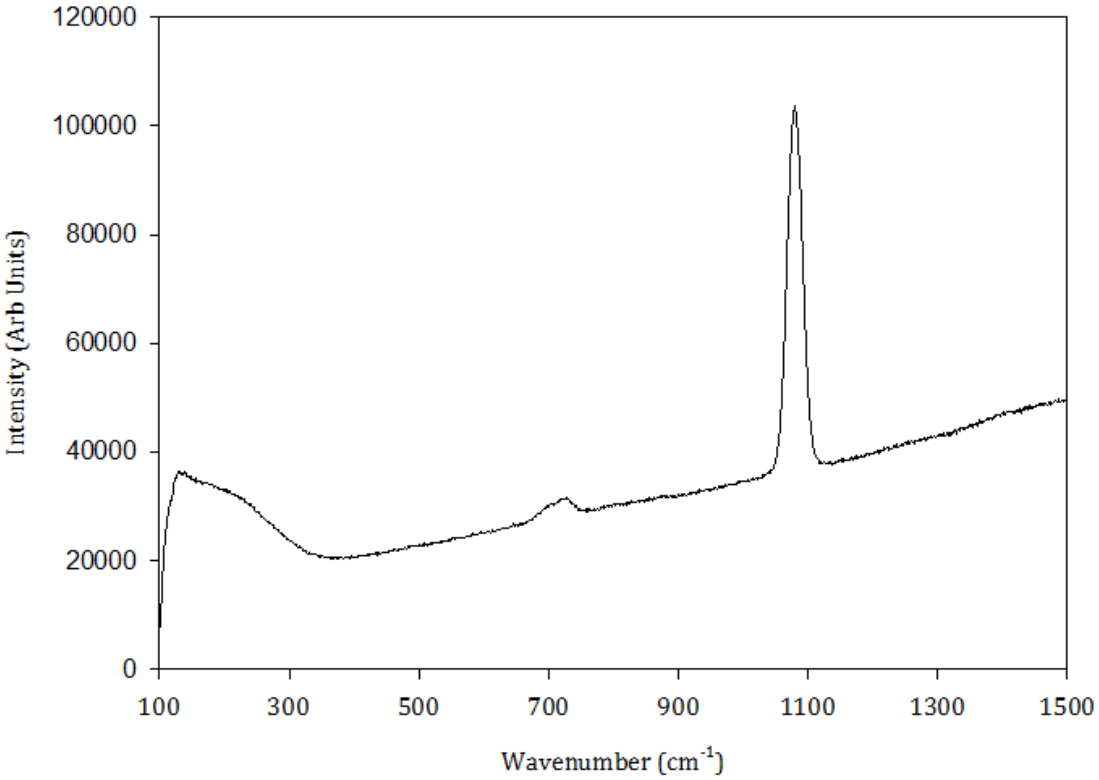

Figure 6.3: Raman spectra of amorphous calcium carbonate (ACC)

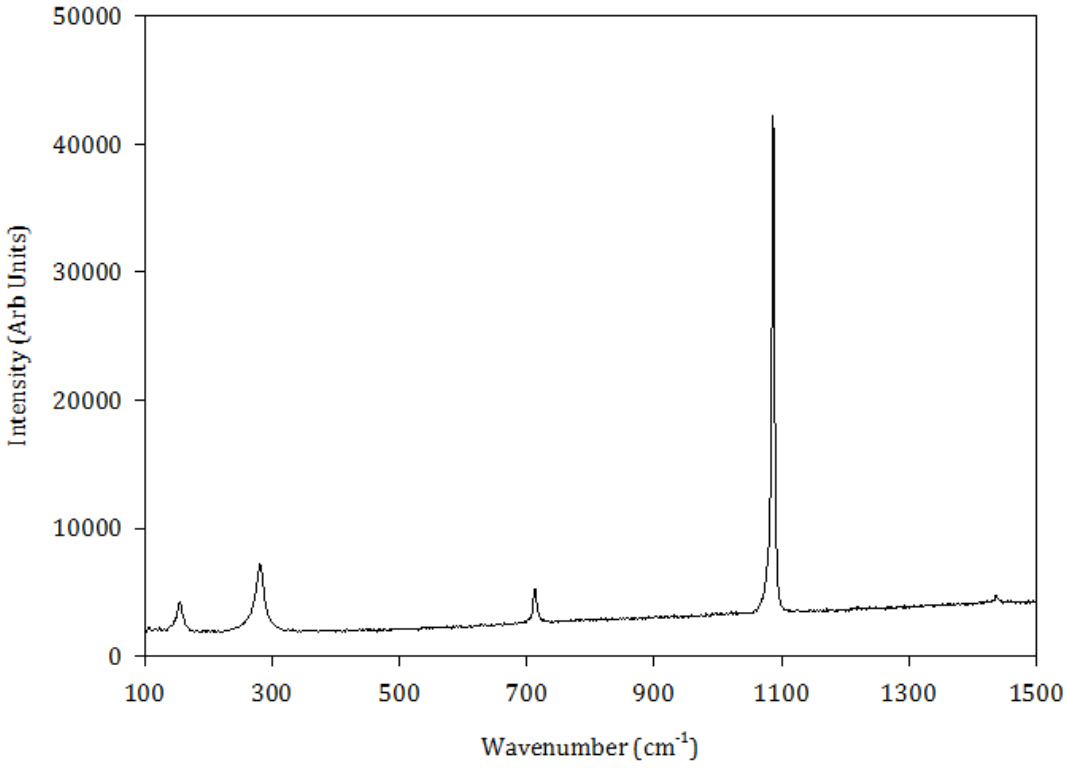

Figure 6.4: Raman spectra of calcite

6.3.1.3 SEM-EDX

The SEM image of the ACC (figure 6.5), indicates a morphology in keeping with an amorphous sample with no evidence of any well defined crystals. Instead the sample consists of small spherical aggregated particles which is typical of ACC.[26]

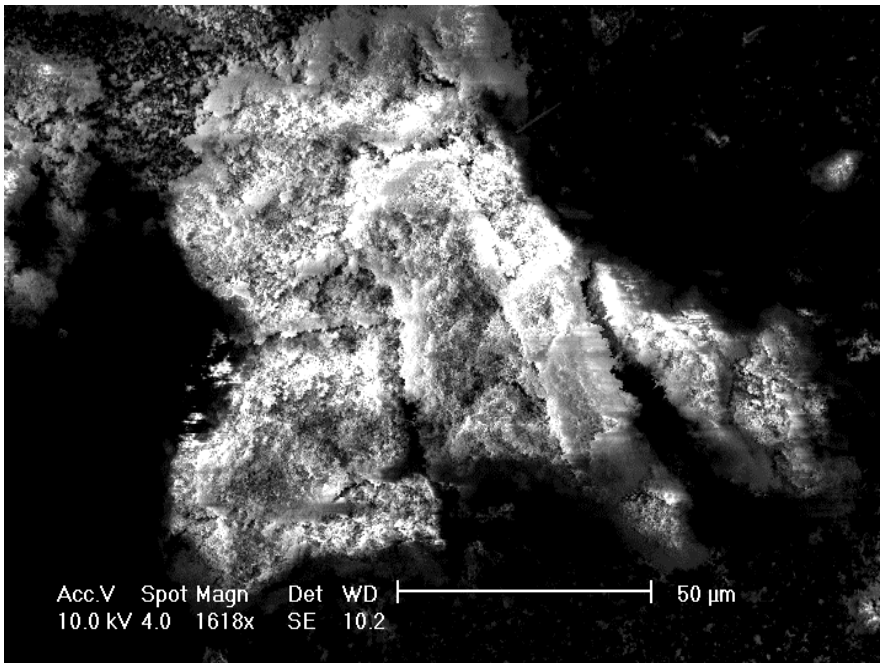

Figure 6.5: SEM Image of amorphous calcium carbonate (ACC)

6.3.1.4 TGA-MS

Synthetic ACC is reported to have a stoichiometry of $CaCO_3 \cdot xH_2O$ ($1 < x$ 1.5) and therefore TGA was employed to confirm the carbonate content and possible stoichiometry of this ACC. From the literature, it has previously been reported that synthetic ACC contains approximately 1.5 moles of water per $CaCO_3$ unit.[15] However, more recently, studies in the Wright group have shown that a stable form of amorphous calcium carbonate with 1.2 moles of water per $CaCO_3$ can be produced.[25]

Figure 6.6 shows the TGA-MS traces for a sample of ACC heated to 1000 °C. The data implies that there are three significant events which take place during the decomposition of ACC, two of which coincide with mass losses. The first mass loss occurs between 50-300 °C and can be attributed to the dehydration of ACC. The loss of water (1.2 moles) is confirmed in the mass spec with a m/z ratio of 18. Then an exothermic event is observed at 316 °C, which suggests that a phase transition has occurred as there is no associated mass loss. This indicates the crystallisation of ACC into calcite and coincides with the loss of any remaining water. The second and final mass loss of ~ 35 % occurs between 575-875 °C and corresponds to loss of CO_2 (0.98 moles). The decomposition of carbonate is confirmed from the mass spec data indicating only ions of m/z ratio of 44 (CO_2) were detected from this event. No further weight losses were evident beyond 875 °C, suggesting that ACC has fully decomposed into calcium oxide (CaO) and this was subsequently confirmed by the PXRD pattern of the TGA sample. From the losses of both H_2O and CO_2, it can be deduced that the composition of this sample of synthetic ACC is $CaCO_3 \cdot 1.2H_2O$ which is in very good agreement with the suggested stoichiometry of ACC previously reported.[25] Further batches of ACC were examined in a similar manner during the course of this study and some deviation in water content was observed, given compositions of ACC of $CaCO_3 \cdot xH_2O$ where $1.20 < x\ 1.44$.

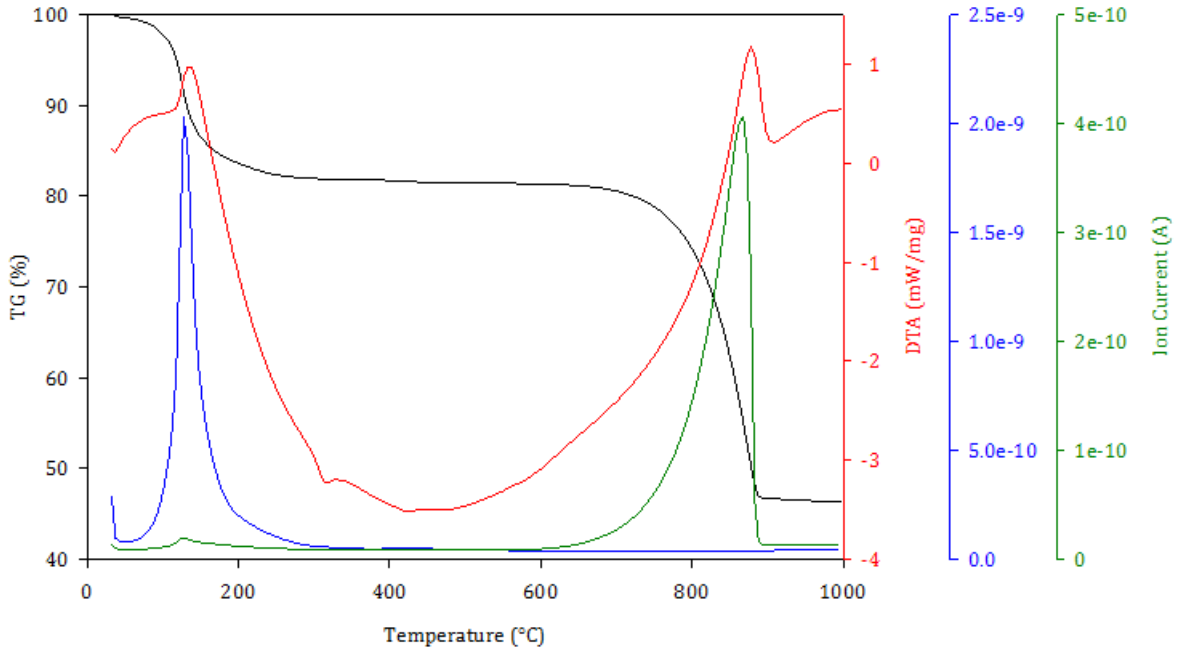

Figure 6.6: TGA-MS plot of amorphous calcium carbonate (ACC), showing the mass loss (black), DTA (red) and the evolution of both water (blue) and carbon dioxide (green) as indicated by the mass spec data

6.3.2 Reactions with Phosphate Species

Previous work in the Wright group investigated the effect of orthophosphate (PO_4^{3-}) on the stability of synthetic ACC as it had been suggested in literature that phosphate played a role in the stabilisation of biogenic ACC.[2, 24, 29] To study this, synthetic ACC was exposed to a range of concentrations greater than 0.1 mol dm^{-3} of phosphate and it was found that 0.3 mol dm^{-3} was the optimum concentration of PO_4^{3-} required in order to inhibit any crystallisation of ACC into calcite (as evident from PXRD). This investigation was repeated and extended to explore the effect of other phosphates species, fluorophosphate (PO_3F^{2-}) and pyrophosphate ($P_2O_7^{2-}$), in the same manner.[30] The reaction procedure was followed as described in section 6.2.1 with an initial phosphate level of 0.1 mol dm^{-3} for each species. PXRD data for these initial

products indicated whether they were crystalline or amorphous and this then dictated whether the concentration of the phosphate species was to be increased or decreased for subsequent reactions. The pH of the solutions after exposure to ACC was found to increase. This is thought to be due to the presence of CO_2 in the solutions which had been released from the ACC. PXRD was used in order to assess whether crystallisation of ACC had been inhibited by assessing the crystallinity of the products through the presence of Bragg reflections. The results are shown in table 6.3. For the reactions of ACC with orthophosphate, fluorophosphate and pyrophosphate concentrations below 0.2, 0.3 and 0.03 were not attempted as the products of these reactions were crystalline, so lowering the concentration further would only yield crystalline products and the aim was to establish the lowest concentration which an amorphous product could be formed.

In all cases, there was an increase in mass after soaking ACC in the various phosphate solutions, suggesting an uptake of the phosphate species. However at present it is unclear as to the mechanism by which the phosphate species are stabilising ACC. There could be dissolution of the ACC and subsequent crystallisation of a new phase containing the phosphate species, or the formation of a phosphate-rich coating on the ACC particles. Unfortunately, the gain in mass appears to be inconsistent from sample to sample and therefore no compositional information could be obtained.

It was found that the minimum concentrations of the phosphates species required to prevent any evidence of ACC crystallisation were 0.3 (1:12), 0.375 (1:15) and 0.04 (1:1.62) for reactions with orthophosphate, fluorophosphate and pyrophosphate respectively. Though similar levels of phosphate (confirming previous findings) and

fluorophosphates are required, it is clear that substantially less pyrophosphate is required. Therefore pyrophosphate is a much more effective inhibitor of calcite formation than the other two species.

Table 6.2: A summary of the crystalline (denoted with ✗)and amorphous products (✓)formed from reactions between ACC and the various phosphate solutions. Reactions denoted with a (-) were the concentrations which were not attempted_

Is product amorphous?				
Concentration of phosphate solution (mol dm^{-3})	**Molar Ratio**	**Na_2HPO_4**	**Na_2PO_3F**	**$Na_4P_2O_7$**
0.0125	1.97	-	-	✗
0.025	0.99	-	-	✗
0.03	0.82	-	-	✗
0.04	0.62	-	-	✓
0.05	0.49	-	-	✓
0.075	0.33	-	-	✓
0.1	0.25	✗	✗	✓
0.2	0.12	✗	✗	-
0.3	0.08	✓	✗	-
0.375	0.07	-	✓	-
0.4	0.06	-	✓	-
0.5	0.05	✓	✓	-

Given the similar nature of both orthophosphate and fluorophosphate, it is unsurprising that the critical concentrations of these phosphate species are of the same order of magnitude compared to that of pyrophosphate where the critical concentration is an order of magnitude lower. This cannot simply be explained by the orthophosphate and fluorophosphate species containing only one PO_4 unit, whereas pyrophosphate contains two per mole and therefore suggests a different mechanism is in operation.

6.3.2.1 SEM

Although PXRD confirms that ACC exposed to the different phosphate species are amorphous above a given threshold, it is unclear whether there are any discernible

differences between the 'stabilised' species resulting from the different phosphates used. This might include evidence of domains of crystalline appearance that would not be observed in the PXRD patterns and therefore SEM was used to investigate the morphology of these materials.

SEM images of two different regions of each of the phosphate exposed materials (all samples of ACC used for SEM were immersed in phosphate solutions for 30 minutes) are shown in figure 6.7 a-f and it is clear that a substantial change in morphology has occurred between the different phosphate treatments. There is evidence of some crystallinity being present and this is in agreement with some evidence of a poorly crystalline material in PXRD (figure 6.8).

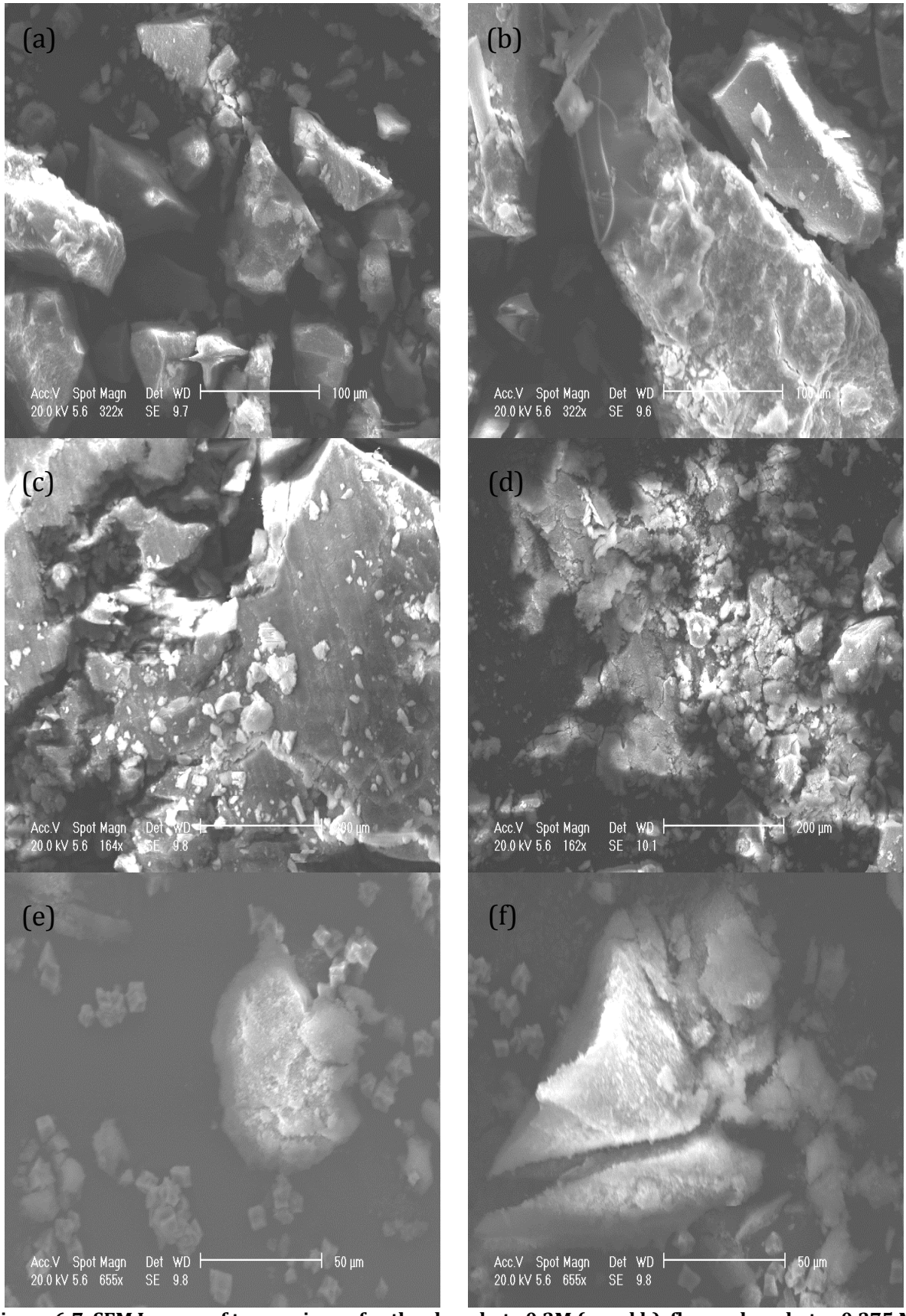

Figure 6.7: SEM Images of two regions of orthophosphate 0.3M (a and b), fluorophosphates 0.375 M (c and d) and pyrophosphate 0.04 M (e and f) containing materials

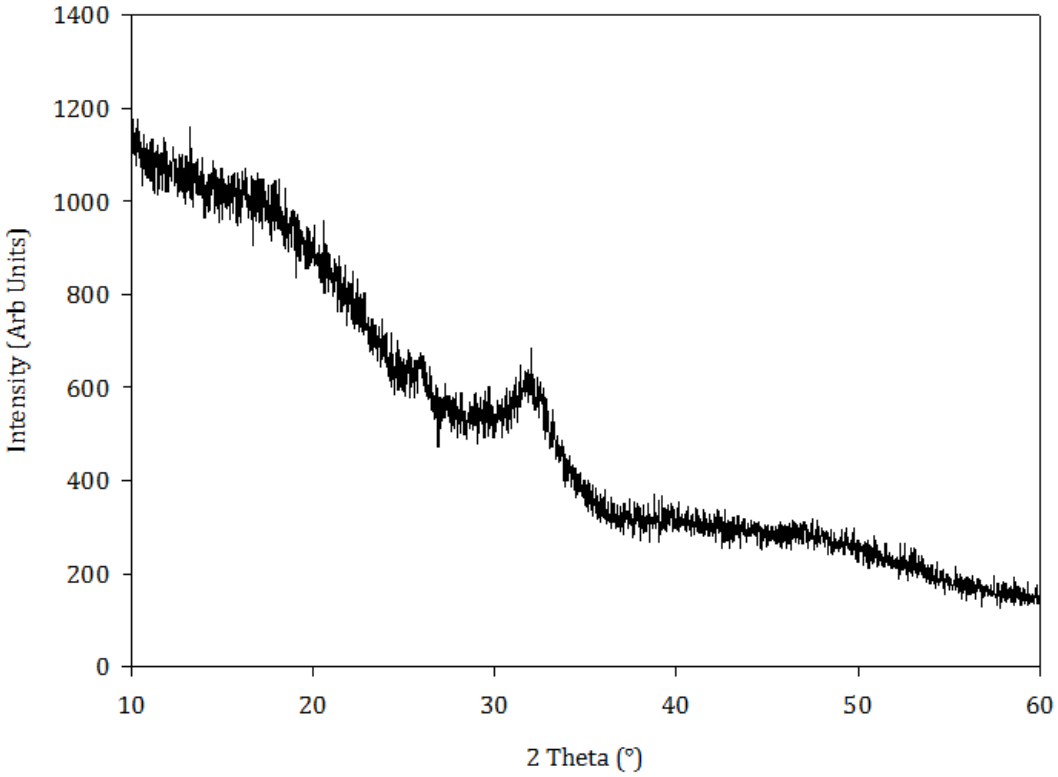

Figure 6.8: PXRD pattern of ACC after being immersed in an orthophosphate solution for 30 minutes

6.3.2.2 Raman Spectroscopy

Raman spectroscopy was utilised to qualitatively assess whether phosphate is present. The results in table 6.4 show the presence of both phosphate and carbonate vibrations in all phosphate exposed products, confirming the uptake of phosphate from the initial solution. Multiple regions of each sample were scanned in order to determine whether the amorphous phosphate containing material was uniformly distributed in the sample. This proved to be the case for both the orthophosphate and pyrophosphate exposed phases but not for the fluorophosphate exposed system where variations in spectra were observed across the sample. However, this technique does not determine whether the phosphate species are present in the bulk or on the surface of ACC or as a separate phase entirely.

Table 6.3: Summary of the data obtained from Raman spectroscopy measurement of both the parent ACC material and the amorphous phosphate containing materials

Sample	Vibrations (cm^{-1})	Assignments
ACC	1080 741	CO_3^{2-} CO_3^{2-}
ACC + 0.3 M PO_4^{3-}	1076 953 583 427	CO_3^{2-} v_1 P-O stretching unknown/unassigned unknown/unassigned
ACC + 0.375 M PO_3F^{2-} Region 1	1080 1004 958 727 531 383	CO_3^{2-} V_s (PO_3) unknown/unassigned CO_3^{2-}/P-F δ($PO_3\rho$
ACC + 0.375 M PO_3F^{2-} Region 2	1153 1079 1039 1005 956 740 531 486 357	V_{as} (PO_3) CO_3^{2-} unknown/unassigned V_s (PO_3) unknown/unassigned CO_3^{2-}/P-F δ(PO_3) unknown/unassigned ρ(PO_3)
ACC + 0.04 M $P_2O_7^{4-}$	1081 1036	CO_3^{2-} $P_2O_7^{4-}$ dimers

6.3.2.3 X-Ray Fluorescence Spectroscopy

As the presence of phosphate had been confirmed qualitatively through Raman spectroscopy, the amount of phosphate present was determined by XRF spectroscopy following the method described in section 2.7.1.

Multiple samples of each of the phosphate containing products were prepared and measured. In order to prepare each sample for XRF analysis, two of each of the phosphate containing products were synthesised, all from separate samples of ACC of which the nature and composition had been checked using PXRD and TGA. By examining the Ca:P ratio of these materials (table 6.5) it was found that the product obtained from

the reaction of ACC and orthophosphate was generally in agreement with a product of an apatitic nature generating an average Ca:P of 1.73 (pure HA has Ca:P ratio of 1.67). However, this result was not significantly different to the results obtained for the pyrophosphate exposure (average 1.87). This suggests that the pyrophosphate is more efficient at preventing crystalline phase formation given its significantly lower initial concentration but similar compositional presence in the resulting product.

Table 6.4: XRF fused bead results from the orthophosphate, fluorophosphate and pyrophosphate containing samples at their minimum stabilising concentrations.

ACC + 0.3 M Na_2HPO_4								
	Sample 1				**Sample 2**			
Elements	**wt %**	**mass**	**Mr**	**mols**	**wt %**	**mass**	**Mr**	**mols**
Ca	28.36	0.09926	40.078	0.0025	28.5	0.0998	40.078	0.0025
P	12.08	0.04228	30.974	0.0014	13.36	0.0468	30.974	0.0015
Na	7.72	0.02702	22.99	0.0012	8.05	0.0282	22.99	0.0012
Ratio								
Ca:Na	2.11 (2)				3.54 (2)			
Ca:P	1.81 (2)				1.65 (2)			
Na:P	0.86 (2)				0.81 (2)			
ACC + 0.375 M Na_2PO_3F								
	Sample 1				**Sample 2**			
Elements	**wt %**	**mass**	**Mr**	**mols**	**wt %**	**mass**	**Mr**	**mols**
Ca	32.08	0.11228	40.078	0.0028	31.66	0.1108	40.078	0.0028
P	4.13	0.014455	30.974	0.0005	4.48	0.0157	30.974	0.0005
Na	5.39	0.018865	22.99	0.0008	5.05	0.0177	22.99	0.0008
Ratio								
Ca:Na	3.41 (2)				6.27 (2)			
Ca:P	6.00 (2)				5.46 (2)			
Na:P	1.76 (2)				1.52 (2)			
ACC + 0.04 M $Na_4P_2O_7$								
	Sample 1				**Sample 2**			
Elements	**wt %**	**mass**	**Mr**	**mols**	**wt %**	**mass**	**Mr**	**mols**
Ca	26.85	0.093975	40.078	0.0023	26.62	0.0932	40.078	0.0023
P	11.08	0.03878	30.974	0.0013	10.96	0.0384	30.974	0.0012
Na	5.21	0.018235	22.99	0.0008	5.71	0.02	22.99	0.0009
Ratio								
Ca:Na	5.15 (2)				4.66 (2)			
Ca:P	1.87 (2)				1.88 (2)			
Na:P	0.63 (2)				0.70 (2)			

It is interesting to note that a much lower level of phosphate (average Ca:P ratio of 5.7) is evident in the fluorophosphates exposed samples, despite the initial concentration at exposure being the highest of the three. It might then be suggested this is the most phosphate efficient means of stabilising ACC were it not for the higher level of PO_3F required to avoid calcite formation. In summary, the XRF data do not provide

any strong evidence of the true identity of phases present within these materials, but do suggest that the mechanisms for each are different.

6.3.2.4 TGA-MS

Though the identities of the amorphous products are unknown, TGA-MS can be used to investigate the thermal decomposition of these products. The TGA-MS measurements of the amorphous phosphate-containing materials were carried out in an identical manner to those of the parent ACC material as is described in section 2.5. The expected loss of both H_2O and CO_2 within these systems was compared to that of the parent ACC. A summary of the TGA-MS results are shown in table 6.6.

Table 6.5: A summary of the temperatures at which a thermal event occurs in the TGA-MS plots for both the parent ACC phase and the amorphous phosphate containing phases

	Temperature of H_2O loss (°C)	**Temperature of CO_2 loss (°C)**	**Crystallisation Temperature of ACC (°C)**
ACC (1)	50-350	75-325 575-850	275-350
ACC (1) + 0.3 M PO_4^{3-}	50-325	50-300 350-575 650-1000	-
ACC (2)	50-300	100-300 575-850	275-350
ACC (2) + 0.375 M PO_3F^{2-}	50-350	50-450 600-1000	325-400
ACC (3)	75-350	100-350 600-875	300-375
ACC (3) + 0.04M $P_2O_7^{2-}$	75-300	90-200 260-600 650-850	300-375

Figure 6.8 shows the TGA-MS plot of the amorphous orthophosphate containing system and confirms the loss of both water and carbon dioxide from this system. The

mass spec data for water (m/z ratio 18) suggests just one water loss, but the CO_2 loss (m/z ratio 44) is more complex, showing two main peaks. The significant loss of CO_2 at 117 °C and 516 °C are not consistent with that of the parent ACC phase suggesting that the carbonate present is in an environment different from ACC itself. It is possible that the CO_2 loss at 516 °C could potentially be due to the decomposition of carbonate from a carbonated apatite material (CHA) but the temperature is slightly lower than the loss of CO_2 from CHA which has reported to be evolved at ~ 600 °C. The broad feature observed between 650-1000 °C suggests a small amount of CO_2 lost within this temperature range, which is likely to be due to the decomposition of carbonate from the parent ACC phase. Although the temperature at which water is lost is in keeping with the water loss from ACC, the amount of H_2O and CO_2 lost from this system cannot be determined due to the simultaneous loss of both H_2O and CO_2.

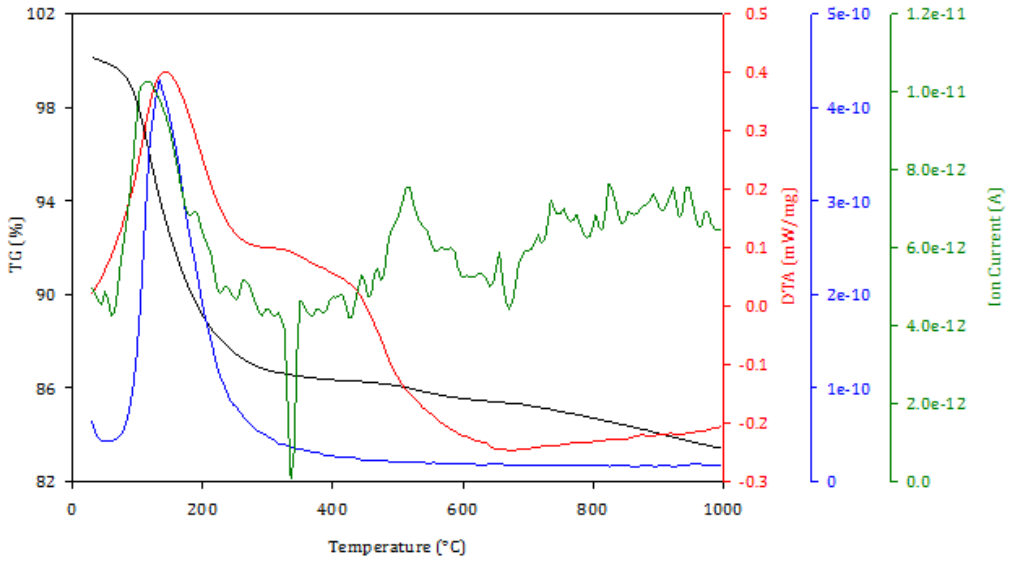

Figure 6.9: TGA-MS plot of the amorphous orthophosphate containing phase, showing the mass loss (black), DTA (red) and the evolution of both water (blue) and carbon dioxide (green) as indicated by the mass spec data

From the TGA plots (figure 6.9), it can be seen that the evolution of H_2O and CO_2 from the amorphous containing fluorophosphates material are consistent with the losses of both water and carbon dioxide from the parent ACC material, as these losses were found to occur at almost identical temperatures (table 6.6). However, the crystallisation temperature for the phosphate containing species appears to be higher (368.9 °C) compared to that of 322.9 °C for ACC. As there was no evidence from the mass spec data of the evolution of any species other than water and carbon dioxide, the level of H_2O and CO_2 could be calculated/determined and were found to be 1.41 and 0.68 respectively. The water content for both ACC and the amorphous fluorophosphates containing phase were within error of one another. However, the amount of CO_2 detected was significantly lower (0.68 moles per $CaCO_3$ unit) than the expected value for ACC. This may suggest that the remaining carbonate was retained within an additional phase.

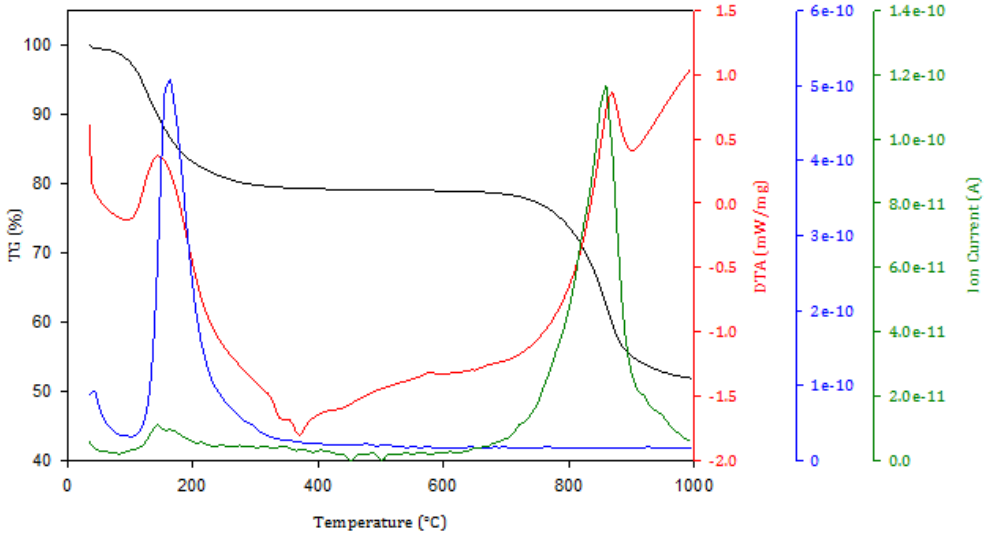

Figure 6.10: TGA-MS plot of the amorphous fluorophosphate containing phase, showing the mass loss (black), DTA (red) and the evolution of both water (blue) and carbon dioxide (green) as indicated by the mass spec data

The amorphous pyrophosphate system does not appear to follow a similar decomposition pathway to that of the parent ACC material, which is indicated from the evolution of CO_2 (figure 6.10). The predominant CO_2 loss is observed at ~ 787 °C, which is not consistent with the loss of CO_2 from amorphous calcium carbonate, where the predominant CO_2 loss occurs at ~ 848 °C suggesting that some of the carbonate present is not associated with ACC. A broad feature is observed between 250-600 °C in the mass spec data for ions of m/z ratio 44, which suggests a small but steady loss of CO_2 in this region. The current loss of CO_2 between 250-600 °C is not in keeping with that of the parent ACC material. A temperature of 250 °C is considered to be reasonably low for the loss but may suggest that carbonate is present in an additional phase. The loss within the region of 250-600 °C may partly be explained due to the presence of some carbonated apatite, where the loss of CO_2 has been reported to occur at approximately 600 °C. This does not however, explain the loss of CO_2 from the earlier temperatures of 250 °C, other than that there is more than one carbonate containing phase and that the carbonate is lost at very similar temperatures in these phases. Due to the overlap in the water and carbon dioxide peaks early on in the mass spec data at 150 °C, the amount of both H_2O and CO_2 of this system cannot accurately be determined. However, the evolution of CO_2 at this temperature was also observed in the TGA-MS plot for the parent ACC materials. It appears that the loss of CO_2 was found to be relatively insignificant in both cases and therefore suggesting minimal loss of CO_2 at this temperature. However, it is still not possible to calculate the amount of H_2O and CO_2 in this system, as the peak relating to the loss of water overlaps slightly with the peak for CO_2 loss which begin at 250 °C.

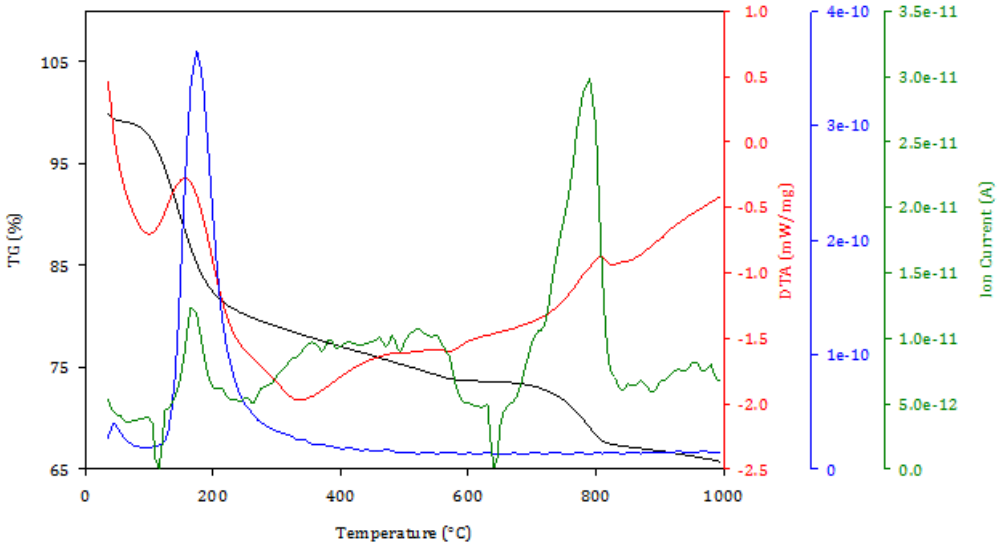

Figure 6.11: TGA-MS plot of the amorphous pyrophosphate containing phase, showing the mass loss (black), DTA (red) and the evolution of both water (blue) and carbon dioxide (green) as indicated by the mass spec data

6.3.2.5 Products from TGA-MS studies

The products obtained from the TGA-MS studies were analysed using PXRD. All products were found to be relatively crystalline. In all cases, evidence of calcium oxide (CaO) was observed which is a decomposition product of the parent ACC phase, however, this may not necessarily suggest that ACC is present before the TGA analyses. All products from the TGA were found to consist of an apatitic phase. For the orthophosphate containing phase, no additional phases were observed in the PXRD pattern, however the PXRD pattern exhibited a relatively high background, which is likely to be due to the presence of some amorphous material. The results obtained were in partial agreement to those previously reported by the Wright group,[25] although in this work, beta tri-calcium phosphate (β-TCP) was present in addition to the main apatite phase.

The TGA products of the amorphous fluorophosphates and pyrophosphate containing materials were found to consist of multiple phases in addition to the apatitic phase and CaO. The potential phases present are summarised in table 6.7.

Table 6.6: Summary of the potential reaction products present in the PXRD patterns of the amorphous phosphate containing materials after TGA

Potential Phases	ACC + Na_2HPO_4	ACC + Na_2PO_3F	ACC + $Na_4P_2O_7$
Include apatite $Ca_5(PO_4)_3OH$ (PDF: 01-076-0694)	✓	×	×
$Ca_2P_2O_7$ (PDF: 00-009-0346)	×	×	✓
$Na_3HP_2O_7 \cdot 9H_2O$ (PDF: 00-011-0360)	×	×	✓
$Na_6(PO_4)_2 \cdot H_2O$ (PDF: 04-011-3397)	×	✓	✓
$Ca_4(PO_4)_2O$ (PDF: 04-011-1625)	×	✓	✓
NaF (PDF: 00-036-1455)	×	✓	×
CaF_2 (PDF: 04-002-2192)	×	✓	×

A combination of these phases provided the best match to the remaining phases in the PXRD pattern. However, this is a tentative assignment as it is unclear as to whether all of the suggested phases are actually present in the reaction products due to the similarities in the peak positions of these phases. It is possible that the unusual XRF results obtained for the Ca:P ratio for the amorphous fluorophosphate and pyrophosphate containing materials can be explained by the presence of multiple phases within the amorphous materials which has been suggested from the TGA results of these materials.

6.4 Conclusions

The synthesis of ACC has proved to be very challenging due to its inherent instability and poor reproducibility. The extreme sensitivity to change in the reaction conditions limited the scope for scale up reactions to produce larger quantities of ACC. Instead multiple batches of ACC were used to investigate the reactivity of ACC with various phosphate species.

This work has demonstrated that the crystallisation of ACC can be inhibited by the presence of phosphate species; orthophosphate, fluorophosphate and pyrophosphate. These appear to prevent the expected conversion of ACC to the more thermodynamically stable polymorph calcite in the presence of water. This study has established that an excess of phosphate with respect to ACC was required in order to stabilise ACC and the minimum concentrations of orthophosphate, fluorophosphate and pyrophosphate required to inhibit the crystallisation of ACC were found to be 0.3, 0.375 and 0.04 mol dm^{-3} respectively. The products of these reactions were found to be amorphous by PXRD and an increase in the mass of the original ACC material after soaking in a phosphate solution suggested that an uptake of phosphate or water may have occurred during the reaction. The presence of phosphate species in the products was confirmed by Raman and XRF spectroscopy. From the XRF results, the nature of the final amorphous phases cannot be determined, but comparisons of the Ca:P ratios suggest that different mechanisms for stabilisation exist for these three phosphate species. TGA-MS measurements showed that water and carbon dioxide were lost from all of the different phosphate containing materials. However, only the TGA-MS of the amorphous containing fluorophosphate materials were found to resemble that of the parent ACC

phase with the loss of both H_2O and CO_2 being observed at similar temperatures. Although the temperature at which water was lost was found to be largely consistent between the parent ACC phase and the amorphous phosphate containing material, it was the evolution of CO_2 which was found to differ between all three phosphate containing materials, which suggested that carbonate was present in a different environment in these phases. This could be due to a possible additional phase/phases rather than just a retention of some of the parent ACC material. Crystalline products were obtained for all three phosphate containing materials after the TGA studies. These primarily consisted of apatite and CaO for the orthophosphate containing material, but both the fluorophosphate and pyrophosphate containing materials were found to consist of multiple phases and therefore the identity of these additional phases is uncertain. From these initial studies, it is difficult to draw any firm conclusions as to how the ACC has been stabilised by the various phosphate species. It may be possible that as the ACC is relatively soluble, some of the calcium and carbonate ions from its dissolution have reacted with the various phosphate species in solution in order to form various products rather than remain as ACC. However, TGA may suggest that not all of the ACC has reacted but its crystallisation has been inhibited due to the presence of phosphate. From this it may be suggested that phosphate has formed a coating on the surface of the ACC but this is not in keeping with the Ca:P ratios obtained from XRF. Clearly there is much further work necessary if more definitive conclusions are to be drawn.

6.5 References

1. C.Jimenez-Lopez, E. Caballero, F. J. Huertas and C. S. Romanek, *Geochimica et Cosmochimica Acta*, 2001, **65**, 3219-3231.
2. L. Addadi, S. Raz and S. Weiner, *Advanced Materials*, 2003, **15**, 959-970.
3. E. Beniash, J. Aizenberg, L. Addadi and S. Weiner, *Proceedings of the Royal Society of London Series B-Biological Sciences*, 1997, **264**, 461-465.
4. I. M. Weiss, N. Tuross, L. Addadi and S. Weiner, *Journal of Experimental Zoology*, 2002, **293**, 478-491.
5. J. Aizenberg, G. Lambert, L. Addadi and S. Weiner, *Advanced Materials*, 1996, **8**, 222-&.
6. J. Aizenberg, G. Lambert, S. Weiner and L. Addadi, *Journal of the American Chemical Society*, 2002, **124**, 32-39.
7. J. Johnston, H. E. Merwin and E. D. Williamson, *American Journal of Science*, 1916, **41**, 473-512.
8. J. Chen and L. Xiang, *Powder Technology*, 2009, **189**, 64-69.
9. M. Faatz, F. Grohn and G. Wegner, *Materials Science & Engineering C-Biomimetic and Supramolecular Systems*, 2005, **25**, 153-159.
10. J. Rieger, J. Thieme and C. Schmidt, *Langmuir*, 2000, **16**, 8300.
11. J. Bolze, B. Peng, N. Dingenouts, P. Panine, N. t. and M. Ballauff, *Langmuir*, 2002, **18**, 8364.
12. H. S. Lee, T. H. Ha and K. Kim, *Materials Chemistry and Physics*, 2005, **93**, 376-382.
13. M. Faatz, F. Grohn and G. Wegner, *Advanced Materials*, 2004, **16**, 996-+.
14. S. R. Dickinson, G. E. Henderson and K. M. McGrath, *Journal of Crystal Growth*, 2002, **244**, 369-378.
15. Y. Kojima, A. Kawanobe, T. Yasue and Y. Arai, *Nippon Seramikkusu Kyokai Gakujutsu Ronbunshi-Journal of the Ceramic Society of Japan*, 1993, **101**, 1145-1152.
16. N. Koga, Y. Nakagoe and H. Tanaka, *Thermochimica Acta*, 1998, **318**, 239-244.
17. H. Nebel and M. Epple, *Zeitschrift Fur Anorganische Und Allgemeine Chemie*, 2008, **634**, 1439-1443.
18. J. Peric, M. Vucak, R. Krstulovic, L. Brecevic and D. Kralj, *Thermochimica Acta*, 1996, **277**, 175-186.
19. Y. Politi, T. Arad, E. Klein, S. Weiner and L. Addadi, *Science*, 2004, **306**, 1161-1164.
20. R. B. Gammage and D. R. Glasson, *Journal of Colloid and Interface Science*, 1976, **55**, 396-401.
21. H. Nebel, M. Neumann, C. Mayer and M. Epple, *Inorganic Chemistry*, 2008, **47**, 7874-7879.
22. R. S. K. Lam, J. M. Charnock, A. Lennie and F. C. Meldrum, *Crystengcomm*, 2007, **9**, 1226-1236.
23. F. M. Michel, J. MacDonald, J. Feng, B. L. Phillips, L. Ehm, C. Tarabrella, J. B. Parise and R. J. Reeder, *Chemistry of Materials*, 2008, **20**, 4720-4728.
24. Y. Levi-Kalisman, S. Raz, S. Weiner, L. Addadi and I. Sagi, *Advanced Functional Materials*, 2002, **12**, 43-48.
25. S.Abdul-Rehman, The University of Birmingham, 2008.
26. N. Koga, Y. Z. Nakagoe and H. Tanaka, *Thermochimica Acta*, 1998, **318**, 239-244.
27. E. Loste and F. C. Meldrum, *Chemical Communications*, 2001, 901-902.

28. S. Bentov, S. Weil, L. Glazer, A. Sagi and A. Berman, *Journal of Structural Biology*, 2010, **171**, 207-215.
29. S. Raz, P. C. Hamilton, F. H. Wilt, S. Weiner and L. Addadi, *Advanced Functional Materials*, 2003, **13**, 480-486.
30. F. Malik, The University of Birmingham, 2012.

CHAPTER 7

Conclusions and Further Work

7.1 Conclusions

The studies in this thesis have investigated the use of the monofluorophosphate unit (PO_3F^{2-}) as a structural building block in an attempt to explore a range of new compositions. Fluorophosphate materials have previously been used in dental care products such as toothpaste, as the presence of fluoride has been found to reduce the solubility of the enamel in acidic conditions, preventing dental caries. These materials could be considered as potential candidate phases for applications as bone replacement materials. Although calcium fluorophosphate had been synthesised in 1972 by Perloff *et al*.,[1] this class of materials have not been investigated as potential biomaterials, despite the compositional similarity to that of bone. However, there has been renewed interest in fluorophosphates materials, with various fluoride-containing framework materials synthesised by Weller *et al*.[2]

Whilst biomaterials are most commonly based on calcium phosphate systems, the use of Sr^{2+} in such applications has been found to show an increase in biocompatibility and bioactivity in certain systems[3] and enhance the osteoblastic differentiation and mineralisation in hydroxyapatite systems.[4-5]

The reported synthesis of the $CaPO_3F{\cdot}2H_2O$ phase provides scope to synthesise new fluorophosphate derivatives with other divalent cations such as strontium.

Chapter three reports the use of the PO_3F^{2-} anion as a structural building block in place of PO_4^{3-}, and as such it has been possible to successfully synthesise two new strontium fluorophosphate phases $SrPO_3F{\cdot}H_2O$ and $SrPO_3F$. The systems were characterised and the unit cells were identified as orthorhombic *(Pbca*) and the monoclinic monazite structure (*$P2_1/n$*) for $SrPO_3F{\cdot}H_2O$ and $SrPO_3F$ respectively. The anhydrous phase ($SrPO_3F$) is the first example of a fluorophosphate system to adopt an anion ordered monazite structure, a structure type usually associated with rare earth orthophosphate materials. Further analysis using NMR and Rietveld analysis of diffraction data show the presence of some amorphous material (up to 25 % in some cases). The overall stoichiometries of both of these systems were confirmed through XRF spectroscopy and this suggested that both the amorphous material and crystalline phases had a similar Sr:P ratio, close to one. The vibrations observed in the Raman spectra for both strontium fluorophosphate systems were consistent with those observed for other fluorophosphate materials.[6-7] The stability and decomposition of these phases were then investigated and it was found that these materials were only stable up to ≤ 150 °C. The corresponding strontium pyrophosphate phase was found to be one of the decomposition products of both strontium fluorophosphate phases which is in keeping with other fluorophosphate materials described in the literature.[8] However, there is evidence to suggest the formation of strontium apatite phase ($Sr_5(PO_4)_3OH$ or $Sr_5(PO_4)_3F$) as a decomposition product of both $SrPO_3F$ and $SrPO_3FH_2O$. These novel phases could prove to be good candidates to be investigated for applications as biomaterials, with both fluorine and strontium incorporated into the material which have both been shown to contribute beneficial properties to other materials in this field. Accessing these new phases could open a path to the development of new biomaterials with enhanced properties that are comparable to that of native bone.

The successful synthesis of $SrPO_3F$ with the monazite structure indicates that this crystal structure is tolerant to substitution of the PO_4^{3-} by PO_3F^{2-}, with incorporation of a divalent cation to counter the aliovalent tetrahedral species. From this, a range of $Sr_xCa_{1-x}PO_3F$ (x = 0-0.4) phases have been synthesised all adopting the monazite structure. Substitutions with $x \geq 0.5$ resulted in the formation of an amorphous phase. For the crystalline phases, a decrease in the unit cell volume was observed with the inclusion of increasing amounts of the smaller Ca^{2+} cation. All of the synthesised materials within this series were found to contain significant levels of amorphous content (up to ~ 50 wt %). The increasing amounts of amorphous content were thought to be related to presence of disorder on the Sr/Ca site.

The tolerance of the monazite structure was further investigated by attempting to accommodate other 2+ cations such as Ba^{2+}. Doping levels of up to 10 mol % suggested a retention of the monazite structure with a shift of the peak positions in the PXRD patterns to lower 2θ and consistent with the incorporation of the larger Ba^{2+}. However, the presence of significant barium-containing impurities suggested the actual level of Ba^{2+} incorporation was much lower. It was not possible to determine the amount of Ba^{2+} incorporated from the Rietveld refinements of the PXRD data.

The presence of Eu^{3+} in monazite structures is well known and such materials exhibit interesting optical properties.[9-11] Given the success with isolating monazite-structured $SrPO_3F$ and the similar ionic radii of Sr^{2+} to Eu^{2+} (1.31 and 1.30 Å respectively), attempts were made to isolate $Sr_{1-x}Eu_xPO_3F$. Unfortunately these proved unsuccessful owing partly to the limited solubility of the Eu^{2+} salt used.

The incorporation of divalent cations into the $M^{III}PO_4$ monazite structure has previously been investigated for applications as high temperature proton conductors or

as an electrolyte in HTPFCs. In particular, the incorporation of low level of Sr^{2+} into the $LaPO_4$ phase has been explored to form $La_{1-x}Sr_xPO_4$ derivatives, which show promising protonic conductivity.[12] To attempt to increase the levels of Sr incorporation in such phases, chapter four describes an investigation into the double substitution of the $SrPO_3F$ phase, partially substituting La^{3+} and PO_4^{3-} for Sr^{2+} and PO_3F^{2-} respectively. Substitutions up to 20 mol % were found to retain the monazite structure, with all other levels of doping beyond this threshold forming the hexagonal $LaPO_4$ structure. Although an increase in lattice parameters were observed from the Rietveld refinements of the NPD data for the above compositions, it has not been possibly to conclusively determine whether the substitution has been successful.

A similar mixed metal strategy was employed for the hydrated system, as the incorporation of calcium was also found to be successful to form a range of compositions with the following stoichiometry $Sr_{1-x}Ca_xPO_3F{\cdot}H_2O$. Compositions up to x = 0.3 were found to retain the structure of the parent $SrPO_3F{\cdot}H_2O$ phase; substitutions higher than this adopt the $CaPO_3F{\cdot}2H_2O$ structure. The PXRD patterns of these materials showed an apparent shift in the peak positions to higher 2θ, which suggested that the incorporation of Ca^{2+} and was further confirmed by the lattice parameters generated from the Rietveld refinements. However, the refinements could not define the occupancies of both Ca^{2+} and Sr^{2+} ions. All samples from x = 0.1-0.3 were found to contain some amorphous content, which is not unexpected as parent phase was found to contain ~ 21 wt % amorphous material.

These calcium derivatives of the strontium fluorophosphate systems could prove promising for further investigation as they contain some of the key components of mineralised tissue. These systems seem to be relatively tolerant to the incorporation of other divalent cations indicating the potential to form a wide range of compositions. The

incorporation of rare earth elements opens this system up to a wide range of applications including protonic conduction and luminescent materials.

Gypsum ($CaSO_4 \cdot 2H_2O$) has been used as a bone replacement material, exhibiting good biocompatibility. However its relatively high solubility causes rapid resorption, limiting its widespread use in this application. In chapter five, the incorporation of PO_3F^{2-} was investigated with the aim of reducing the solubility. As the PO_3F^{2-} unit is isoelectronic and of a similar size to SO_4^{2-}, attempts were made to isolate a solid solution of composition $Ca(SO_4)_x(PO_3F)_{1-x} \cdot 2H_2O$. Synthesis of the solid solution was successfully achieved with x = 0.7-1.0 resembling the Gypsum structure and x = 0-0.6 resembling the structure of $CaPO_3F \cdot 2H_2O$. Significant shifts in peak positions were observed in the PXRD patterns suggesting that PO_3F^{2-} had successfully been substituted. This was particularly prominent for high levels of PO_3F^{2-} doping. Rietveld refinements of the NPD data confirmed this observation, showing a change in the unit cell parameters. In order to directly compare all members of the series the solid solution series were modelled onto one unit cell ($I\bar{1}$). A monoclinic to triclinic structural transition was observed between doping levels of x = 0.2-0.3 and similarly a triclinic to triclinic transition was observed between doping levels of x = 0.7 and 0.8. These structural transitions could not be investigated due to the quality of the NPD data. The presence of the P-F vibration in the Raman spectrum of these products provides evidence that PO_3F^{2-} was present and these results were supported by XRF spectroscopy. The successful synthesis of this series could prove to reduce the solubility of the gypsum phase, as initial tests have suggested. Further investigations into the integrity of these phases in cement form would give an insight into their mechanical properties and behaviour in an appropriate form to be used in biomaterials applications.

Previous studies have investigated the reactivity of ACC towards orthophosphate and results have showed the formation of a carbonated apatite material, thus preventing the crystallisation of ACC to calcite. Chapter six extends this further to investigate reactions of ACC towards other phosphate species such as fluorophosphate and pyrophosphate. The results from this chapter confirm that PO_3F^{2-} and $P_2O_7^{4-}$ also inhibited the crystallisation of ACC. The minimum concentrations required to prevent this crystallisation were found to be similar for PO_4^{3-} and PO_3F^{2-} , but significantly lower for $P_2O_7^{4-}$. The presence of phosphate was confirmed by Raman and XRF spectroscopy however, it is unclear as to the composition of the amorphous phosphate containing species. Whilst it is clear that the presence of these species is unclear, there is still much speculation as to the mechanism by which this occurs. The drawing of conclusive evidence from these investigations is yet hindered by the inherent instability and sensitivity of the ACC phase, causing issues with reproducibility and continuity between samples synthesised under the 'same conditions'. What is evident is that the mechanism by which the different phosphate species stabilise the ACC appears to be different based on the results of XRF spectroscopy. From these preliminary studies the need for more in-depth mechanistic studies is evident. Understanding the stabilisation of synthetic ACC may shed light on the processes occurring naturally in biological systems.

7.2 Further Work

7.2.1 Chapter 3

- Fully investigate decomposition pathway of both strontium fluorophosphate phases.

7.2.2 Chapter 4

- Further characterise these mixed metal fluorophosphate systems using NPD and NMR spectrometry.
- Establish the level of doping achieved in these mixed metal fluorophosphate systems, to be achieved through XRF spectroscopy using the fused bead method.
- Attempt to achieve higher levels of Ba^{2+} doping by modifying reaction conditions and using different Ba^{2+} salts.
- Attempt to synthesis $Sr_{1-x}Eu_xPO_3F$ phases through reactions with different Eu(II) salts.
- Investigate the potential of these systems as candidates bone replacement materials through investigating the materials physical characteristics including setting times, strength tests and solubility tests.

7.2.3 Chapter 5

- Fully establish the composition of each member of the $Ca(SO_4)_x(PO_3F)_{1-x}\cdot 2H_2O$ series using XRF spectroscopy to establish whether the composition is close to the predicted stoichiometry.
- Continue initial tests on strength and solubility of the cements.
- Look at strontium doping into the $Ca(SO_4)_x(PO_3F)_{1-x}\cdot 2H_2O$ systems perform strength and solubility measurement on these systems.

7.2.4 Chapter 6

- Repeat XRF measurement on amorphous phosphate containing species and investigate the reproducibility of these results.
- Use the Pair Distribution Function (PDF) to analyse the structure of the amorphous phosphate containing species.

7.3 References

1. A. Perloff, *Acta Crystallographica Section B-Structural Crystallography and Crystal Chemistry*, 1972, **B 28**, 2183-2191.
2. J. A. Armstrong, E. R. Williams and M. T. Weller, *Journal of the American Chemical Society*, 2011, **133**, 8252-8263.
3. J. Zhang and G. H. Nancollas, *Journal of Crystal Growth*, 1992, **118**, 287-294.
4. X. P. Wang and J. D. Ye, *Journal of Materials Science-Materials in Medicine*, 2008, **19**, 1183-1186.
5. N. Takahashi, T. Sasaki, Y. Tsouderos and T. Suda, *Journal of Bone and Mineral Research*, 2003, **18**, 1082-1087.
6. M. Weil, M. Puchberger and E. J. Baran, *Inorganic Chemistry*, 2004, **43**, 8330-8335.
7. M. Weil, M. Puchberger, E. Fuglein, E. J. Baran, J. Vannahme, H. J. Jakobsen and J. Skibsted, *Inorganic Chemistry*, 2007, **46**, 801-808.
8. D. H. Menz, K. Heide, C. Kunert, C. Mensing and L. Kolditz, *Zeitschrift fur Anorganische und Allegemeine Chemie*, 1986, **541**, 191-197.
9. J. Dexpert-Ghys, R. Mauricot and M. D. Faucher, *Journal of Luminescence*, 1996, **69**, 203-215.
10. M. Ferhi, K. Horchani-Naifer and M. Férid, *Journal of Rare Earths*, 2009, **27**, 182-186.
11. S. Hachani, B. Moine, A. El-akrmi and M. Férid, *Optical Materials*, 2009, **31**, 678-684.
12. K. Amezawa, H. Maekawa, Y. Tomii and N. Yamamoto, *Solid State Ionics*, 2001, **145**, 233-240.

Appendix 1

1.1 Crysfire Results

1.1.1 Phase 1

Table 1.1: Results obtained from indexing of Phase 1 using the Crysfire software

I20	Merit	Index Program	Pedig	Volume	a	b	c	alpha	beta	gamma
20	10	TREOR90/log	Ort__1	862.823	7.9875	8.4361	12.8047	90	90	90
20	5.4	DICVOL91/log	Ort__1	3551.353	4.3829	17.9145	45.2299	90	90	90
20	5.4	DICVOL91/log	Mon__1	1555.466	11.1871	11.6692	12.8433	90	90	111.915

1.1.2 Phase 2

Table 1.2: Results obtained from indexing of Phase 2 using the Crysfire software

I20	Merit	Index Program	Pedig	Volume	a	b	c	alpha	beta	gamma
19	79	TREOR90/log	Mon__2	326.665	6.973	7.1216	6.7191	90	101.756	90
18	6	TREOR90/log	Mon__1	1460.353	12.9172	9.8617	11.755	90	102.775	90
17	6	TREOR90/log	Ort__2	1967.204	17.9021	11.1543	9.8515	90	90	90
17	6	TREOR90/log	Ort__1	1967.204	17.9021	11.1543	9.8515	90	90	90

1.2 Cell Refinements

1.2.1 $SrPO_3F \cdot H_2O$ (Phase 1): Cycle 5

A	B	C	ALPHA	BETA	GAMMA	ABS	ZERO
INIT :							
12.815076	8.441284	7.992423	90	90	90	0	0.028911
FINAL :							
12.815076	8.441284	7.992422	90	90	90	0	0.02891
ESD :							
0.009615	0.004103	0.004279	0	0	0	0	0.021192

2THET(O)	2THET(C)	H	K	L	D(O)	D(C)	DIF	WEIGHT	SIN**2 (O-C)
13.882	13.838	2	0	0	6.374	6.394	0.02	1.00E+00	0.00009
16.81	16.785	1	1	1	5.27	5.278	0.008	1.00E+00	0.00006
17.785	17.756	2	0	1	4.983	4.991	0.008	1.00E+00	0.00008
20.685	20.661	2	1	1	4.291	4.296	0.005	1.00E+00	0.00007
21.087	21.061	0	2	0	4.21	4.215	0.005	1.00E+00	0.00008
22.263	22.256	0	0	2	3.99	3.991	0.001	1.00E+00	0.00002
24.655	24.657	0	1	2	3.608	3.608	0	1.00E+00	-0.00001
24.879	24.856	1	2	1	3.576	3.579	0.003	1.00E+00	0.00008
25.639	25.632	1	1	2	3.472	3.473	0.001	1.00E+00	0.00003
25.915	25.906	3	1	1	3.435	3.437	0.001	1.00E+00	0.00003
26.293	26.29	2	0	2	3.387	3.387	0	1.00E+00	0.00001
27.871	27.853	4	0	0	3.199	3.201	0.002	1.00E+00	0.00007
29.783	29.762	3	2	0	2.997	2.999	0.002	1.00E+00	0.00009
30.054	30.054	4	0	1	2.971	2.971	0	1.00E+00	0
31.616	31.616	1	2	2	2.828	2.828	0	1.00E+00	0
31.837	31.842	3	2	1	2.809	2.808	0	1.00E+00	-0.00002
33.92	33.913	2	2	2	2.641	2.641	0.001	1.00E+00	0.00003
35.156	35.167	4	2	0	2.551	2.55	-0.001	1.00E+00	-0.00006
36.456	36.525	2	0	3	2.463	2.458	-0.005	1.00E+00	-0.00036
40.619	40.657	1	2	3	2.219	2.217	-0.002	1.00E+00	-0.00021
42.785	42.793	5	2	1	2.112	2.111	0	1.00E+00	-0.00005
43.454	43.452	1	4	0	2.081	2.081	0	1.00E+00	0.00001
44.166	44.207	4	0	3	2.049	2.047	-0.002	1.00E+00	-0.00025
47.275	47.273	1	1	4	1.921	1.921	0	1.00E+00	0.00001
48.765	48.789	0	4	2	1.866	1.865	-0.001	1.00E+00	-0.00016
49.353	49.337	1	4	2	1.845	1.846	0.001	1.00E+00	0.00011
50.986	50.956	2	4	2	1.79	1.791	0.001	1.00E+00	0.0002
53.183	53.207	4	4	1	1.721	1.72	-0.001	1.00E+00	-0.00017

54.129	54.075	4	0	4	1.693	1.695	0.002	1.00E+00	0.00038

Wavelength for the above lines is 1.54060

R FACTOR = 0.00000055

1.2.2 $SrPO_3F$ (Phase 2): Cycle 5

A	B	C	ALPHA	BETA	GAMMA	ABS	ZERO
INIT:							
6.72033	7.12124	6.972837	90	101.75536	90	0	0.00126
FINAL :							
6.720326	7.12124	6.972833	90	101.75521	90	0	0.00126
ESD :							
0.000993	0.000875	0.001036	0	0.006653	0	0	0.00575

2THET(O)	2 THET(C)	H K L	D(O)	D(C)	DIF	WEIGHT	SIN**2 (O-C)
16.691	16.689	1 0 -1	5.307	5.308	0.001	1.00E+00	0.00001
17.985	17.987	0 1 1	4.928	4.928	-0.001	1.00E+00	-0.00001
18.35	18.345	1 1 0	4.831	4.832	0.001	1.00E+00	0.00001
20.548	20.553	1 0 1	4.319	4.318	-0.001	1.00E+00	-0.00002
20.844	20.856	1 1 -1	4.258	4.256	-0.002	1.00E+00	-0.00004
24.085	24.085	1 1 1	3.692	3.692	0	1.00E+00	0
24.989	24.989	0 2 0	3.561	3.56	0	1.00E+00	0
26.095	26.087	0 0 2	3.412	3.413	0.001	1.00E+00	0.00003
27.083	27.085	2 0 0	3.29	3.29	0	1.00E+00	-0.00001
28.243	28.246	0 2 1	3.157	3.157	0	1.00E+00	-0.00001
28.971	28.987	0 1 2	3.08	3.078	-0.002	1.00E+00	-0.00007
29.902	29.896	2 1 0	2.986	2.986	0.001	1.00E+00	0.00003
30.349	30.345	2 1 -1	2.943	2.943	0	1.00E+00	0.00002
32.581	32.57	1 2 1	2.746	2.747	0.001	1.00E+00	0.00005
33.74	33.743	2 0 -2	2.654	2.654	0	1.00E+00	-0.00002
34.929	34.922	2 1 1	2.567	2.567	0	1.00E+00	0.00003
36.095	36.086	2 1 -2	2.486	2.487	0.001	1.00E+00	0.00005
37.001	37	1 2 -2	2.428	2.428	0	1.00E+00	0.00001
37.55	37.553	2 2 -1	2.393	2.393	0	1.00E+00	-0.00002
39.116	39.133	1 0 -3	2.301	2.3	-0.001	1.00E+00	-0.00009
40.368	40.363	1 3 0	2.233	2.233	0	1.00E+00	0.00003
40.514	40.528	3 0 -1	2.225	2.224	-0.001	1.00E+00	-0.00008
40.916	40.924	1 2 2	2.204	2.203	0	1.00E+00	-0.00005
41.202	41.211	1 1 -3	2.189	2.189	0	1.00E+00	-0.00005
41.639	41.634	0 1 3	2.167	2.167	0	1.00E+00	0.00003
43.148	43.126	3 1 0	2.095	2.096	0.001	1.00E+00	0.00013
43.471	43.471	1 3 1	2.08	2.08	0	1.00E+00	0
43.769	43.78	2 1 2	2.067	2.066	0	1.00E+00	-0.00007
44.677	44.676	1 0 3	2.027	2.027	0	1.00E+00	0
45.389	45.385	2 1 -3	1.997	1.997	0	1.00E+00	0.00002
45.943	45.934	3 0 1	1.974	1.974	0	1.00E+00	0.00006
46.549	46.553	1 1 3	1.949	1.949	0	1.00E+00	-0.00002
47.036	47.029	1 3 -2	1.93	1.931	0	1.00E+00	0.00005

47.18	47.179	2 3 0	1.925	1.925	0	1.00E+00	0.00001
47.379	47.375	0 2 3	1.917	1.917	0	1.00E+00	0.00002
47.481	47.485	2 3 -1	1.913	1.913	0	1.00E+00	-0.00003
48.733	48.727	3 2 0	1.867	1.867	0	1.00E+00	0.00004
50.31	50.315	1 3 2	1.812	1.812	0	1.00E+00	-0.00003
50.755	50.749	2 3 1	1.797	1.798	0	1.00E+00	0.00004
51.285	51.276	0 4 0	1.78	1.78	0	1.00E+00	0.00006
51.615	51.617	2 3 -2	1.769	1.769	0	1.00E+00	-0.00001
53.119	53.123	0 4 1	1.723	1.723	0	1.00E+00	-0.00003
53.663	53.662	0 0 4	1.707	1.707	0	1.00E+00	0.00001
54.24	54.212	1 1 -4	1.69	1.691	0.001	1.00E+00	0.0002
55.018	55.03	2 1 3	1.668	1.667	0	1.00E+00	-0.00009
55.306	55.31	0 1 4	1.66	1.66	0	1.00E+00	-0.00003
55.844	55.851	4 0 0	1.645	1.645	0	1.00E+00	-0.00005
56.251	56.252	4 1 -1	1.634	1.634	0	1.00E+00	0
57.457	57.456	4 1 0	1.603	1.603	0	1.00E+00	0.00001
57.665	57.67	2 3 2	1.597	1.597	0	1.00E+00	-0.00004
58.412	58.419	0 4 2	1.579	1.578	0	1.00E+00	-0.00005
58.996	58.994	2 3 -3	1.564	1.564	0	1.00E+00	0.00001

Wavelength for the above lines is 1.54060

R FACTOR = 0.00000013

1.3 Bond Valence Sum

1.3.1 $SrPO_3F \cdot H_2O$

Table 1.3: Bond Valence Sum calculations for strontium and phosphorus in $SrPO_3F \cdot H_2O$ (where s = bond valence of contributing atoms and V_i =oxidation state)

$SrPO_3F \cdot H_2O$			
Bonds	**Bond Lengths (Å)**	**s**	**V_i**
Sr-F	2.635	0.247	
Sr-O2	2.505	0.351	
Sr-O3	2.560	0.303	
Sr-O3	2.712	0.201	
Sr-O4	2.625	0.254	
Sr-O4	2.486	0.370	
Sr-O5w	2.751	0.181	
Sr-O5w	2.626	0.253	
			Sr = +2.16
P-F	1.610	1.014	
P-O2	1.500	1.365	
P-O3	1.507	1.340	
P-O4	1.518	1.300	
			P = +5.02

1.3.2 $SrPO_3F$

Table 1.4: Bond Valence Sum calculations for strontium and phosphorus in $SrPO_3F$ (where s = bond valence of contributing atoms and V_i =oxidation state)

$SrPO_3F$			
Bonds	**Bond Lengths (Å)**	**s**	**V_i**
Sr-O1	2.596	0.275	
Sr-O1	2.520	0.337	
Sr-O2	2.904	0.119	
Sr-O2	2.565	0.299	
Sr-O2	2.670	0.225	
Sr-O3	2.626	0.253	
Sr-O3	2.548	0.313	
Sr-F	2.869	0.131	
Sr-F	2.670	0.223	
			Sr = +2.18
P-O1	1.514	1.314	
P-O2	1.517	1.303	
P-O3	1.505	1.346	
P-F	1.575	1.114	
			P = +5.08

1.4 XRF Fused Bead Calibration Curves and Results

1.4.1 Calibration Curves

1.4.2 $SrPO_3F \cdot H_2O$

Table 1.5: Calibrated XRF Results for multiple samples of $SrPO_3F \cdot H_2O$

Elements (wt %)	Expected (wt %)	$SrPO_3F \cdot H_2O$ Samples (Actual wt %)								
		Sample 1			Sample 2			Sample 3		
		Run 1	Run 2	Run 3	Run 1	Run 2	Run 3	Run 1	Run 2	Run 3
Sr	43.03	42.93	43.03	43.01	42.93	42.93	42.79	42.43	42.49	42.39
P	15.21	15.20	15.14	15.23	15.18	15.17	15.12	15.27	15.28	15.24
O	31.43	40.72	40.72	40.62	40.77	40.78	40.95	41.18	41.05	41.19
F	9.33									
H	0.99									
Na	-	0.67	0.66	0.67	0.64	0.64	0.66	0.69	0.70	0.70
K	-	0.48	0.46	0.47	0.48	0.48	0.48	0.46	0.48	0.48
Sr:P Ratio	1.00	0.995	1.001	0.995	0.996	0.997	0.997	0.979	0.980	0.980

* XRF finds it difficult to detect elements below sodium, so quantitative analysis of oxygen, fluorine and hydrogen was not possible. As the samples were prepared via the fused bead method, fluorine and water would be lost during the sample preparation. The wt % values stated for both oxygen and fluorine are combined. All of the elements sum up to 100 %.

1.4.3 $SrPO_3F$

Table 1.6: Calibrated XRF results for multiple samples of $SrPO_3F$

Elements (wt %)	Expected (wt %)	$SrPO_3F$ Samples (Actual wt %)								
		Sample 1			Sample 2			Sample 3		
		Run 1	Run 2	Run 3	Run 1	Run 2	Run 3	Run 1	Run 2	Run 3
Sr	42.71	45.05	45.09	45.05	44.64	44.69	44.73	44.27	44.24	44.45
P	16.69	15.83	15.90	15.87	16.06	16.08	16.12	16.01	16.00	16.05
O	25.86	37.03	36.97	37.02	37.24	37.16	37.12	37.71	37.75	37.48
F	10.24									
Na	-	1.59	1.58	1.59	1.58	1.59	1.56	1.57	1.56	1.54
K	-	0.50	0.46	0.47	0.48	0.47	0.47	0.45	0.45	0.48
Sr:P Ratio	1.00	1.003	0.999	1.000	0.979	0.979	0.977	0.974	0.975	0.976

* XRF finds it difficult to detect elements below sodium, so quantitative analysis of oxygen and fluorine was not possible. As the samples were prepared via the fused bead method, fluorine would be lost during the sample preparation. The wt. % values stated for both oxygen and fluorine are combined. All of the elements sum up to 100 %.

1.5 SEM-EDAX

1.5.1 $SrPO_3F \cdot H_2O$

Figure 1.1: EDAX results obtained from a sample of $SrPO_3F \cdot H_2O$

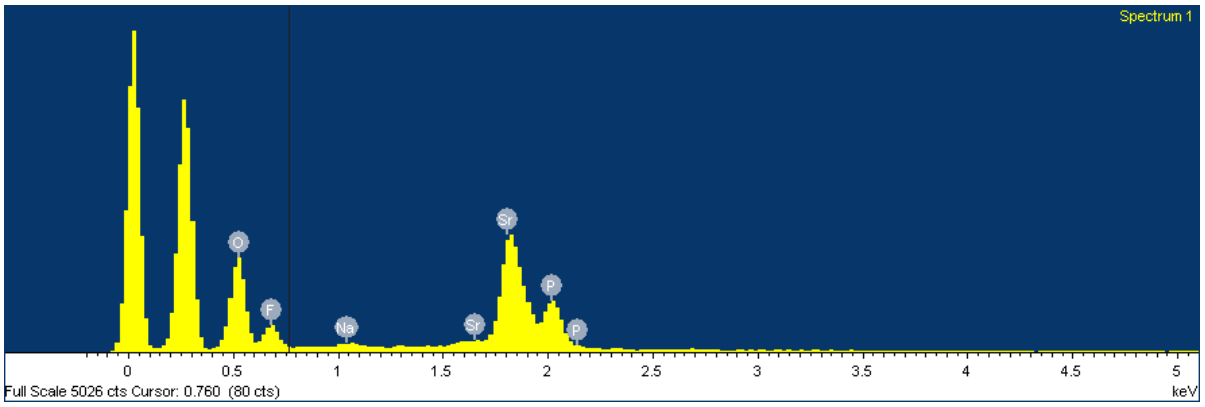

Table 1.7: A comparison of the experimental and expected weight percentages of elements in $SrPO_3F \cdot H_2O$

Element	Weight % determined by EDAX	Expected Weight %
Sr	44.61	43.03
P	12.69	15.21
O	32.08	31.43
F	10.02	9.33
H	-	0.99
Na	0.60	-
Sr:P	1.24	1.00

1.5.2 $SrPO_3F$

Figure 1.2: EDAX results obtained from a sample of $SrPO_3F$

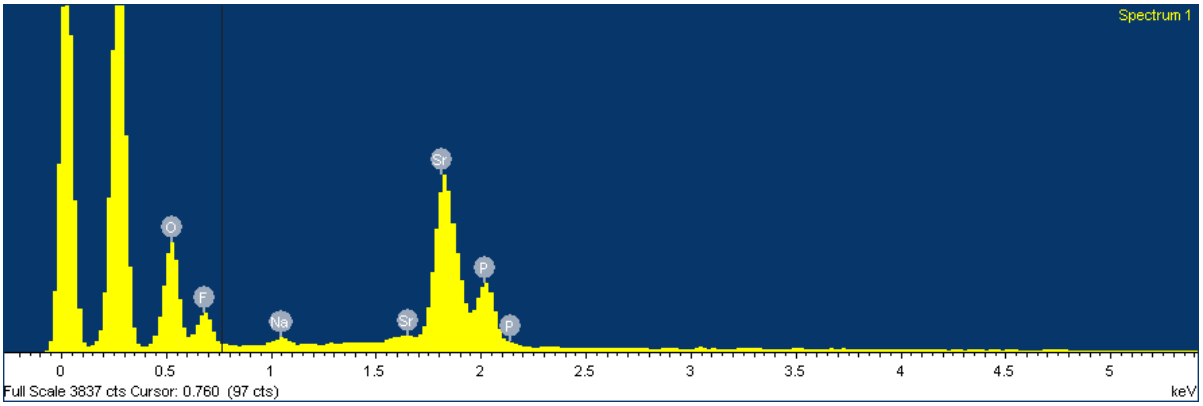

Table 1.8 : A comparison of the experimental and expected weight percentages of elements in $SrPO_3F$

Element	Weight % determined by EDAX	Expected Weight %
Sr	48.01	42.71
P	12.53	16.69
O	28.35	25.86
F	10.23	10.24
Na	0.89	-
Sr:P	1.35	1.00

1.6 Solid State NMR Results

1.6.1 $SrPO_3F{\cdot}H_2O$

Table 1.9: Solid State NMR Results obtained from the ^{31}P, ^{1}H and ^{19}F experiments for a sample of $SrPO_3F{\cdot}H_2O$

	δ_{iso} / ppm ± 0.5 ppm	% Content ± 2 %	$^{1}J_{PF}$ / Hz ± 2 Hz
^{31}P (One Pulse)			
Impurity	-4.66	13	-
$SrPO_3F{\cdot}H_2O$	-2.74	87	855
^{31}P (^{1}H Decoupled)			
Impurity	-4.66	26	-
$SrPO_3F{\cdot}H_2O$	-2.74	74	-
^{31}P (^{19}F Decoupled)			
Impurity	-5.37	23	-
$SrPO_3F{\cdot}H_2O$	-2.57	77	-
^{19}F (One Pulse)			
SrF_2	-87.86	3	-
$SrPO_3F{\cdot}H_2O$	-73.20	72	855
Impurity	-71.86	25	-
^{19}F (^{31}P Decoupled)			
SrF_2	-87.86	1	-
$SrPO_3F{\cdot}H_2O$	-73.20	75	-
Impurity	-71.86	24	-

1.6.2 $SrPO_3F$

Table 1.10: Solid State NMR Results obtained from the ^{31}P and ^{19}F experiments for a sample of $SrPO_3F$

	δ_{iso} / ppm ± 0.5 ppm	% Content ± 2 %	$^1J_{PF}$ / Hz ± 2 Hz
^{31}P One Pulse			
Impurity	0.14	27.3	-
$SrPO_3F$	-2.12	72.7	-
^{31}P (19F Decoupled)			
Impurity	0.14	20.3	-
$SrPO_3F$	-	79.7	667
^{19}F One Pulse			
SrF_2	-88.5	24.61	-
$SrPO_3F$	-	53.64	664
Impurity 1	-63.2	20.63	-
Impurity 2	-80.0	1.13	-
^{19}F (^{31}P Decoupled)			
SrF_2	-88.6	45.32	-
$SrPO_3F$	-64.88	47.53	-
Impurity 1	-63.2	7.15	-

1.7 Amorphous Content within Strontium Fluorophosphate Phases

1.7.1 Two Phase Rietveld Refinement: $SrPO_3F \cdot H_2O$ (40°C) and TiO_2

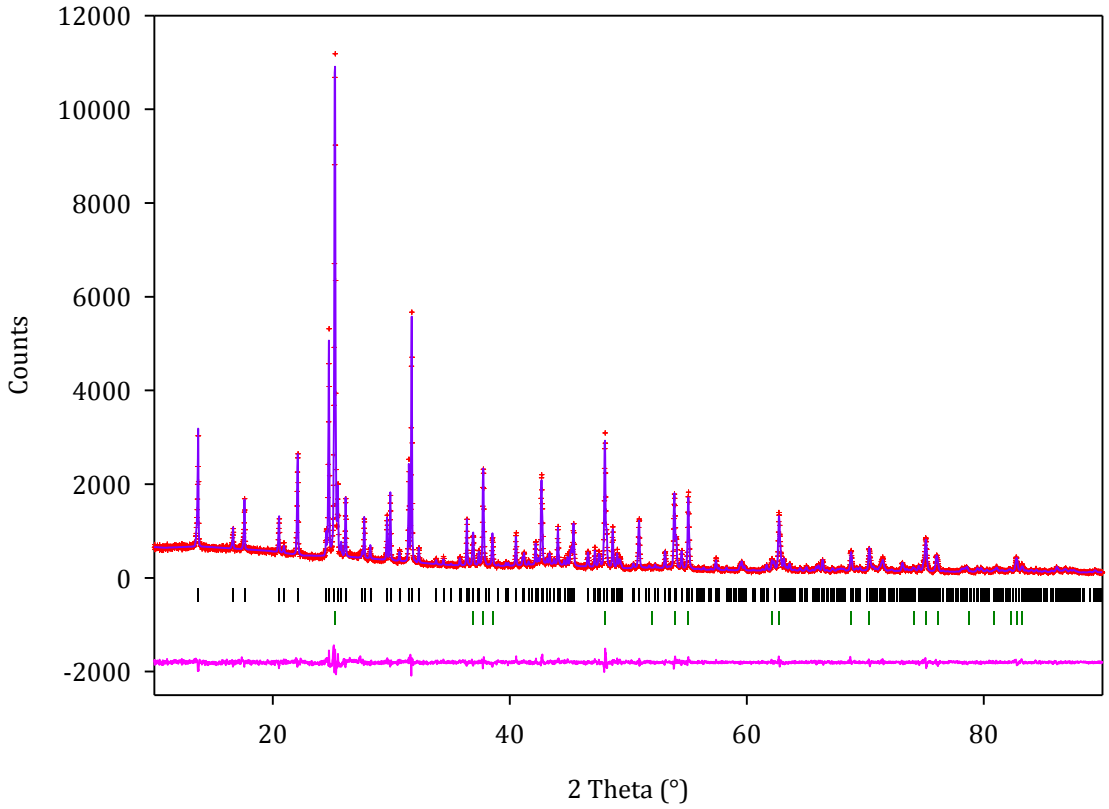

Figure 1.3: Final observed (red), calculated (purple) and difference profiles (pink) of the PXRD refinement of $SrPO_3F \cdot H_2O$ and TiO_2. Reflection positions for $SrPO_3F \cdot H_2O$ and TiO_2 are shown as black and green vertical tick marks respectively

Table 1.11: Summarised data obtained from the two phase Rietveld refinements of $SrPO_3F{\cdot}H_2O$ and TiO_2

	$SrPO_3F{\cdot}H_2O$ (synthesised at 40 °C) + TiO_2 refinement
Mass of $SrPO_3F{\cdot}H_2O$ (g)	1.00
Mass of TiO_2 (g)	0.70
Total mass of $SrPO_3F{\cdot}H_2O/TiO_2$ sample (g)	1.70
Actual wt % of $SrPO_3F{\cdot}H_2O$ in sample	58.82
Actual wt % of TiO_2 in sample	41.18
Wt % of $SrPO_3F{\cdot}H_2O$ from Rietveld analysis	48.20
Wt % of TiO_2 from Rietveld analysis	51.80
Calculated amorphous content (wt %)	21

1.7.2 Two Phase Rietveld Refinement: $SrPO_3F$ (80°C) and TiO_2

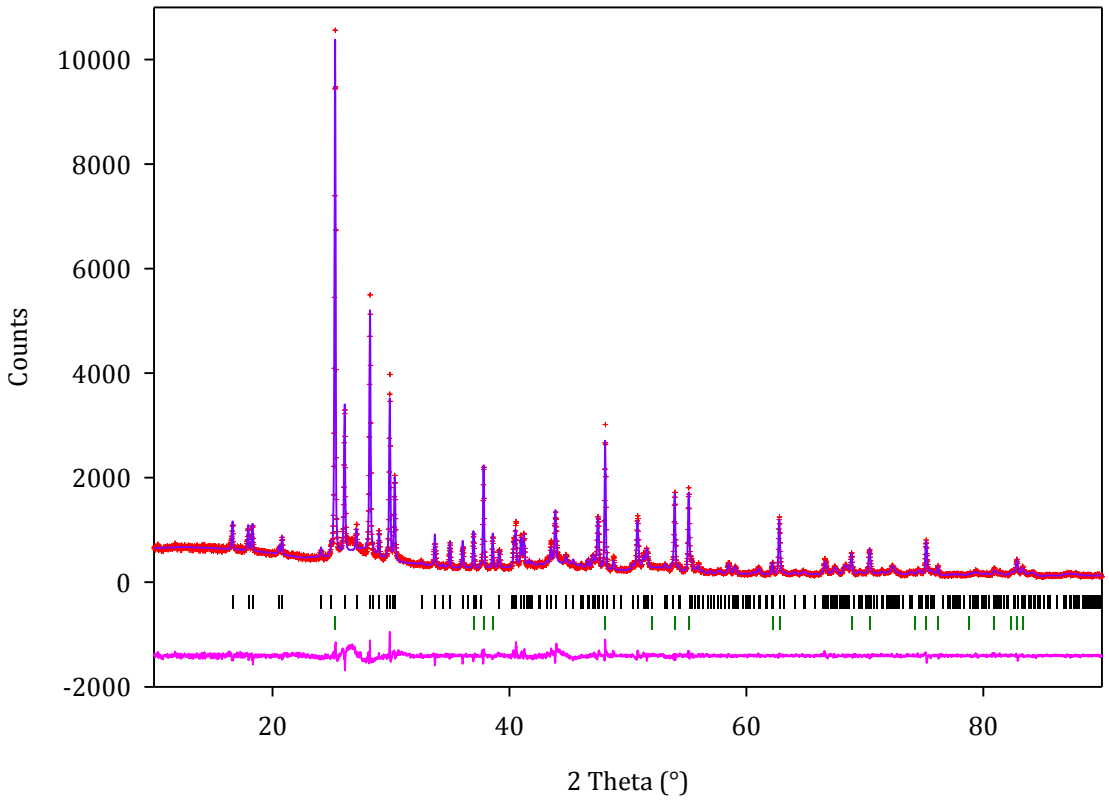

Figure 1.4: Final observed (red), calculated (purple) and difference profiles (pink) of the PXRD refinement of $SrPO_3F$ and TiO_2. Reflection positions for $SrPO_3F$ and TiO_2 are shown as black and green vertical tick marks respectively

Table 1.12: Summarised data obtained from the two phase Rietveld refinements of $SrPO_3F$ and TiO_2

	$SrPO_3F$ (synthesised at 80 °C) + TiO_2 refinement
Mass of $SrPO_3F$ (g)	1.00
Mass of TiO_2 (g)	0.55
Total mass of $SrPO_3F/TiO_2$ in sample (g)	1.55
Actual wt % of $SrPO_3F$ in sample	64.52
Actual wt % of TiO_2 in sample	35.48
Wt % of $SrPO_3F$ from Rietveld analysis	52.49
Wt % of TiO_2 from Rietveld	47.51
Calculated amorphous content (wt %)	25

1.8 X-Ray Fluorescence Spectroscopy: Fluorine Emission

1.8.1 Heat Treatments of $SrPO_3F$

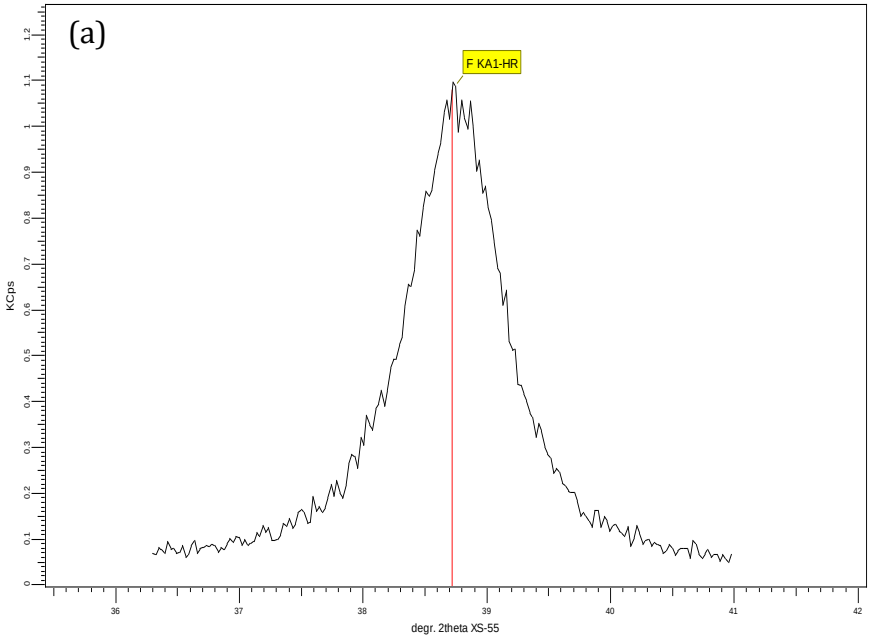

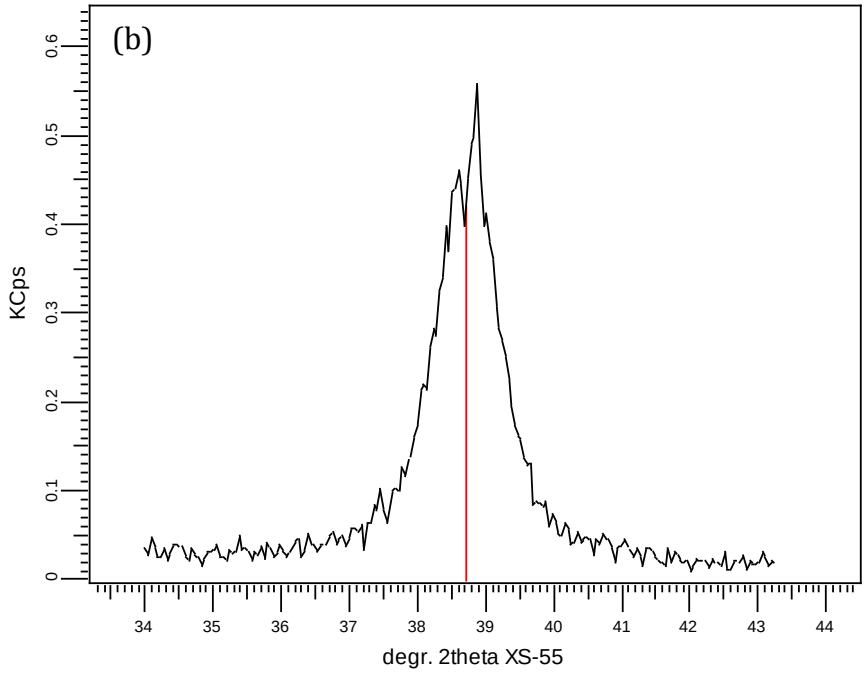

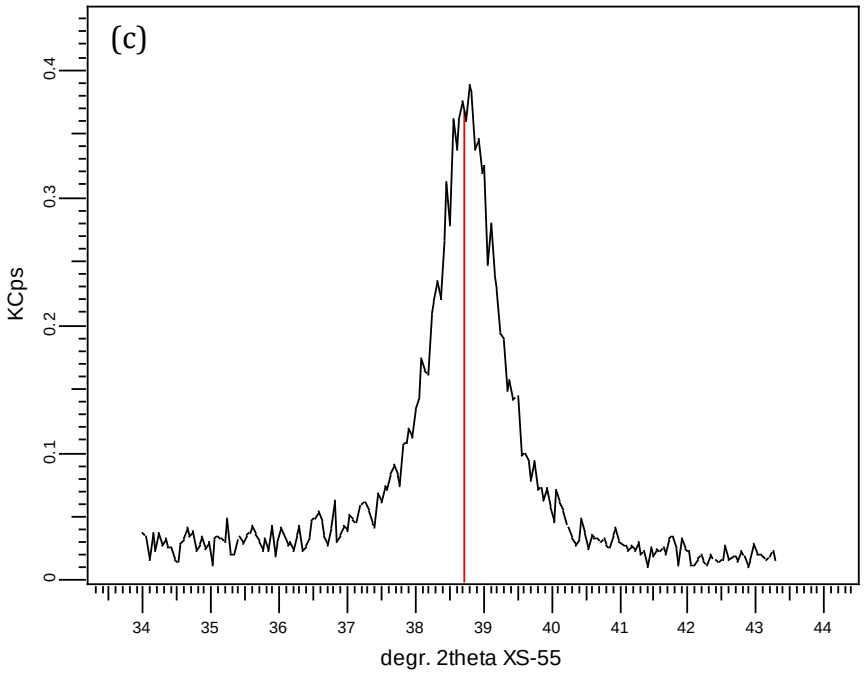
(c)
KCps
0
0.1
0.2
0.3
0.4
34
35
36
37
38
39
40
41
42
43
44
degr. 2theta XS-55

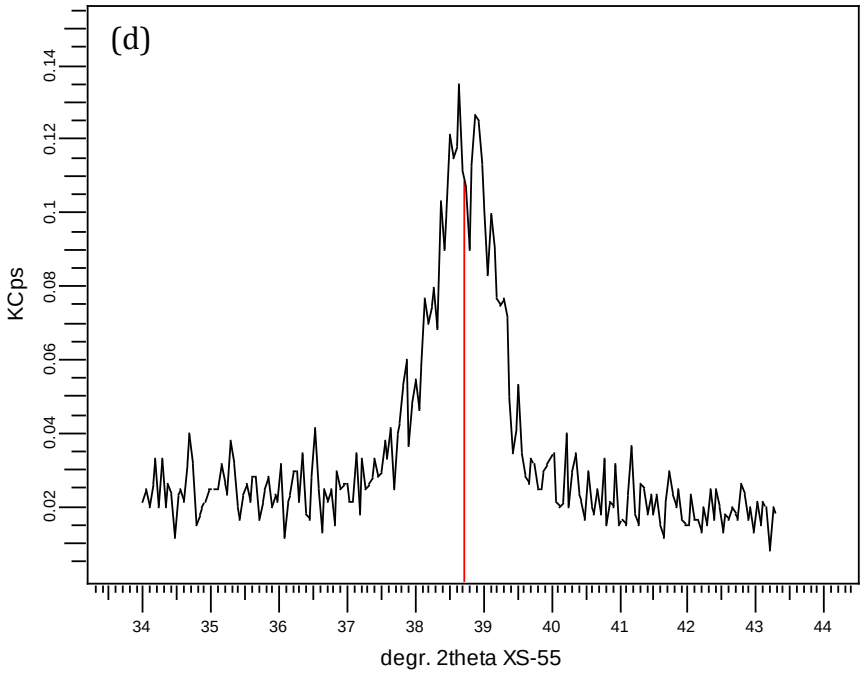
(d)
KCps
0.02
0.04
0.06
0.08
0.1
0.12
0.14
34
35
36
37
38
39
40
41
42
43
44
degr. 2theta XS-55

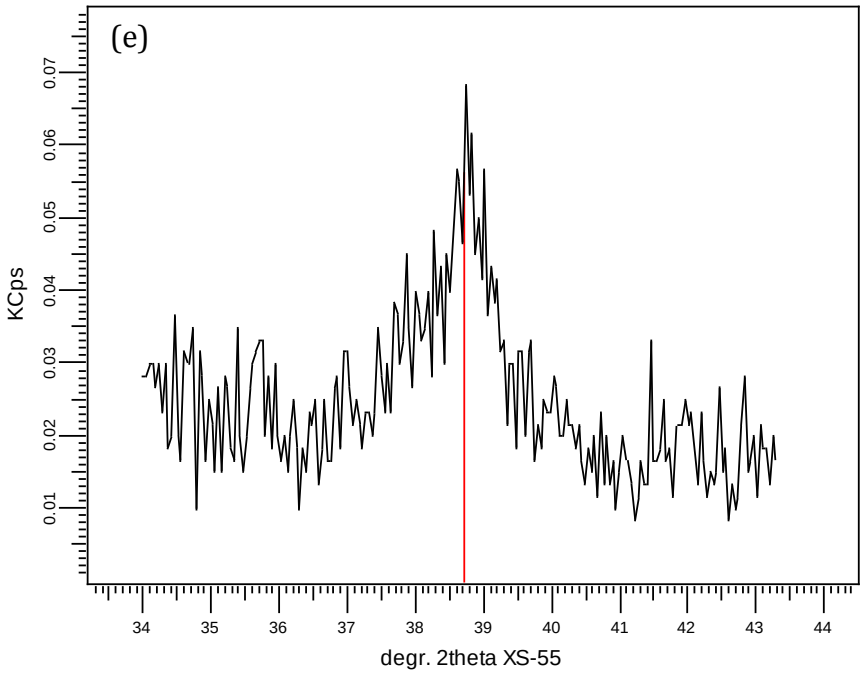

Figure 1.5: Emission signal obtained from the Fluorine Kα_1 line for heat treated samples of $SrPO_3F$ (a) $SrPO_3F$ (b) 200°C, (c) 300°C, (d) 500°C (e) 750°C

Appendix 2

2.1 $Sr_{1-x}Ca_xPO_3F$ Systems

2.1.1 Amorphous Content within the $Sr_{1-x}Ca_xPO_3F$ systems

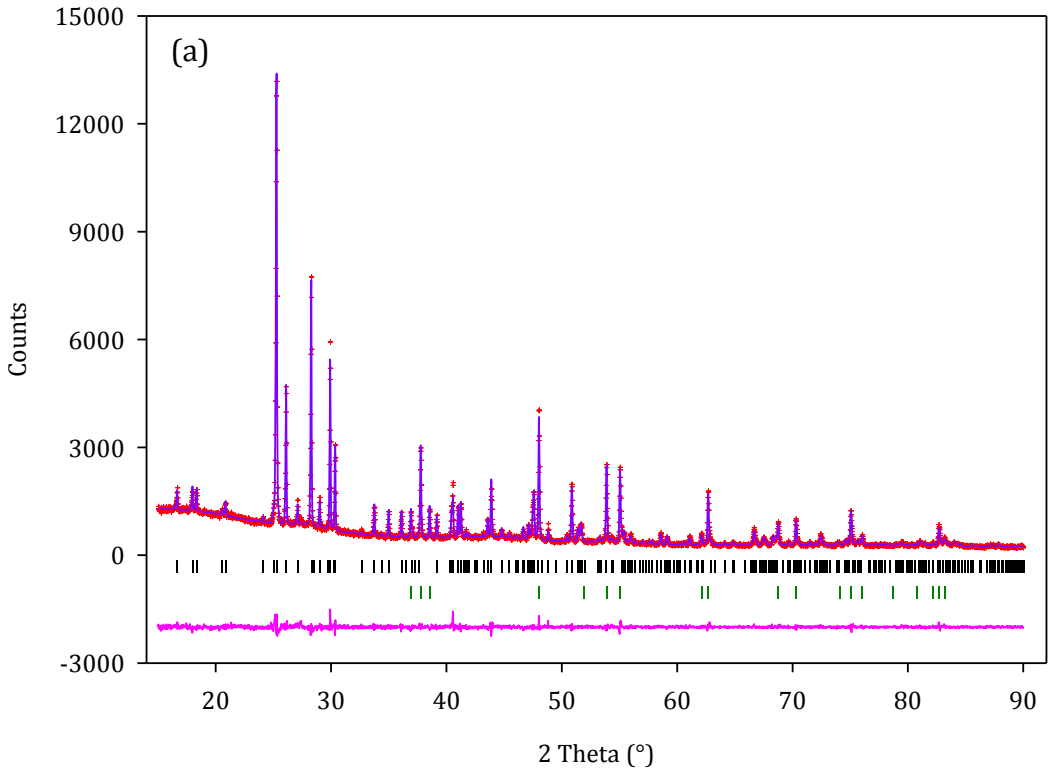

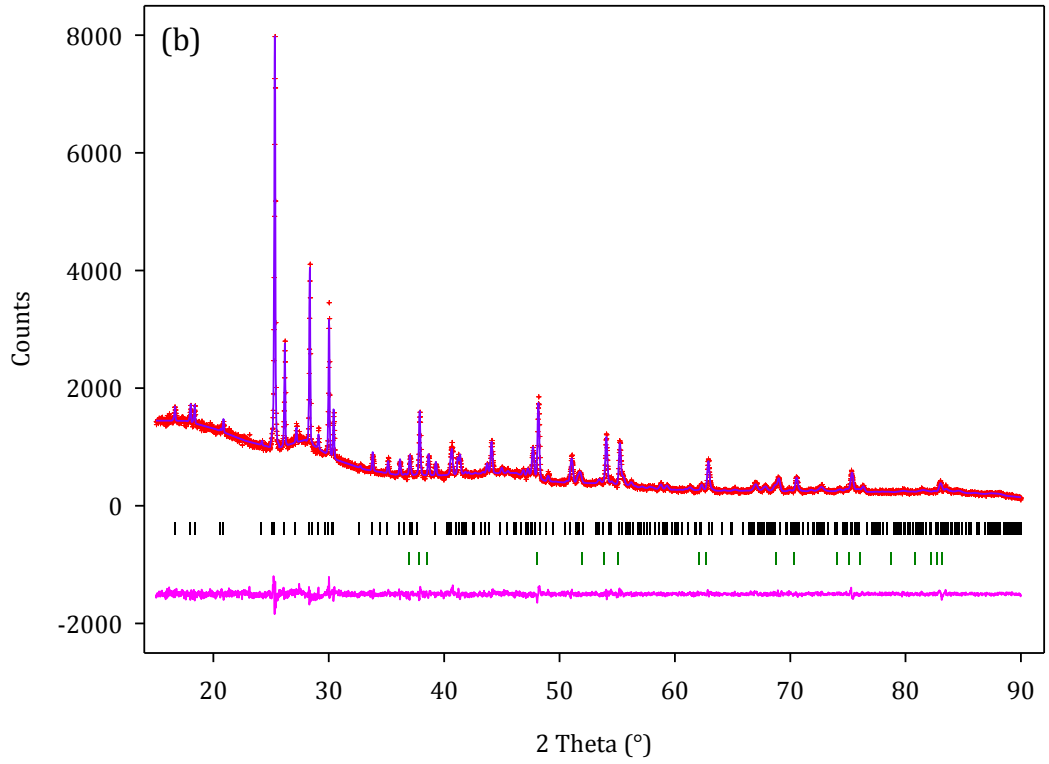

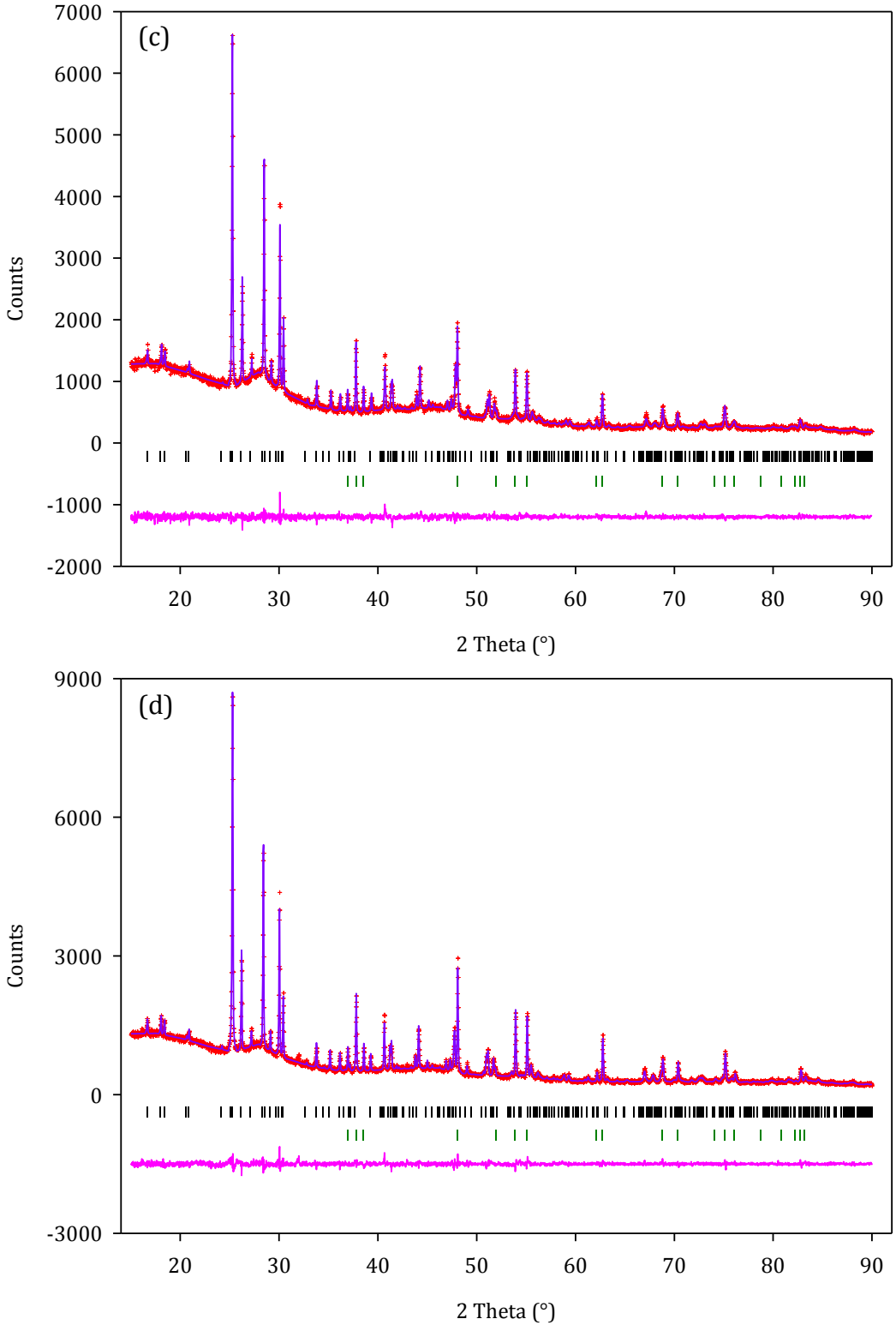

Figure 2.1: Final observed (red), calculated (purple) and difference profiles (pink) of the PXRD refinements for the x = 0.1-0.4 members of the $Sr_{1-x}Ca_xPO_3F$ series with TiO_2 (a-d). Reflection positions for the Calcium doped systems and TiO_2 are shown as vertical tick marks (black and green respectively)

Table 2.1: Summarised data obtained from the two phase Rietveld refinements of each member of the $Sr_{1-x}Ca_xPO_3F$ series with TiO_2

	Calcium Doped Systems				
	$SrPO_3F$	$Sr_{0.9}Ca_{0.1}PO_3F$	$Sr_{0.8}Ca_{0.2}PO_3F$	$Sr_{0.7}Ca_{0.3}PO_3F$	$Sr_{0.6}Ca_{0.4}PO_3F$
Mass of Monazite phase (g)	1.00	0.30	0.30	0.30	0.30
Mass of TiO_2 (g)	0.55	0.12	0.09	0.09	0.06
Mass of Monazite/TiO_2 in sample (g)	1.55	0.42	0.39	0.39	0.36
Actual wt % of Monazite in sample	64.52	62.50	76.92	76.92	83.33
Actual wt % of TiO_2 in sample	35.48	37.50	28.57	28.57	16.67
Wt % of Monazite from Rietveld analysis	52.49	48.61	47.23	51.29	58.89
Wt % of TiO_2 from Rietveld analysis	47.51	51.39	52.77	48.71	41.11
Calculated Amorphous Content (wt %)	25	27	56	53	59

2.1.2 NPD Rietveld Refinements

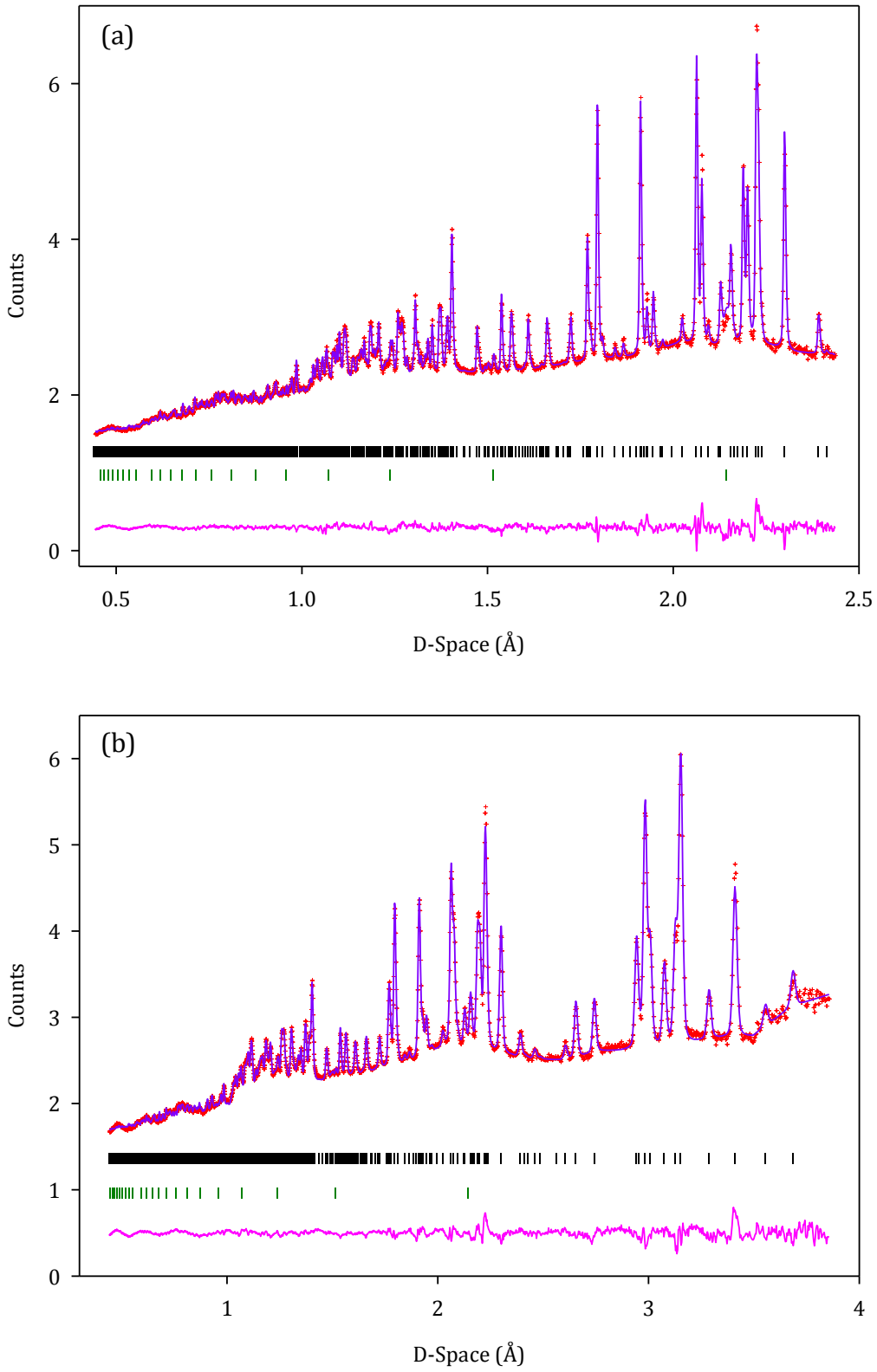

Figure 2.2: Final observed (red), calculated (purple) and difference profiles (pink) of the NPD refinement of $Sr_{0.9}Ca_{0.1}PO_3F$ (a) back scattering bank (b) 90° bank. Reflections positions for $Sr_{0.9}Ca_{0.1}PO_3F$ and the impurity from the vanadium can are shown as vertical tick marks (black and green respectively)

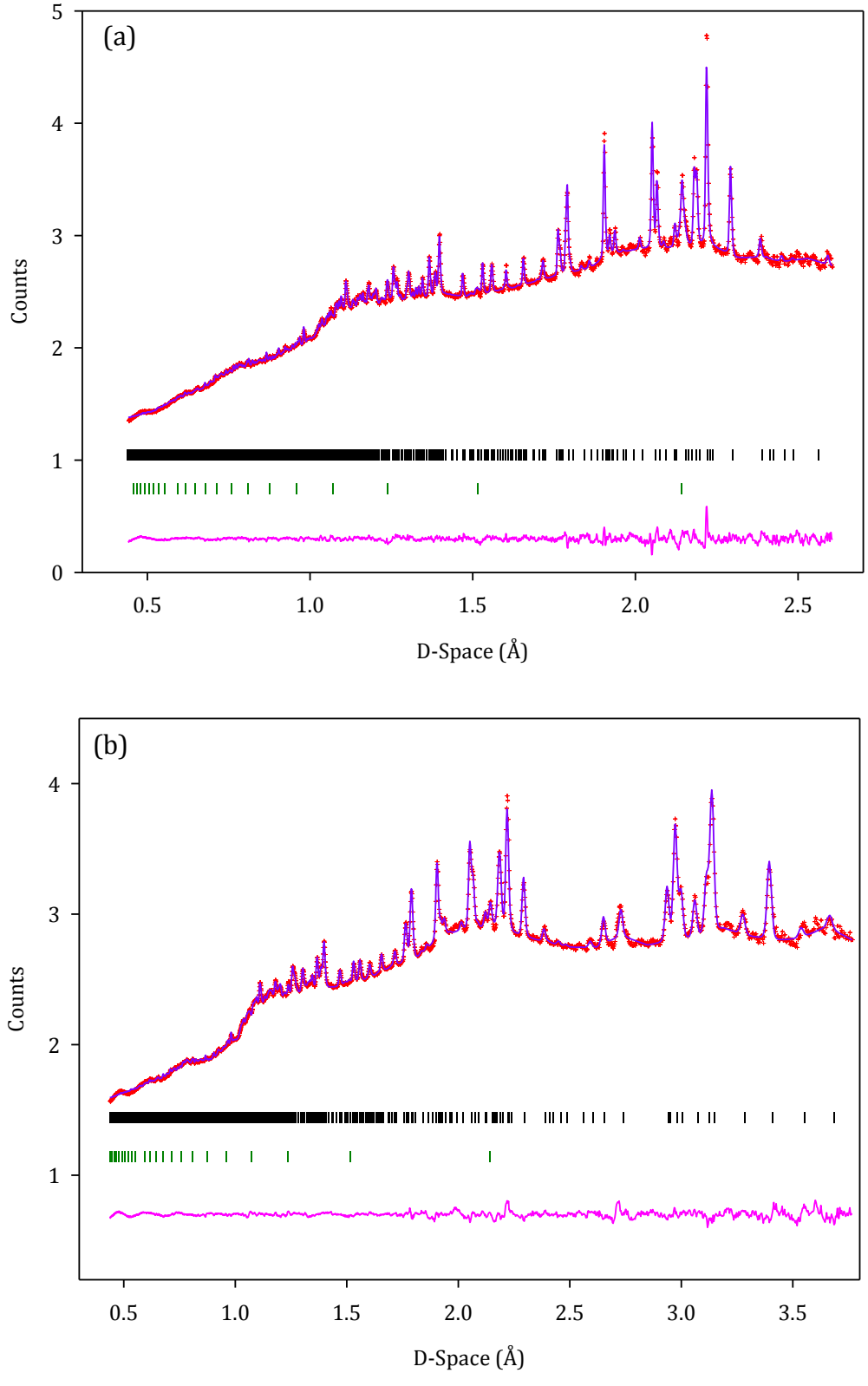

:

Figure 2.3: Final observed (red), calculated (purple) and difference profiles (pink) of the NPD refinement of $Sr_{0.7}Ca_{0.3}PO_3F$ (a) back scattering bank (b) 90° bank. Reflections positions for $Sr_{0.7}Ca_{0.3}PO_3F$ and the impurity from the vanadium can are shown as vertical tick marks (black and green respectively)

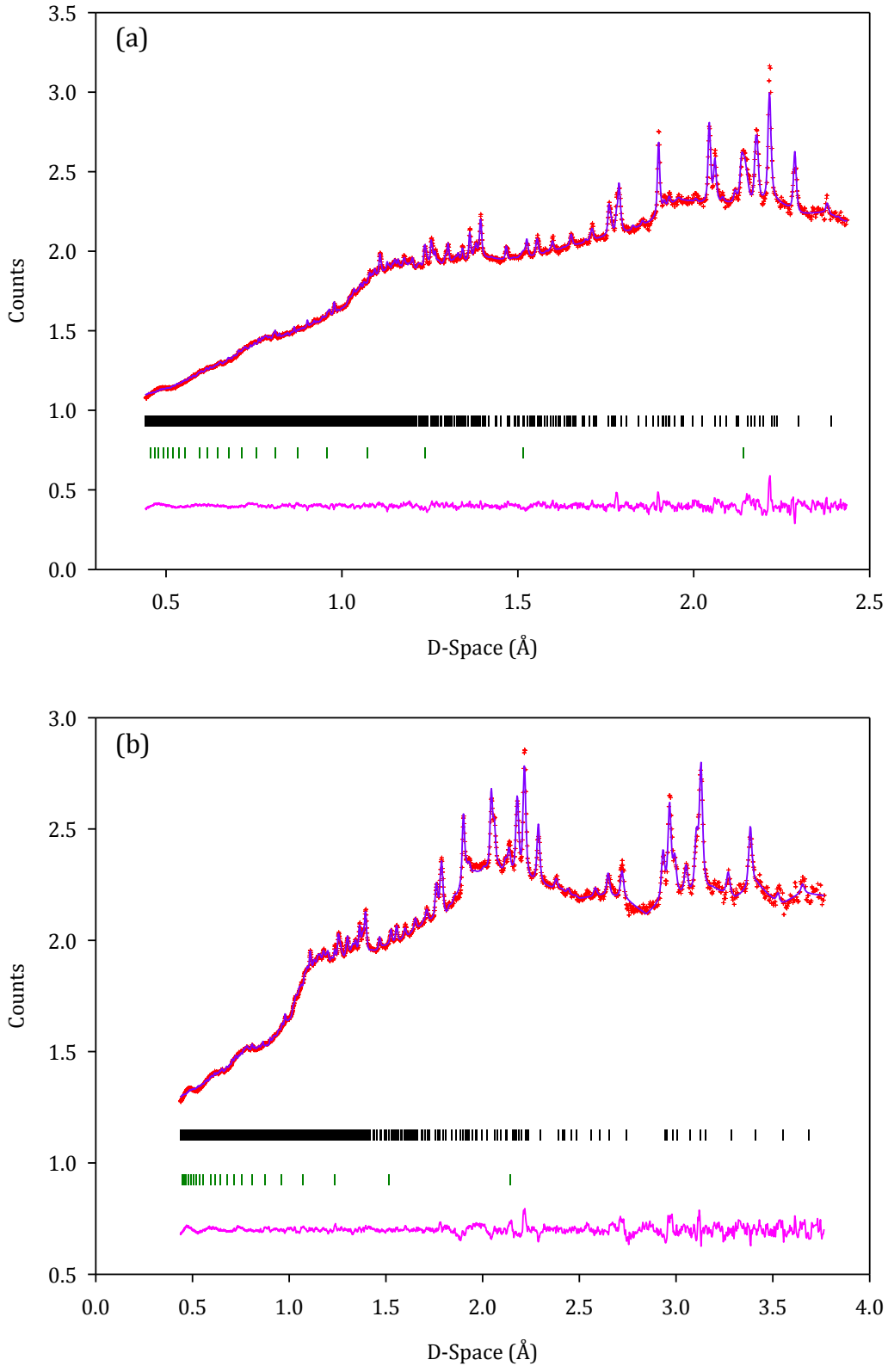

Figure 2.4: Final observed (red), calculated (purple) and difference profiles (pink) of the NPD refinement of $Sr_{0.6}Ca_{0.4}PO_3F$ (a) back scattering bank (b) 90° bank. Reflections positions for $Sr_{0.6}Ca_{0.4}PO_3F$ and the impurity from the vanadium can are shown as vertical tick marks (black and green respectively)

Table 2.2: Refined structural parameters obtained from the NPD refinements of each member of the $Sr_{1-x}Ca_xPO_3F$ series

			x = 0			
Atom	**Multiplicity**	**x**	**y**	**z**	**Uiso*100/Å²**	**Fractional Occupancy**
Sr	4	0.2694(2)	0.1392(2)	0.1029(2)	1.15(5)	1
P	4	0.3150(3)	0.1468(3)	0.6037(4)	1.99(5)	1
O1	4	0.2528(3)	-0.0133(3)	0.4525(3)	2.23(6)	1
O2	4	0.3841(3)	0.3175(3)	0.4988(3)	1.40(5)	1
O3	4	0.4516(3)	0.0997(3)	0.8009(4)	2.60(7)	1
F	4	0.1248(3)	0.2038(3)	0.6803(3)	2.55(7)	1
			x = 0.1			
Atom	**Multiplicity**	**x**	**y**	**z**	**Uiso*100/Å²**	
Sr	4	0.2701(3)	0.1388(3)	0.1018(3)	1.04(4)	0.90
Ca	4	0.2701(3)	0.1388(3)	0.1018(3)	1.04(4)	0.10
P	4	0.3149(4)	0.1465(4)	0.6030(4)	0.95(5)	1
O1	4	0.2544(4)	-0.0105(4)	0.4526(4)	1.21(5)	1
O2	4	0.3846(4)	0.3166(4)	0.4989(4)	1.11(5)	1
O3	4	0.4495(4)	0.1015(5)	0.8025(4)	1.64(6)	1
F	4	0.1209(5)	0.2056(5)	0.6740(5)	2.32(6)	1
			x = 0.2			
Atom	**Multiplicity**	**x**	**y**	**z**	**Uiso*100/Å²**	
Sr	4	0.2657(5)	0.1389(5)	0.0999(5)	0.55(6)	0.80
Ca	4	0.2657(5)	0.1389(5)	0.0999(5)	0.55(6)	0.20
P	4	0.3097(10)	0.1525(10)	0.6013(10)	1.93(12)	1
O1	4	0.2541(7)	-0.0118(6)	0.4515(7)	1.20(9)	1
O2	4	0.3848(7)	0.3161(8)	0.4908(7)	1.11(9)	1
O3	4	0.4530(8)	0.1020(8)	0.8020(7)	1.02(9)	1
F	4	0.1180(9)	0.2030(9)	0.6767(9)	2.45(13)	1
			x = 0.3			
Atom	**Multiplicity**	**x**	**y**	**z**	**Uiso*100/Å²**	
Sr	4	0.2689(5)	0.1403(5)	0.1024(5)	0.83(7)	0.70
Ca	4	0.2689(5)	0.1403(5)	0.1024(5)	0.83(7)	0.30
P	4	0.3118(8)	0.1467(8)	0.6027(8)	1.62(10)	1
O1	4	0.2512(6)	-0.0125(6)	0.4492(7)	1.44(9)	1
O2	4	0.3848(6)	0.3181(8)	0.4987(7)	1.61(9)	1
O3	4	0.4491(7)	0.1023(7)	0.8000(7)	1.47(9)	1
F	4	0.1231(9)	0.2020(9)	0.6786(10)	3.26(14)	1
			x = 0.4			
Atom	**Multiplicity**	**x**	**y**	**z**	**Uiso*100/Å²**	
Sr	4	0.2610(7)	0.1360(7)	0.1008(7)	0.12(8)	0.60
Ca	4	0.2610(7)	0.1360(7)	0.1008(7)	0.12(8)	0.40
P	4	0.3118(14)	0.1508(14)	0.5986(14)	2.04(16)	1
O1	4	0.2614(9)	-0.0161(7)	0.4499(9)	0.71(10)	1
O2	4	0.3920(9)	0.3161(10)	0.4956(10)	0.92(10)	1
O3	4	0.4610(11)	0.1070(11)	0.8030(11)	1.37(13)	1
F	4	0.1198(16)	0.1965(17)	0.6858(17)	5.07(31)	1

Table 2.3: Selected bond lengths and angles obtained from the NPD Rietveld refinements of each member of the $Sr_{1-x}Ca_xPO_3F$ series

Bonds	Bond Lengths (Å)				
	x = 0	x = 0.1	x = 0.2	x = 0.3	x = 0.4
M-O1	2.612(3)	2.606(3)	2.606(6)	2.587(6)	2.568(8)
M-O1	2.520(2)	2.520(3)	2.504(6)	2.479(6)	2.477(7)
M-O2	2.909(3)	2.910(3)	2.873(6)	2.894(6)	2.896(9)
M-O2	2.561(3)	2.561(4)	2.541(7)	2.546(6)	2.517(9)
M-O2	2.653(2)	2.651(3)	2.618(6)	2.626(6)	2.524(8)
M-O3	2.620(3)	2.590(3)	2.616(6)	2.607(6)	2.663(9)
M-O3	2.566(3)	2.574(4)	2.579(6)	2.581(6)	2.554(8)
M-F	2.851(2)	2.886(4)	2.848(7)	2.839(7)	2.773(12)
M-F	2.672(3)	2.635(4)	2.646(7)	2.649(7)	2.699(12)
P-O1	1.530(3)	1.505(4)	1.533(8)	1.523(7)	1.532(10)
P-O2	1.531(3)	1.525(4)	1.530(8)	1.536(7)	1.517(12)
P-O3	1.504(3)	1.503(4)	1.541(8)	1.491(7)	1.559(11)
P-F	1.570(3)	1.580(4)	1.560(7)	1.551(7)	1.593(12)
Angles	**Bond Angles (°)**				
O1-P-O2	111.0(2)	110.6(2)	109.0(5)	110.4(4)	110.5(7)
O1-P-O3	117.5(2)	118.5(3)	115.2(6)	118.5(5)	115.7(8)
O1-P-F	105.5(2)	105.1(2)	105.9(4)	105.9(4)	107.4(7)
O2-P-O3	112.4(2)	112.3(3)	111.8(4)	110.9(5)	108.2(7)
O2-P-F	108.2(2)	107.5(2)	112.4(5)	109.3(5)	115.1(9)
O3-P-F	101.2(2)	101.7(2)	102.2(4)	100.9(4)	99.7(7)

2.1.3 PXRD Rietveld Refinements

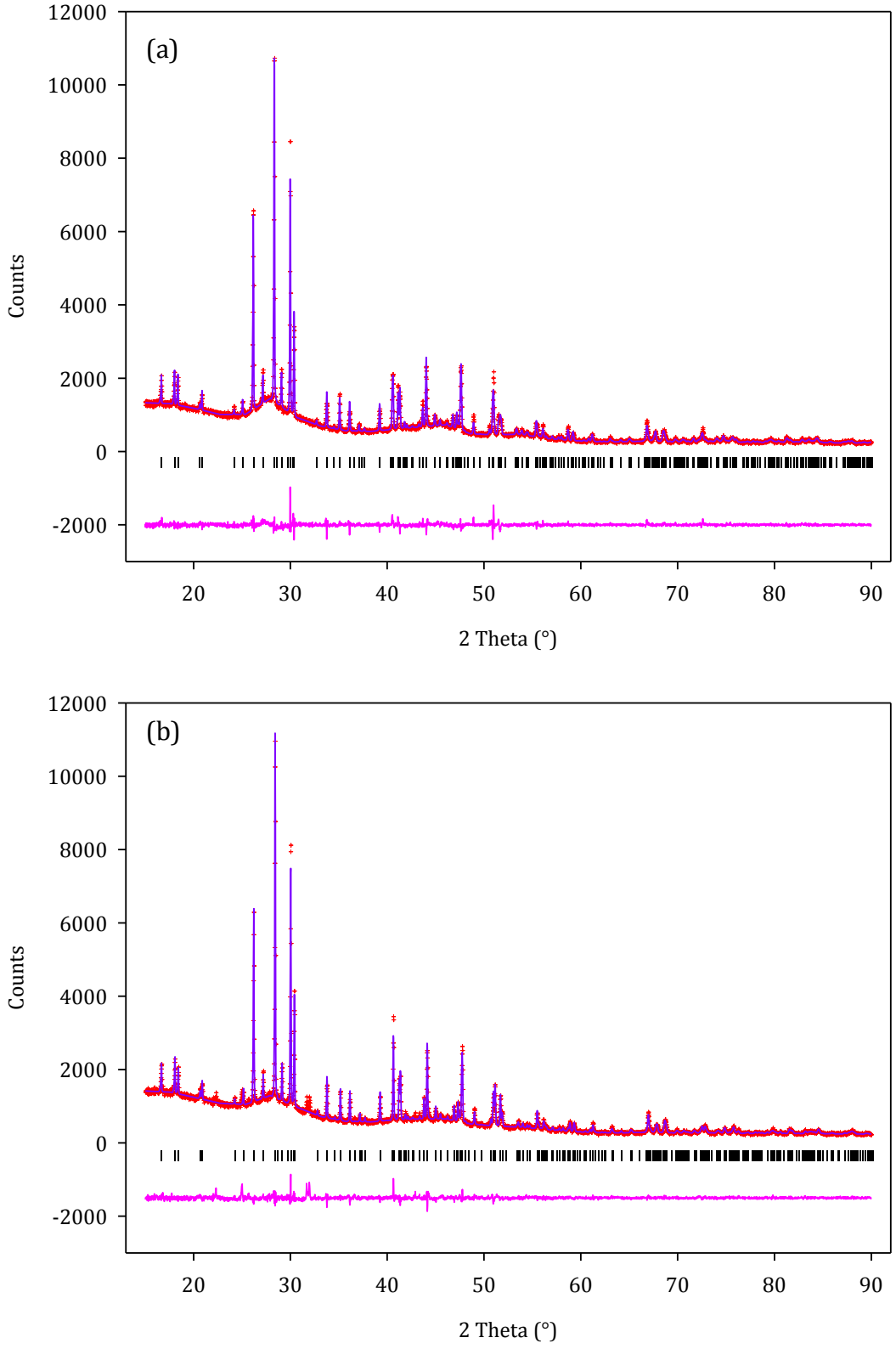

Figure 2.5: Final observed (red), calculated (purple) and difference profiles (pink) of the PXRD refinements of the x = 0.2 (a) and x = 0.3 (b) systems from the $Sr_{1-x}Ca_xPO_3F$ series. Reflection positions are shown as vertical tick marks (black)

Figure 2.6: Selected bond lengths and angles obtained from the PXRD Rietveld refinements of each member of the $Sr_{1-x}Ca_xPO_3F$ series

	Bond Lengths (Å)				
Bonds	**x = 0**	**x = 0.1**	**x =0.2**	**x = 0.3**	**x = 0.4**
M-O1	2.598(7)	2.580(6)	2.576(12)	2.570(13)	2.536(17)
M-O1	2.506(7)	2.491(6)	2.488(13)	2.495(13)	2.476(15)
M-O2	2.907(7)	2.915(6)	2.930(12)	2.943(13)	2.924(16)
M-O2	2.550(7)	2.508(7)	2.486(6)	2.503(12)	2.544(15)
M-O2	2.651(7)	2.640(6)	2.645(6)	2.599(11)	2.522(15)
M-O3	2.630(6)	2.626(6)	2.627(6)	2.579(11)	2.607(14)
M-O3	2.520(8)	2.535(7)	2.544(7)	2.541(13)	2.458(17)
M-F	2.900(7)	2.890(5)	2.887(5)	2.901(10)	2.879(13)
M-F	2.654(7)	2.634(6)	2.632(5)	2.623(11)	2.565(15)
P-O1	1.519(8)	1.535(7)	1.527(7)	1.517(14)	1.549(18)
P-O2	1.531(7)	1.574(7)	1.594(7)	1.565(13)	1.581(15)
P-O3	1.525(8)	1.507(7)	1.502(7)	1.545(14)	1.549(18)
P-F	1.561(7)	1.583(6)	1.587(5)	1.557(10)	1.614(13)
Angles	**Bond Angles (°)**				
O1-P-O2	111.9(5)	111.9(4)	113.4(9)	108.8(8)	110.6(11)
O1-P-O3	114.6(6)	117.2(5)	113.5(11)	116.4(10)	114.0(13)
O1-P-F	104.5(5)	106.9(4)	106.9(9)	105.5(8)	104.2(10)
O2-P-O3	113.8(5)	112.5(5)	112.8(9)	114.0(8)	113.5(10)
O2-P-F	108.3(5)	106.0(4)	108.6(9)	107.7(8)	111.1(11)
O3-P-F	102.6(5)	101.9(4)	100.5(7)	103.6(7)	102.8(9)

2.1.4 Raman Spectroscopy

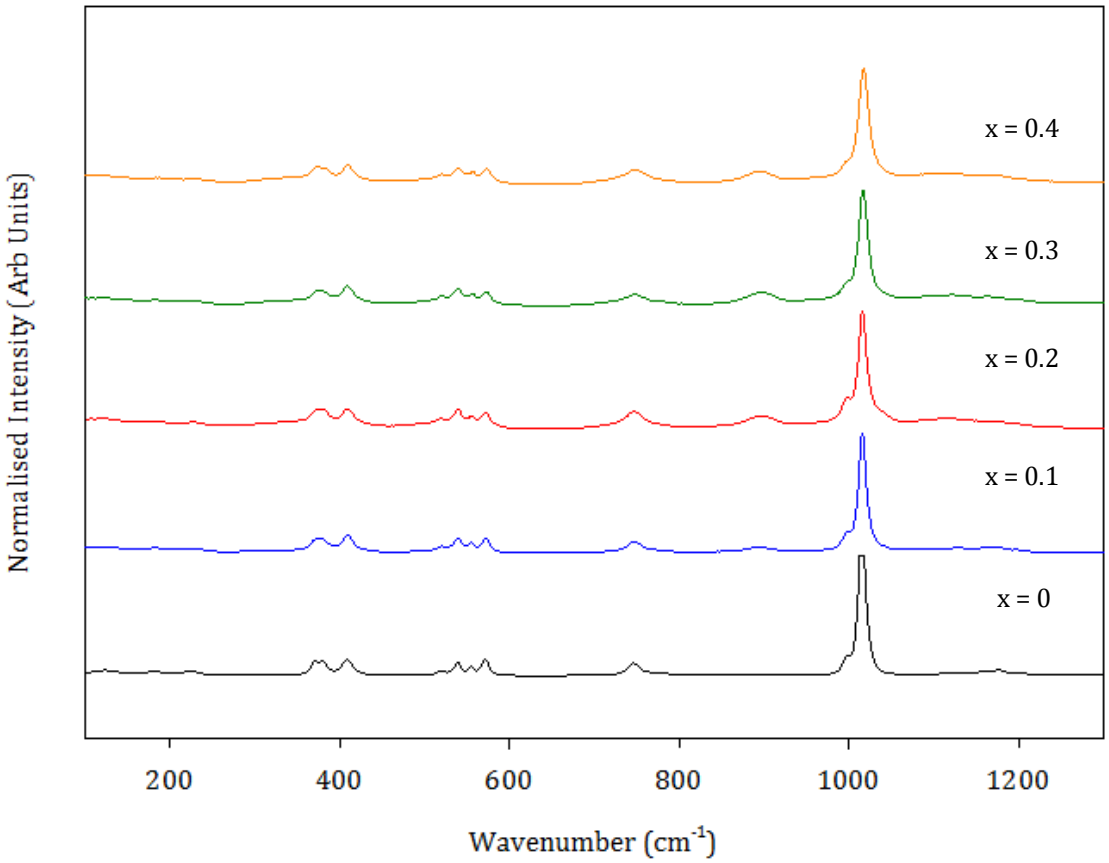

Figure 2.7: A stack plot of the Raman Spectroscopy data obtained from each member of the $Sr_{1-x}Ca_xPO_3F$ series

2.2 $Sr_{1-x}Ba_xPO_3F$ Systems

2.2.1 PXRD Rietveld Refinements

Table 2.4: Refined structural parameters obtained from the PXRD refinements of the x = 0, 0.03 and 0.1 systems of the $Sr_{1-x}Ba_xPO_3F$ series

x = 0						
Atom	**Multiplicity**	**x**	**y**	**z**	**Uiso*100/Å²**	**Fractional Occupancy**
Sr	4	0.2698(2)	0.1384(2)	0.1032(2)	1.85(6)	1
P	4	0.3133(6)	0.1467(7)	0.6009(7)	2.57(14)	1
O1	4	0.2518(11)	-0.0131(9)	0.4514(12)	0.06(14)	1
O2	4	0.3846(10)	0.3179(11)	0.4986(10)	0.06(14)	1
O3	4	0.4501(11)	0.0901(12)	0.7988(11)	0.06(14)	1
F	4	0.1211(10)	0.2019(12)	0.6727(11)	0.06(14)	1
x = 0.03						
Atom	**Multiplicity**	**x**	**y**	**z**	**Uiso*100/Å²**	**Fractional Occupancy**
Sr	4	0.2708(3)	0.1400(3)	0.1032(3)	2.37(7)	0.97
Ba	4	0.2708(3)	0.1400(3)	0.1032(3)	2.37(7)	0.03
P	4	0.3143(7)	0.1471(10)	0.6036(9)	3.06(2)	1
O1	4	0.2543(2)	-0.0077(13)	0.4458(16)	1.05(9)	1
O2	4	0.3871(13)	0.3183(14)	0.5005(14)	1.05(9)	1
O3	4	0.4486(14)	0.0954(17)	0.7945(14)	1.05(9)	1
F	4	0.1172(13)	0.2068(15)	0.6710(14)	1.05(9)	1
x = 0.1						
Atom	**Multiplicity**	**x**	**y**	**z**	**Uiso*100/Å²**	**Fractional Occupancy**
Sr	4	0.2705(4)	0.1403(4)	0.1030(4)	2.62(11)	0.90
Ba	4	0.2705(4)	0.1403(4)	0.1030(4)	2.62(11)	0.10
P	4	0.3140(11)	0.1486(15)	0.6049(13)	3.71(25)	1
O1	4	0.2566(21)	-0.0050(18)	0.4483(22)	0.74(26)	1
O2	4	0.3857(18)	0.3159(20)	0.4991(19)	0.74(26)	1
O3	4	0.4526(19)	0.0935(23)	0.7942(20)	0.74(26)	1
F	4	0.1139(18)	0.1998(22)	0.6669(19)	0.74(26)	1

Table 2.5: Selected bond lengths and angles obtained from the PXRD Rietveld refinements of the x= 0, 0.03 and 0.1 systems from the $Sr_{1-x}Ba_xPO_3F$ series

Bonds	Bond Lengths (Å)		
	x = 0.00	x = 0.03	x = 0.10
M-O1	2.598(7)	2.553(10)	2.565(14)
M-O1	2.505(7)	2.528(9)	2.550(13)
M-O2	2.906(7)	2.915(9)	2.906(13)
M-O2	2.550(7)	2.572(10)	2.589(14)
M-O2	2.652(7	2.637(9)	2.654(12)
M-O3	2.630(6)	2.643(8)	2.669(12)
M-O3	2.519(8)	2.559(11)	2.540(15)
M-F	2.900(7)	2.919(9)	2.946(12)
M-F	2.654(7)	2.603(10)	2.611(14)
P-O1	1.519(8)	1.526(11)	1.518(15)
P-O2	1.531(7)	1.538(10)	1.525(14)
P-O3	1.525(8)	1.471(10)	1.487(15)
P-F	1.561(7)	1.589(9)	1.580(13)
Angles	**Bond Angles (°)**		
O1-P-O2	111.2(2)	109.1(6)	107.9(9)
O1-P-O3	117.8(2)	117.4(9)	115.9(12)
O1-P-F	105.6(2)	105.1(7)	103.2(9)
O2-P-O3	112.9(2)	112.4(7)	112.8(10)
O2-P-F	107.0(2)	107.5(7)	109.6(11)
O3-P-F	101.9(2)	104.6(6)	106.9(9)

2.3 $Sr_{1-x}La_x(PO_3F)_{1-x}(PO_4)_x$ Systems

2.3.1 Raman Spectroscopy

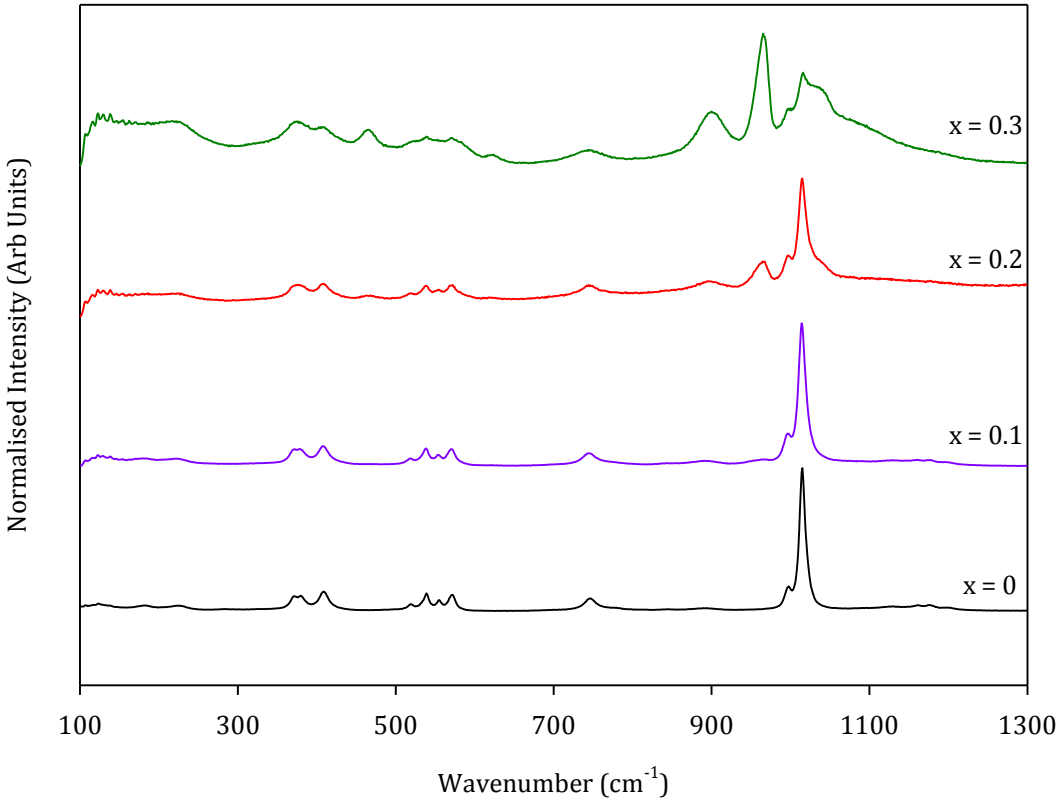

Figure 2.8: A stack plot of the Raman Spectroscopy data obtained from the x = 0-0.3 systems of the $Sr_{1-x}La_x(PO_3F)_{1-x}(PO_4)_x$ series

Table 2.6: Raman spectroscopy data obtained from x = 0-0.3 systems of the $Sr_{1-x}La_x(PO_3F)_{1-x}(PO_4)_x$ series

x = 0-0.3	Region: 100-700 cm^{-1}		Region: 700-900 cm^{-1}		Region: 900-1200 cm^{-1}	
	Vibrations (cm^{-1})	Assignment	Vibrations (cm^{-1})	Assignment	Vibrations (cm^{-1})	Assignment
0	571 555 538 519 409 381 372	$\delta(PO_3)$ $\rho(PO_3)$	746	P-F	1176 1014 997	$\nu_{as}(PO_3)$ $\nu_s(PO_3)$
0.1	571 554 538 518 408 375	$\delta(PO_3)$ $\rho(PO_3)$	891 745	P-F	1015 996 968	$\nu_s(PO_3)$
0.2	571 554 538 518 408 375	$\delta(PO_3)$ $\rho(PO_3)$	897 745	P-F	1015 996 964	$\nu_s(PO_3)$
0.3	624 571 539 518 465 410 374	 $\delta(PO_3)$ $\rho(PO_3)$	899 741	P-F	1017 965	$\nu_s(PO_3)$

2.3.2 X-Ray Fluorescence Spectroscopy

Table 2.7: XRF results obtained from each member of the $Sr_{1-x}La_x(PO_3F)_{1-x}(PO_4)_x$ run as loose powders

Elements (wt %)	$Sr_{1-x}La_x(PO_3F)_{1-x}PO4)_x$										
	x										
	0	**0.1**	**0.2**	**0.3**	**0.4**	**0.5**	**0.6**	**0.7**	**0.8**	**0.9**	**1**
Sr	38.1 47.21	32.56	25.63	22.41	10.31	6.07	5.32	4.34	3.82	2.60	-
La	-	11.17	25.70	40.96	50.79	59.63	62.98	64.13	62.25	64.61	65.31 59.39
P	10.6 16.69	10.50	10.86	11.33	10.39	11.63	11.26	11.36	10.84	10.64	10.58 13.24
Na	0.59	0.62	0.62	0.85	0.80	-	-	-	-	-	-
Cl	0.48	0.56	0.46	0.56	0.50	0.60	-	-	-	-	-

2.4 $Sr_{1-x}Ca_xPO_3F{\cdot}H_2O$ Systems

2.4.1 Raman Spectroscopy

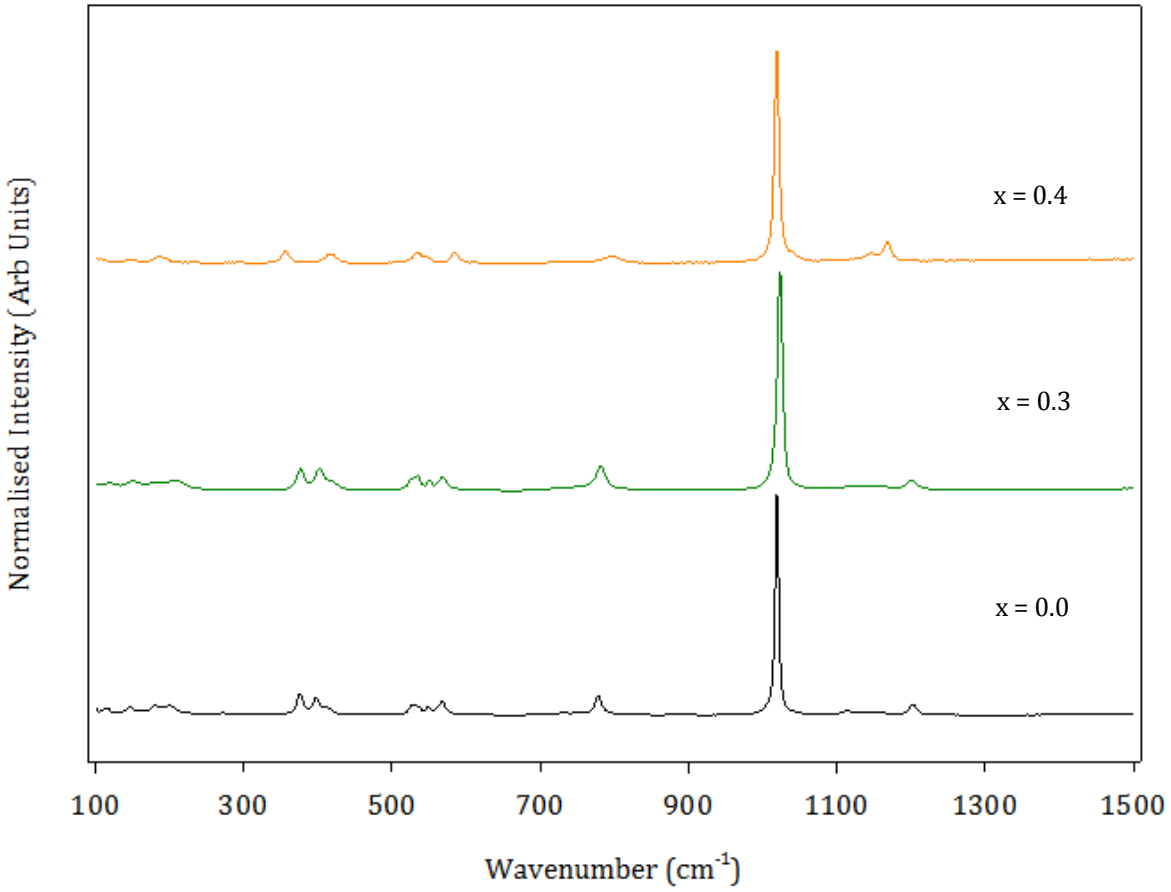

Figure 2.9: A stack plot of the Raman Spectroscopy data obtained from the x = 0, 0.3 and 0.4 systems of the $Sr_{1-x}Ca_xPO_3F{\cdot}H_2O$ series, whereby x = 0 and 0.3 resemble that of $SrPO_3F{\cdot}H_2O$ and x = 0.4 resembles that of $CaPO_3F{\cdot}2H_2O$

2.4.2 PXRD Rietveld Refinements

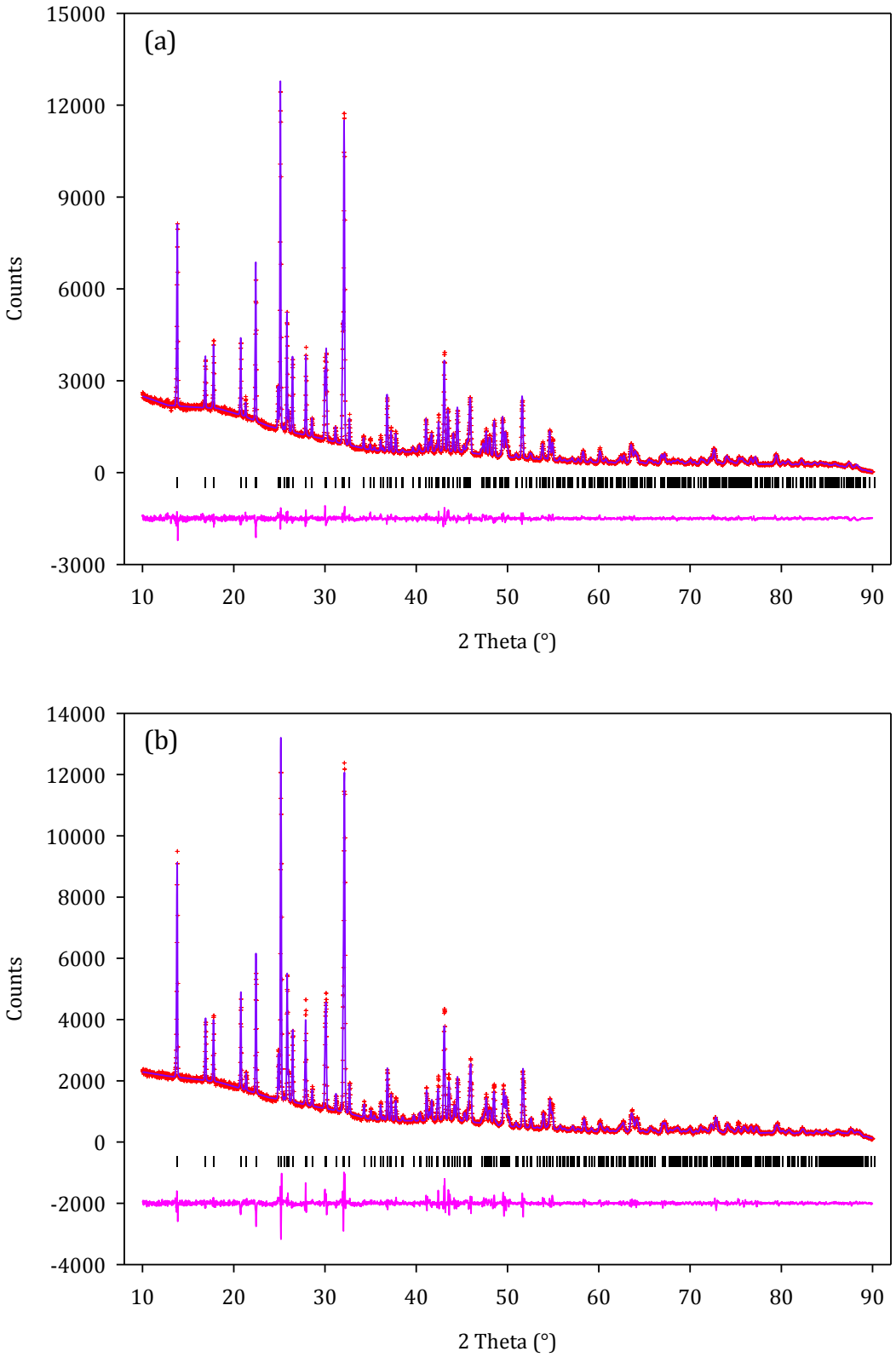

Figure 2.10: Final observed (red), calculated (purple) and difference profiles (pink) of the PXRD refinements of the x = 0.2 (a) and x = 0.3 (b) systems from the $Sr_{1-x}Ca_xPO_3F{\cdot}H_2O$ series. Reflection positions are shown as vertical tick marks (black)

Table 2.8: Refined structural parameters obtained from the PXRD refinements of the x = 0-0.3 systems of the $Sr_{1-x}Ca_xPO_3F{\cdot}H_2O$ series

			x = 0			
Atom	**Multiplicity**	**x**	**y**	**z**	**Uiso*100 (Å²)**	**Fractional Occupancy**
Sr	8	0.2635(1)	0.1080(1)	0.3202(2)	1.46(4)	1
P	8	0.1254(3)	0.3791(4)	0.1303(2)	1.54(8)	1
F	8	0.2022(5)	0.4264(5)	0.0196(3)	1.23(16)	1
O2	8	0.0208(6)	0.2361(7)	0.1031(5)	2.14(22)	1
O3	8	0.2740(6)	0.3448(6)	0.1969(3)	1.07(16)	1
O4	8	0.0344(6)	0.5230(6)	0.1695(4)	1.00(16)	1
O5(w)	8	0.0869(6)	0.3563(7)	0.4017(4)	1.41(6)	1
H1	8	-0.0020	0.3470	0.3600	2.50	1
H2	8	0.0670	0.3470	0.4560	2.50	1
			x = 0.1			
Atom	**Multiplicity**	**x**	**y**	**z**	**Uiso*100 (Å²)**	**Fractional Occupancy**
Sr	8	0.2641(2)	0.1073(1)	0.3209(8)	1.96(5)	0.9
Ca	8	0.2641(2)	0.1073(1)	0.3209(8)	1.96(5)	0.1
P	8	0.1240(4)	0.3788(5)	0.1298(2)	1.35(10)	
F	8	0.1994(6)	0.4249(6)	0.0203(4)	1.69(20)	1
O2	8	0.0182(8)	0.2368(10)	0.1032(6)	2.72(29)	1
O3	8	0.2738(8)	0.3440(8)	0.1959(4)	1.99(23)	1
O4	8	0.0343(7)	0.5242(9)	0.1697(5)	1.10(24)	1
O5(w)	8	0.0871(8)	0.3523(9)	0.4007(5)	1.61(21)	1
H1	8	-0.0020	0.3470	0.3600	2.50	1
H2	8	0.0670	0.3470	0.4560	2.50	1
			x =0.2			
Atom	**Multiplicity**	**x**	**y**	**z**	**Uiso*100 (Å²)**	**Fractional Occupancy**
Sr	8	0.2644(1)	0.1062(2)	0.3216(1)	2.30(6)	0.8
Ca	8	0.2644(1)	0.1062(2)	0.3261(1)	2.30(6)	0.2
P	8	0.1255(5)	0.3773(6)	0.1313(6)	1.38(11)	1
F	8	0.2005(7)	0.4293(7)	0.0233(4)	1.25(23)	1
O2	8	0.0142(9)	0.2413(12)	0.1028(7)	2.91(34)	1
O3	8	0.2721(9)	0.3412(9)	0.1965(5)	1.26(26)	1
O4	8	0.0305(9)	0.5246(9)	0.1702(6)	1.38(28)	1
O5(w)	8	0.0866(9)	0.3565(11)	0.3999(5)	2.17(25)	1
H1	8	-0.0020	0.3470	0.3600	2.50	1
H2	8	0.0670	0.3470	0.4560	2.50	1

x = 0.3						
Atom	**Multiplicity**	**x**	**y**	**z**	**Uiso*100 (Å²)**	**Fractional Occupancy**
Sr	8	0.2650(3)	0.1055(2)	0.3217(1)	2.14(8)	0.7
Ca	8	0.2650(3)	0.1055(2)	0.3217(1)	2.14(8)	0.3
P	8	0.1177(6)	0.3783(7)	0.1314(3)	1.19(14)	1
F	8	0.2015(9)	0.4330(8)	0.0260(5)	1.54(30)	1
O2	8	0.0093(11)	0.2349(13)	0.1059(9)	2.29(42)	1
O3	8	0.2682(11)	0.3406(11)	0.1963(6)	0.78(3)	1
O4	8	0.0243(11)	0.5223(12)	0.1718(8)	1.43(25)	1
O5(w)	8	0.0848(11)	0.3517(13)	0.3984(7)	1.65(32)	1
H1	8	-0.0020	0.3470	0.3600	2.50	1
H2	8	0.0670	0.3470	0.4560	2.50	1

Table 2.9: Selected bond lengths and angles obtained from the PXRD Rietveld refinements of x = 0-0.3 systems of the $Sr_{1-x}Ca_xPO_3F{\cdot}H_2O$ series

Bonds	**Bond Lengths (Å)**			
	x = 0	**x = 0.1**	**x =0.2**	**x = 0.3**
M-F	2.622(4)	2.616(5)	2.637(5)	2.674(7)
M-O2	2.530(6)	2.491(7)	2.469(8)	2.395(10)
M-O3	2.551(5)	2.548(6)	2.523(7)	2.522(9)
M-O3	2.745(5)	2.740(6)	2.735(7)	2.730(9)
M-O4	2.622(5)	2.607(6)	2.613(7)	2.628(9)
M-O4	2.495(5)	2.476(6)	2.703(9)	2.388(9)
M-O5(w)	2.738(5)	2.690(7)	2.587(9)	2.674(10)
M-O5(w)	2.656(6)	2.646(7)	2.431(7)	2.606(11)
P-F	1.600(4)	1.572(5)	1.570(6)	1.567(7)
P-O2	1.509(6)	1.496(8)	1.463(9)	1.502(11)
P-O3	1.494(5)	1.489(6)	1.477(7)	1.483(9)
P-O4	1.505(5)	1.501(7)	1.508(8)	1.495(10)
O2-H2	2.044(6)	2.046(8)	2.055(10)	2.058(9)
O3-H1	1.937(5)	1.922(7)	1.927(7)	1.953(9)
O5(w)-H1	0.894(5)	0.880(6)	0.869(6)	0.844(9)
O5(w)-H2	0.719(5)	0.726(6)	0.736(7)	0.750(9)
Angles	**Bond Angles (°)**			
F-P-O2	101.9(3)	101.9(4)	103.0(5)	106.4(6)
F-P-O3	104.5(3)	104.4(4)	103.6(4)	101.7(6)
F-P-O4	106.3(3)	106.5(4)	104.8(5)	105.9(6)
O2-P-O3	115.0(4)	115.1(5)	116.9(6)	114.4(7)
O2-P-O4	117.1(3)	117.1(4)	115.2(5)	115.2(6)
O3-P-O4	110.5(3)	110.3(4)	111.5(5)	111.7(6)
H1-O5(w)-H2	113.2(6)	113.3(8)	112.9(9)	114.5(11)

Appendix 3

3.1 Raman Spectroscopy

Table 3.1:Raman spectroscopy data obtained for each member of the $Ca(SO_4)_x(PO_3F)_{1-x}\cdot 2H_2O$ series

x = 0-1	Region: 100-700 cm^{-1}		Region: 700-900 cm^{-1}		Region: 900-1200 cm^{-1}	
	Vibrations (cm^{-1})	Assignment	Vibrations (cm^{-1})	Assignment	Vibrations (cm^{-1})	Assignment
1	671 620 494 415	v_4, SO_4^{2-} v_2, SO_4^{2-}			1137 1008	v_3, SO_4^{2-} v_1, SO_4^{2-}
0.9	671 619 494 416 359	v_4, SO_4^{2-} v_2, SO_4^{2-} v_2, SO_4^{2-}/ v_6, $\rho(PO_3)$ v_6, $\rho(PO_3)$			1136 1029 1013	v_3, SO_4^{2-} v_2, v_s (PO_3) v_1, SO_4^{2-}
0.8	671 618 494 416 358	v_4, SO_4^{2-} v_2, SO_4^{2-} v_2, SO_4^{2-}/ v_6, $\rho(PO_3)$ v_6, $\rho(PO_3)$			1136 1029 1013	v_3, SO_4^{2-} v_2, v_s (PO_3) v_1, SO_4^{2-}
0.7	671 617 494 416 359	v_4, SO_4^{2-} v_2, SO_4^{2-} v_2, SO_4^{2-}/ v_6, $\rho(PO_3)$ v_6, $\rho(PO_3)$			1135 1028 1007	v_3, SO_4^{2-} v_2, v_s (PO_3) v_1, SO_4^{2-}
0.6	671 615 591 528 494 417 358	v_4, SO_4^{2-} v_5, $\delta(PO_3)$ v_2, SO_4^{2-} v_2, SO_4^{2-}/ v_6, $\rho(PO_3)$ v_6, $\rho(PO_3)$			1135 1027 1007	v_3, SO_4^{2-} v_2, v_s (PO_3) v_1, SO_4^{2-}
0.5	671 615 591 530 494 418 358	v_4, SO_4^{2-} v_5, $\delta(PO_3)$ v_2, SO_4^{2-} v_2, SO_4^{2-}/ v_6, $\rho(PO_3)$ v_6, $\rho(PO_3)$	790	v_1, P-F	1133 1027 1010	v_3, SO_4^{2-} v_2, v_s (PO_3) v_1, SO_4^{2-}

0.4	671 613 591 533 495 420 358	v_4, SO_4^{2-} v_5, $\delta(PO_3)$ v_2, SO_4^{2-} v_2, SO_4^{2-}/ v_6, $\rho(PO_3)$ v_6, $\rho(PO_3)$	793	v_1, P-F	1133 1026 1005	v_3, SO_4^{2-} v_2, v_s (PO_3) v_1, SO_4^2
0.3	670 611 591 535 496 421 357	v_4, SO_4^{2-} v_5, $\delta(PO_3)$ v_2, SO_4^{2-} v_2, SO_4^{2-}/ v_6, $\rho(PO_3)$ v_6, $\rho(PO_3)$	798	v_1, P-F	1168 1129 1025 1003	v_4, v_{as} (PO_3) v_3, SO_4^{2-} v_2, v_s (PO_3) v_1, SO_4^2
0.2	670 610 590 536 497 422 356	v_4, SO_4^{2-} v_5, $\delta(PO_3)$ v_2, SO_4^{2-} v_2, SO_4^{2-}/ v_6, $\rho(PO_3)$ v_6, $\rho(PO_3)$	798	v_1, P-F	1170 1124 1025 1002	v_4, v_{as} (PO_3) v_3, SO_4^{2-} v_2, v_s (PO_3) v_1, SO_4^2
0.1	589 536 495 421 356	v_5, $\delta(PO_3)$ v_2, SO_4^{2-} v_2, SO_4^{2-}/ v_6, $\rho(PO_3)$ v_6, $\rho(PO_3)$	800	v_1, P-F	1171 1146 1023 999	v_4, v_{as} (PO_3) v_2, v_s (PO_3) v_1, SO_4^2
0	587 535 419 356	v_5, $\delta(PO_3)$ v_6, $\rho(PO_3)$	803	v_1, P-F	1169 1144 1020	v_4, v_{as} (PO_3) v_2, v_s (PO_3)

3.2 XRF Spectroscopy: Fluorine Content

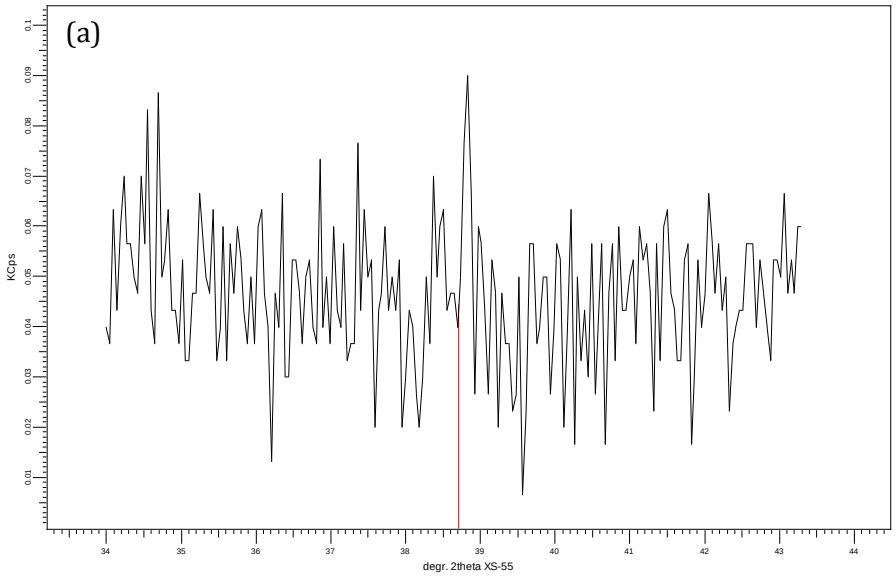

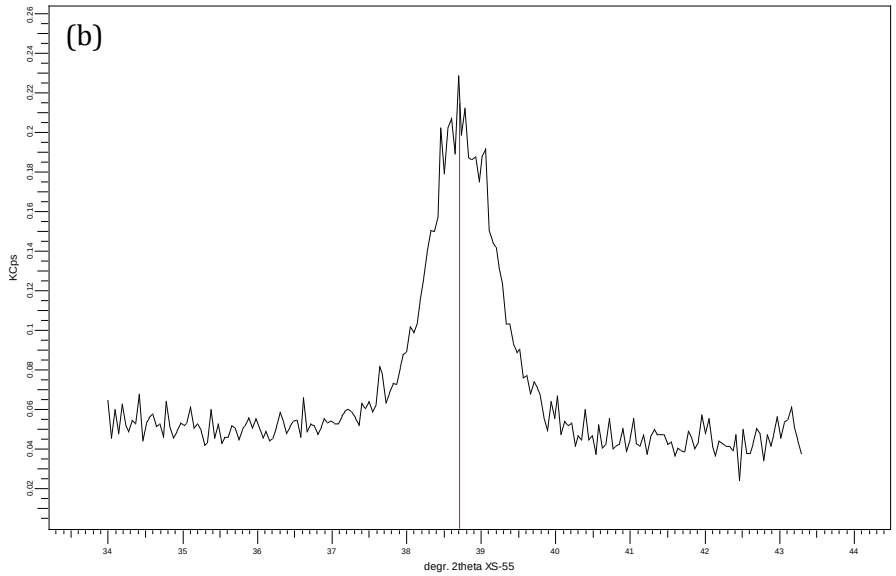

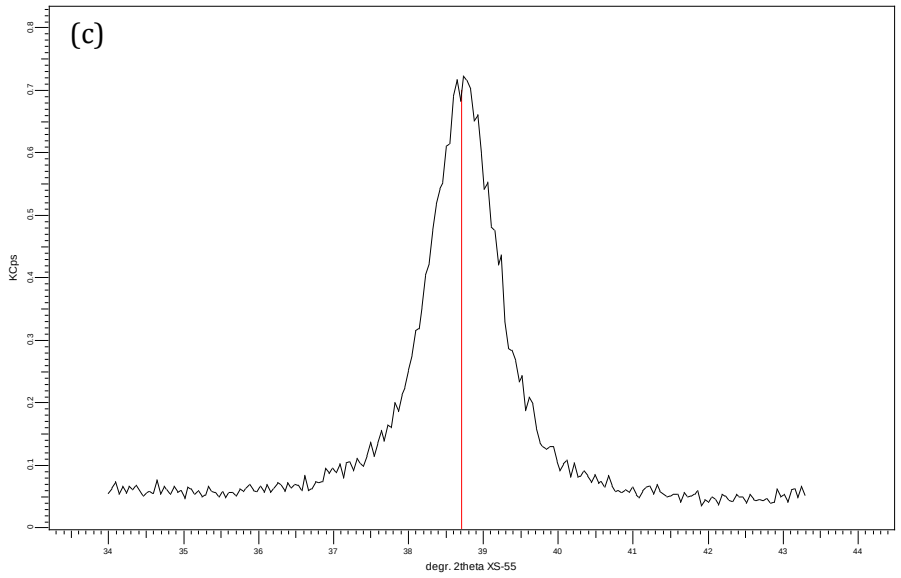

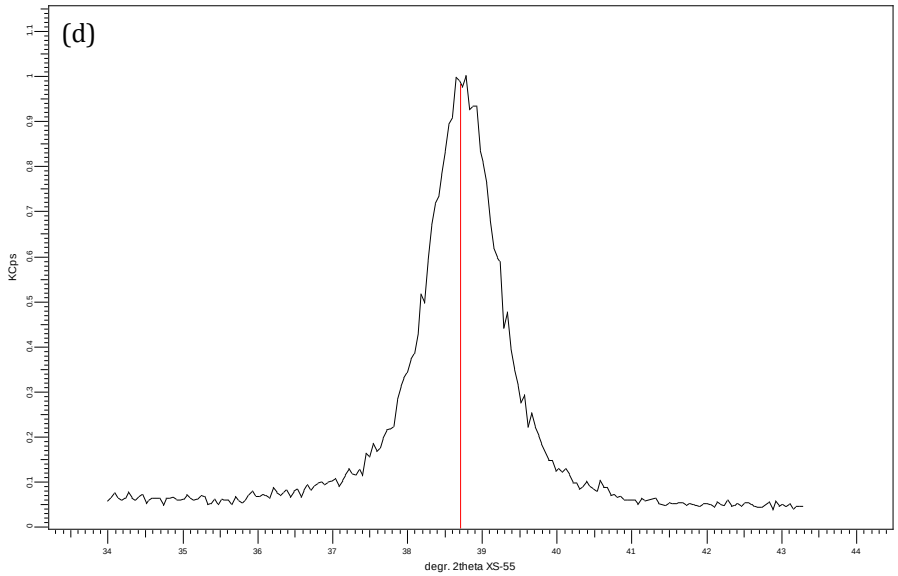
(d)
KCps
degr. 2theta XS-55

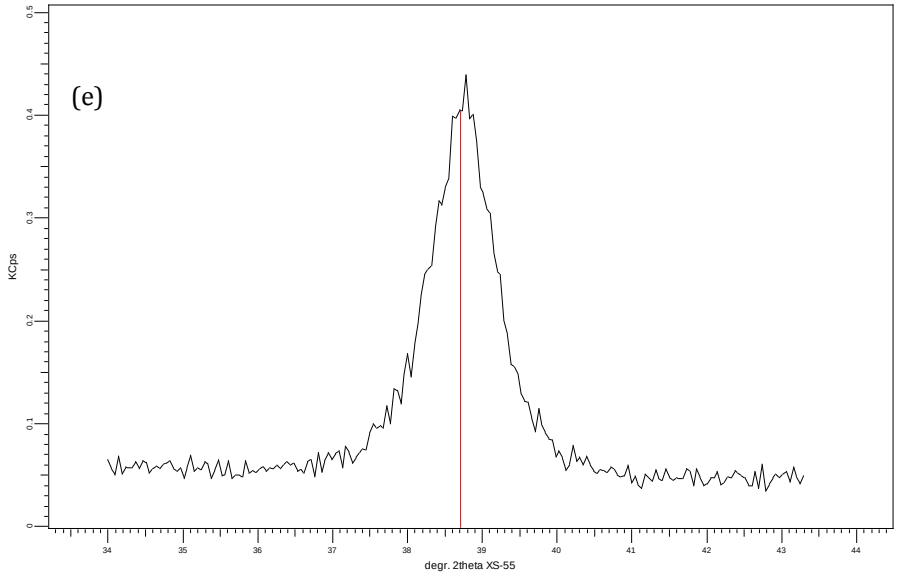
(e)
KCps
degr. 2theta XS-55

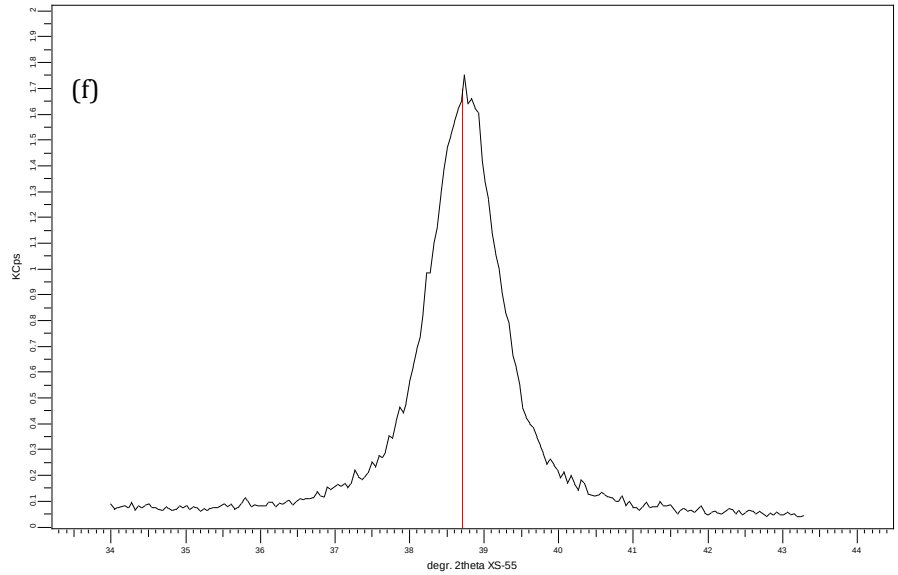
(f)
KCps
degr. 2theta XS-55

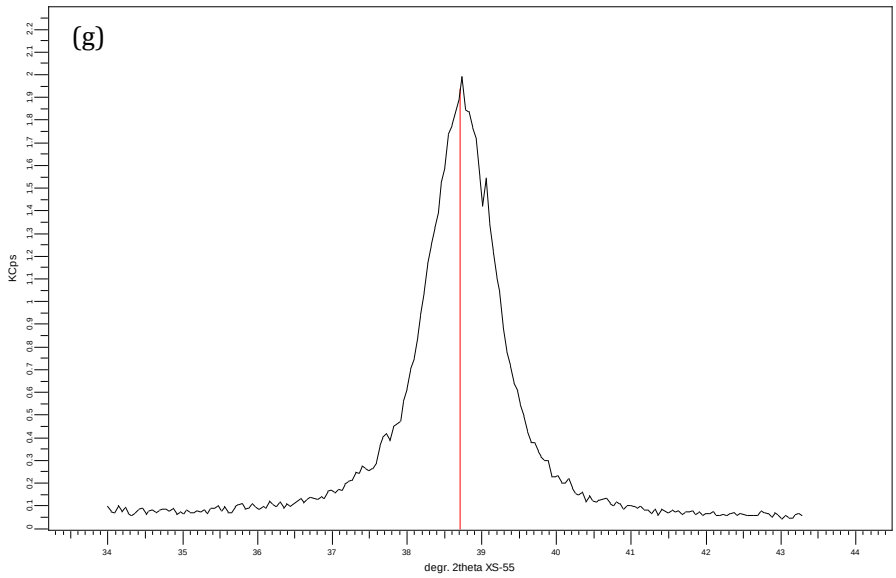
(g)
KCps
degr. 2theta XS-55

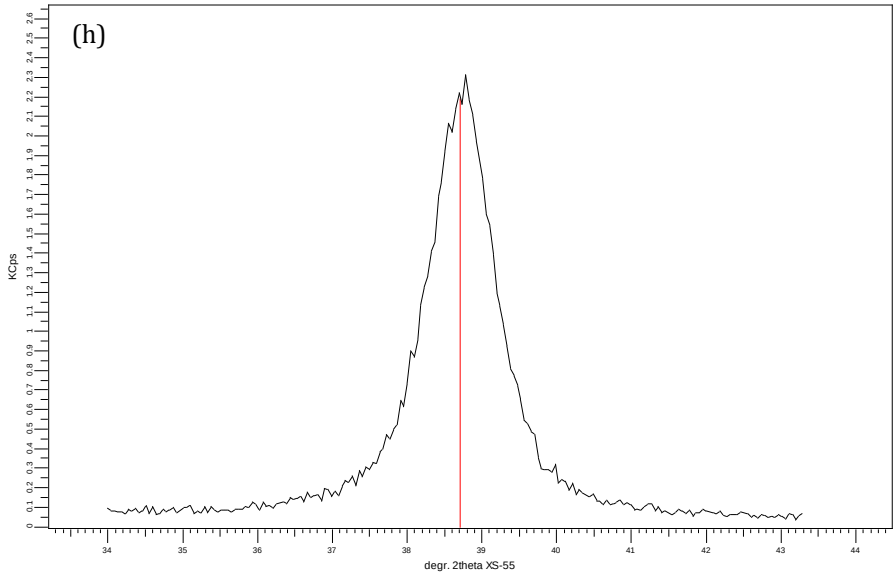
(h)
KCps
degr. 2theta XS-55

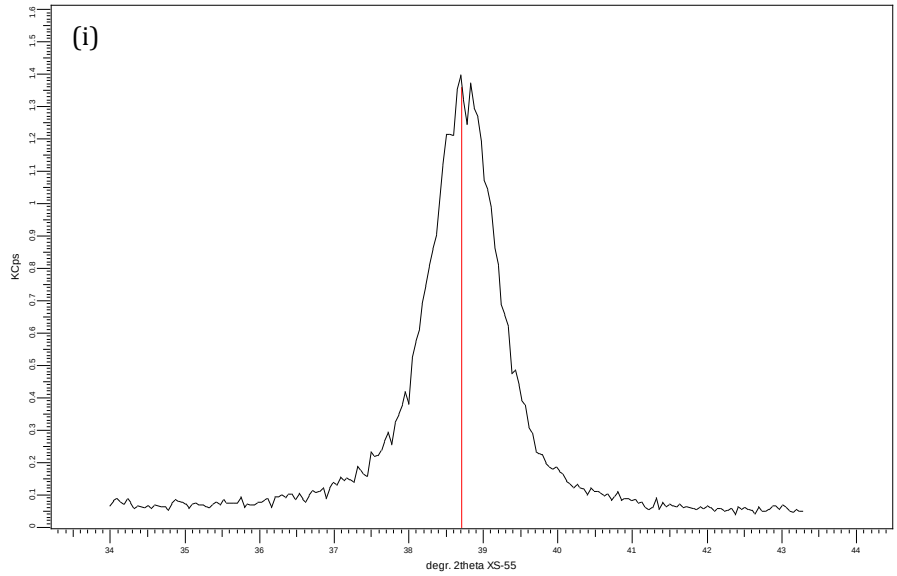
(i)
KCps
degr. 2theta XS-55

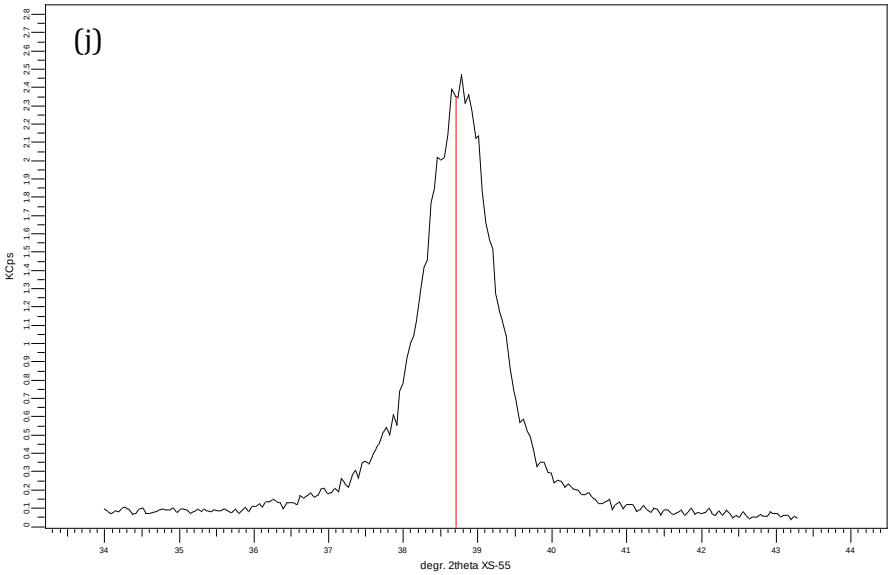

Figure 3.1: Fluorine signal obtained from the Fluorine Kα1 high sensitivity line for members of the $Ca(SO_4)_x(PO_3F)_{1-x}\cdot 2H_2O$ series, x = 0-0.9 (a-j)

3.3 TGA-MS Analysis of the $Ca(SO_4)_x(PO_3F)_{1-x}\cdot 2H_2O$ series

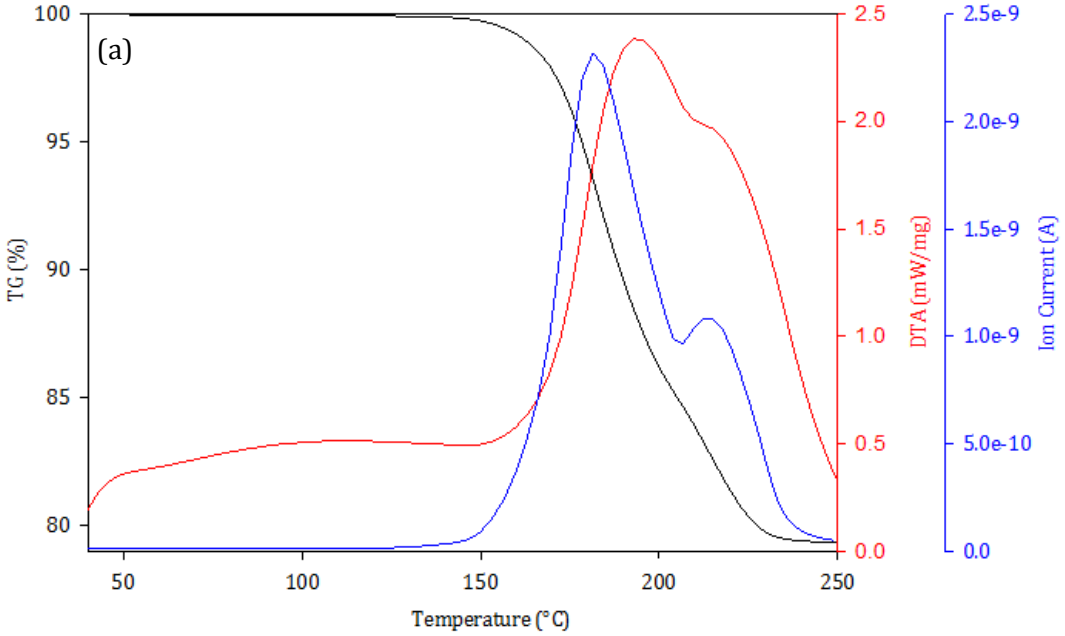

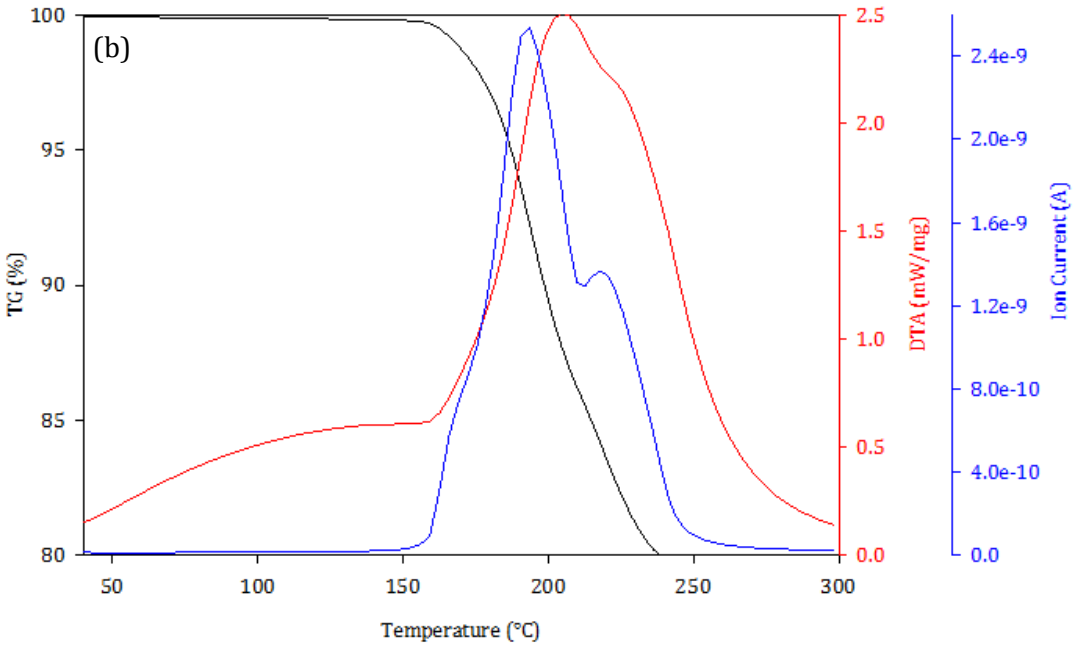

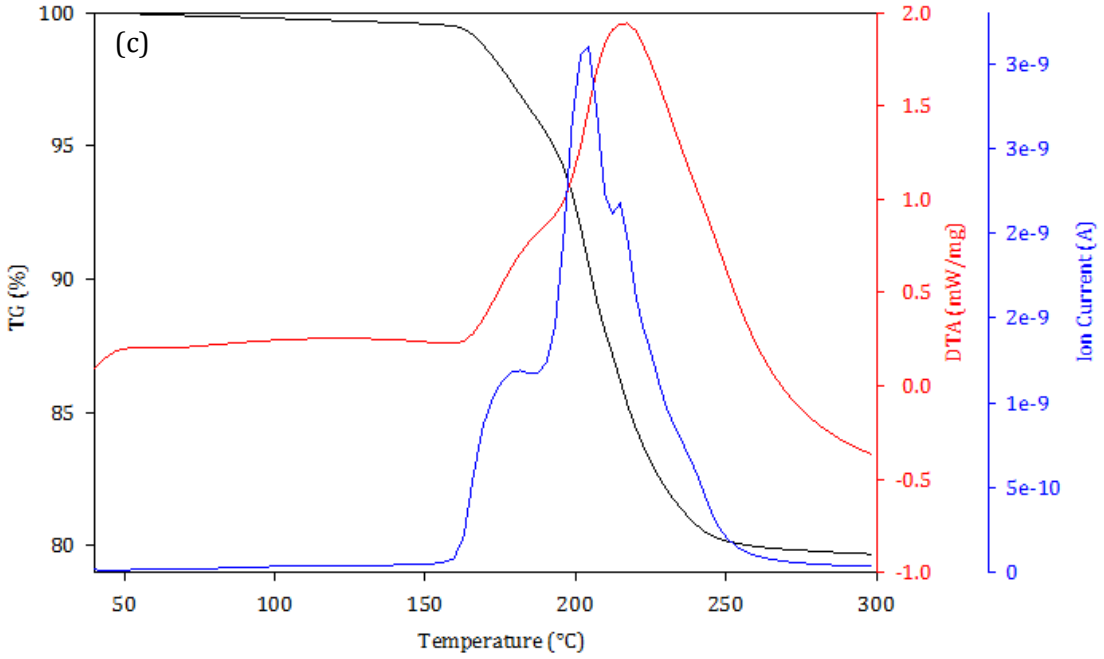
(c)
TG (%)
DTA (mW/mg)
Ion Current (A)
Temperature (°C)
100
95
90
85
80
2.0
1.5
1.0
0.5
0.0
-0.5
-1.0
3e-9
3e-9
2e-9
2e-9
1e-9
5e-10
0
50
100
150
200
250
300

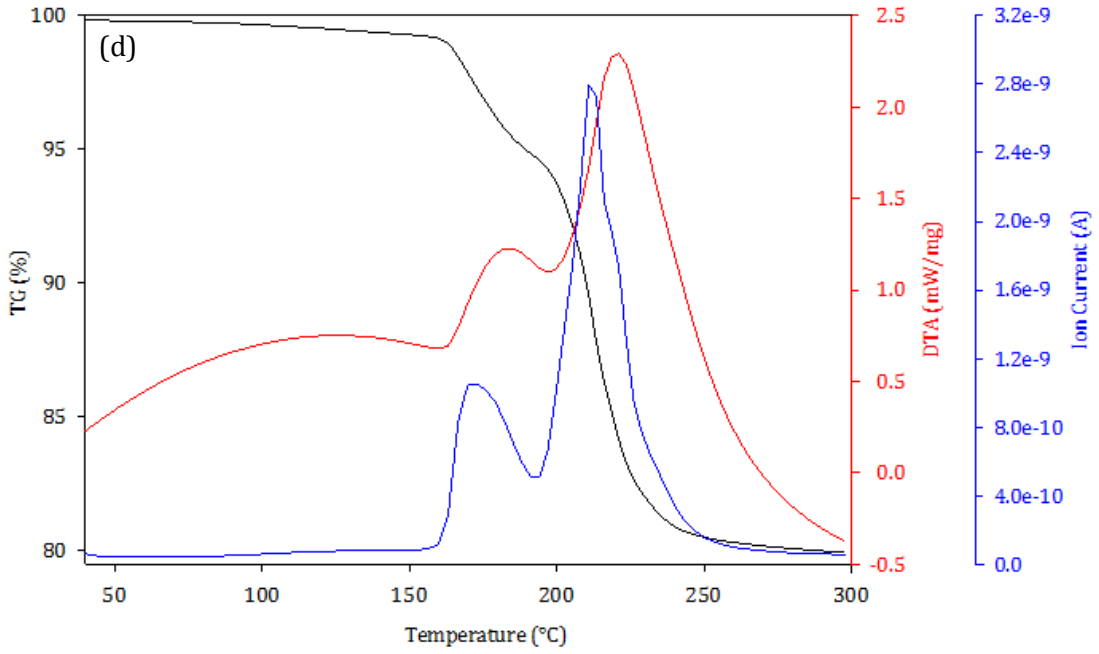
(d)
TG (%)
DTA (mW/mg)
Ion Current (A)
Temperature (°C)
100
95
90
85
80
2.5
2.0
1.5
1.0
0.5
0.0
-0.5
3.2e-9
2.8e-9
2.4e-9
2.0e-9
1.6e-9
1.2e-9
8.0e-10
4.0e-10
0.0
50
100
150
200
250
300

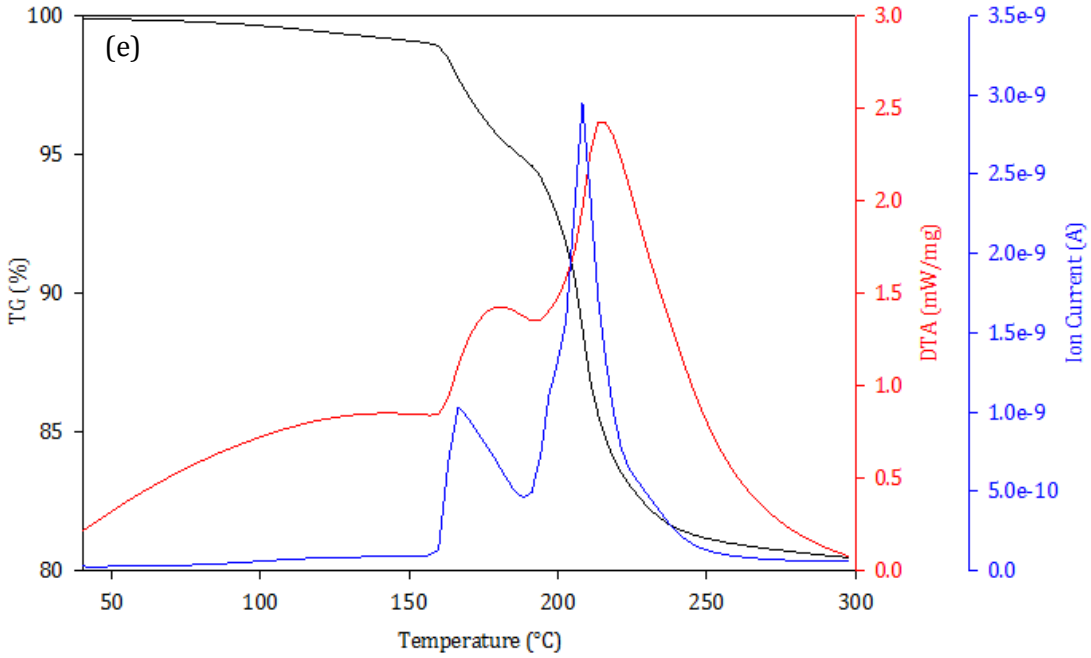
(e)
TG (%)
DTA (mW/mg)
Ion Current (A)
Temperature (°C)
100
95
90
85
80
50
100
150
200
250
300
3.0
2.5
2.0
1.5
1.0
0.5
0.0
3.5e-9
3.0e-9
2.5e-9
2.0e-9
1.5e-9
1.0e-9
5.0e-10
0.0

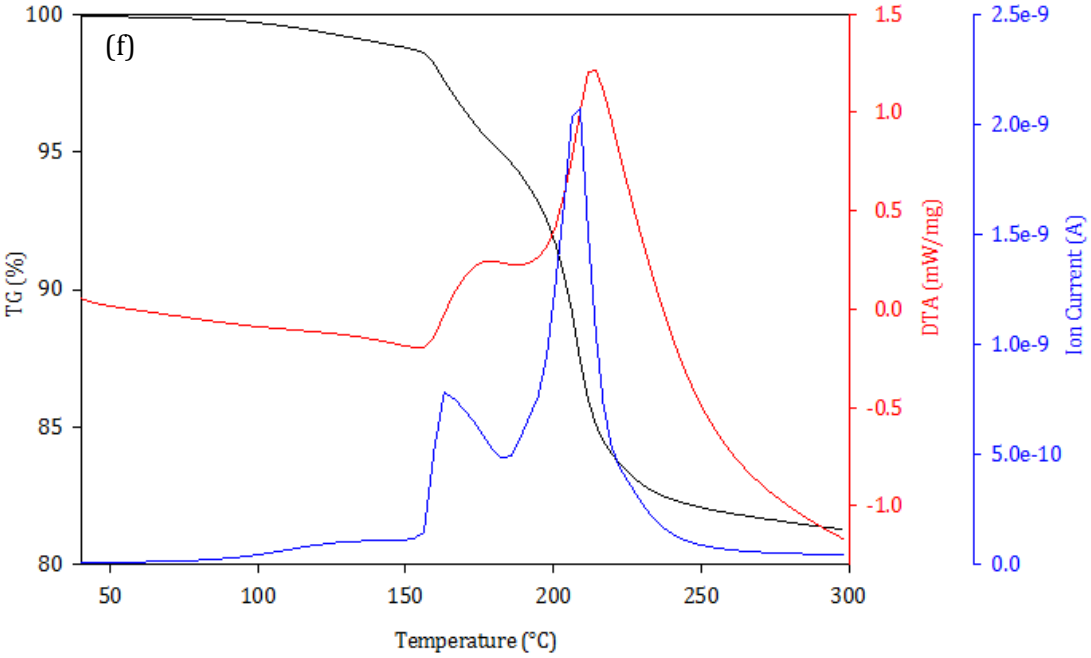
(f)
TG (%)
DTA (mW/mg)
Ion Current (A)
Temperature (°C)
100
95
90
85
80
50
100
150
200
250
300
1.5
1.0
0.5
0.0
-0.5
-1.0
2.5e-9
2.0e-9
1.5e-9
1.0e-9
5.0e-10
0.0

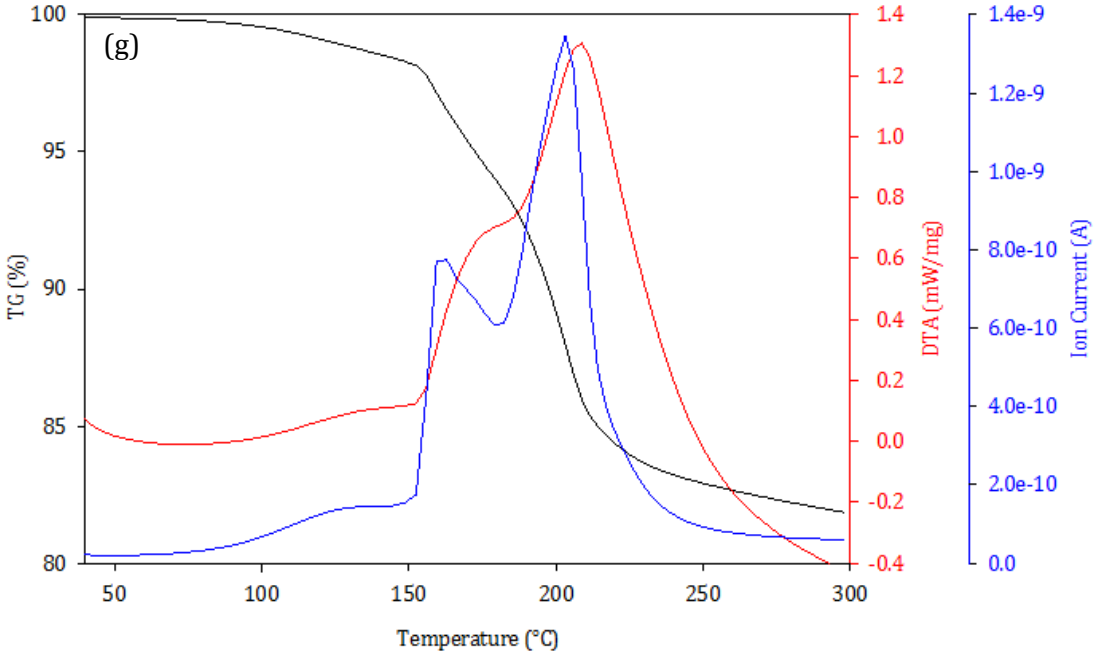
(g)
TG (%)
DTA (mW/mg)
Ion Current (A)
Temperature (°C)

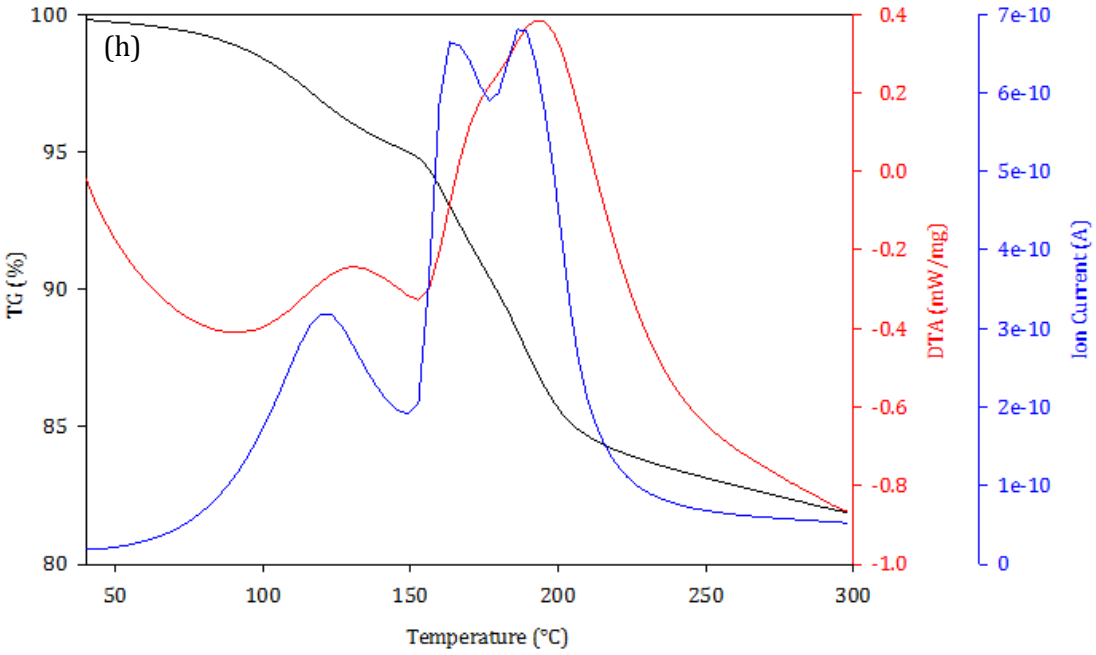
(h)
TG (%)
DTA (mW/mg)
Ion Current (A)
Temperature (°C)

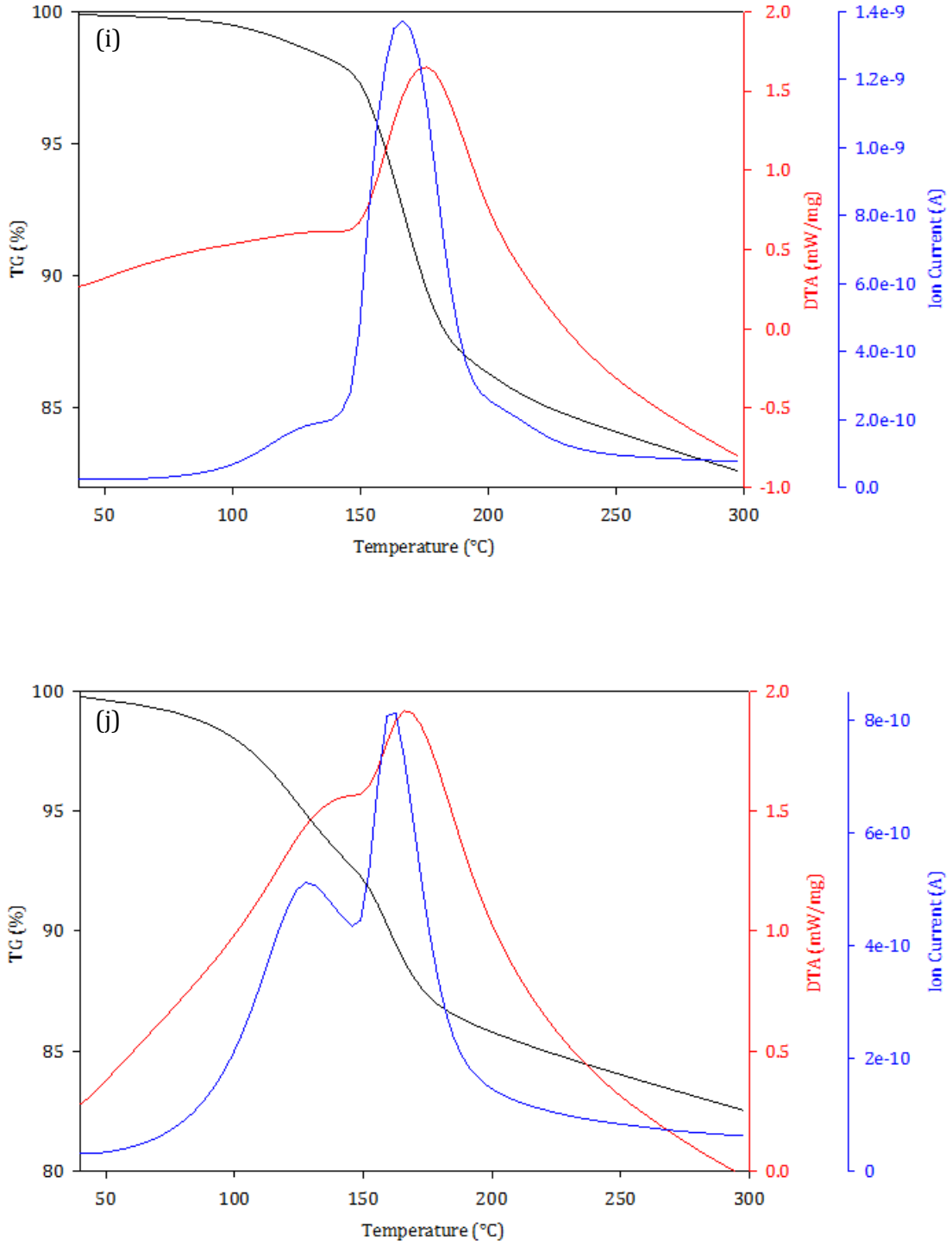

Figure 3.2: TGA-MS plots of the fluorophosphate doped sulphate series $Ca(SO_4)_x(PO_3F)_{1-x}\cdot 2H_2O$ for compositions x = 0.9-0 (a-j). The plots show the mass loss (black), the DTA line (red) and the ions with m/z ratio of 18 (blue)

Table 3.2: Summarised TGA data for two identical batches of the fluorophosphate doped sulphate materials showing the water losses and temperatures

$Ca(SO_4)_x(PO_3F)_{1-x}\cdot xH_2O$ Systems														
Composition	**Overall H_2O Content**		**Water Loss 1**				**Water Loss 2**				**Water Loss 3**			
	Batch 1	**Batch 2**	**Batch 1**	**Temp (°C)**	**Batch 2**	**Temp (°C)**	**Batch 1**	**Temp (°C)**	**Batch 2**	**Temp (°C)**	**Batch 1**	**Temp (°C)**	**Batch 2**	**Temp (°C)**
$CaSO_4\cdot xH_2O$	1.97	1.97	1.54	-	1.44	167.2	0.44	-	0.52	211.8	-	-	-	-
$Ca(SO_4)_{0.9}(PO_3F)_{0.1}\cdot xH_2O$	1.97	1.97	1.42	-	1.14	182.4	0.55	-	0.83	213.2	-	-	-	-
$Ca(SO_4)_{0.8}(PO_3F)_{0.2}\cdot xH_2O$	1.97	1.97	1.21	-	1.17	192.0	0.76	-	0.80	218.8	-	-	-	-
$Ca(SO_4)_{0.7}(PO_3F)_{0.3}\cdot xH_2O$	1.95	1.92	0.55	-	0.44	180.9	1.40	-	0.64	203.9	-	-	0.84	214.1
$Ca(SO_4)_{0.6}(PO_3F)_{0.4}\cdot xH_2O$	1.93	1.91	0.43	-	0.49	171.5	1.45	-	1.42	211.8	-	-	-	-
$Ca(SO_4)_{0.5}(PO_3F)_{0.5}\cdot xH_2O$	1.81	1.84	0.52	-	0.52	166.5	1.29	-	1.32	207.2	-	-	-	-
$Ca(SO_4)_{0.4}(PO_3F)_{0.6}\cdot xH_2O$	1.78	1.77	0.55	-	0.55	162.8	1.22	-	1.22	208	-	-	-	-
$Ca(SO_4)_{0.3}(PO_3F)_{0.7}\cdot xH_2O$	1.99	1.69	0.57	-	0.68	159.7	1.42	-	1.01	204.8	-	-	-	-
$Ca(SO_4)_{0.2}(PO_3F)_{0.8}\cdot xH_2O$	1.72	1.69	-	-	0.49	120.8	-	-	1.21	163.1	-	-	0.75	187.1
$Ca(SO_4)_{0.1}(PO_3F)_{0.9}\cdot xH_2O$	1.40	1.62	0.37	-	0.22	132.2	1.03	-	1.40	165.7	-	-	-	-
$CaPO_3F\cdot xH_2O$	1.33	1.63	0.56	-	0.66	126.8	0.77	-	0.97	179.6	-	-	-	-

3.4 NPD Rietveld Refinements of the $Ca(SO_4)_x(PO_3F)_{1-x}\cdot 2H_2O$ series

3.4.1 $CaSO_4\cdot 2H_2O$ (x = 1)

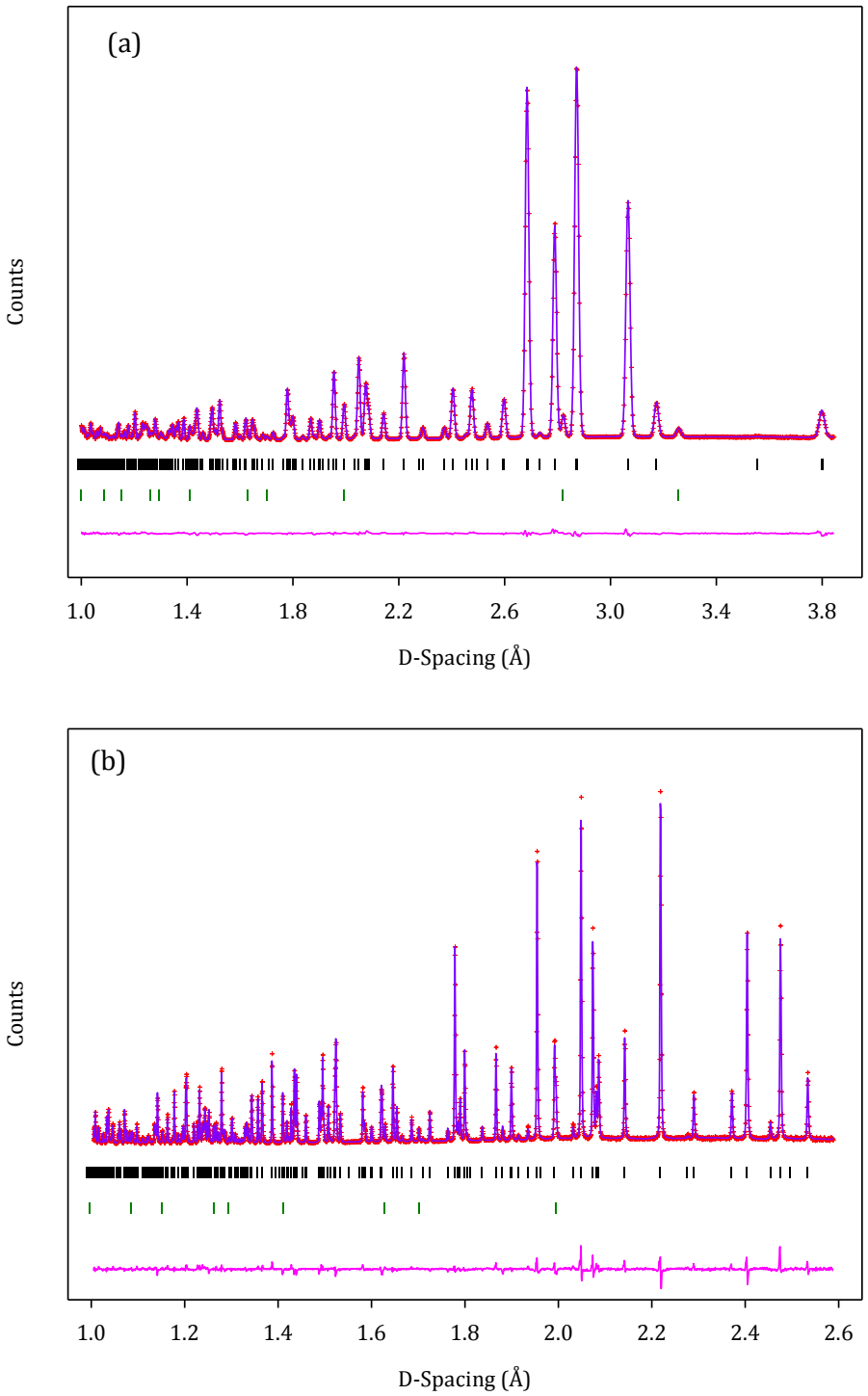

Figure 3.3: Final observed (red), calculated (purple) and difference profiles (pink) of the NPD refinement of $CaSO_4\cdot 2H_2O$ (a) 90° bank (b) back scattering bank
Reflection positions for $CaSO_4\cdot 2H_2O$ and NaCl are shown as vertical tickmarks (black and green respectively)

3.4.2 $Ca(SO_4)_{0.8}(PO_3F)_{0.2}\cdot 2H_2O$ (x = 0.8)

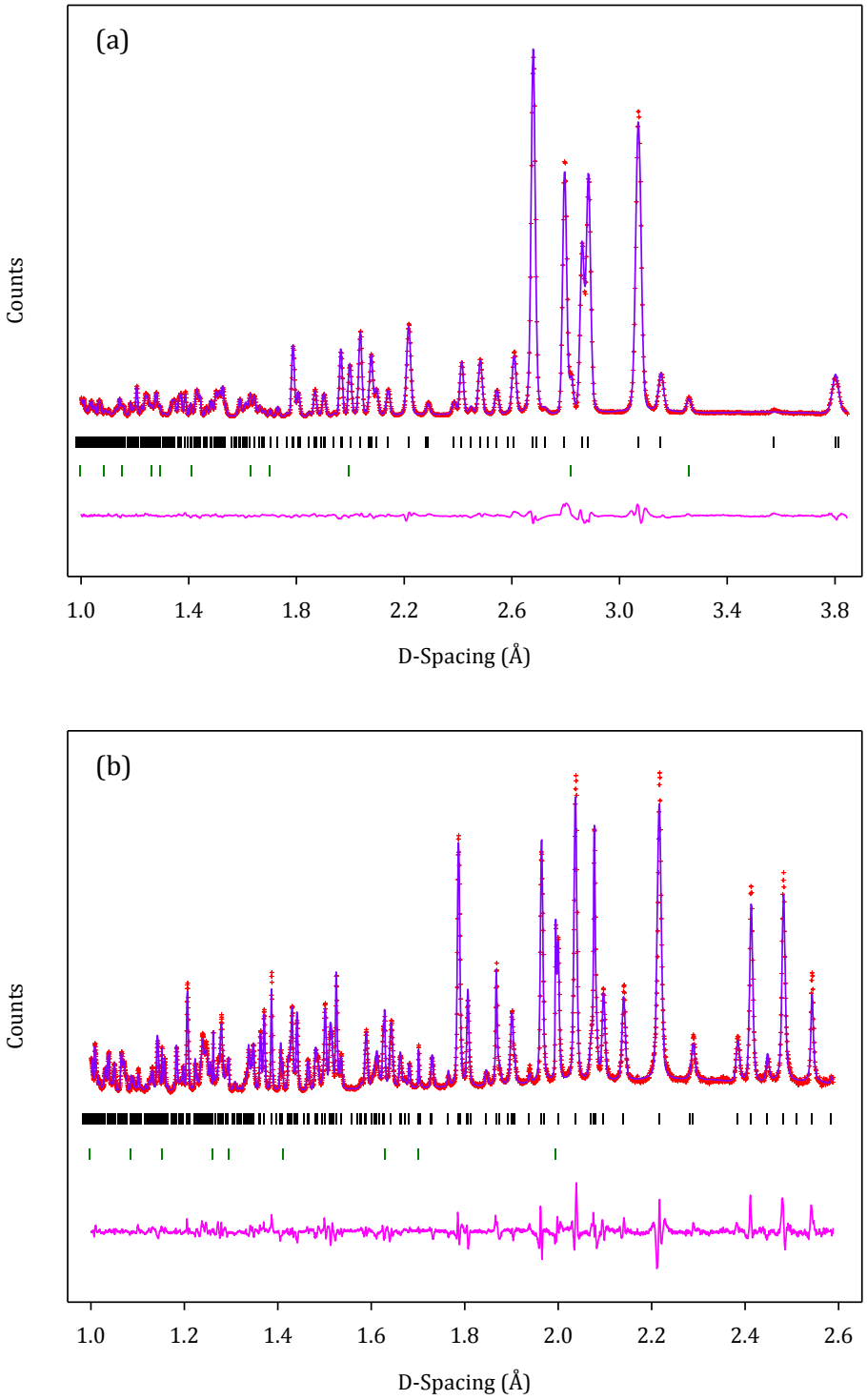

Figure 3.4: Final observed (red), calculated (purple) and difference profiles (pink) of the NPD refinement of $Ca(SO_4)_{0.8}(PO_3F)_{0.2}\cdot 2H_2O$ (a) 90° bank (b) back scattering bank Reflection positions for $Ca(SO_4)_{0.8}(PO_3F)_{0.2}\cdot 2H_2O$ and NaCl are shown as vertical tickmarks (black and green respectively)

3.4.3 $Ca(SO_4)_{0.6}(PO_3F)_{0.4}\cdot 2H_2O$ (x = 0.6)

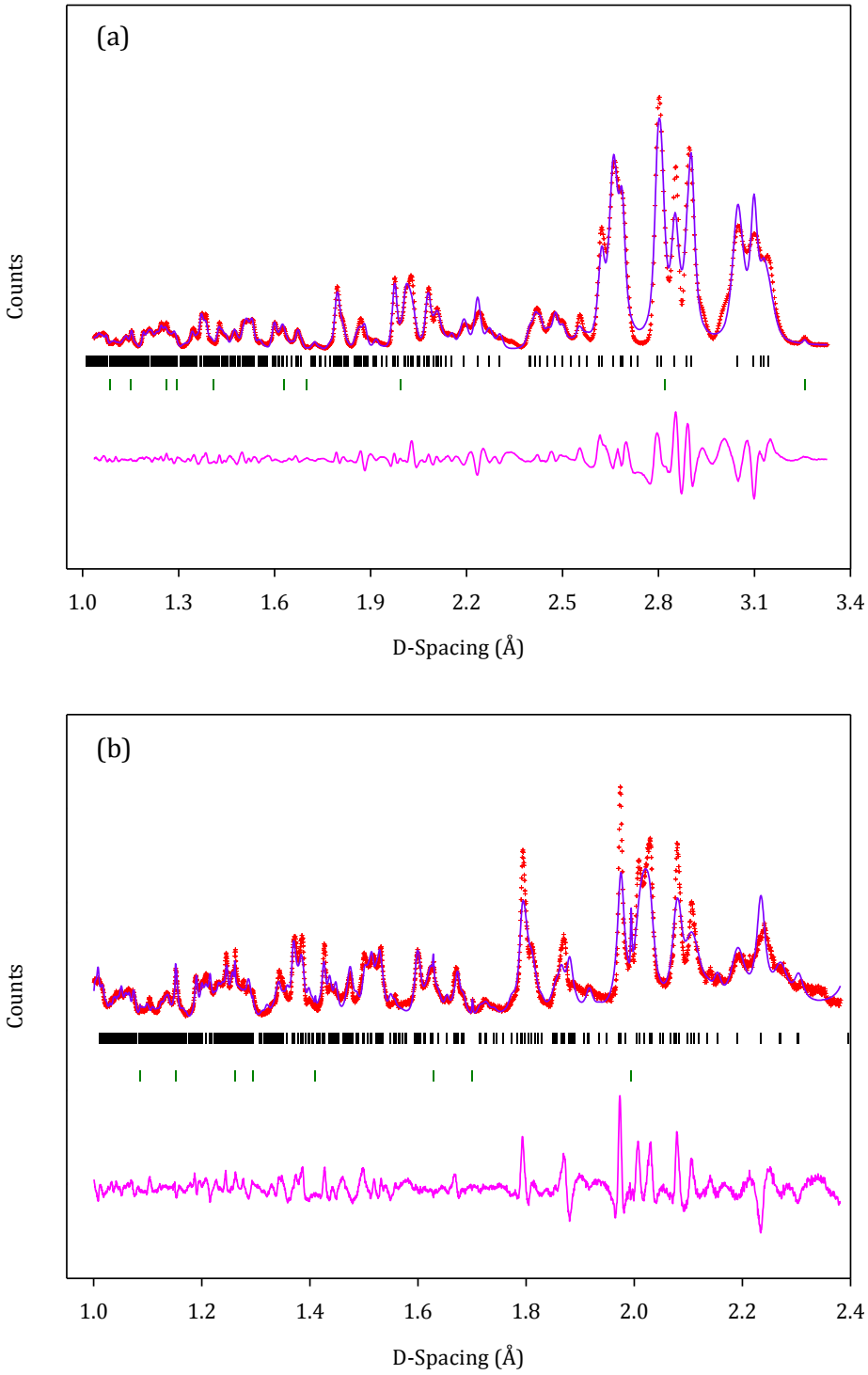

Figure 3.5: Final observed (red), calculated (purple) and difference profiles (pink) of the NPD refinement of $Ca(SO_4)_{0.6}(PO_3F)_{0.4}\cdot 2H_2O$ (a) 90° bank (b) back scattering bank Reflection positions for $Ca(SO_4)_{0.6}(PO_3F)_{0.4}\cdot 2H_2O$ and NaCl are shown as vertical tickmarks (black and green respectively)

3.4.4 $Ca(SO_4)_{0.4}(PO_3F)_{0.6}\cdot 2H_2O$ (x = 0.4)

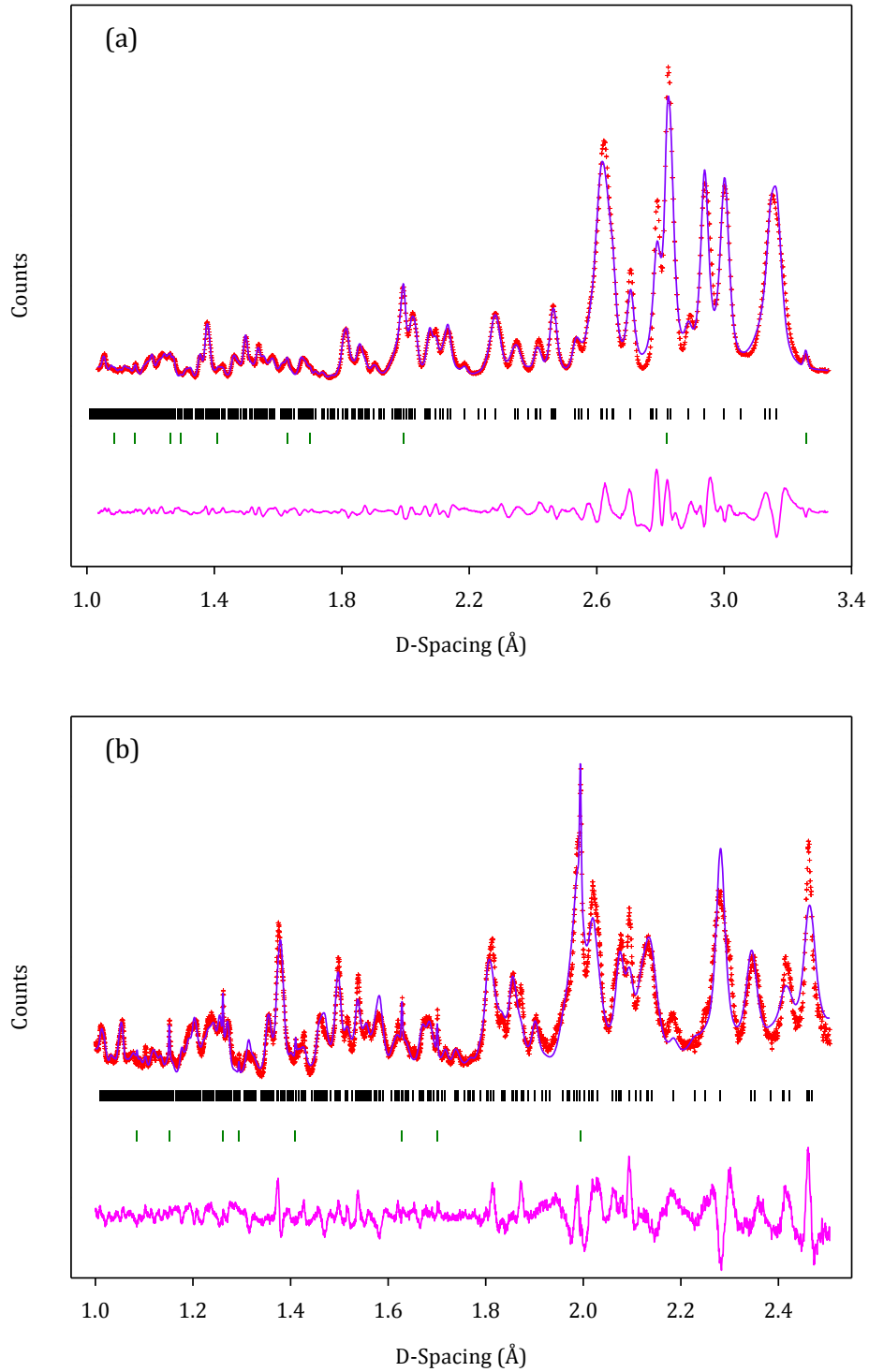

Figure 3.6: Final observed (red), calculated (purple) and difference profiles (pink) of the NPD refinement of $Ca(SO_4)_{0.4}(PO_3F)_{0.6}\cdot 2H_2O$ (a) 90° bank (b) back scattering bank Reflection positions for $Ca(SO_4)_{0.4}(PO_3F)_{0.6}\cdot 2H_2O$ and NaCl are shown as vertical tickmarks (black and green respectively)

3.4.5 $Ca(SO_4)_{0.3}(PO_3F)_{0.7}\cdot 2H_2O$ (x = 0.3)

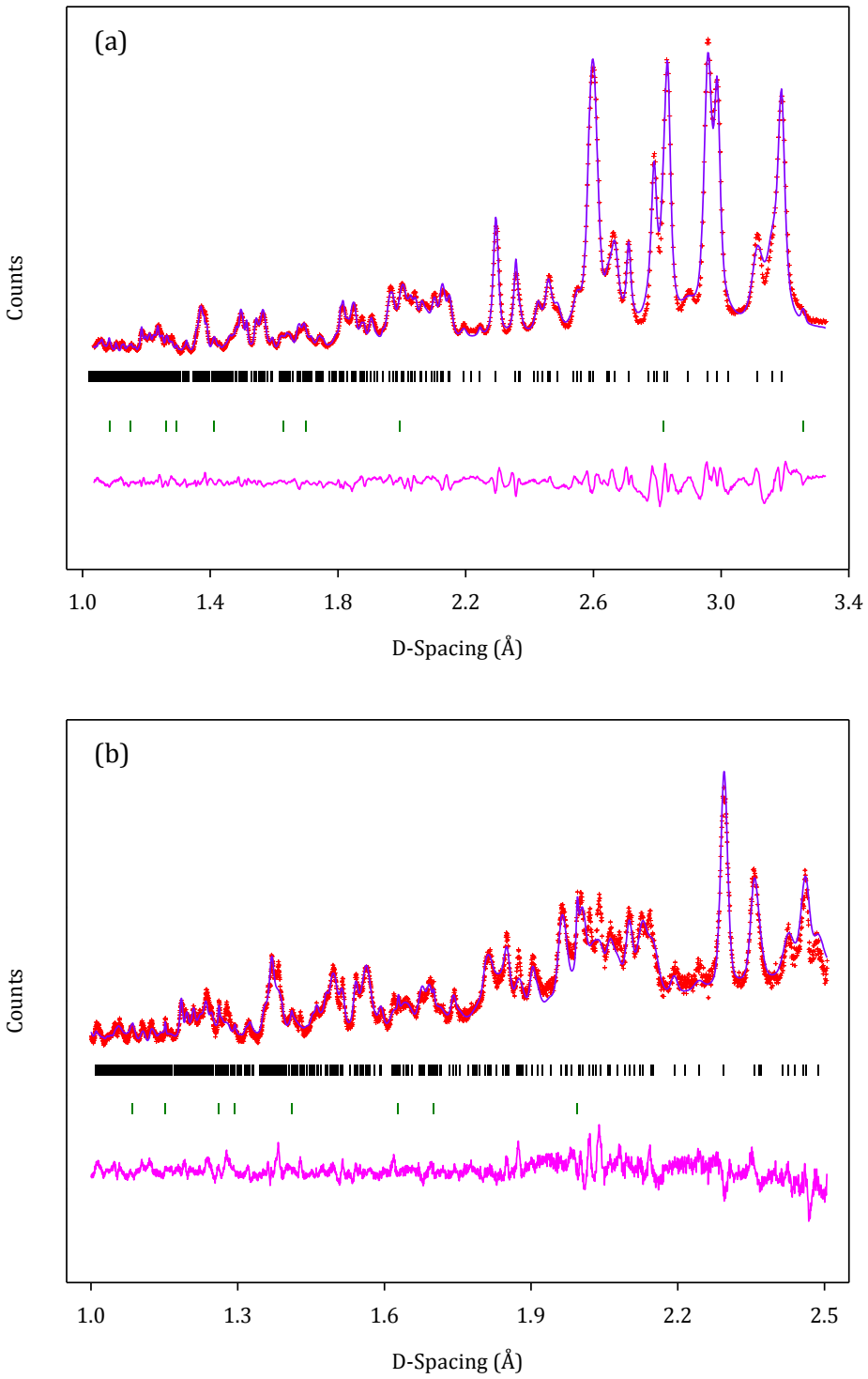

Figure 3.7: Final observed (red), calculated (purple) and difference profiles (pink) of the NPD refinement of $Ca(SO_4)_{0.3}(PO_3F)_{0.7}\cdot 2H_2O$ (a) 90° bank (b) back scattering bank Reflection positions for $Ca(SO_4)_{0.3}(PO_3F)_{0.7}\cdot 2H_2O$ and NaCl are shown as vertical tickmarks (black and green respectively)

3.4.6 $CaPO_3F{\cdot}2H_2O$ (x = 0)

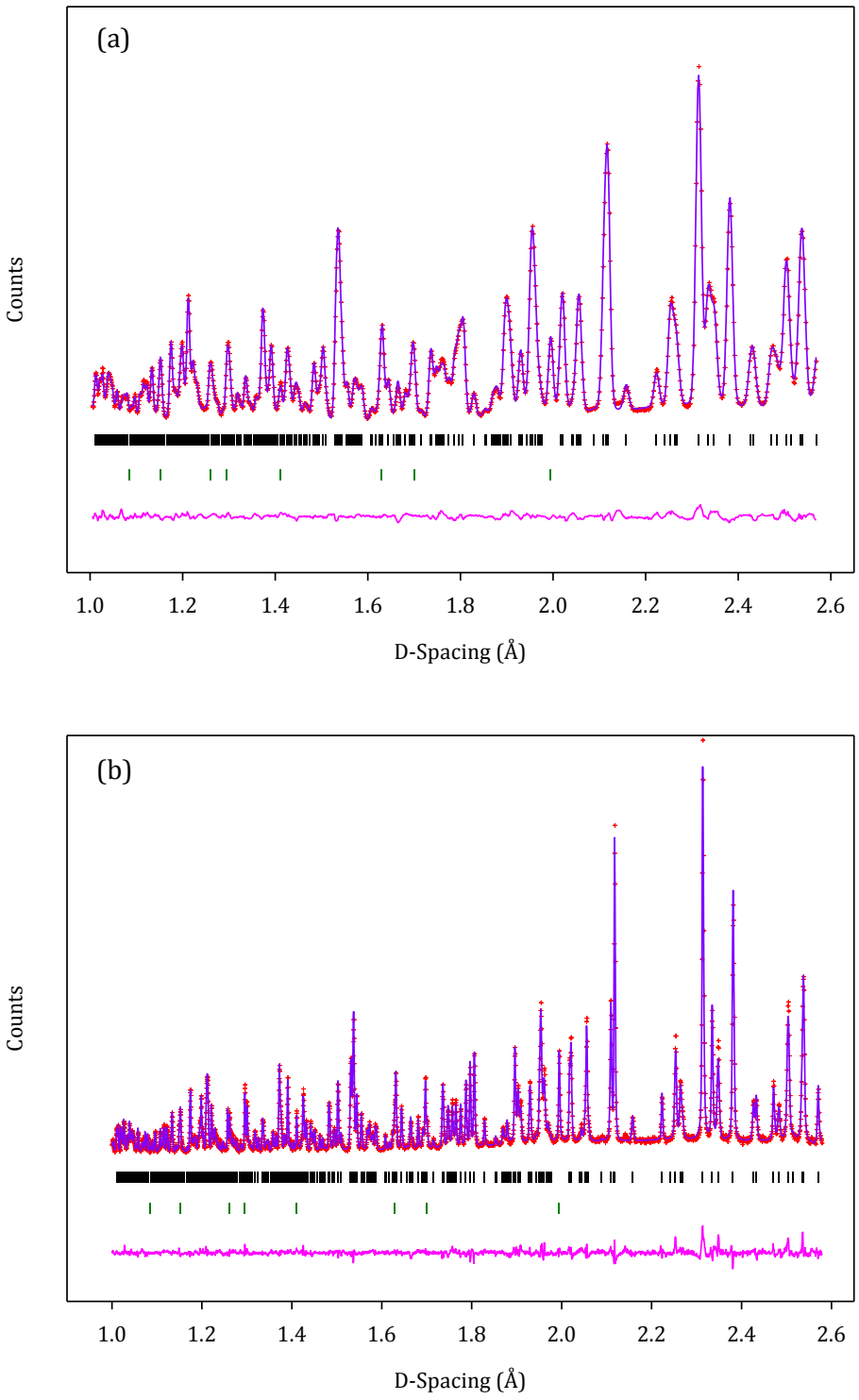

Figure 3.8: Final observed (red), calculated (purple) and difference profiles (pink) of the NPD refinement of $CaPO_3F{\cdot}2H_2O$ (a) 90° bank (b) back scattering bank
Reflection positions for $CaPO_3F{\cdot}2H_2O$ and NaCl are shown as vertical tickmarks (black and green respectively)

3.5 Unit Cell Conversion

Conversion of triclinic unit cell ($P\bar{1}$) system to a pseudo monoclinic system ($I\bar{1}$)

The original unit cell parameters a, b, c, α, β, and ɣ were converted to the new unit cell parameters a_2, b_2, c_2, α_2, β_2, and γ_2 in space group $I\bar{1}$, using the following equations:-

$$\boldsymbol{a_2} = c$$

$$\boldsymbol{b_2} = \sqrt{4a^2 + b^2 + c^2 + 4ab\cos(\gamma) + 4ab\cos(\beta) + 2bc\cos(\alpha)}$$

$$\boldsymbol{c_2} = b$$

$$\boldsymbol{\alpha_2} = \frac{\left[\cos^{-1}\left(\frac{2a\cos(\gamma) + b_1 + c\cos(\alpha)}{b_2}\right)\right] \times 180}{\pi}$$

$$\boldsymbol{\beta_2} = \frac{180 \times \alpha}{\pi}$$

$$\boldsymbol{\gamma_2} = \frac{\left[\cos^{-1}\left(\frac{2a\cos(\beta) + c_1 + \mathrm{b}\cos(\alpha)}{b_2}\right)\right] \times 180}{\pi}$$

Table 3.3: Original Lattice Parameters for all members of the $Ca(SO_4)_x(PO_3F)_{1-x}\cdot 2H_2O$ Series obtained from both PXRD (black) and NPD data (purple)

Composition	Original Lattice Parameters for XRD and NPD Data						
	a **(Å)**	***b*** **(Å)**	***c*** **(Å)**	***α*** **(°)**	***β*** **(°)**	***γ*** **(°)**	**Volume (Å³)**
$CaSO_4\cdot xH_2O$	5.67327(4) 5.67903(1)	15.1955(2) 15.20049(9)	6.52131(5) 6.52768(4)	90 90	118.4767(4) 118.4995(2)	90 90	494.172(9) 495.230(4)
$Ca(SO_4)_{0.9}(PO_3F)_{0.1}\cdot 2H_2O$	5.67656(6)	15.2153(2)	6.4979(7)	90	118.2871(5)	90	494.21(1)
$Ca(SO_4)_{0.8}(PO_3F)_{0.2}\cdot 2H_2O$	5.6817(1) 5.69019(6)	15.2404(4) 15.2566(2)	6.4829(1) 6.48505(8)	90 90	118.129(1) 118.1083(7)	90 90	495.06(2) 496.586(11)
$Ca(SO_4)_{0.7}(PO_3F)_{0.3}\cdot 2H_2O$	5.6620(3)	15.1977(10)	6.4348(3)	90	117.951(2)	90	489.12(5)
$Ca(SO_4)_{0.6}(PO_3F)_{0.4}\cdot 2H_2O$	9.1911(12) 9.1763(8)	6.3045(6) 6.3140(4)	5.6922(6) 5.7024(4)	115.288(8) 115.428(5)	117.740(6) 117.649(5)	94.239(12) 93.997(7)	248.15(5) 248.934(34)
$Ca(SO_4)_{0.5}(PO_3F)_{0.5}\cdot 2H_2O$	9.1280(14)	6.3133(9)	5.6911(7)	115.651(9)	117.263(7)	93.738(14)	248.19(6)
$Ca(SO_4)_{0.4}(PO_3F)_{0.6}\cdot 2H_2O$	9.0328(10) 9.0405(7)	6.3171(5) 6.3365(5)	5.6882(5) 5.7093(5)	116.286(7) 116.479(5)	116.651(5) 116.438(5)	92.706(9) 92.378(6)	247.55(5) 250.10(4)
$Ca(SO_4)_{0.3}(PO_3F)_{0.7}\cdot 2H_2O$	8.9567(7) 9.0055(4)	6.3261(3) 6.3602(3)	5.6892(4) 5.7207(2)	117.096(4) 117.199(3)	115.925(3) 115.915(3)	91.898(6) 91.713(4)	246.00(3) 251.094(23)
$Ca(SO_4)_{0.2}(PO_3F)_{0.8}\cdot 2H_2O$	8.9274(8) 8.9409(15)	6.3800(4) 6.3895(10)	5.7235(4) 5.7321(9)	117.697(4) 117.721(3)	115.191(4) 115.113(3)	91.851(6) 91.757(4)	250.18(4) 251.63(7)
$Ca(SO_4)_{0.1}(PO_3F)_{0.9}\cdot 2H_2O$	8.7918(7)	6.4185(4)	5.7208(4)	118.241(4)	113.230(4)	93.020(5)	249.664(3)
$CaPO_3F\cdot 2H_2O$	8.6348(2) 8.65312(10)	6.4446(1) 6.45878(7)	5.7217(1) 5.73849(9)	118.961(1) 118.9996(8)	110.983(1) 110.9081(5)	94.088(2) 94.1504(6)	248.17(1) 249.938(6)

Table 3.4: Converted Lattice Parameters for all members of the $Ca(SO_4)_x(PO_3F)_{1-x}\cdot 2H_2O$ Series obtained from both PXRD (black) and NPD data (purple)

Composition	Converted Lattice Parameters for XRD and NPD Data ($I\bar{1}$)						
	a **(Å)**	***b*** **(Å)**	***c*** **(Å)**	***α*** **(°)**	***β*** **(°)**	***γ*** **(°)**	**Volume (Å³)**
$CaSO_4\cdot xH_2O$	5.67327(4) 5.67903(1)	15.1955(2) 15.20049(9)	6.52131(5) 6.52768(4)	90 90	118.4767(4) 118.4995(2)	90 90	494.172(9) 495.230(4)
$Ca(SO_4)_{0.9}(PO_3F)_{0.1}\cdot 2H_2O$	5.67656(6)	15.2153(2)	6.4979(7)	90	118.2871(5)	90	494.21(1)
$Ca(SO_4)_{0.8}(PO_3F)_{0.2}\cdot 2H_2O$	5.6817(1) 5.69019(6)	15.2404(4) 15.2566(2)	6.4829(1) 6.48505(8)	90 90	118.129(1) 118.1083(7)	90 90	495.06(2) 496.59(1)
$Ca(SO_4)_{0.7}(PO_3F)_{0.3}\cdot 2H_2O$	5.6620(3)	15.1977(10)	6.4348(3)	90	117.951(2)	90	489.12(5)
$Ca(SO_4)_{0.6}(PO_3F)_{0.4}\cdot 2H_2O$	5.6922(6) 5.7024(4)	16.274(5) 16.279(3)	6.3045(6) 5.7024(4)	81.11(2) 80.86(1)	115.288(8) 115.428(5)	109.97(2) 109.84(2)	496.30(5) 497.87(3)
$Ca(SO_4)_{0.5}(PO_3F)_{0.5}\cdot 2H_2O$	5.6911(7)	16.255(4)	6.3133(9)	80.583(2)	115.651(1)	109.42(2)	496.38(6)
$Ca(SO_4)_{0.4}(PO_3F)_{0.6}\cdot 2H_2O$	5.6882(5) 5.7093(5)	16.243(3) 16.309(3)	6.3171(5) 6.3365(5)	79.55(2) 79.26(1)	116.286(7) 116.479(5)	108.72(2) 108.47(2)	495.10(5) 500.20(4)
$Ca(SO_4)_{0.3}(PO_3F)_{0.7}\cdot 2H_2O$	5.6892(4) 5.7207(2)	16.2442(3) 16.353(2)	6.3261(3) 6.3602(3)	78.85(1) 78.70(2)	117.096(4) 117.199(3)	108.02(2) 108.017(9)	492.00(3) 502.19(2)
$Ca(SO_4)_{0.2}(PO_3F)_{0.8}\cdot 2H_2O$	5.7235(4) 5.7321(9)	16.247(3) 16.290(4)	6.3800 (4) 6.3895(10)	78.85(1) 78.76(1)	117.697(4) 117.721(3)	107.24(1) 107.24(2)	500.36(4) 503.26(7)
$Ca(SO_4)_{0.1}(PO_3F)_{0.9}\cdot 2H_2O$	5.7208(4)	16.035(3)	6.4185(4)	80.00(1)	118.241(4)	105.38(1)	499.328(3)
$CaPO_3F\cdot 2H_2O$	5.7225(1) 5.73849(9)	15.8188(8) 15.8477(4)	6.4455(1) 6.45878(1)	81.114(4) 81.202(2)	118.963(1) 119.0000(9)	103.094(3) 103.014(2)	496.54(1) 499.876(6)

3.6 SEM Images

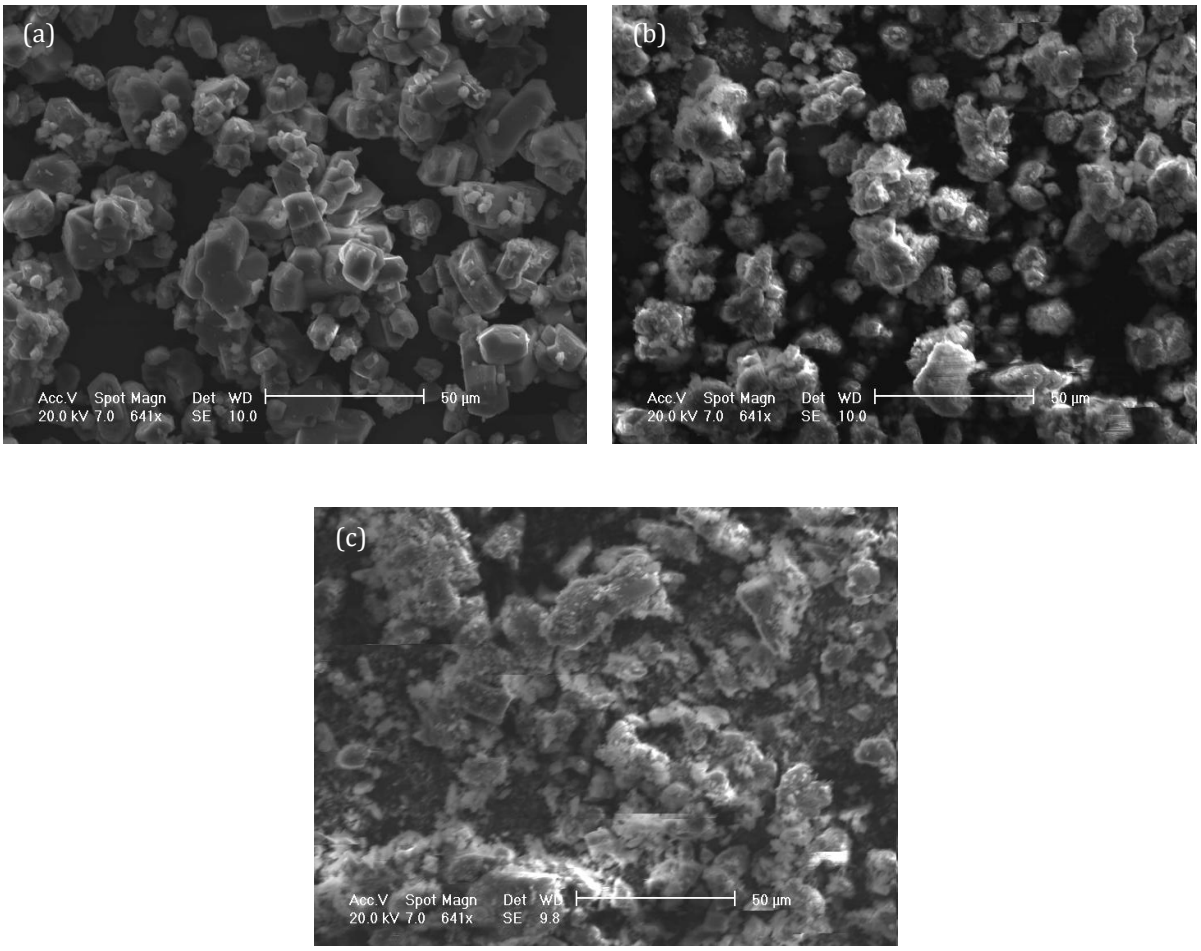

Figure 3.9: SEM Images of fluorophosphate doped calcium sulphate systems, $Ca(SO_4)_x(PO_3F)_{1-x}\cdot 2H_2O$ where x = 0.75, 0.50 and 0.25 (a-c) respectively.